Optical Modelling and Optimisation of Spheral Solar™ Cells

Raffaella Bisconti

A thesis submitted in partial requirements of the
University of Northumbria at Newcastle
for the degree of Doctor of Philosophy

In collaboration with the European Solar Test Installation (ESTI),
European Commission - Joint Research Centre, Ispra (Va) - Italy.

April 1997

Author's Declaration

I declare that the work in this thesis is my own work, and references are provided when contributions are made from other sources.

Acknowledgements

I would like to thank Professor R. Hill, Dr. H. A. Ossenbrink and Dr. N. M. Pearsall for their expert supervision and excellent guidance as well as Texas Instruments (Dallas, USA) for providing the samples.

I would also like to acknowledge the technical support provided by Mr. W. J. Zaaiman, Mr. M. Lundqvist, Dr. J. Bishop, Dr. E. Dunlop and the entire staff of the European Solar Test Installation, and Ms. J. Rundle for proof reading.

Moreover, I would like to acknowledge Prof. R. Hezel, Dr. A. Aberle, the students of ISFH in Emmerthal as well as the students of FhG ISE for their hospitality and for many fruitful discussions.

Finally, a special thanks to my family and Marcello for their constant support and patience.

Abstract

Spheral Solar™ Cells are new technology photovoltaic devices originally developed and patented by Texas Instruments Inc. in the USA and since the beginning of 1996 owned by Ontario Hydro Technologies (Canada).

Despite the extensive work at Texas Instruments on the production technology, only very little effort has been devoted to studying the optical characteristics of the cells and to optimising the light gathering by specific reflectance-reducing cover structures. Therefore, this was the main aim of this research project.

The approach to this study was based first on the acquisition of a complete understanding of the optical behaviour of the cells by carrying out a set of performance measurements followed by an optical characterisation, and then on the development of tools to be employed for the optimisation process.

The innovation and relevance of the project is mainly related to the unique geometry of these devices. In fact, the optical modelling of Spheral Solar™ Cells required the development of a dedicated simulation programme, based on a spherical co-ordinate system as well as on Monte Carlo ray-tracing techniques, which could reproduce the optics of the devices and allow the cover modelling and optimisation.

In order to validate the optical modelling, two experimental facilities were designed and set-up as a part of this project: a spectrophotometer and a multi-laser scanner. These facilities are working to the desired specifications and are now available also for other applications.

The results obtained indicated the presence of indirect trapping mechanisms and also defined the active areas of the single spheres.

On the basis of this information specific reflectance-reducing cover structures have been analysed. The proposed cover structures could improve the cell efficiency by about 25 % with an AR-coating layer and by about 15 % without it.

The results of this work could be applied to design an optimised cover for the commercial product, but this will depend on the conclusion of satisfactory agreements with the manufacturers.

Table of Contents

List of Figures

List of Tables

Nomenclature

β	Beam Inclination Angle
ϕ	Latitude (Spherical co-ordinate)
θ	Elevation (Spherical co-ordinate)
μ	Micron
λ	Wavelength (nm)
η	Efficiency
$\alpha(E)$	Absorption Coefficient for Photons of Energy E
α_{inc}	Angle of Incidence
α_{inrefl}	Angle of Internal Reflection
A	Absorptance
a-Si	Amorphous Silicon
AR	AntiReflective
A_{sr}	Direct Cell Absorptance
BB	Backbond
BSE	Backside Etch
CBD	Chemical Bath Deposition
CSS	Close Spaced Sublimation
CSVT	Close Spaced Vapour Transport
CVD	Chemical Vapour Deposition
CZ	Chockalzky
D	Diode Thermal Voltage
E	Energy of a Photon
e	Electron Charge (1.602×10^{-19} C)
ED	Electrodeposition
F_{al}	Aluminium Factor
FB	Front Bond
FF	Fill Factor
F_{sh}	Shadowing Factor
FST	Thinned Frontside
HWE	Hot Wall Epitaxy
I	Current Output of a Solar Cell
I	Irradiance

IR	Infrared Radiation
Isc	Short-Circuit Current of a Solar Cell
Jsc	Short-Circuit Current Density of a Solar Cell
k	Index of Refraction (Imaginary Component)
LBIC	Light Beam Induced Current
LBIV	Light Beam Induced Voltage
MC	Monte Carlo
MCZ	Magnetic Confinement Growth on CZ Silicon
MG	Metallurgical Grade
n	Index of Refraction (Real Component)
NIR	Near Infrared Radiation
PECVD	Plasma Enhanced Chemical Vapour Deposition
PERL	Passivated Emitter Rear Locally Diffused Cell
PESC	Passivated Emitter Solar Cell
Pmax	Maximum Power Output of a Solar Cell under Standard Test Conditions
PV	Photovoltaic
PVD	Physical Vapour Deposition
q	Electronic Charge (C)
r	Sphere Radius
R	Reflectance
R_{al}	Aluminium Reflectance
R_{dr}	Direct Reflections Reflectance
RMS	Mean Squared Root
S_{al}	Aluminium Surface
SC	Scribing
SD	Sputter Deposition
SED	Electro-Dissolution
SG	Semiconductor Grade
Si	Silicon
S_{it}	Indirect trapping Surface
SLR	Stacked Layer Reaction
SP	Screen Printing
SPL	Spray Phyrolysis
SR	Spectral Responsivity of a Solar Cell
S_{sh}	Shadowed Surface
S_{sph}	Sphere Surface

STC	Standard Test Conditions
SVR	Solid Vapour Reaction
T	Transmittance
TIR	Total Internal Reflection
UV	Ultra Violet Radiation
V	Voltage across a Solar Cell
VIS	Visible radiation
Voc	Open-Circuit Voltage of a Solar Cell

Introduction

Today, nations around the globe are turning to renewables as clean energy alternatives. Photovoltaics (PV), in particular, are gaining interest as an effective and convenient approach for supplying power close to its point of use. From individual dwellings, to villages, to commercial and residential homes (and an abundance of other different applications in-between) PV is proving itself to be a viable option.
Just as importantly, PV holds tremendous economic promise. For those countries investing early solar energy could become the fuel for economic development through new jobs and increased revenues.
But, despite these advantages, there are some significant barriers that PV must still overcome. Topping the list is price, followed closely by efficiency limits and integration issues associated with weight and durability. Since the silicon slices used in conventional PV module manufacturing are rigid and extremely fragile, they must be protected with heavy glass coverings that represent greater then 65 percent of the total module weight. Along with contributing to module costs, this extra weight can impact the balance of the system, adding money for such things as construction and structural requirements.

Efforts to develop a low cost flexible and durable solar technology were carried out for more than a decade at Texas Instruments (TI), Dallas, USA. Since 1985, this research was co-funded by Southern California Edison, the second largest investor-owned utility in the United States.

The TI approach uses a unique silicon process and energy efficient crystal growth, which holds the potential for significant price break-throughs as market volumes increase.
In addition, TI cells (made up of tens of thousands of purified silicon spheres bonded into aluminium) are quite flexible and durable, unlike other crystalline silicon approaches.
In a flexible configuration, weight can be significantly reduced, further decreasing costs while providing a new range of architectural possibilities.

Since the end of 1995, the entire pilot production line of TI cells and modules has been transferred to Ontario Hydro Technologies (OHT) which is the main energy utility of Ontario, Canada. OHT is nowadays setting up and testing the facility in order to manufacture more and more efficient devices, to be able to penetrate the PV market as soon as possible.

Today, the module efficiency is in the 10 percent range and if the efficiency is calculated on the total cell area, these levels increase to about 11 percent. This further improves to more than 13 percent when measured on the active cell area.

Despite the fact that a quite good knowledge of the influence of the material purity and minority carrier diffusion lengths and lifetimes on the device electrical performance has been acquired by the manufacturers in the last few years, a deep understanding of the optics of the devices was still missing and detailed studies needed to be undertaken. Preliminary studies carried out by TI, have shown that by enhancing light gathering by conformable optical coatings and flexible encapsulants, there is an opportunity to gain as much as a 20 percent efficiency boost. TI tests have shown that acrylic coatings have a lensing effect on the curved surface of each sphere, repeatedly showing efficiency boosts in the 15-20 percent range.

This was the background of the present thesis work which first aims to reproduce the optics of TI cells by ray-tracing modelling and thus to investigate how to increase their efficiency by means of a reflection-reducing structured and possibly flexible cover.

The objectives, approach, results and spin-off of the research work are illustrated in detail in the six sections in which the thesis is subdivided. A great effort has been undertaken in order to keep theoretical and experimental sections balanced.

Section I starts with an overview of the present state of the art of terrestrial solar cell technologies. Besides silicon, which still represents the "work horse" for the PV industry, alternative solar cell materials and designs employed in terrestrial applications are briefly discussed to give a complete idea of the many different PV options.
Efficiency record values are reported for a large variety of cells since the very first prototypes developed in the early forties.
The second part of Section 1 is dedicated to introducing the new technology of TI Spheral Solar™ Cells and Spheral Power™ Modules as well as their manufacturing processes and working principles.
The innovative aspects of the Spheral technology are pointed out, such as the potential low costs, flexibility and durability which could in future remove the main barriers to widespread use of PV.

The first part of Section 2 focuses on the electrical characterisation performed at the ESTI laboratories through performance measurements at Standard Test Conditions (STC).
The second part describes the optical characterisation of the devices, carried out by photometrical and laser scanning techniques.
A brief description of the experimental set-up employed both for electrical and optical measurements is also provided.
Particular attention is paid to the multi-laser scan facility *ESTIScan*, which has been expressly developed (designed and realised) during this research work and that is presently available at the ESTI laboratories also for other research purposes.

The development of the simulation tool necessary to reproduce the optics of Spheral Solar™ Cells is illustrated in Section 3. This Section accurately analyses all the aspects of the optical model employed for the simulation of PV silicon devices made up of many spherical layers.
It also describes the model which was the basis of the Monte Carlo ray-tracing code *WinTrace*, expressly developed for simulating the unique light gathering features of Spheral Solar™ Cells.
New concepts such as those of local (or direct) and non-local (or indirect) light trapping are introduced. Furthermore, the effect on the cell performance of combined optical factors, typical of the spherical devices, is analysed. Angular dependencies of these factors are also taken into consideration for a complete and successful simulation of Spheral Solar™ Cells, based not only on different light wavelengths but also on various illumination angles.

As already mentioned the ray-tracing code *WinTrace* has a Monte Carlo *core* which means that it has a statistical nature. Therefore, statistical considerations preliminary to the choice of meaningful statistics for the simulations are necessary. These considerations, together with the basics of the Monte Carlo and Random Numbers Generation techniques, are summarised in Section 4.

Section 5 is dedicated to the validation of the mathematical algorithms introduced into the code. This validation is of fundamental importance to demonstrate the reliability of *WinTrace* simulations, in view of the utilisation of the code for optimising the optical performances of the devices under study.
Several results of *WinTrace* are illustrated in this Section both compared to those of other simulation codes and to experimental measurements.

The good agreement among the various results discussed in Section 5 suggests the possibility of employing the code for the design of an optimised reflectance-reducing cover for Spheral Solar™ Cells. The performance of such a reflectance-reducing cover on a Spheral Solar™ Cell has been simulated and optimised by the ray-tracing code *WinTrace*, and is illustrated in Section 6. To achieve the design optimisation, several encapsulants of different materials, geometries and structures have been investigated, verifying the enhancement of the cell performance on the basis of experimental measurements made on bare cells.
Cost evaluations and manufacturing implications are also discussed in Section 6, as well as the spin-off of the work consisting of the practical realisation of the designed cover.

The appendices annexed to the work contain the most important optical data of the involved materials and several details on the input/output files of the code. The most interesting simulation routines are also reported.

SECTION 1

BACKGROUND

1.1. Photovoltaic Terrestrial Cells: an Overview

During the past 10 years the Photovoltaic module industry has experienced a steady growth of 15 % per annum, however on a still fairly small absolute scale. The 1995 module production amounted to about 80 MWp (p=peak) world-wide.

Today's solar cell production is almost exclusively based on silicon. About 80 % of all module are fabricated using crystalline silicon cells (polycrystalline and single crystalline) and about 20 % are based on amorphous silicon thin film cells.

On a laboratory and/or pilot production scale, there are several alternative thin film solar cells under development which may penetrate the market in the future [1].

The presently dominant crystalline silicon solar cell has the disadvantage of low light absorption and, as a consequence it requires a cell thickness of 200 to 350 μm. With a proper application of light trapping schemes it would be possible to reduce substantially the thickness of silicon wafer in the future. Therefore, a considerable material and cost reduction is expected from thin film solar cells, whose thickness is at least one or two orders of magnitude smaller and which can be produced by using thin film technologies.

The most advanced thin film cells are:

1. a-Si:H (amorphous silicon) and a-(Si,Ge):H
2. CdTe/CdS
3. CIS or CIGS (copper indium diselenide or copper indium/gallium diselenide)
4. Crystalline silicon thin film
5. nanocrystalline dye sensitised electrochemical cell

Among these type of cells the a-Si:H one is produced in large quantities, however with still too low on efficiency, while the CdTe/CdS is produced only on a small production scale. Pilot productions are under preparation also for the CIS/CIGS cell.

This chapter, reviews some milestones in the history of silicon solar cells, discusses the features of modern cell design and outlines possible performance improvements which might be expected in the future.

1.1.1 Silicon Technology

1.1.1.1 Early Cell Design

The first silicon cells [2, 3, 4] resulted from interest in silicon for use in point contact rectifiers. The rectifying properties of sharp metal contacts to various crystals have been known since at least 1874. In the early days of radio, such crystals were employed as radio

receivers. With the development of thermoionic tubes, these crystals were almost all displaced, except for ultra high frequency work. The most suitable contacts for this work proved to be tungsten points to silicon surfaces. This provided the incentive for improving the purity of silicon and further understanding its properties. In studies of recrystallised melts of pure silicon prepared for these purposes, at the Bell Laboratories, well defined barriers in polycrystalline ingots grown from commercial high purity silicon were discovered. These "grown-in" junctions resulted from impurity segregation during the recrystallisation process. Furthermore, it was found that one side the junction reached a negative potential when samples were illuminated or heated. The same side had to be biased negatively to show low resistance to current flow across the barrier or across a point contact to this material. This led to the terminology of *"negative"* or *n-type* silicon for the material on this side and *"positive"* or *p-type* silicon for the material on the opposite side.

In 1941, the first photovoltaic devices based on these "grown-in" junctions were described [5].

Fig. 1.1 illustrates the evolution of the geometry of early silicon solar cells.

The rapid practical evolution of silicon technology in the 1950s provided the first prospects for practical power generation using Photovoltaics. The next performance increase arose as a result of placing one contact on the top surface and finally extending this concept to contact fingers. By the early 1960's, cell design had reached a stage which was to remain relatively stable for a decade. In that period, due to the increasing interest in using solar cells in spacecraft, there was a shift in emphasis from n-type to p-type substrates. In fact, p-type substrates show a better radiation resistance fundamental for space application. The evolution of cell design in the sixties is shown in Fig. 1.2.

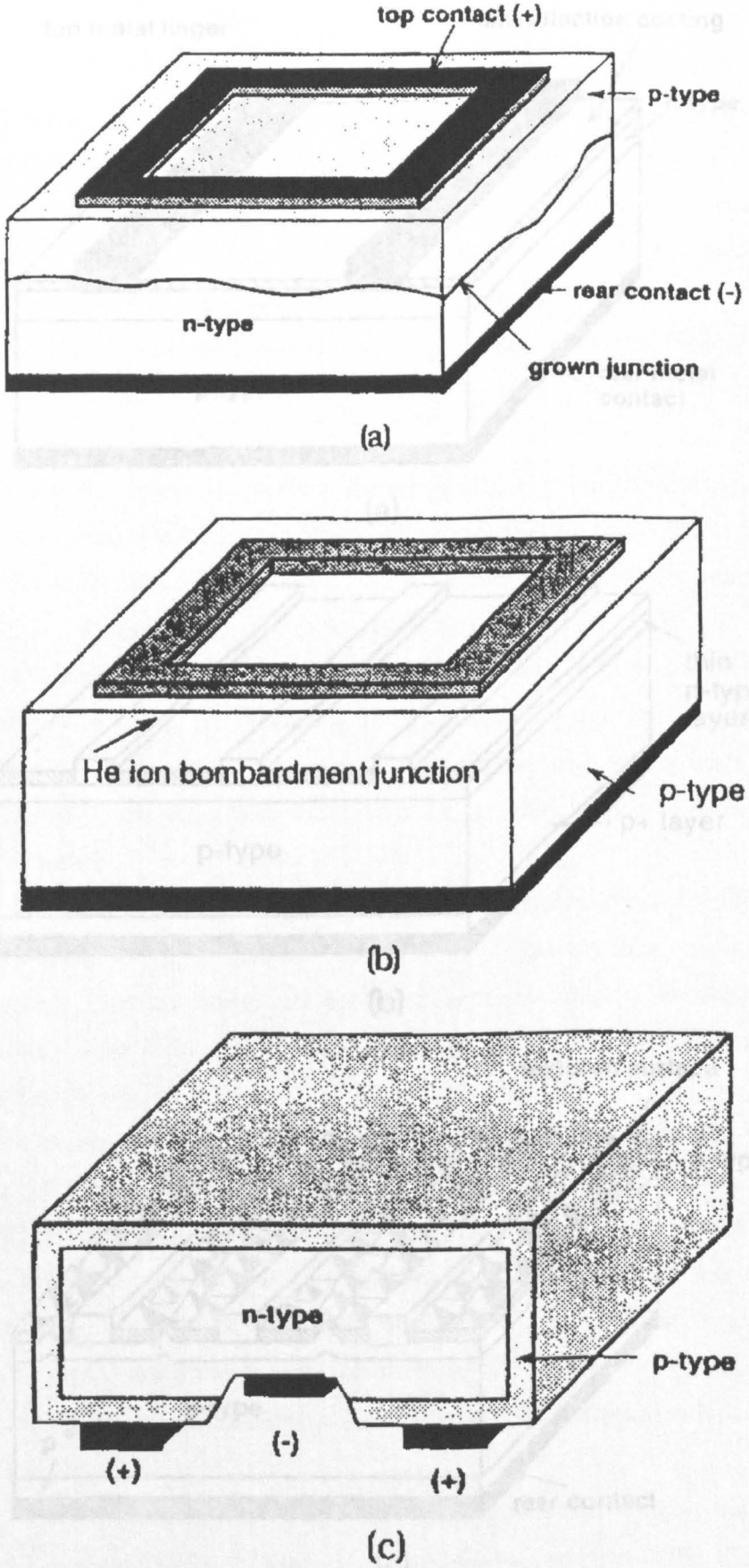

Fig. 1.1- (a) Early silicon solar cell (1941); (b) helium-ion bombarded junction device (1952); (c) first modern silicon cell (1954), fabricated on single crystalline silicon wafer, with the p-n junction formed by dopant diffusion. (Reproduced from [2])

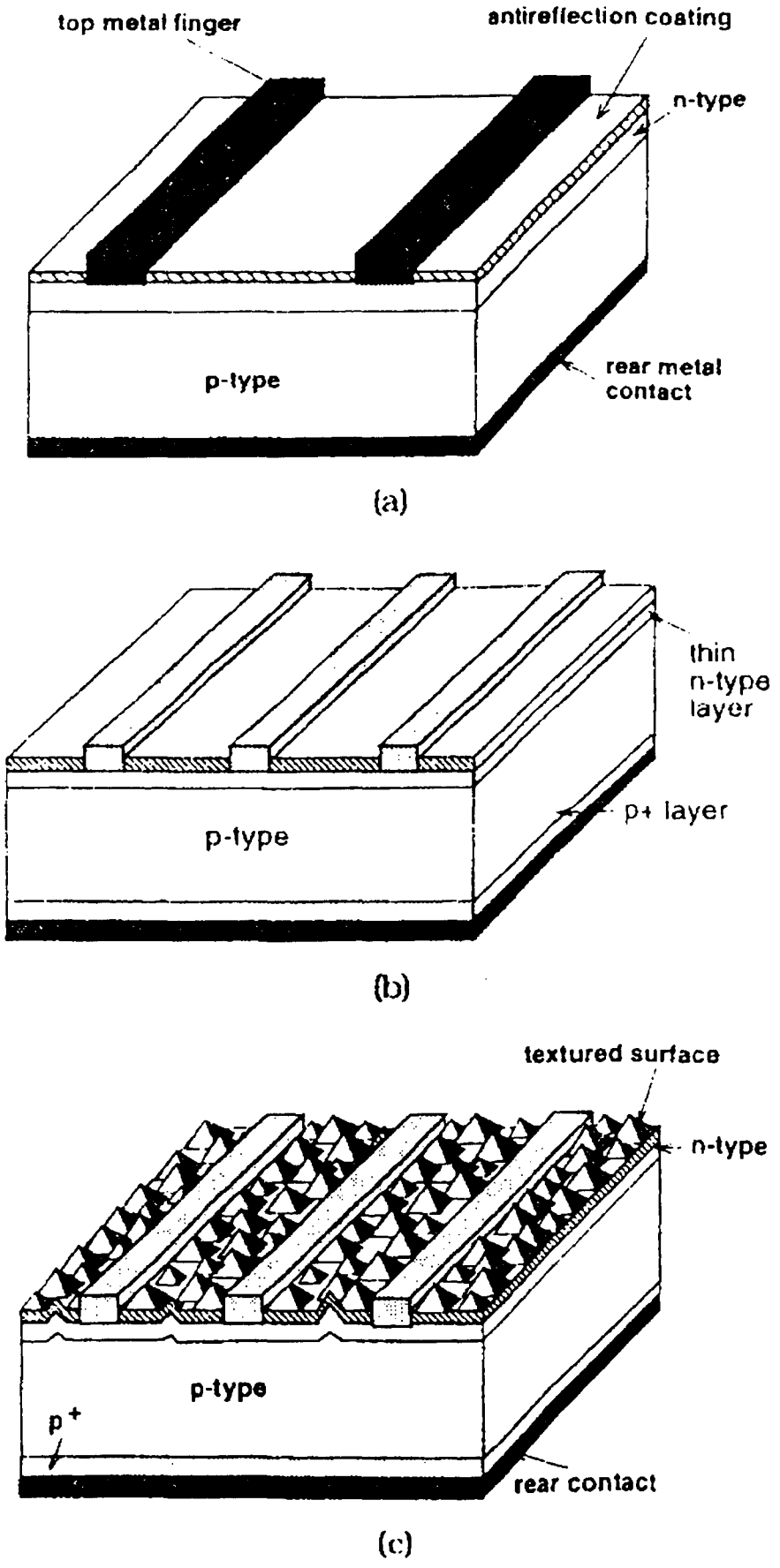

Fig. 1.2 - (a) Space silicon cell design developed in the early 1960's; (b) shallow junction "violet" cell; (c) chemically textured non reflective "black" cell. (Reproduced from [2])

1.1.1.2 Modern Cell Processing

To make silicon cells of reasonable performance, large-grained multicrystalline or single crystalline substrates of high purity are required. The main technique for preparing crystalline silicon is the CZ method. High purity, fine-grained polysilicon is melted in a quartz crucible. A seed is inserted into this melt and slowly withdrawn. Oxygen from the crucible is incorporated as an impurity into the growing crystal. Carbon is also introduced from heating elements, with boron usually added as a p-type dopant.

Cell manufacturers growing their own ingots often use polysilicon "off-specification" for microelectronics. Purchased wafers correspondingly are either "off-spec" or grown under relaxed quality control.

A recent refinement in microelectronics is the use of magnetic confinement (MCZ growth). By placing strong magnets around crucibles, melt convection can be controlled, improving growth conditions. MCZ silicon is suitable for fabricating very high efficiency cells, with better control over oxygen, carbon and crystal defects.

After growth, ingots can be cut into appropriate geometries, or they can alternatively be ground to uniform diameter for processing as round wafers. Frequently, NaOH etches are used to remove saw damage as to prepare the surface for texturing, which is one of the most difficult processing steps. After texturing, wafers are prepared for junction diffusion by de-ionised water rinsing.

For multicrystalline wafers, only a small fraction of grains is correctly oriented for texturing. Anisotropic etching also gives different etch rates for different grains, producing steps at grain boundaries. This can complicate the subsequent screening of metal pastes. Often, isotropic etching is used for multicrystalline material to give flat surfaces, with texturing deliberately eliminated.

Since, wafers are usually boron doped, an n-type junction is generally diffused into the cell. Phosphorus is the usual n-type diffusant. Various, phosphorus sources are used commercially. In some cases, phosphine gas is passed down the diffusion tube, in other cases, a carrier gas is passed down the tube after bubbling through liquid sources such as $POCL_3$ or PBr_3. Alternatively, a solid source such as P_3O_5 is heated at the end of the furnace tube. In all these cases, oxygen is simultaneously passed down the tube with wafers forming phosphorus-doped surface oxides. At temperatures of about 850°-950° C, phosphorus diffuses from the oxide into the cell.

Regardless of the source, sufficient phosphorus is introduced to give a sheet resistivity of 25-30 Ω/cm^2, for screen printed metalisation sequences. In some processes, after diffusion, the

diffusion oxides are removed by HF-based etches. More simply, the diffusion oxide is left and the metal contacts are fired through it.

Next, the contacts are screened onto the wafer front and rear. For top contacts, the screened paste normally consists of Ag powder combined with frit (low melting point glass composites) and organic binders. For rear surface paste, Al is often added to dope underlying regions p^+-type.

Immediately after screening each side, pastes are dried by heating to 350°- 400° C.

Contacts must be fired at above 700°C to give reasonable metal resistivity. The final contact resistance to silicon can be very sensitive to firing conditions. Infrared lamps are often used for firing, rather then normal furnace heating elements. Rear contact firing can also be critical to ensure that the rear junction is neutralised. Temperature gradient zone melting can be an important issue when attempting to form back surface fields by alloying of Al paste components [6].

For textured crystalline cells, surface reflection is low without antireflection (AR) coating. Since multicrystalline cells cannot be readily textured, AR-coating is essential in present manufacturing sequences. Common AR-coatings are SiO_2, spray-deposited TiO_2 and SiN deposited by CVD or PECVD.

Although the screen-printing sequence can be equally well applied to multicrystalline and single crystalline wafers, more complicated sequences can give rewards in terms of increased multicrystalline cell performance. In particular, hydrogen exposure during processing (passivation) can neutralise grain boundary activity. A way to obtain a good hydrogen incorporation is the deposition of SiN.

The screen-printing process that has become the commercial standard, provides a simple way of manufacturing moderate efficiency cells with the structure shown in Fig. 1.3.

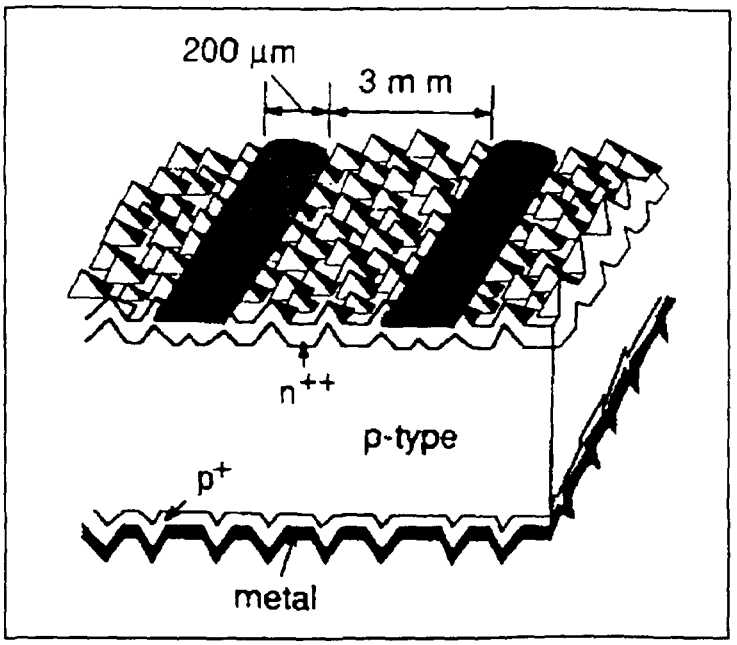

Fig. 1.3 - Commercial screen-printed silicon cell. (Reproduced from [2])

For independent measurements under the air mass 1.5 (AM 1.5) spectrum at 25°C, corresponding efficiencies for crystalline cells would be 13 % -15 % and 10 % -13 % for multicrystalline cells.

The turning point in the crystalline cells efficiency history has been in 1985, when the first 20% efficiency cell was obtained at the University of New South Wells (UNSW). The cell that first reached this record efficiency was the UNSW passivated emitter solar cell (PESC cell).

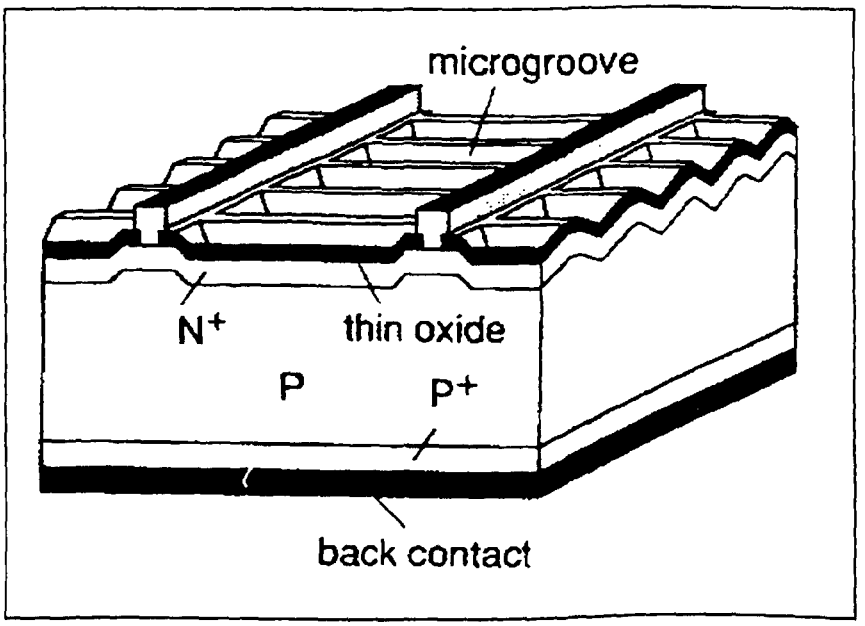

Fig. 1.4 - UNSW PESC cell: passivated emitter solar cell. (Reproduced from [2])

The PESC cell (Fig. 1.4) had an alloyed Al rear to form a conventional back surface field and on the top surface, a thin oxide layer was used to reduce recombination. The improved surface quality allowed shallow phosphorus diffusion while maintaining high V_{oc}. Furthermore, to improve V_{oc}, also a top metal contact was made by narrow stripes through this oxide, with only 0.3% of the top surface contacted. The cells also used crystallographic surface texturing. Photolithography allowed microgrooves to be anisotropically etched into the surface. Grooves were chosen rather than randomly located pyramids, primarily for processing convenience. Since the oxides for these cells were thin, a double layer AR-coating of MgF_2/ZnS was deposited, which gave a very low overall reflection.

The next two major improvements in silicon cells technology came from Stanford University and again from UNSW respectively with rear point contact cells shown in Fig. 1.5 and passivated emitter, rear locally diffused cell (PERL cell) shown in Fig. 1.6.

In particular, the PERL cell combined the PESC approach with some feature of the point contact cell. Microelectronics-quality oxide enshrouds the cell surface. Chlorine-based sequences, both in cleaning tubes and during oxide growth, gave improved oxide quality and higher post processing lifetimes. With these changes, Al gettering at the rear to ensure high post-processing lifetime could be eliminated.

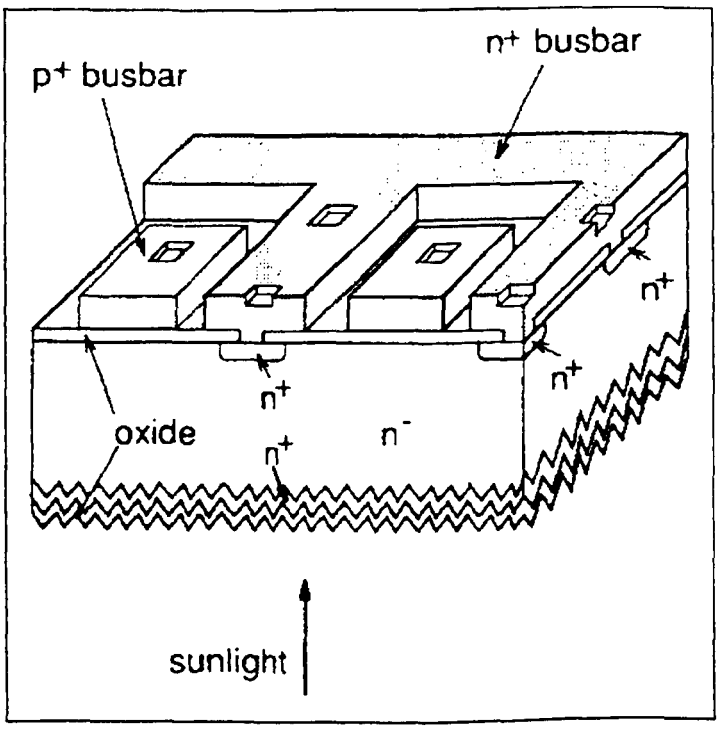

Fig. 1.5 - Stanford rear contact cell. (Reproduced from [2])

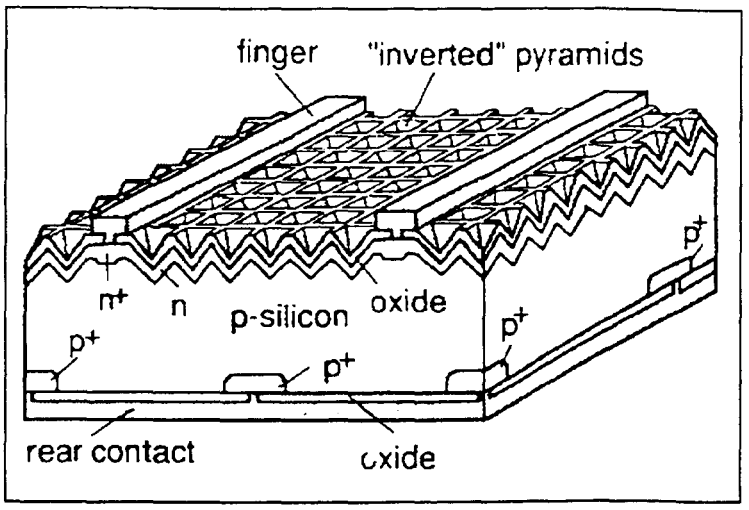

Fig. 1.6 - UNSW PERL cell: passivated emitter, rear locally diffused. (Reproduced from [2])

Even though the top surface of the PERL cell resembles that of the earlier PESC device, major changes are apparent at the rear. Most is passivated by oxide, with p-type contact made to small regions diffused with boron, similarly to the approach for both contacts in the point contact cell. One important difference is that the rear metal is isolated from the cell by an oxide overlying material of only one polarity. This rear treatment provides for superior surface passivation than the earlier PESC approach and allows a much wider choice of substrate resistivity. Furthermore, the separation of the rear metal from the silicon by an intervening oxide improves the cell reflectance, which is also exploited by the inverted pyramids along the top surface.

Today's efficiencies of these cells are around 23.5%, constituted by Voc around 705 mV, Jsc of 41 mA/cm^2 and fill factors around 81% [7]. Each of these parameters can be improved. Voc as high as 717 mV has been confirmed for recent test devices, reduced top surface reflection can improve Jsc since these cells use only a rudimentary oxide AR-coating, improved light trapping can also improve current and fill factor can also be improved by improving rear oxide quality.

Efficiencies around 25% would appear feasible without changing the basic cell structure.

"Cast" multicrystalline material is likely to remain lower quality than the best crystalline material. Different approaches may be needed to extract its full potential. The best laboratory results with multicrystalline material to date, were obtained using an earlier version of the PESC structure shown in Fig. 1.4.

To improve multicrystalline cell performance further, surface texturing is extremely desirable. Not only is reflection reduced, but the oblique light coupling is particularly important in multicrystalline cells due to shorter collection distances. Therefore, evolution in

casting processes and implementation of customised cell structures are expected to increase multicrystalline cell performance further in the future.

Another interesting approach, satisfying all criteria for producing high efficiency cells on large-scale commercial manufacture, is the buried contact approach.

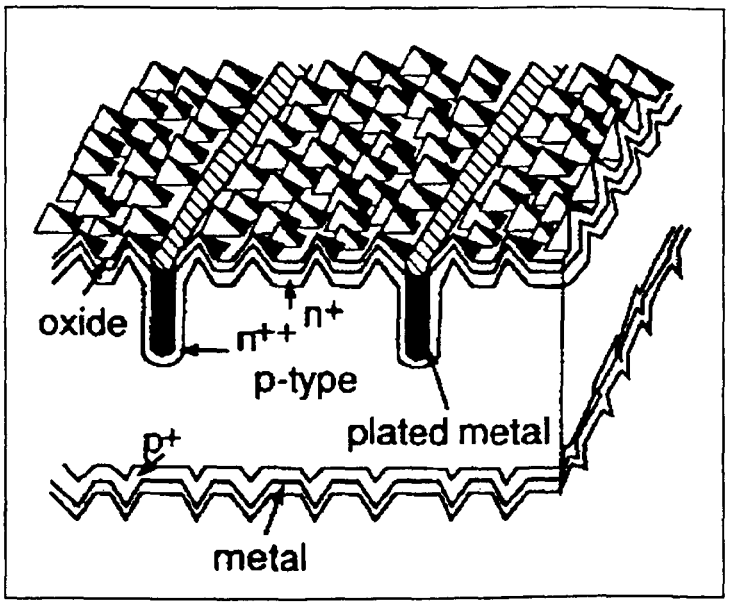

Fig. 1.7 - UNSW buried contact solar cell

The UNSW buried contact solar cell shown in Fig. 1.7, has been developed as a low-cost version of the PESC cell. Wafers are processed initially as in a normal screen-printing operation. After saw damage removal and texturing, the wafer surface is diffused, although more lightly than normally, and the wafer oxidised. The deep grooves apparent in Fig. 1.7 are then formed in the top surface by either laser or mechanical grooving. This is followed by a grooved etch and a second heavy diffusion confined to the grooves by the oxide covering non-groove areas. Al is then applied to the cell rear, by either screen-printing or evaporation, and alloyed. The cells are then plated by electroless nickel, sintered, and plated in electroless copper and silver solutions. Edge junctions are isolated by laser scribing of the cell at this stage or by normal "coin-stack" etching after the first junction diffusion.

Compared with a screen-printed process, additional steps are laser grooving of the top surface, groove etching, diffusion and contact plating. The top surface screen-printing is not required, and the process eliminates expensive silver pastes. A survey of published results of the cost of this sequence with the laser grooving, suggests that it is comparable with that of the screen-printing process. Mechanically grooved sequences offer lower cost.

1.1.2 Other Technologies

An obvious way to reduce the costs of silicon cells is to fabricate them using thin films deposited onto supporting substrates or super-strates. Work in this area in the 1970's did not produce very promising results. At the end of the decade, a review of earlier work concluded that it may be possible to fabricate 10% efficient polycrystalline cells from 20 μm thick material if the grain size exceeds 500 μm [8]. Nevertheless, rapidly growing interest in thin films of amorphous Si:H alloys pushed this polycrystalline film work to the background.
With the development of a better understanding of light trapping and limits upon silicon voltage and efficiency in the early 1980's. it became apparent that much better performance was possible, from thin film cells then previously thought. This stimulated a reawakening of interest in polycrystalline thin films which gathered momentum in the 1990's.

1.1.2.1 Thin Film Photovoltaics

As compared with crystalline photovoltaic cells and modules, thin film Photovoltaics are the technologies which provide most promising outlooks. These technologies [9], such as those based on $CuISe_2$, hydrogenated amorphous Si, or CdTe, rely on very low cell cost per unit area to deliver power at an acceptably low price. In fact, thin-film technology generally provides high production capacity at reduced material consumption and energy input in the fabrication process and integration in the structure of modules by the deposition process.
Thin film Photovoltaics make use of compound semiconductor materials which are deposited on substrates at relatively low temperatures. Thin film materials under consideration are of amorphous or polycrystalline nature which demand high optical absorption and/or high optical confinement. Typical thicknesses in the order of 1 μm lead to less stringent requirements for low defect density, i.e. diffusion length and carrier lifetime, as compared with compact crystalline materials. The inherent advantages of thin film technology have led to mainly three options for photovoltaic modules, namely amorphous devices on the basis of a-Si (or a-Si alloys), and polycrystalline structures on the basis of semiconducting compounds CdTe, $CuInSe_2$ (CIS) etc..
Up to now, amorphous silicon modules have penetrated considerably in the market, mainly for the supply of consumer electronics rather then for large scale power generation.
Even though there is continuous work in R&D going on to get a better understanding of the material and processes, and to improve performance and stability, polycrystalline modules on the basis of CdTe and CIS are not widely commercially available, but production lines are presently under construction.
Thin films for solar cells and modules can be deposited by a variety of different processes which led to different deposition rates and widely varying material quality.

The deposition processes present the basis for an economical analysis of production technology.

Table 1.1- Deposition methods for thin film Photovoltaics (Reproduced from [9])

Vacuum Processes	
Physical Vapour Deposition	PVD
Hot Wall Epitaxy	HWE
Close Spaced Sublimation	CSS
Sputter Deposition	SD
Processes Based on Chemical Reactions from the Vapour Phase	
Chemical Vapour Deposition	CVD
Plasma Enhanced CVD	PECVD
Solid Vapour Reaction	SVR
Close Spaced Vapour Transport	CSVT
Other Processes	
Chemical Bath Deposition	CBD
Spray Phyrolysis	SPL
Electrodeposition	ED
Stacked Layer Reaction	SLR
Screen Printing	SP
Scribing	SC

Table 1.1 reviews the deposition methods applicable for photovoltaic module production. Special attention has to be paid to the absorber and window films demanding high quality of opto-electronical performance, whereas contact layers and AR-coating yield a higher flexibility with the deposition methods.

1.1.2.2 Amorphous Silicon Cells

The basic structures of a-Si cells are illustrated in Fig. 1.8, where a single junction and a multi-junction are represented. The deposition method applied is the Plasma-CVD from silane mixtures.

The highest efficiencies achieved with the two cell types are respectively 7.7 % and 14.5 %. These efficiencies are subject to degradation by light soaking.

The quality of performance, which is characterised by conversion efficiency and stability, strongly depends on the defect density of the a-Si:H and Si alloys films.

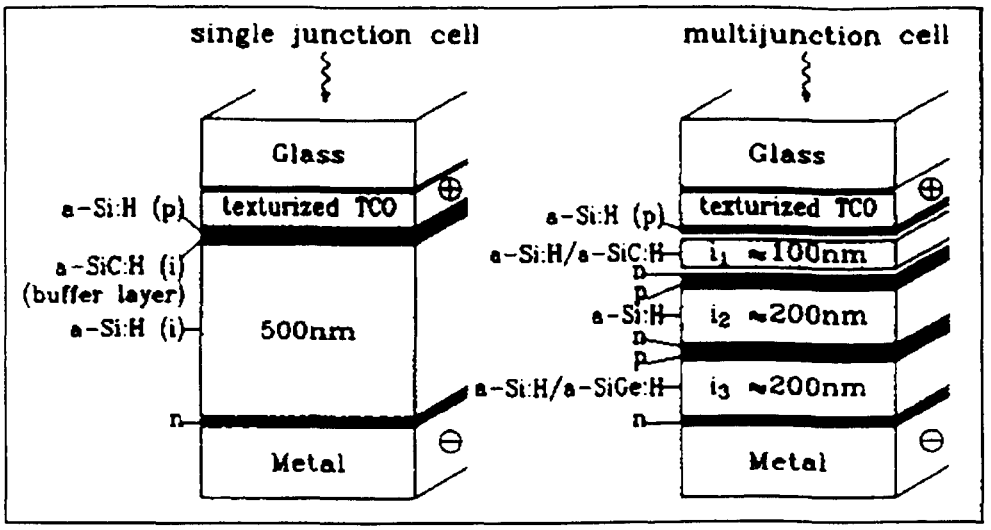

Fig. 1.8 - (a) Example of single junction solar cell; (b) multi-junction amorphous solar cell. (Reproduced from [9])

1.1.2.3 II-VI Compound Materials

There is a very large variety of compound semiconductor materials as potential candidates for photovoltaic applications, especially those based on chalcopyrites which have not yet been analysed. So far, successful attempts have been made with CdTe and Cu(In, Ga)$(SeS)_2$ compounds, which yield high conversion efficiencies and exhibit excellent stability in operation.

The performance characteristic of these polycrystalline materials is strongly influenced by the grain size and orientation, and loss mechanisms originating from the grain boundaries. The type of conduction of these materials is governed by the chemical composition and generally, no doping process is required.

Intense research activities have led to substantial progress in the development of highly efficient CdTe cells. Different deposition methods with promising cost effectiveness have been applied. Besides close spacing sublimation and chemical deposition methods, also spraying, electro-deposition, sintering of screen-printed films have been successfully applied. In Fig. 1.9 the structure of CdTe and CdS are shown.

Cell efficiencies of about 15.8 % have been reported by T. L. Chu [10] and C. Ferekides [11], which prove the potential in economy, especially in view of the simple basic structure.

Also $CuInSe_2$ (= CIS) material has been very successful in the last few years. First the CIS cell, which is an hetero-junction cell of a p-doped CIS absorber and a n-type CdS emitter (seeFig. 1.10) was explored with best cell efficiencies above 15 %.

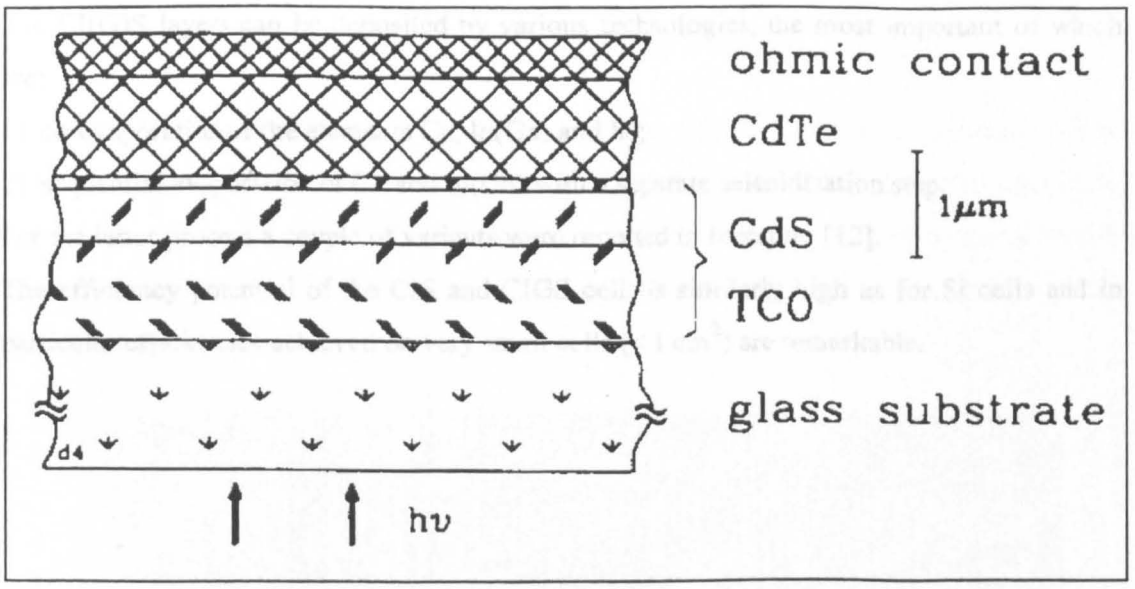

Fig. 1.9 - Structure of CdTe based cells. (Reproduced from [9])

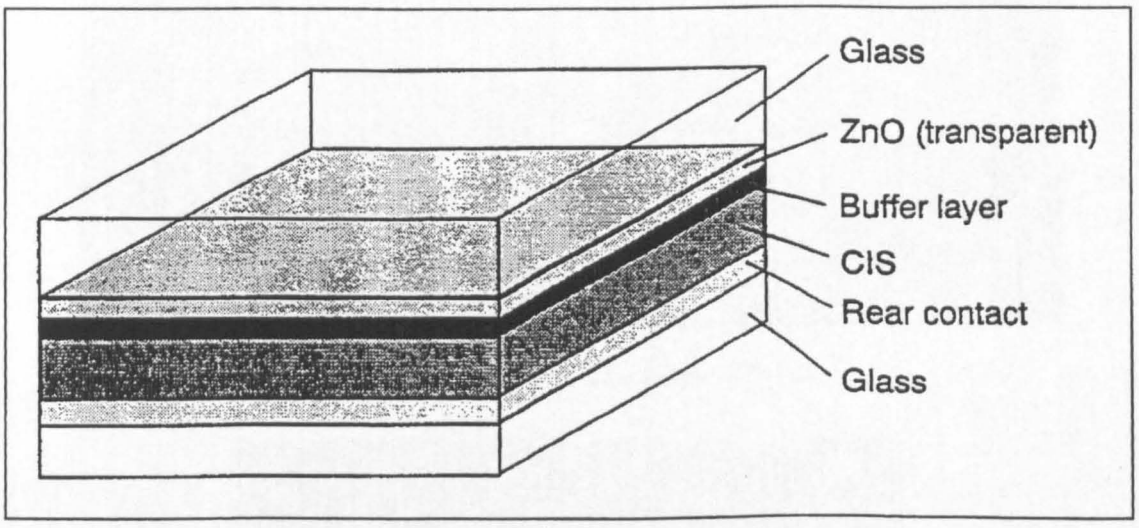

Fig. 1.10 - Layer structure of a CIS solar cell. (Reproduced from [1])

Increasing the bandgap of CIS by alloying indium with gallium (CIGS) allowed considerably higher efficiencies of almost 18 %. A further increase in bandgap could be achieved by replacing the selenium by sulphur resulting in $CuInS_2$ or $CuInGaS_2$ cells.

Another present activity aims at the replacement of the CdS emitter by a non-cadmium compound like InOHS.

In the new high efficiency compound cells the pn-junction is rather a homo- then a hetero-junction resulting from a change of the stochiometry of the CIGS absorber layer. The CdS layer serves as a buffer between the cell and the TCO contact layer.

The CI(G)S layers can be deposited by various technologies, the most important of which are:

1) co-evaporation of the elements Cu, In(Ga) and Se;

2) sequential evaporation of Cu and In(Ga) with a separate selenidisation step.

For the latter process a couple of variants were reported in literature [12].

The efficiency potential of the CIS and CIGS cells is similarly high as for Si cells and in particular efficiencies achieved on very small cells (< 1 cm^2) are remarkable.

1.2. Basic Properties of Spheral Solar™ Cells

Spheral Solar™ Cells [13, 14, 15], are made up of more than 17,000 crystalline silicon spheres (0.7 mm diameter), arranged in a hexagonal *lattice* (see Fig. 1.1 and Fig. 1.2) and embedded in a 100 cm^2 section of aluminium foil. This foil allows the finished product to be flexible, lightweight and durable. Each silicon sphere is an independent, working cell which is connected in parallel to the others.

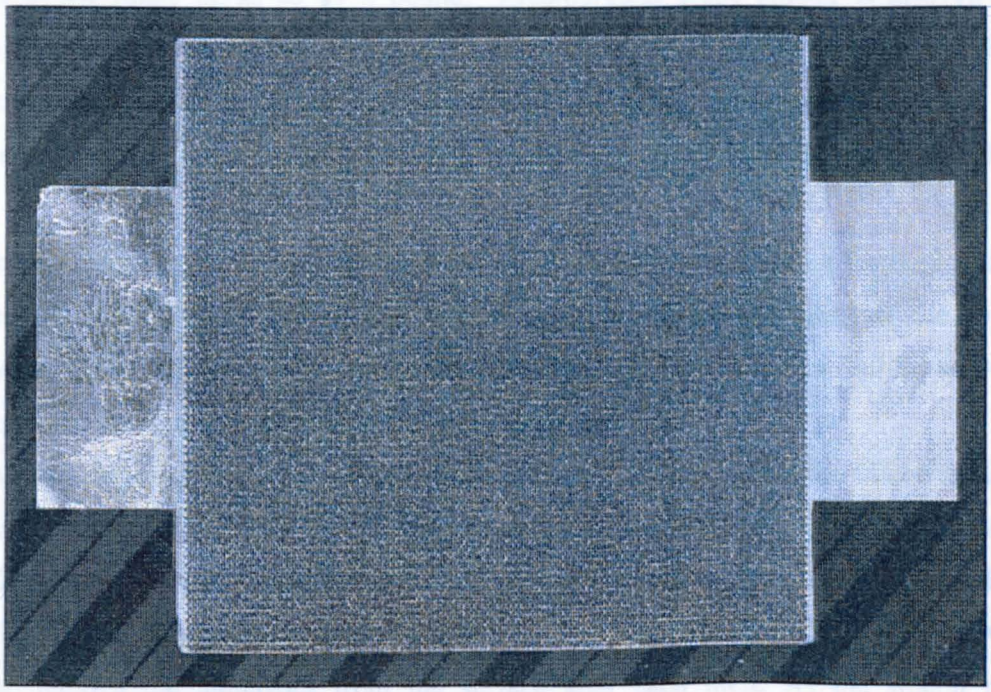

Fig. 1.11 - Front view of a Spheral Solar™ Cell

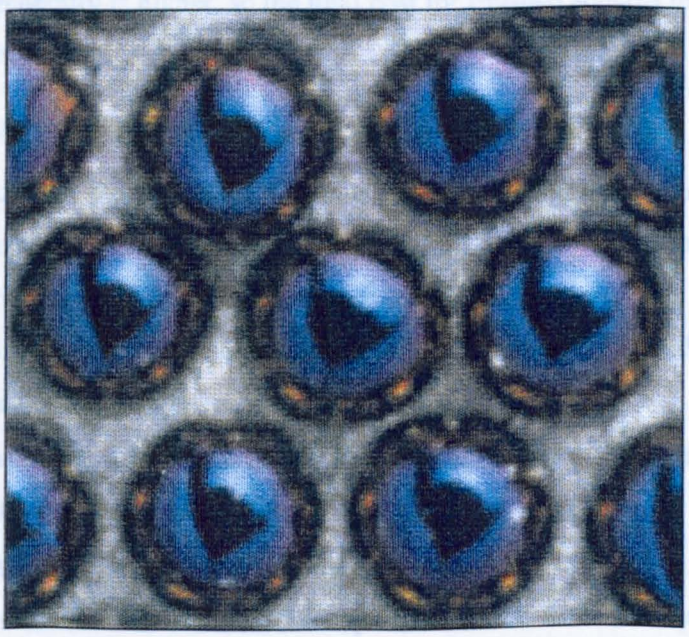

Fig. 1.12 - Close-up of a Spheral Solar™ Cell

1.2.1 Material Choice for Sphere Processing

Metallurgical-Grade Silicon (MG-Si) has long been recognised as a desirable material source for solar cells because of its low cost and great abundance.

Spheral Solar™ Technology begins with MG-Si, previously thought unusable in photovoltaic applications. This silicon material differs from solar- or electronic grade silicon in that it is only 99.4 percent pure. The primary benefit of MG-Si is substantially lower cost, ranging at about a $1 per pound versus off-spec semiconductor and solar grade silicon that begins in the range of $5 to $7 a pound. Metallurgical grade silicon is also virtually unlimited, since over 1 million tonnes p.a. are produced for the steel industry. The Texas Instrument manufacturing process upgrades this metallurgical solar silicon into useable solar spheres. When the process is complete each sphere becomes an independent solar cell [13, 14].

Efforts were undertaken to evaluate the impact of other silicon sources on the performances of Spheral Solar™ Cells and on the processing steps required to fabricate the spheres themselves [16]. This study included standard semiconductor grade silicon (SG-Si) as well as various forms of reject, or off-spec semiconductor grade silicon.

One of the unique aspects of the process used to form the spheres is that the silicon feedstock can be in powder form. This ability to use powder, along with the in-situ purification, enables the use of a wide variety of silicon sources. The purification process used to upgrade the MG-Si relies on repetitive melt cycles to bring the impurities to the surface, coupled with a step to remove the impurities from the surface after each melt. As the silicon purity increases, the processing sequence is simplified. However, the cost of the higher purity grades of silicon generally is higher, so the total cost for finished spheres must be used as the key figure of merit.

1.2.1.1 Metallurgical Grade Silicon

MG-Si is obtained form the supplier's grinding operation in the form of irregularly shaped particles. Each particle has many grains and many impurities as shown schematically below. Impurities are shown as black dots distributed among the many grains.

Particles of MG-Si are placed on a boat and melted in an open-air furnace that grows a native oxide on the surface of the silicon.

The material then moves into the furnace's second stage, where the silicon melts and the oxide layer acts like the skin of a balloon. Surface tension overcomes gravity, with the particle seeking its lowest energy form, a sphere.

A slag forms on the surface and some of the impurities diffuse from the liquid to the slag and are gettered there.

The material then goes into the "freeze" stage. Upon solidification, single crystal spheres are formed. The last sphere portion to freeze is the sphere surface. Many impurities are located in this last-to-freeze surface region where they can be ground away by mechanical means. This melt/removal sequence is repeated a few times until the desired purity is achieved. Known solid state treatments such as denuding, oxygen precipitation, phosphorous gettering are then used to tie up the remaining impurities inside the core of the sphere.

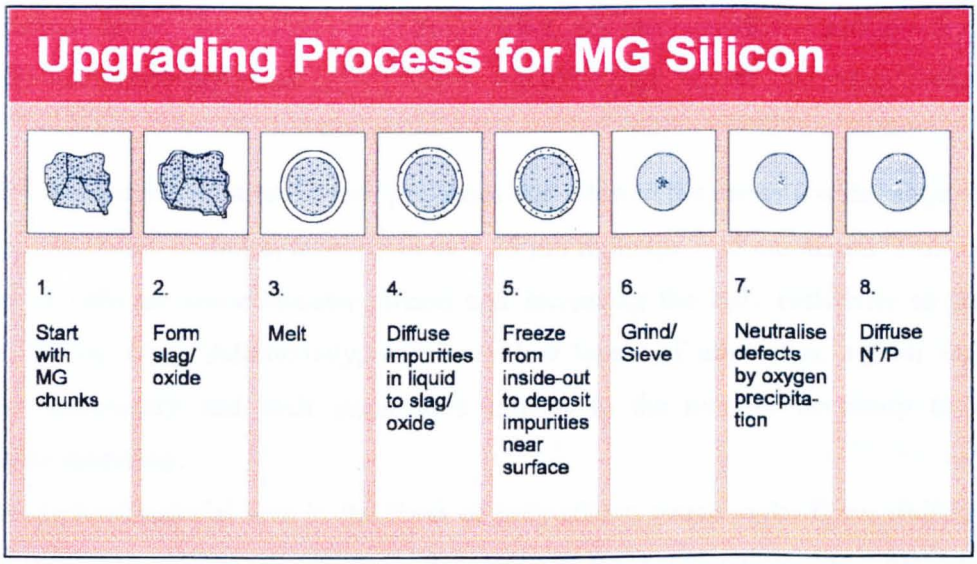

Fig. 1.13 - Sphere fabrication process.

In step #7 some of the black dots change colour to signify that they are passivated or otherwise complexed. At this stage the sphere is about 0.75 mm in diameter and the residual boron makes the sphere P-type with a range of resistivities depending on the MG-Si feedstock and the processing.

Finally, a deep N+ layer is formed with phosphorous diffusion and this completes the sphere process as shown in step #8.

1.2.1.2 Other Silicon Sources

Over the past few years the purity and acceptable forms of raw silicon for the Spheral Solar™ Technology have changed significantly. Initially, chemical grade MG silicon (see Table 1.1) was processed through several melt and removal steps to reduce the impurity levels.

In particular, the phosphorous level was brought well below the level of boron. Due to the aggressive nature of this upgrading sequence, even the prevalent metal contaminants would be reduced to levels below 1 ppmw. Several years of work with refined MG-Si demonstrated the benefit of higher resistivity through reduced boron content. The relatively high phosphorous

concentration (with respect to boron concentration) precluded the development of a process with > 50 % silicon mass yield.

Table 1.2 - Impurity levels of the three basic grades of silicon taken into consideration. All values are in parts per million by weight (ppmw)

	B	*P*	*Fe*	*Al*	*Ca*	*Ti*
Chemical Grade MG	8-12	15-25	750	750	500	100
Refined MG	2	5-8	80	10	250	5
Semiconductor Off-grade	<0.3	<0.05	<1	<1	<1	<1

Further development work led to new processes that allowed the use of a wide range of sizes of silicon feedstock particles, from powders < 25 μm to lumps > 15 cm across. This allowed the use of off-spec semiconductor silicon and increasing the bulk resistivity to increase current density (Jsc). Additionally, with very low levels of impurities, silicon removals became unnecessary and melt steps were limited to the number necessary to obtain acceptable sphericity.

The *as-received* material was in the form of poly-silicon chuck ends, fines, rods, pellets, powder and single crystal *"heads and tails"*. None of these materials posed a problem with meeting the purity requirements, but they needed different processing. In fact, the chuck ends, fines and rods require additional crushing steps to reduce the silicon into a useable size range. In addition to crushing, single crystal heads and tails pose the problem of already being doped at various resisitivity levels which reduces the processing flexibility. Poly-silicon powder is the most attractive form from a silicon yield aspect.

As the resistivity of the *as-received* feedstock is greater than 100 ohm-cm, a boron doping step is required in order to get down to the range needed to produce solar cells. This doping process consists of using a liquid boron dopant source and driving it into the silicon during a high temperature anneal.

Following the anneal the silicon is melted to transform it from poly-crystalline to single crystalline. Because of the pure state of the SG-Si, many of the melt steps and all of the grind steps had to be removed from the process. Therefore, the spheres are loaded into a high temperature furnace where denuding process takes place to reduce the amount of oxygen within the bulk. The denude process improves the minority carrier lifetime by providing a 50-75 μm oxygen-free region around the perimeter of the sphere, as well as gettering impurities within the core of the sphere where the oxygen precipitates form.

Once the denuded region is formed the p-type silicon is doped with phosphorous to form a p-n junction. The phosphorous deposition process uses phosphorous oxychloride ($POCl_3$) as

source. Following the formation of the p-n junction the spheres are annealed to allow phosphorous gettering of impurities from the active region of the spheres to the outer inactive surface.

The electrical quality of the spheres is quantified at any point in the sphere fabrication process sequence using a radio-frequency photoconductance decay technique [16]. This technique is used both before and after the formation of the p-n junction, although after the junction is formed the measurement is not the true minority carrier lifetime.

To test the performances of the finished spheres they are bonded into a perforated aluminium foil, etched to remove the n-type layer from the backside of the spheres and etched to thin the p-n junction on the front side of the spheres. The cells are then loaded into a one-sun simulator where the open circuit voltage (Voc) and the short circuit current (Isc) are measured by testing each single sphere individually.

The performance of cells made with off-spec SG-Si was found to be significantly higher then that of MG-Si cells [14]. As one would expect, the SG-Si showed greater lifetimes at both post-denude and post-diffusion. The obtained lifetimes where 0.71 μsec for MG-Si post-denude, 1.39 μsec for MG-Si post-diffusion and 1.93 μsec for SG-Si post-diffusion [17]. The average efficiency of cell made with MG-Si resulted to be about 9.3 %, while cells made with SG-Si have shown an average efficiency of 10.5 %.

1.2.2 Cell Processing

The overall processing schedule is shown in Fig. 1.4.

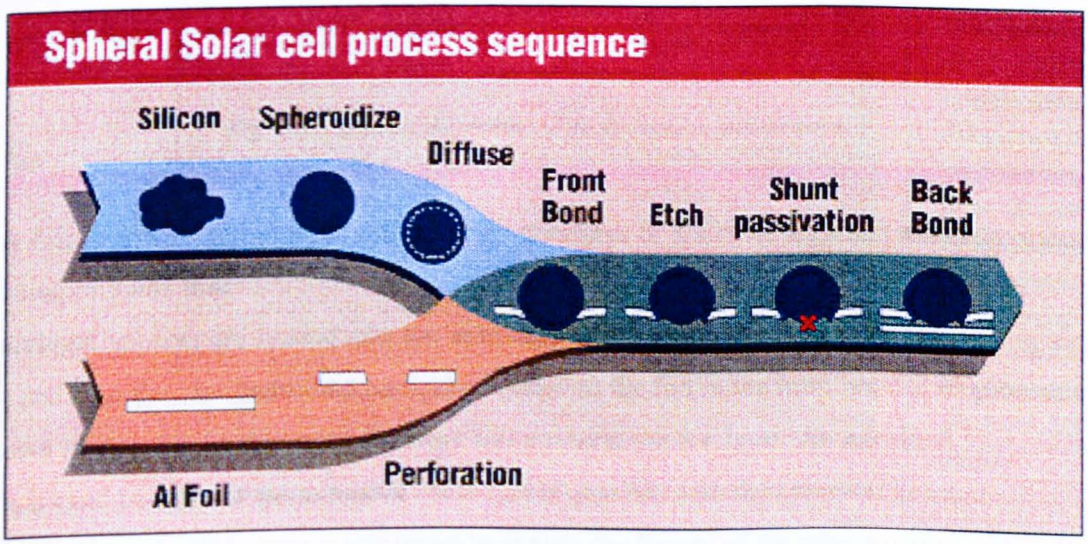

Fig. 1.14 - Spheral Solar™ Cell process sequence

In parallel with upgrading the silicon, the process also begins with a sheet of aluminium foil. The aluminium foil is critical because it serves the following four functions in the cell:

1. a flexible matrix to hold the spheres in place;
2. an electrical bus to collect the current;
3. a mask for backside etch;
4. a back-reflector of light.

The cell fabrication process begins when a smooth aluminium foil is embossed by a pressure process - 18,000 points/cm^2 - in an hexagonal pattern. Then the embossed foil is etched with KOH to remove the indentations and part of the foil, resulting in a screen of approximately 12 inches by 4 inches with 54,000 holes, obtaining apertures appearing as shown in Fig. 1.15 (step #1).

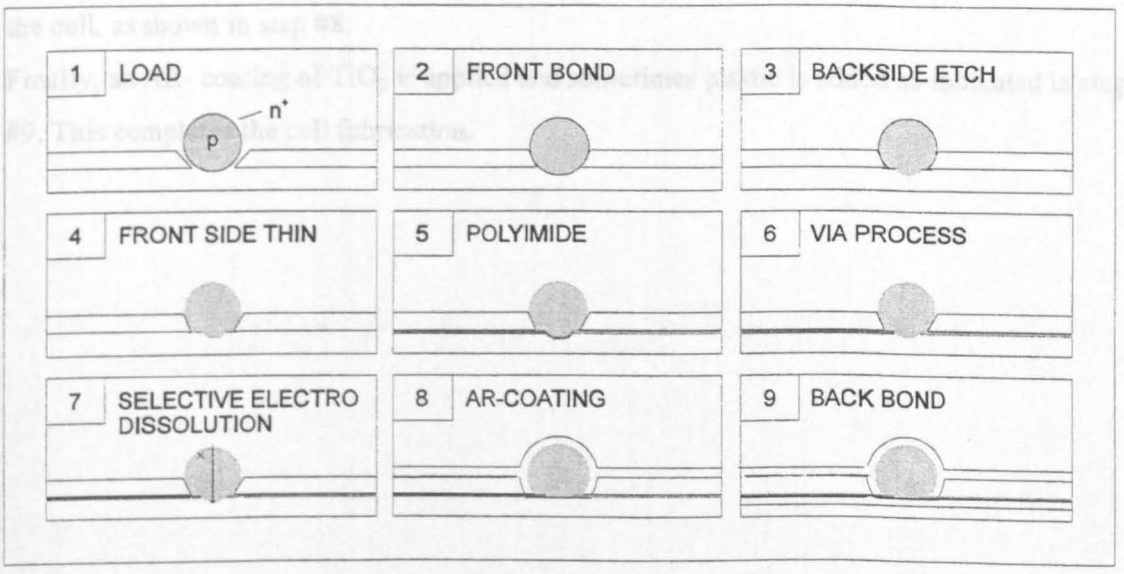

Fig. 1.15 - Detailed description of the fabrication process steps

The foil is now 0.06 mm thick with uniform apertures of diameter 0.53 mm and inter-sphere spacing of 0.081 mm.

Individual spheres are loaded into the apertures by vacuum as shown schematically in step #1, and then they are thermomechanically bonded to the foil in the front bond (FB) process as shown in step #2. At this point the front foil contacts the N+ layer. An excellent Si-Al bond is achieved because of the extensive shear forces possible with the spherical geometry.

A backside etch (BSE) step is employed to expose the P-core of the sphere, using a chemical etch for silicon and using the Al foil as a self-regulating etch mask. This BSE process is shown in step #3.

A thin layer of polyamide insulator is applied to the backside of the cell and cured to a solid film as shown in step #4. Selective abrasion on the sphere tip is used to open a via in the polyamide, as shown in step #5. The front side is thinned with a FST process, which is used to etch away substantially all of the heavily doped region from the N+ diffusion as shown in step #6. This FST process provides a short circuit current enhancement.

A selective electro-dissolution process (SED) is used to isolate the small fraction (0.3 % typically) of the shunted or shorted spheres in the MG-Si feedstock, to prevent ohmic contact when they are backbonded. The process has no effect on good spheres having a diode characteristic, but provides a rugged insulator layer on shunted spheres. The insulator layer isolates the shunted spheres from the cell during subsequent processing. SED is shown as step #7, with the schematic picture of a shunted sphere to the left and a good sphere to the right of a centreline. Only the one on the left has SED isolation.

The backbond (BB) is applied by thermomechanically bonding a second Al foil to the rear of the cell, as shown in step #8.

Finally, an AR- coating of TiO_2 is applied and sometimes plastic is added as indicated in step #9. This completes the cell fabrication.

SECTION 2

CHARACTERISATION

OF

SPHERAL SOLAR™ CELLS

2.1. Electrical Performance

The electrical characterisation of Spheral Solar™ Cells was carried out both under the Pasan single pulse Solar Simulator and under the SpectroLab single pulse Solar Simulator available at ESTI laboratories.

All the test were performed at the so-called Standard Test Conditions (STC), defined as a standard set of conditions to which the electrical performance data of the device under test are translated from the set of actual test conditions. These conditions are mainly a device temperature of 25 ± 2 °C, an irradiance of 1000 $W \cdot m^{-2}$, and the reference solar spectral irradiance distribution data from CEI/IEC 904-3 (1989).

2.1.1 Current-Voltage Characteristics

Current-Voltage characterisation of Spheral Solar™ Cells was carried out under the Pasan single pulse Solar Simulator according to the procedures for temperature and irradiance corrections to measured I-V characteristics of crystalline silicon photovoltaic devices CEI/IEC 891 (1987).

The principle of this measurement is the determination of the current-voltage characteristic of a photovoltaic devices using a single flash solar simulator as light source and an electronic load as electrical load. The electronic load imposes a rising voltage (during the duration of the light pulse) on the PV-device. During this voltage sweep both voltage and current as well as the irradiance intensity are recorded. From that data-triplet the full I-V curve can be generated. The electronic load is built by a function generator driving a Bipolar Operational Power Supply Amplifier and a precision shunt. In addition a time delay gate is used in order to delay the start of the rising voltage until the irradiance has fallen to the required level.

This method requires the use of a reference cell as a calibrated effective irradiance measuring cell. Coplanar mounting of the two cells is necessary for accurate measurements.

The mean irradiance level is checked and reported after a measurement. Adjustments of the irradiance level during the measurement are possible by variation of the delay on the delay gate generator.

The values of Irradiance, Voltage and Current are recorded with a Transient Recorder, the value of the specimen and reference device temperature is recorded by the software program *WinPasan*.

The translation of the measured I-V data to STC, is achieved by using the following equations to correct for irradiance:

$$dI = I \cdot (E_0/E - 1) \qquad \textit{Eq. 2. 1}$$

$$I_{\_STC} = I + \delta I \qquad \textit{Eq. 2. 2}$$

$$V_{\_STC} = V \qquad \textit{Eq. 2. 3}$$

where $I_{\_STC}$, $V_{\_STC}$ and E_0 are current, voltage and irradiance, respectively, at STC. The non subscribed variables refer to the measured values.

There is no temperature correction procedure as the measurements have been carried out at (25± 1)°C.

The values of P_{max}, I_{mp}, and V_{mp} are calculated by the program *WinPasan*. The value of the output power P is the arithmetic multiplication of the recorded values of the current I_{STC} (corrected for irradiance) and the voltage V_{STC} of the device under test. The maximum value of these multiplication is defined as P_{max}. The values of I_{mp}, V_{mp} are defined, respectively, as current and voltage at P_{max}.

The efficiency of the cell is calculated according to the following equation:

$$\eta_{cell} = Pmax_{\_cell} / P_{in} \cdot Area_{\_cell} \qquad \textit{Eq. 2. 4}$$

The fill factor of the device is calculated from:

$$FF = \frac{V_{MP} \cdot I_{MP}}{V_{OC} \cdot I_{SC}} \qquad \textit{Eq. 2. 5}$$

The measurement results of the I-V characteristics of the Spheral Solar™ Cell (TE004) are summarised in Table 2.1 and plotted in Fig. 2.1.

Table 2.1 - IV characteristics at STC, no spectral mismatch correction applied. Reference detector SOL533

Simulator	**Isc**	**Voc**	**Imp**	**Vmp**	**Pmax**	**FF**	η_c
LAPSS	**[A]**	**[mV]**	**[A]**	**[mV]**	**[W]**	**[%]**	**[%]**
Pasan	2.148	558.6	1.931	455.7	0.879	73.33	8.79
	2.148	559.1	1.931	455.7	0.879	73.20	8.79
	2.148	558.6	1.942	454.3	0.882	73.53	8.82
Average	**2.148**	**558.8**	**1.934**	**455.2**	**0.880**	**73.35**	**8.80**

The same measurements have been carried out also at different angle of incidence (from 0 to 80 degrees, step 10) in order to analyse the angular dependencies of Spheral Solar™ Cells. The measured IV-curves are plotted in Fig. 2.3.

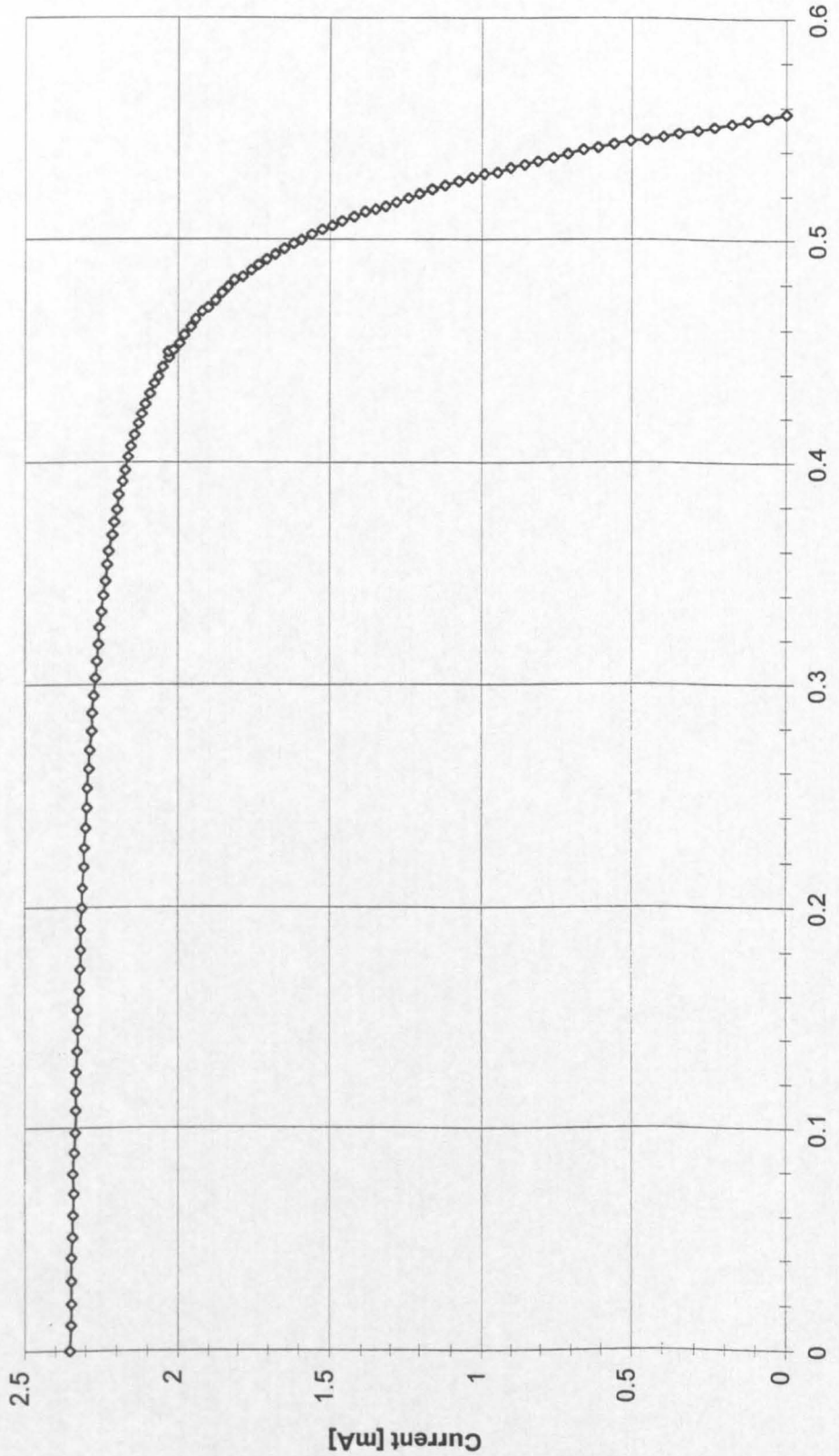

Fig. 2.1 - IV Curve of Cell TE004 [18]

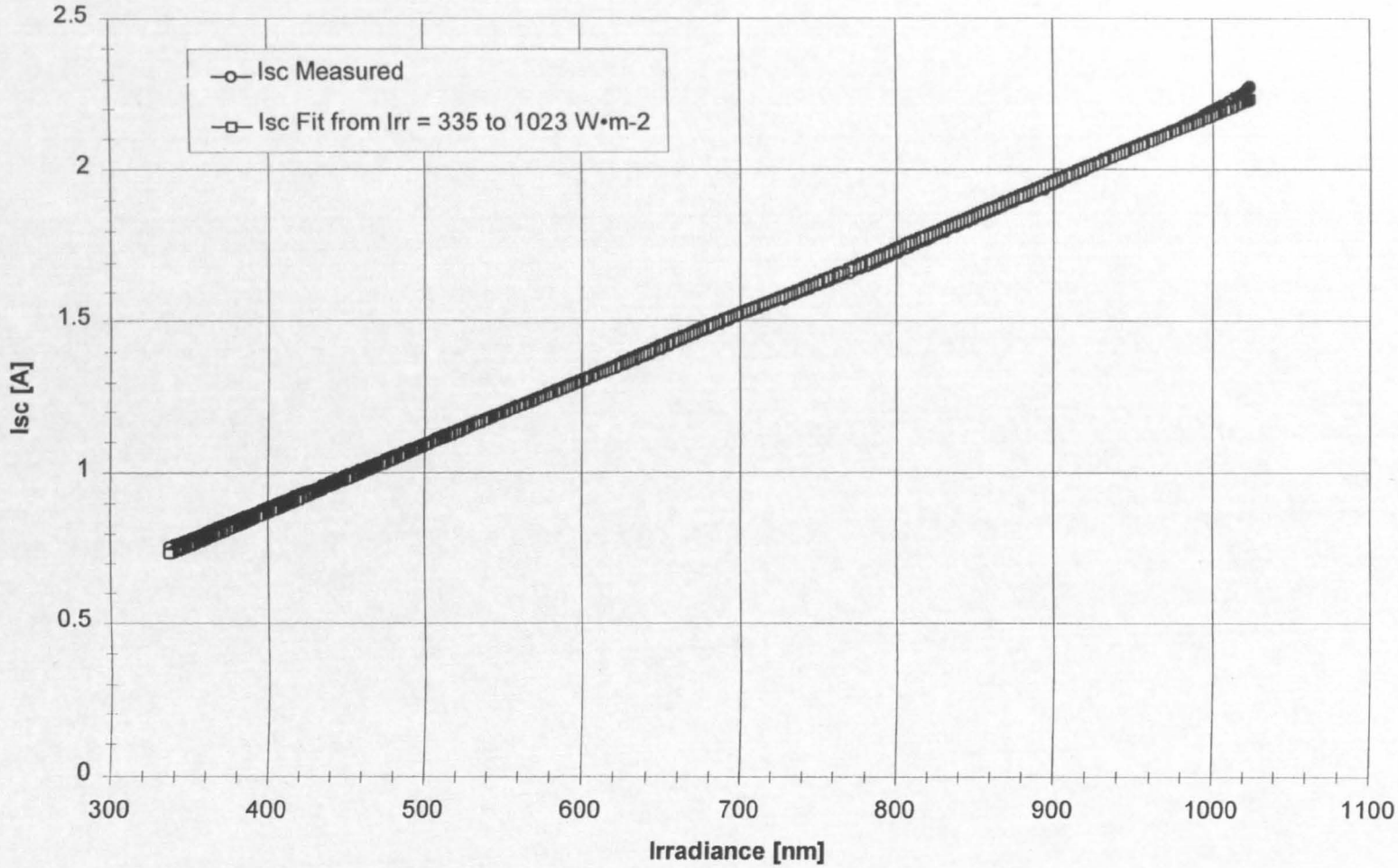

Fig. 2.2 - Linearity of Isc vs. Irradiance

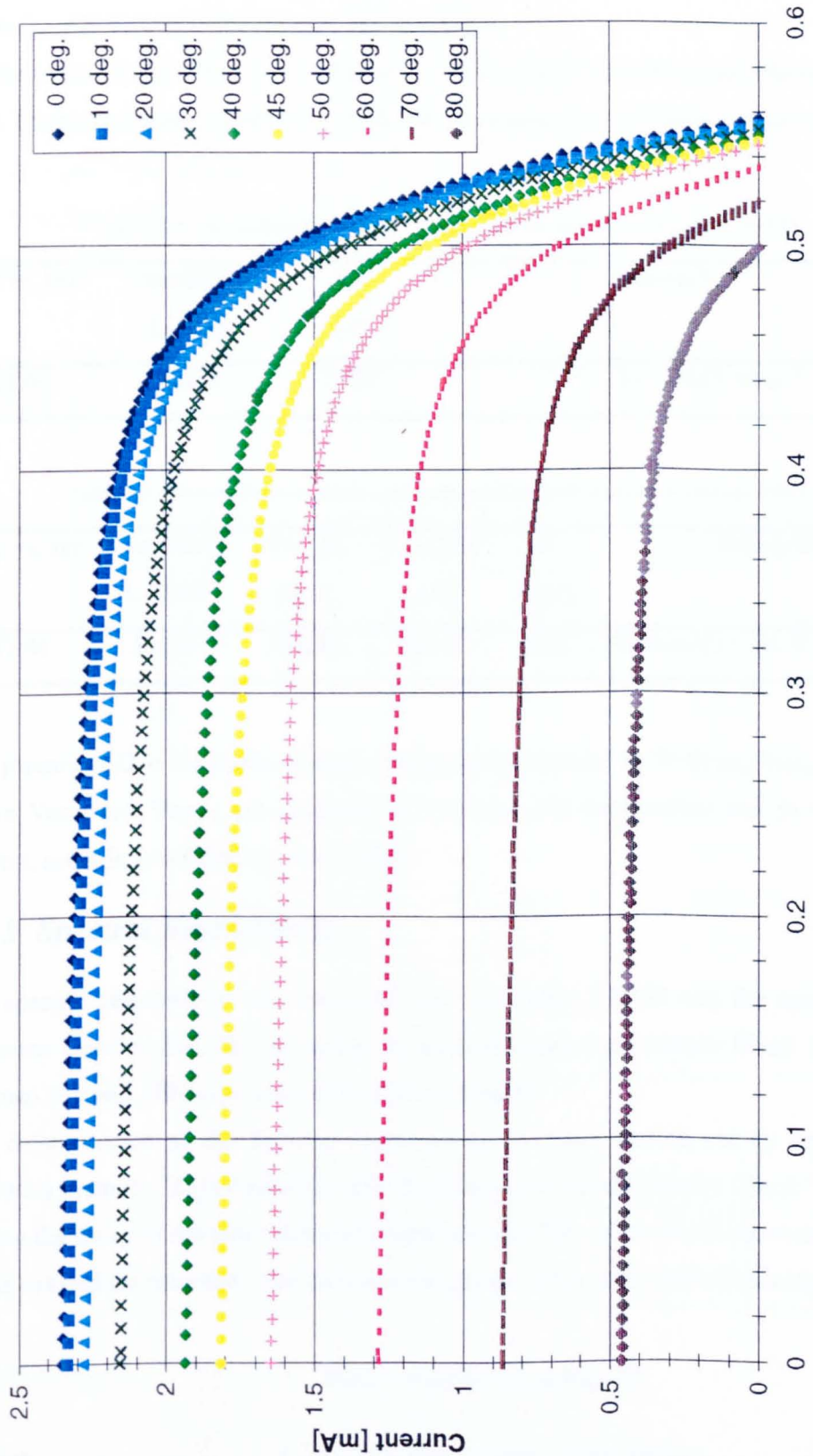

Fig. 2.3 - IV-Curves vs. angle of incidence

2.1.2 Isc and Voc Calibration

Another interesting characterisation has been carried out by determining the spectral region where Isc and Voc vary linearly with the irradiance.

For the tests of Isc and Voc vs. irradiance the Pasan LAPSS and the same reference cell were used. The measurement results on cell TE004 are summarised in Table 2.2 and Table 2.3.

Table 2.2 - Isc calibration results, no SMC applied. Reference detector SOL533

Isc vs. Irr	Simulator LAPSS	Isc [A]	Remarks
TE04	Pasan	**2.197**	335 < Irr < 1023 W·m^{-2}

Table 2.3 - Voc calibration results and determination of D. Reference detector SOL533

Voc vs. Irr	Simulator LAPSS	Voc_M [mV]	Voc_Fit [mV]	D [mV]	Remarks
TE04	Pasan	**562.0**	**563.3**	**40.5**	Fit from 91 < Irr < 1047 W·m^{-2}

The parameter D is the diode thermal voltage and is defined as $D=(Voc_n-Voc_{n-1})/\ln(I_n/I_{n-1})$, where Voc_n, and Voc_{n-1} are measured at the same cell temperature and in the range of interest, according to CEI/IEC 904/5, 1993.

2.1.3 Spectral Responsivity

The spectral responsivity was measured with the Pasan LAPSS and the same calibrated reference detector SOL533, by using 18 monochromatic interference filters (wavelengths between 359 and 1096 nm) with calibrated wavelength.

The determination of the Spectral Responsivity has been carried out by employing the following method: *"Differential Spectral Responsivity without Linearity Check"*.

During the decay of the monochromatic light intensity 800 values of the short circuit currents of the devices are recorded. For each wavelength the value of the ratio is calculated by:

$$R(\lambda) = \text{Average}\ (J_{test}(t)/J_{ref}(t)) \qquad \textit{Eq. 2. 6}$$

with

$$J_{test}(t) = \text{Current Density of Test Device} \qquad \textit{Eq. 2. 7}$$

$$J_{refl}(t) = \text{Current Density of Reference Device} \qquad \textit{Eq. 2. 8}$$

After every measurement the *WinPasan* program writes the chosen current ratios to a standard file. Additionally, it is possible to calculate the data for the Absolute Spectral Responsivity Curve and the Mismatch factor, by importing the standard file into an appropriate mismatch EXCEL sheet.

The results from this EXCEL sheet are:

- Absolute Spectral Responsivity Curve;
- Calculated Mismatch factor;
- Calculated Current for Air Mass 1.5 Global.

All calculations are done in accordance with IEC904-3.

The values of absolute spectral responsivity and mismatch factor are reported in Table 2.4 and Table 2.5.

Table 2.4 - Spectral Responsivity and mismatch factor for AM1.5, IEC 904-7. Reference detector SOL533

Wavelength [nm]	**Resp** SOL533 **[A/W]**	**Wavelength [nm]**	**Resp** SOL533 **[A/W]**
359	0.0114	701	0.3897
382	0.0351	746	0.4049
397	0.0620	798	0.4049
442	0.1080	842	0.3925
447	0.1515	897	0.3479
501	0.2383	953	0.2607
547	0.2812	995	0.1720
595	0.3232	1048	0.0785
652	0.3627	1096	0.0577

Table 2.5 - Mismatch factor for AM1.5, IEC 904-7

Mismatch factor {Reference detector SOL533}	**1.0267**
Isc as calc. with mismatch calculation [A]	**2.2561**

The plot of the measured data is given in Fig. 2.4.

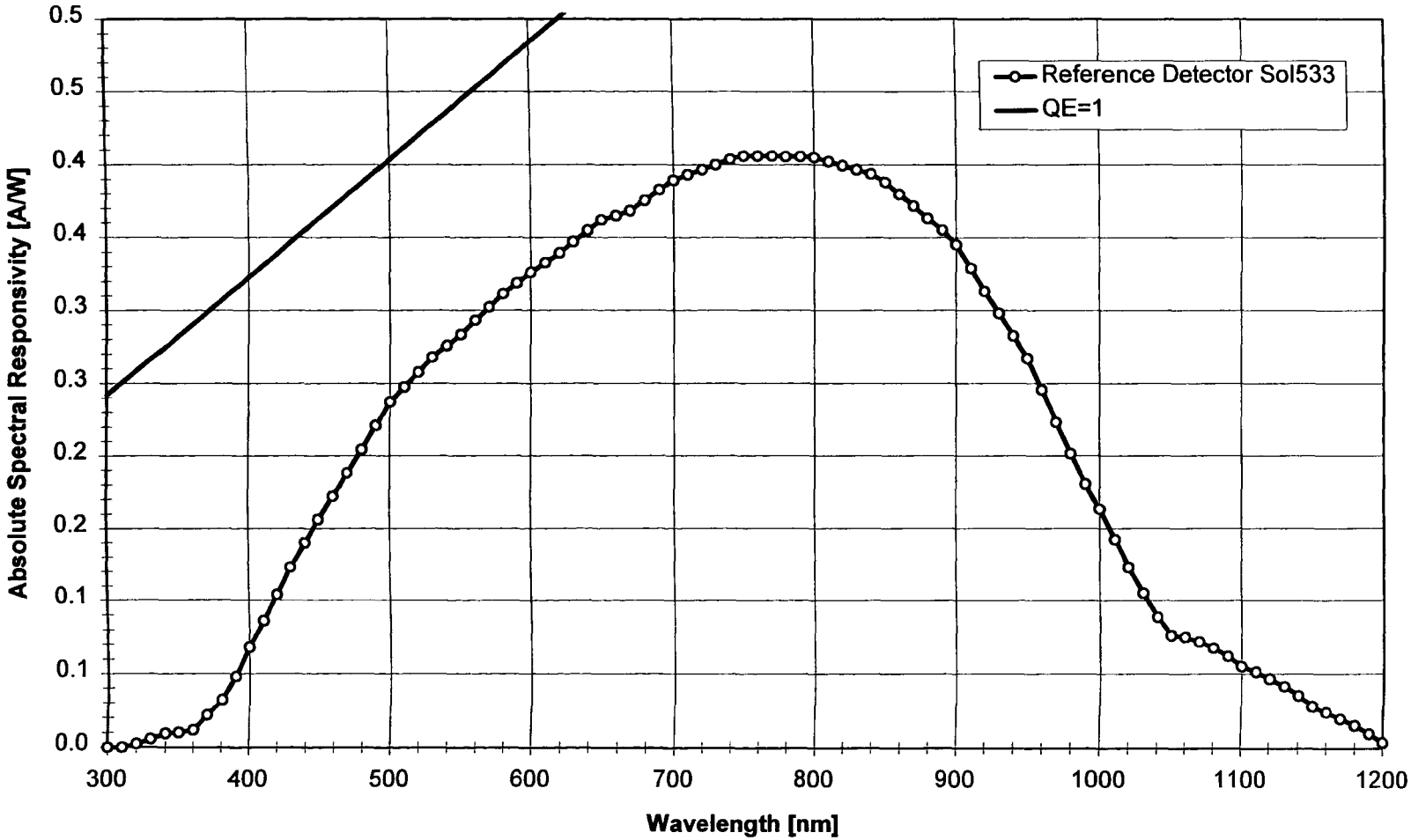

Fig. 2.4 - Spectral responsivity of cell TE004

2.1.4 Spectral Responsivity, Isc and Voc vs. Angle of Incidence

The spectral response of a cell is the output current under short-circuit conditions per unit incident power in monochromatic light, as a function of wavelength. Measurement of the spectral response is very important to provide detailed information about the design parameters of any particular solar cell.

The response of the Spheral Solar™ Cell was measured for both for normal (0 deg.) and oblique illumination (from 10 to 80 degrees, step 10) under the Pasan LAPSS and with the same calibrated reference detector SOL533.

The way chosen to show the spectral response data is the plot of the sensitivity in A/W as a function of wavelength, as shown in Fig. 2.5 and Fig. 2.6. The quantum limit has also been indicated.

The angular dependency of the spectral responsivity is of particular interest for the comparison of the optics of Spheral Solar™ Cells to the optics of other standard devices.

The enhancement with respect to the cosine response is very clear from the plot of Isc vs. Angle of Incidence (Fig. 2.7). The relative enhancement of the response presents a maximum between 40 and 60 deg. This behaviour will be explained and reproduced further on (in Fig. 5.18), by means of ray-tracing simulations.

Voc vs. angle of incidence (Fig. 2.8), presents a similar behaviour.

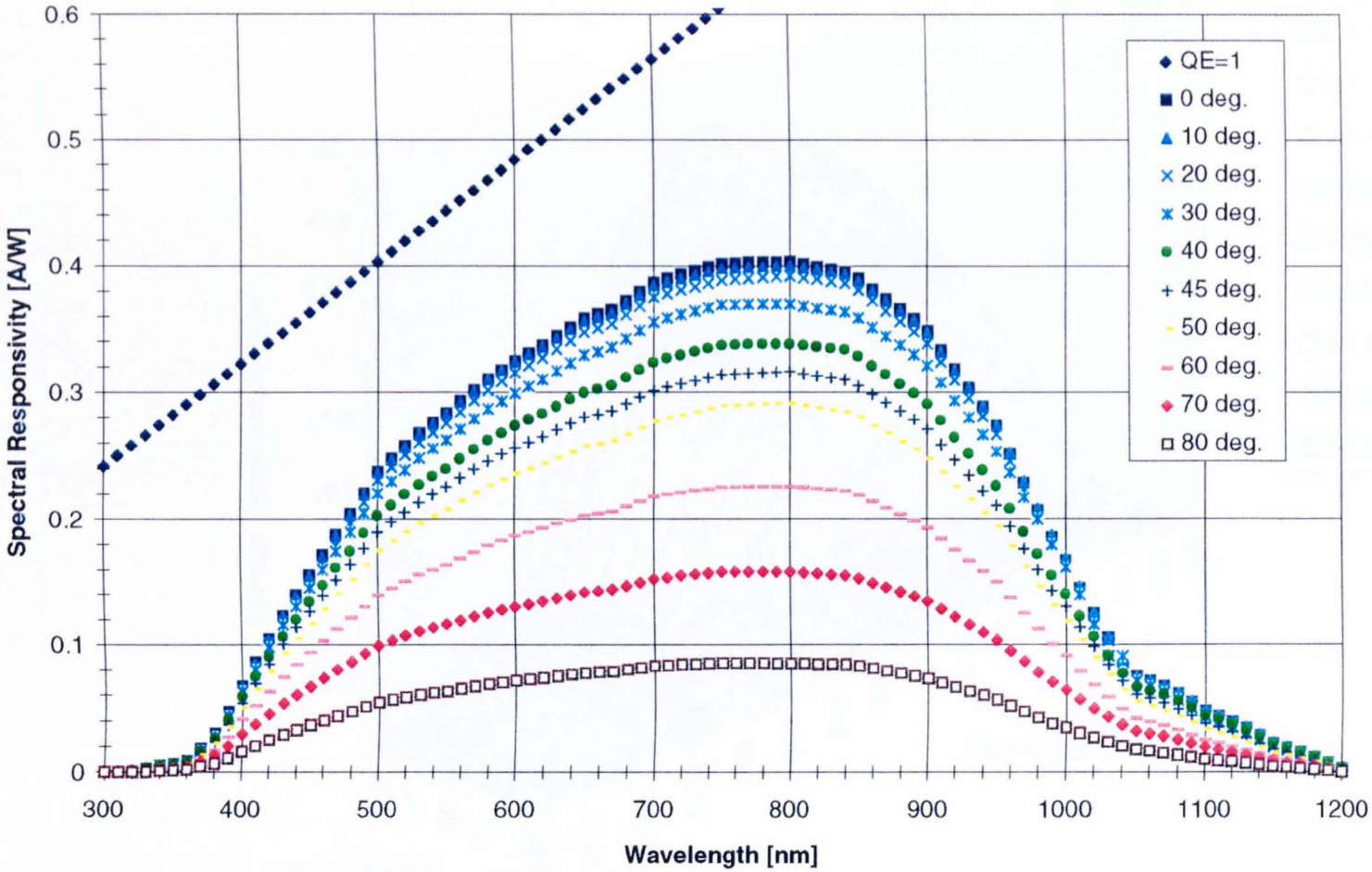

Fig. 2.5 - 2d plot of the spectral responsivity vs. angle of incidence.

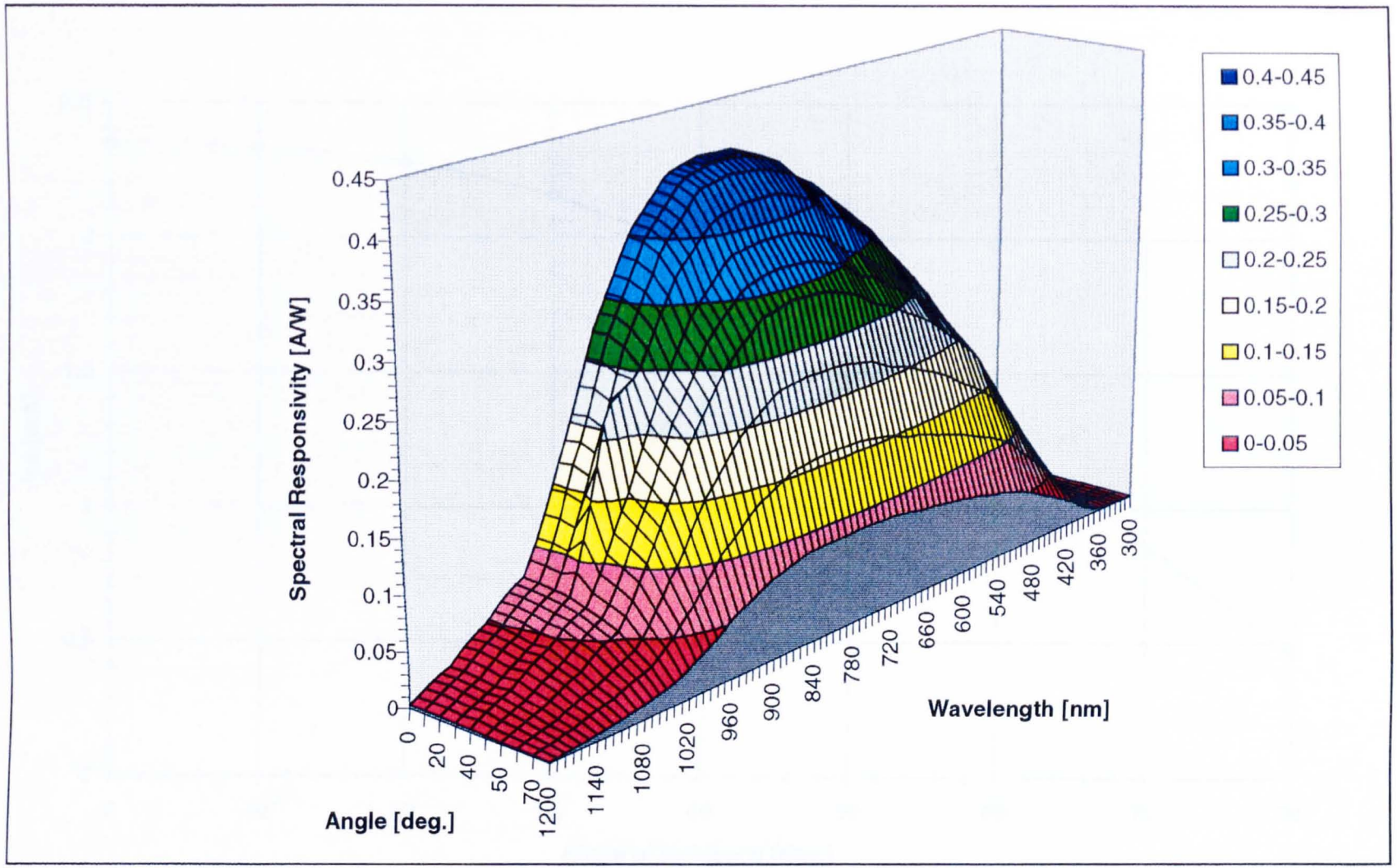

Fig. 2.6 - 3d plot of the spectral responsivity vs. angle of incidence

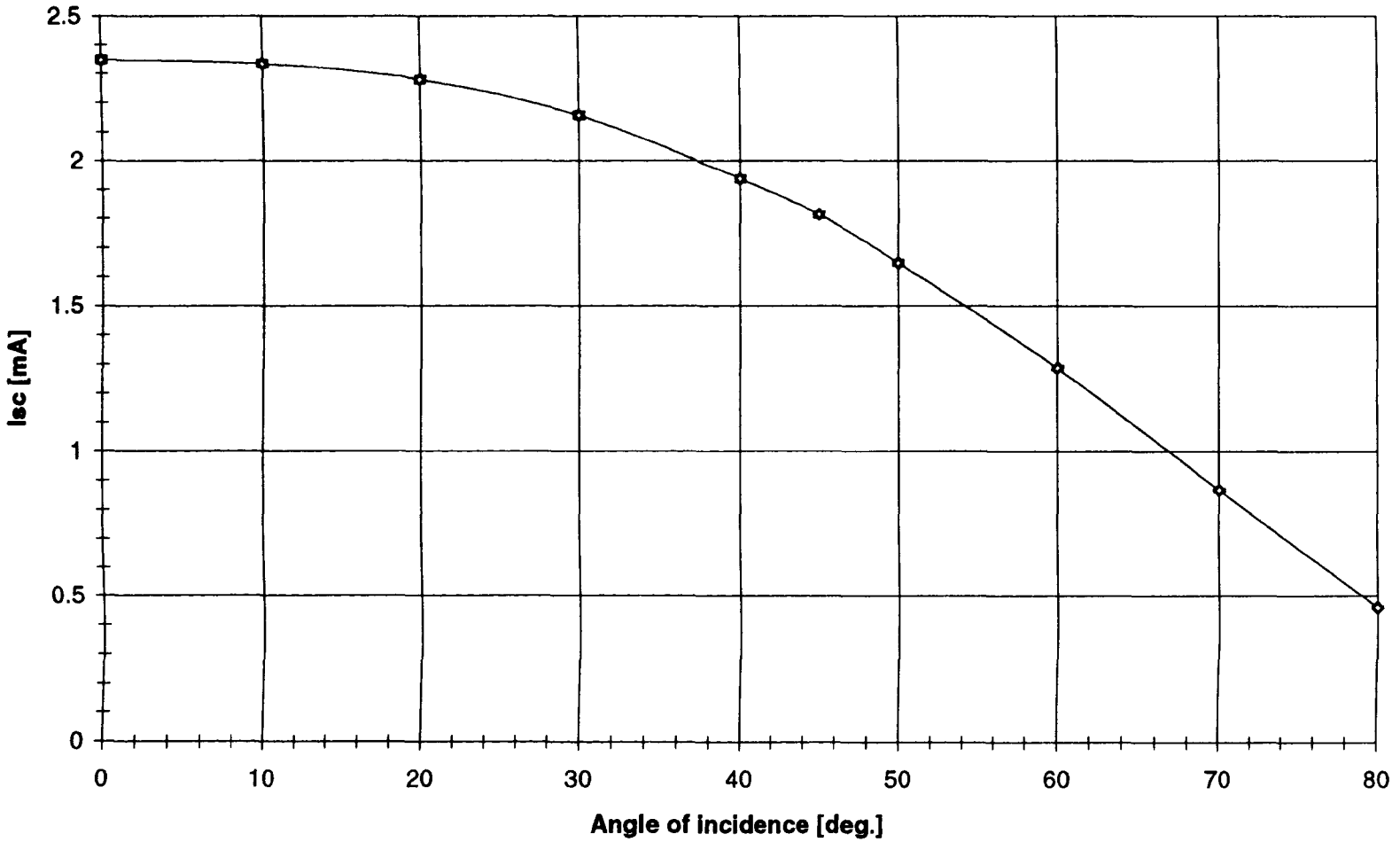

Fig. 2.7 - Isc vs. Angle of Incidence

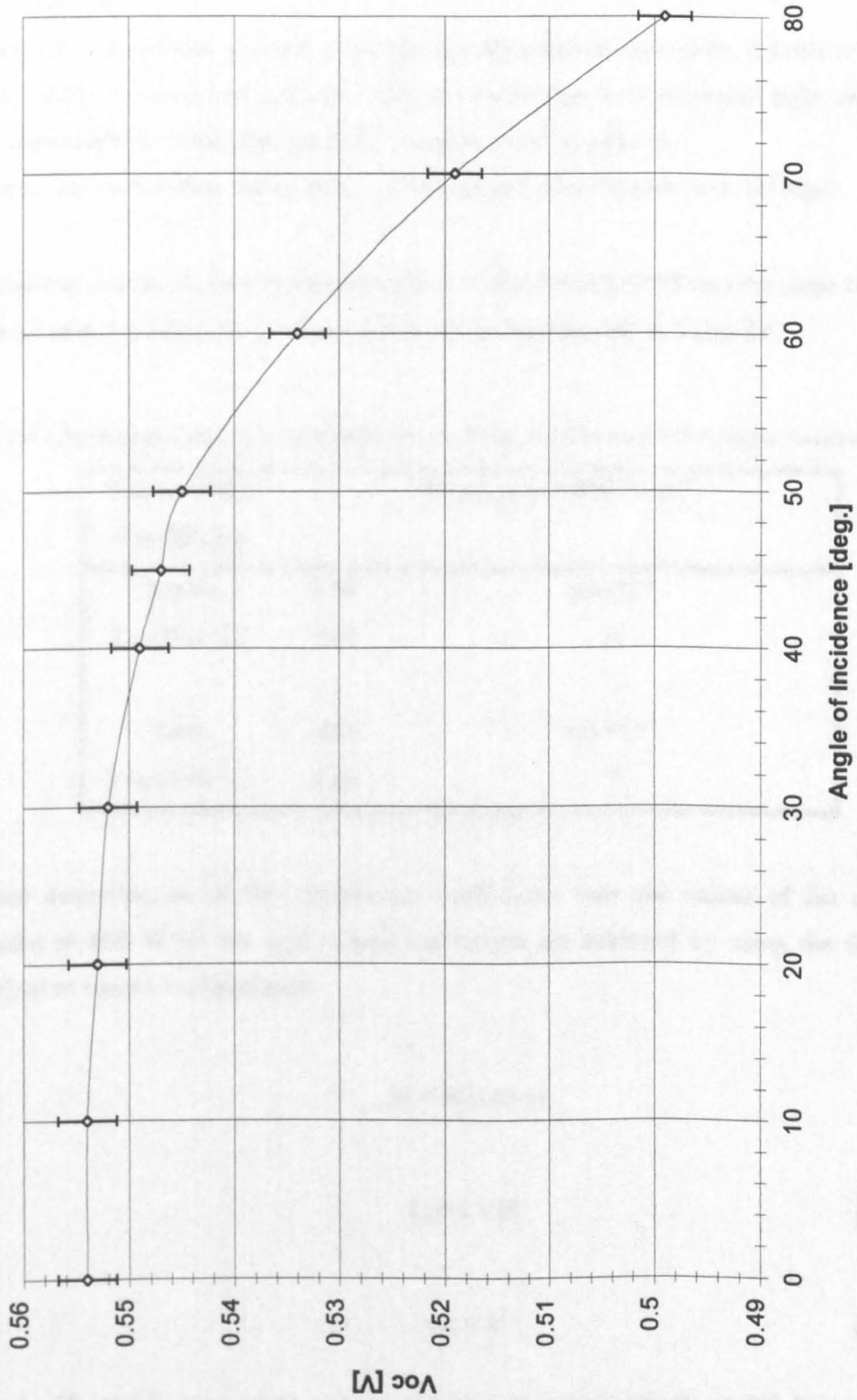

Fig. 2.8 - Voc vs. Angle of Incidence

2.1.5 Temperature Coefficients

Since the operating temperature of solar cells in the field can vary over wide extremes, it is necessary, for a complete electrical characterisation, to understand the effect of temperature on performance.

The short circuit current of a cell is not strongly temperature-dependent. It tends to increase slightly with increasing temperature. This can be attributed to increased light absorption, since semiconductor band gaps generally decrease with temperature.

The other cell parameters, the open circuit voltage and the Fillfactor, both decrease.

The temperature coefficients were measured with the Pasan LAPSS and the same calibrated reference detector SOL533. The values obtained are summarised in Table 2.6.

Table 2.6 - Temperature coefficient measurement on cell TE004, with Pasan LAPSS. Reference detector SOL533

Temperature Coefficients	**Irradiance = 800 W·m^{-2}**	
Alpha	**6.68**	μA·°C^{-1}
Isc (T=0 °C)	1.61	A
Beta	**-2.06**	mV·°C^{-1}
Voc (T=0 °C)	0.60	V

For the determination of the temperature coefficients only the values of Isc and Voc corrected at 800 W/m² are used. These corrections are achieved by using the following equations to correct for irradiance:

$$\delta I = I \cdot (E_0/E - 1) \qquad \textit{Eq. 2. 9}$$

$$I_{sc} = I + \delta I \qquad \textit{Eq. 2. 10}$$

$$V_{oc} = V \qquad \textit{Eq. 2. 11}$$

where I_{sc}, V_{oc} and E_0 are current, voltage and irradiance, respectively, at 800 W/m², the non subscribed variables refer to the measured values. The measured current and voltage values

are then interpolated linearly and the values of alpha (mA/°C/cm²) and beta (mV/°C/cm²) are determined by the slope of the interpolation.

2.1.6 Error Analysis and Extrapolation Procedures

The error analysis of the performed measurements is summarised in Table 2.7.

Table 2.7 - Error Analysis

Estimated Error source [± %]	Photovoltaic Current	Photovoltaic Voltage	Fill Factor I/I_{sc}	Fill Factor V/V_{oc}
Data acquisition system	0.1	0.1	0.14	0.14
Shunt / Voltage Divider	0.1	0	0	0
Temperature (25 ± 2) °C	0.04	0.8	0	0
Calibration of ref. device	2.0	0	0	0
Mismatch Correction	1.0	0	0	0
RMS	2.24	0.81	0.14	0.14

As the Fill Factor is a relative measurement the only error introduced is the RMS. (Root Mean Squared) value of both data acquisition errors.

$$\text{Error in FF} = [(0.1)^2+(0.1)^2]^{1/2} = 0.14\ \% \qquad \textit{Eq. 2. 12}$$

As no voltage divider was used, the error in voltage values is set to 0 %.
From the table above we may conclude that the overall error of P_{max}_STC, calculated using the formula:

$$P_{max} = I_{sc} \cdot V_{oc} \cdot FF\ [(I/I_{sc}) \cdot (V/V_{oc})] \qquad \textit{Eq. 2. 13}$$

will be the RMS value of the Current, Voltage and Fill Factor errors.

$$\text{Error in } P_{max} = [(2.24)^2+(0.81)^2+(0.14)^2+(0.14)^2]^{1/2} = 2.39\ \% \qquad \textit{Eq. 2. 14}$$

This will result in an overall uncertainty of 2.4 % in P_{max}.

The extrapolation procedures for the I-V Characteristics (1000 Wm^{-2}, 25 °C) are performed according to IEC 904-1. The I-V measurements are performed at a device and reference

temperature of (25 ± 2) °C. This means no corrections for temperature on the current and voltage values.

The correction to AM1.5 Global (IEC 904-3) using the mismatch factor (IEC 904-7) determined during the spectral responsivity (IEC 904-8) will bring the current value measured under the simulated light nearer to the "Real I_{sc}" at AM1.5 Global, but introduces an error. This error is introduced by the assumption of the spectrum of the Test Spectrum (light source). As both light sources are single pulsed solar simulators using the same kind of light sources, the mismatch factor is applied on both current values.

Presently both simulators are equipped with the same kind of electronic load (voltage sweep in 1.5 - 2 ms from I_{sc} to V_{oc}), data acquisition system and elaborating software. This allows us to take the average of both simulator readings.

2.2. Optical Performance

Unlike transmittance spectroscopy, where the radiant energy passing through a sample is measured, in diffuse reflectance spectroscopy, the amount of radiant energy reflected from the sample is measured. The data from reflectance spectroscopy are often given as percent reflectance:

$$\% R = I_R/I_0 \cdot 100 \qquad \textit{Eq. 2. 15}$$

where I_R is the intensity of radiant energy reflected from the sample, and I_0 is the intensity of radiant energy reflected from a reference material.

2.2.1 Spectrophotometer Optical System

The instrument employed for reflectance measurements is the Perkin Elmer Spectrometer Lambda 19 (scheme of the instrument shown in Fig. 2.9). Lambda 19 is a high performance double beam, double monochromator UV/VIS/NIR spectrometer, equipped with a 60 mm integrating sphere (see Fig. 2.10).

Two radiation sources, a deuterium lamp (DL) and a halogen lamp (HL), cover the working wavelength range of the spectrometer. For operation in the near infrared (NIR) and visible (VIS) ranges, source mirror M1 reflects the radiation from the halogen lamp onto mirror M2. At the same time, it blocks radiation from the other lamp. For operation in the ultraviolet range, source mirror M1 is raised to permit radiation from DL to strike mirror M2. Source change is automatic during monochromator slewing.

Source radiation is reflected from mirror M2 via mirror M3 through an optical filter on filter wheel assembly FW to mirror M4. The filter wheel is driven by a stepping motor which is synchronised to the monochromators. Depending on the wavelength to be produced an appropriate filter is located in the beam path to prefilter the radiation beam before it enters the first monochromator. Filter change is automatic during monochromator slewing.

From mirror M4 the radiation is reflected through the entrance slit of monochromator 1. All slits are located on slit assembly SA. The radiation is collimated at mirror M5 and reflected to grating table G1. Depending on the wavelength range, the collimated radiation beam strikes either the NIR grating or the UV/VIS grating. The radiation is dispersed at the grating to produce a spectrum. The rotational position of the grating effectively selects a segment of the spectrum, reflecting this segment to mirror M5 and thence to the exit slit. The exit slit

restricts the spectrum segment to a near-monochromatic radiation beam. Grating change is automatic during monochromator slewing.

The exit slit of monochromator 1 serves as the entrance slit of monochromator 2. The radiation is reflected via mirror M6 to the appropriate grating on grating table G2 and thence back via mirror M6 through the exit slit to mirror M7. The rotational position of grating table G2 is synchronised to that of G1. The radiation emerging from the exit slit exhibits high spectral purity with an extremely low stray radiation content.

From M7 the radiation beam is reflected via torroid mirror M8 to the chopper assembly C. As the chopper rotates, a mirror segment, a window segment and dark segments are brought alternatively into the radiation beam. When a mirror segment enters the beam, radiation is reflected via mirror M10, creating the reference beam R. When a dark segment is in the beam no radiation reaches the detector. This permits the detector to create the dark signal.

In the cell plane, each radiation beam is 10 mm high. The width of the radiation beams is dependent on the slit width. At a slit width of 5 nm, each radiation beam is 4.5 mm wide.

The radiation passing alternatively through the sample and reference beams is reflected by the optics of the detector assembly onto the appropriate detector. A photomultiplier is used for the UV/VIS range while a PbS detector is used in the NIR range. Detector change is automatic during monochromator slewing.

Only optically matched mirrors are used in the sample and reference beams. The number of reflections, the angle of reflection, and the optical pathlength are identical in both beams. These measures guarantee optimum photometric conditions at all wavelengths.

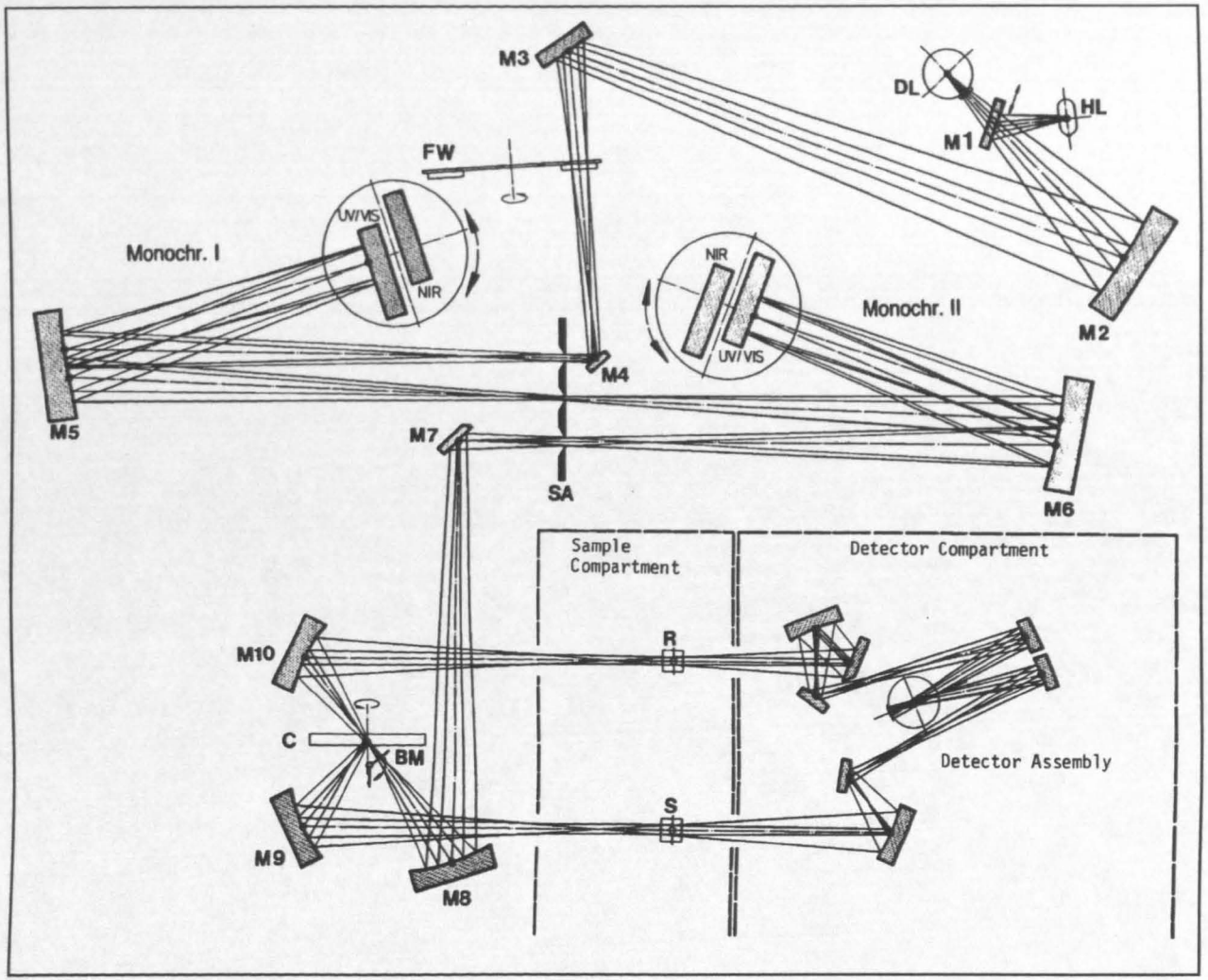

Fig. 2.9 - Spectrophotometer Lambda 19: schematic of the optical system

For hemispherical reflectance measurements the standard detector assembly has to be supplanted by an integrating sphere. This device consists of a spherical cavity, coated with barium sulphate reflective paint, which collects the scattered light, either in transmission or reflection methodologies, and measures this integrated light, using detectors appropriate to the wavelength region. The integrating sphere incorporates photomultiplier and lead sulphide detectors and allows the measurement of scattered transmission spectra. Cuvette and optical components are accommodated prior to the light entering the sphere. With this design, light scattered by a non-homogeneous sample is collected by the sphere. The sphere includes a specular or gloss trap located at a position on the periphery of the sphere such that light reflected at the angle of incidence can be omitted from the diffuse or hemispherical measurement. This trap can be replaced by a white reflective plate so that the specular light is collected by the sphere along with the diffuse light and the net result is the total reflectance of the sample.

The 60 mm integrating sphere allows measurement across the wavelength range from 200 to 2500 nm. The total light reflected from a solid sample is composed of diffuse and specular components. With the specular trap installed in the Lambda 19 integrating sphere, the specular light is absent from the measured spectrum, and subtraction of this spectrum from the total reflectance spectrum yields the specular reflectance spectrum.

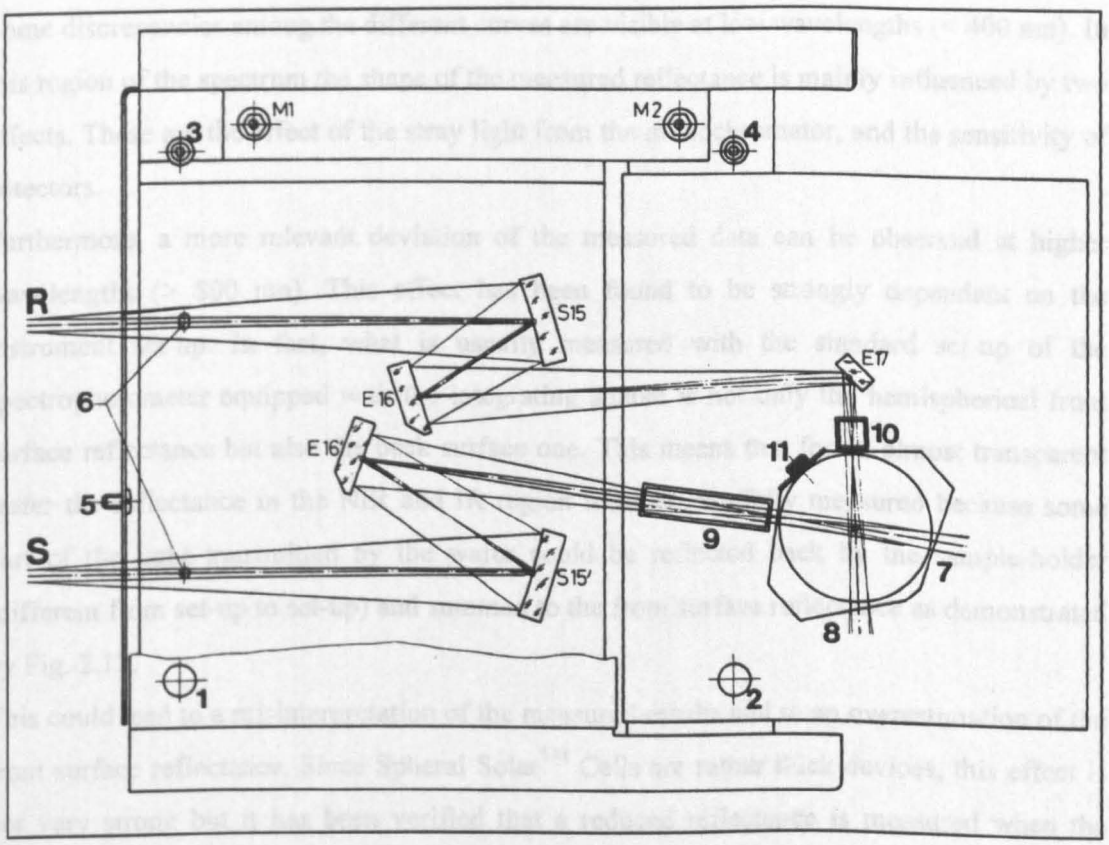

Fig. 2.10 - 60 mm Integrating Sphere

2.2.2 Accuracy Validation

An intercomparison of different reflectance measurements has been performed in order to check the reliability of the instrument available at ESTI laboratories. This validation represent a necessary step for determining the accuracy of the measured results which will be considered, further on, as reference results for the device simulation.

The spectrophotometer described above (*Par. 2.2.1*) has been compared to the following four instruments:

1. Lambda 9 - Perkin Elmer (EI-JRC-Ispra-Italy);
2. Lambda 19 - Perkin Elmer (Perkin Elmer - Uberlingen - Germany);
3. Lambda 9 - Perkin Elmer (Fraunhofer ISE - Freiburg - Germany);
4. Home-made instrument (ISFH GmbH, Emmerthal, Germany).

The measured reflectance spectra of a Spheral Solar™ Cell (TE004) are shown in Fig. 2.11. All the reported curves have been measured at the same experimental conditions, at an incidence angle of 8 deg.

A very good agreement among the different curves is present at visible wavelengths (400÷800 nm). In fact, in this region of the spectrum a negligible uncertainty (<<1%) has been evaluated.

Some discrepancies among the different curves are visible at low wavelengths (< 400 nm). In this region of the spectrum the shape of the measured reflectance is mainly influenced by two effects. These are the effect of the stray light from the monochromator, and the sensitivity of detectors.

Furthermore, a more relevant deviation of the measured data can be observed at higher wavelengths (> 800 nm). This effect has been found to be strongly dependant on the instrument set-up. In fact, what is usually measured with the standard set-up of the spectrophotometer equipped with the integrating sphere is not only the hemispherical front surface reflectance but also the back surface one. This means that for an almost transparent wafer the reflectance in the NIR and IR region must be carefully measured because some part of the light transmitted by the wafer could be reflected back by the sample-holder (different from set-up to set-up) and summed to the front surface reflectance as demonstrated by Fig. 2.12.

This could lead to a misinterpretation of the measured results and to an overestimation of the front surface reflectance. Since Spheral Solar™ Cells are rather thick devices, this effect is not very strong but it has been verified that a reduced reflectance is measured when the

sample is simply laterally held by an adhesive film instead of being held by the standard sample holder of the instrument. The slight shift at 860 nm is due to the change of detector.

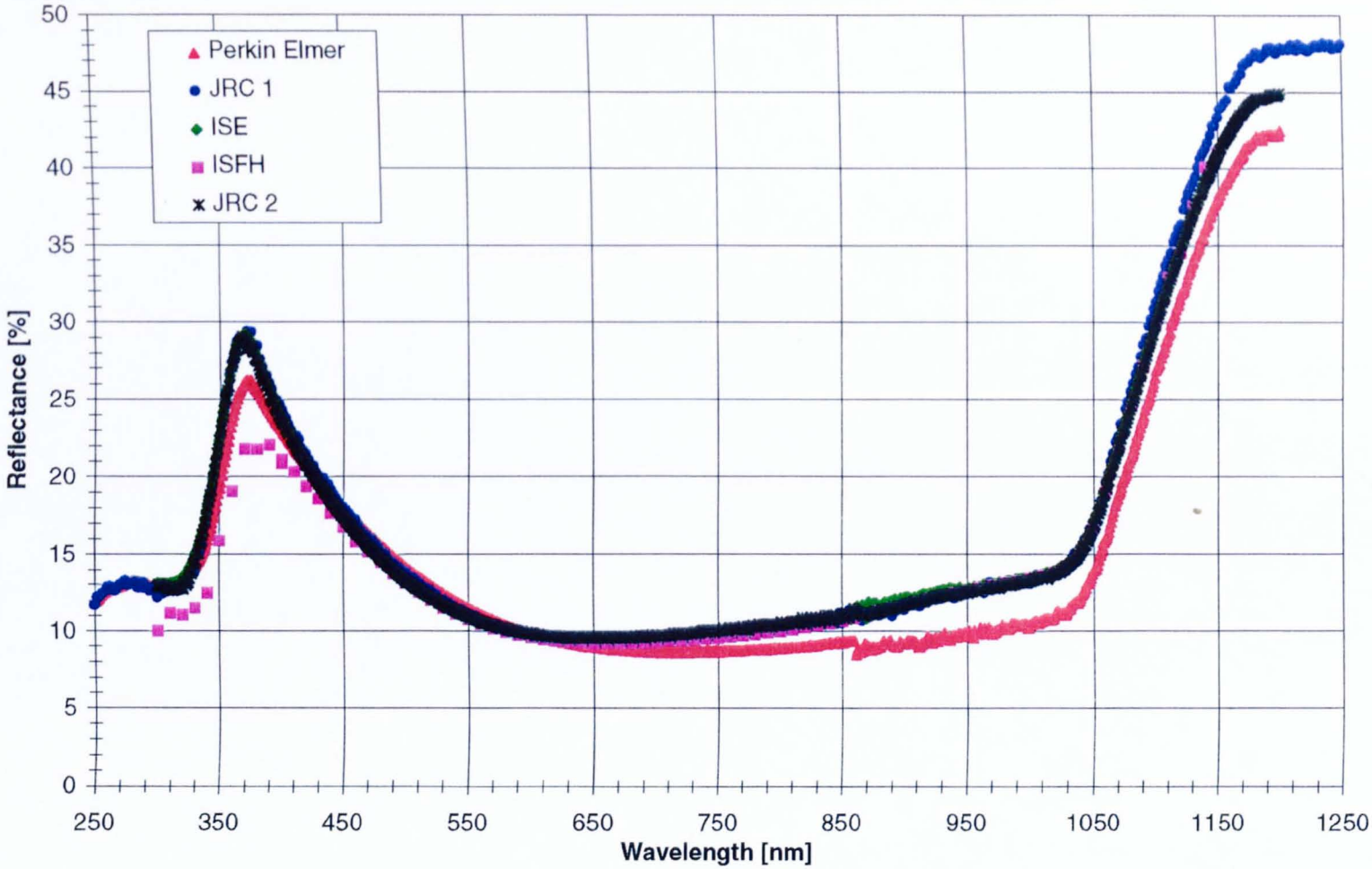

Fig. 2.11 - Reflectance vs. Wavelength of TE004, measured with different spectrophotometers.

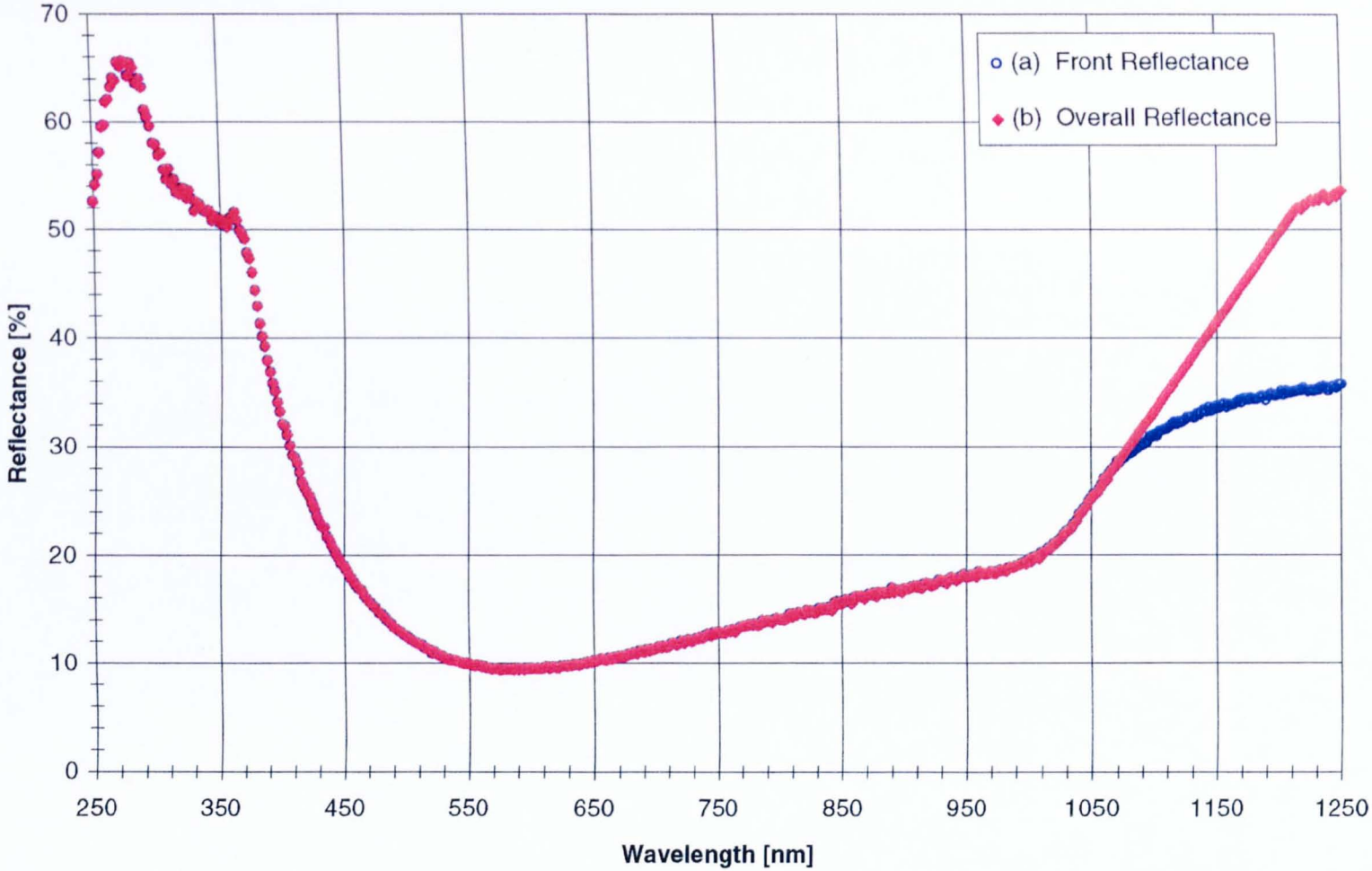

Fig. 2.12 - Silicon wafer reflectance measured with two different set-up.
Curve (a) takes into account the front and back reflectance, while curve (b) estimates only the front reflectance of the wafer.

2.2.3 Hemispherical Reflectance vs. Angle of Incidence

The measurement of diffuse reflectance vs. angle of incidence was performed by mounting on the spectrophotometer a dedicated 150 mm integrating sphere, equipped with a clip style centre mount. A graduated scale allowed the desired sample inclination to be set.
The samples were measured at different incidence angles (between 0 and 80 deg., step 10); the obtained absorptance curves are plotted in Fig. 2.13.

Due to the geometry of the instrument, the real measured quantities are the hemispherical diffused reflectance at 8 deg. and the hemispherical transmittance at 0 deg.
The absorptance spectrum has consequently been analytically evaluated assuming that the sum of absorptance, transmittance and reflectance must be equal to the unity. The error introduced into the measured data, by assuming both reflectance and transmittance being measured at 0 deg., is negligible at short wavelengths (< 1000 nm), where the transmittance is almost zero, and is less then 2% over the rest of the spectrum.

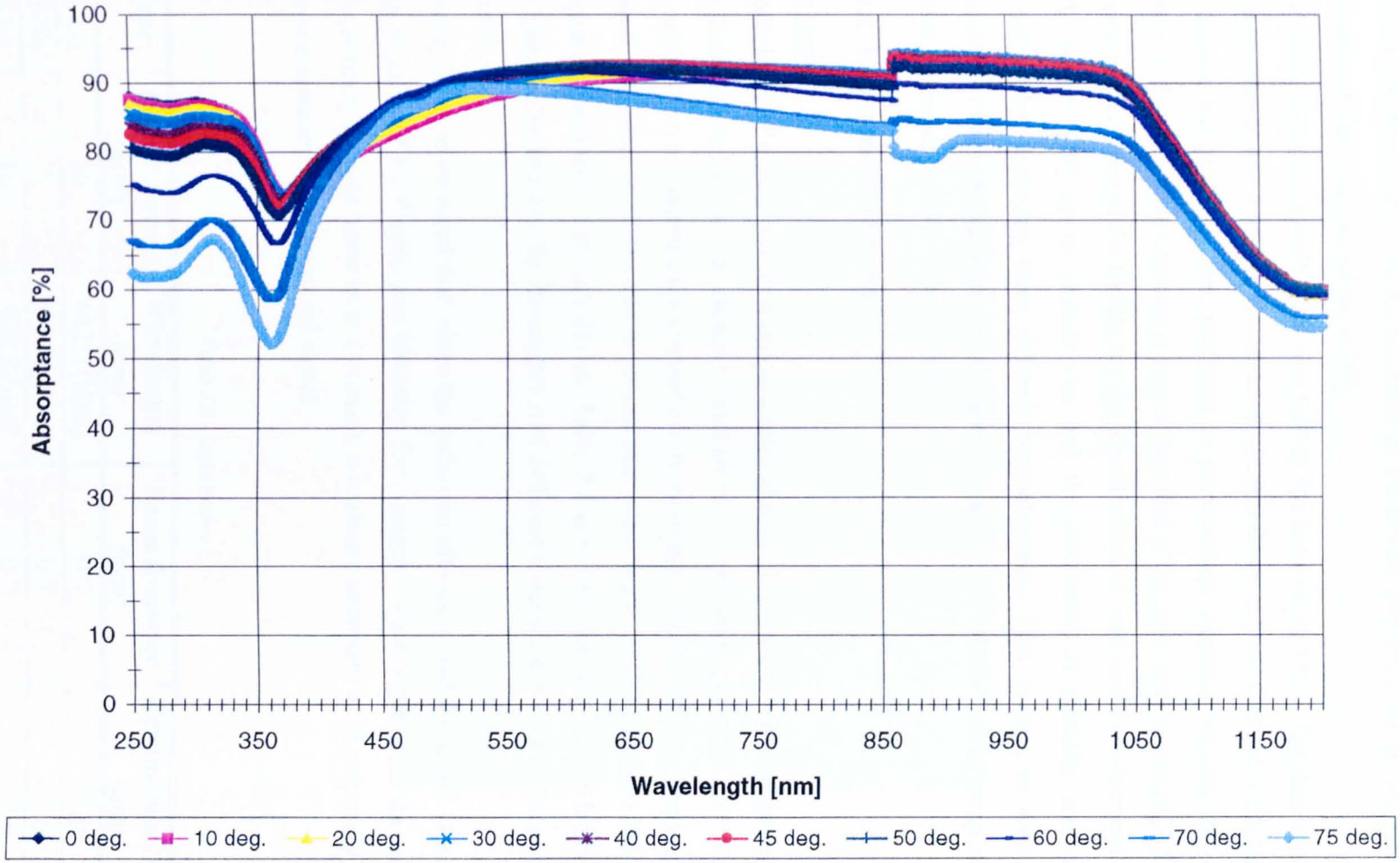

Fig. 2.13 - Absorptance vs. angle of incidence

2.2.4 Design and Realisation of the Laser Scan Facility "ESTIScan"

Laser scanning is a well known non-destructive analytical technique with high spatial resolution for the electrical characterisation of PV-device performances as well as for the verification of light trapping schemes [19].

At the ESTI laboratory a multi-laser scan facility has been set up with a fast data acquisition system in order to allow on-line visualisation of Light Beam Induced Current (LBIC) images. Photocurrent mapping has been preferred to photovoltage mapping because the relative variation of the short circuit current is greater than that of the open circuit voltage [20].

The main applications of the facility are the identification of structural and electrical defects in PV devices [19] up to module size and the evaluation of spatially resolved cell responsivity by employing three different monochromatic light sources as well as the verification of the trapping schemes simulated by ray-tracing calculations in many different PV-devices, mainly Spheral Solar™ Cells.

2.2.4.1 Experimental Set-up

Light Sources

The efficiency of a solar cell for monochromatic illumination is much higher than that under solar illumination. In fact, the photon utilisation of a single band gap solar cell is at most 50%, while for a monochromatic wavelength, theoretically, all the photon energy could be absorbed. Therefore, it is possible to choose laser-wavelengths such as to have the highest cell quantum efficiency for each device. Table 2.8 describes the selection of lasers which have been chosen to allow the investigation of different materials showing different spectral responses.

However, it has to be noted that, since the collection efficiency and the LBIC signal are a strong function of the illumination intensity, for intensities much higher then the solar one (i.e. with finely focused lasers as in this case), it is always necessary to be extremely careful in the interpretation of the measured signal.

Table 2.8 - Light Sources

Type	*Output-Power (mW)*	*Wavelength (nm)*	*Beam Diameter (mm)*	*Penetration Depth (μm)*
He-Cd	30	442.0 (blue)	0.7	~1.0
He-Ne	3	543.5 (green)	0.7	~1.8
He-Ne	10	632.8 (red)	0.7	3.5

System 1: High Precision Guiding Rails

The high precision system has been developed to scan small size (up to 25 x 25 cm) PV-devices of any manufacturing process. It consists of a motorised X-Y table controlled by two 5-phase stepping motors, providing excellent positioning accuracy (1 μm) and repeatability (1 μm). The stage is entirely positioned from a PC, through a dedicated digital interface board.

An inter-changeable microscope lens is fixed over the centre of the table to allow the focusing of the laser beam. Three different spot sizes can be chosen: 50 μm, 20 μm and 10 μm. A photograph of the focused spot is shown in Fig. 2.14. The ring around the spot is the light reflected by the tip of the microscope lens. This light does not influence the acquired signal since it can be considered as a constant light bias.

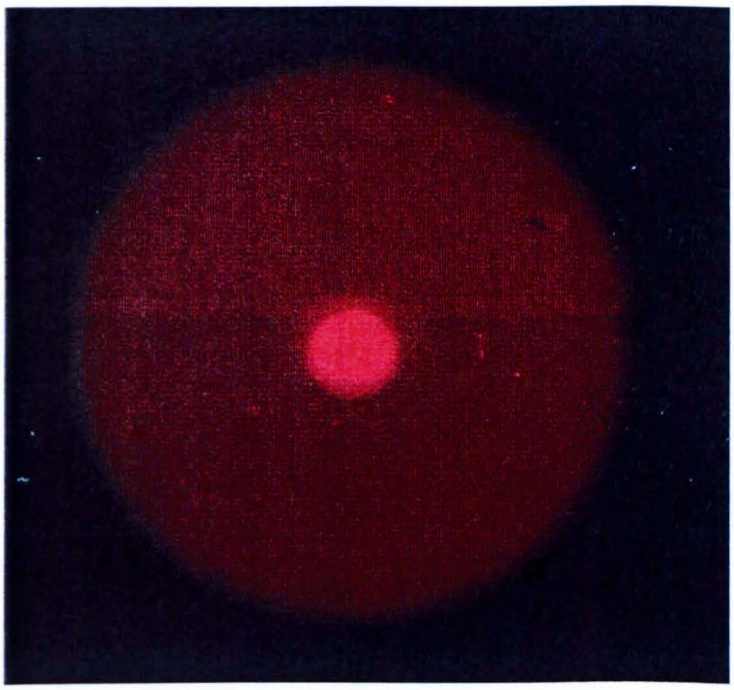

Fig. 2.14 - Close-up of the focused laser spot

A universal sample holder with needle point contacts is available, which also allows very small bare samples to be contacted.

System 2: Large Area Deflecting Unit

A pre-objective scanning configuration which allows to scan a flat image plane has been chosen. An f-theta lens (focal length of 19 cm, deflection angle of ± 12.5 deg. and focused spot diameter of 16 µm, over a 30x30 cm scan surface) with an exactly defined negative (barrel) distortion ensures proportionality between the deflection angle and the beam position on the scanning surface.

Examples of the distorted and corrected image are shown in Fig. 2.15.

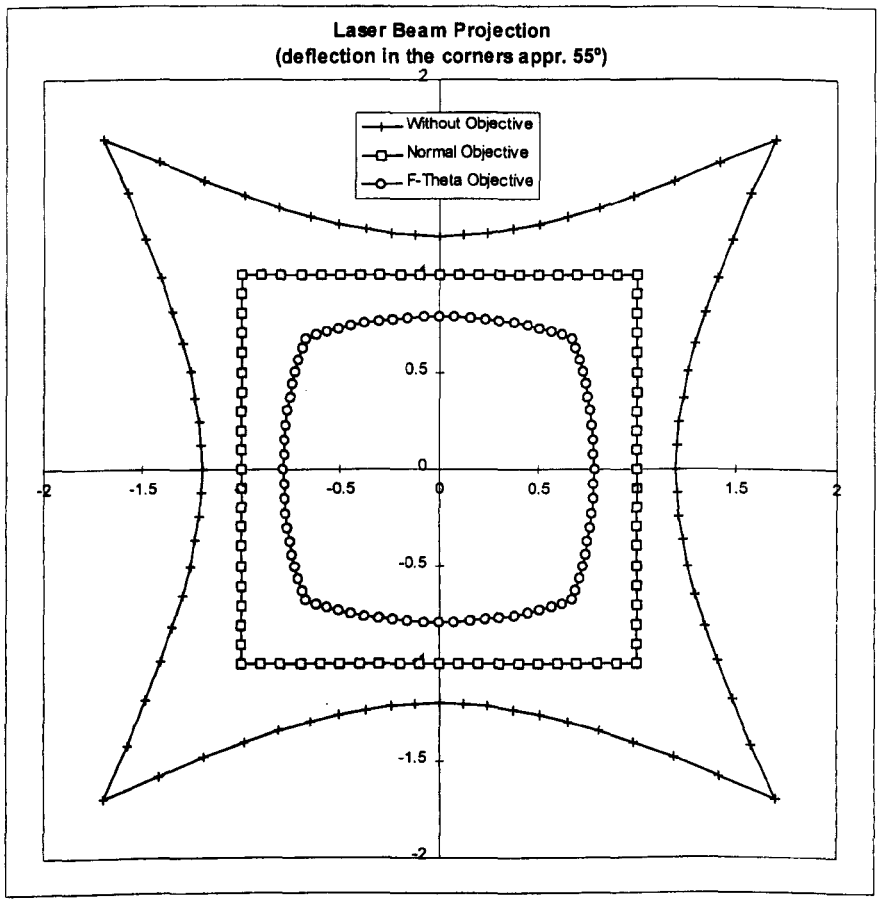

Fig. 2.15 - Image correction by a normal objective and by an F-theta objective

The laser beam is deflected by two galvo-driven mirrors, operated by a driver circuit controlled by a PC through a digital interface board. The data transfer (bit-serial for each channel) occurs at a maximum rate of 200 kS/s (100 k XY-pairs).

A unified housing contains the twin axis oscillating mirrors in a dust proof and water resistant enclosure.

A simplified scheme of both systems is illustrated in Fig. 2.16. It is interesting to notice that the laser beam is transmitted to the two scanning systems through optical fibres in order to maximise beam uniformity and minimise intensity losses.

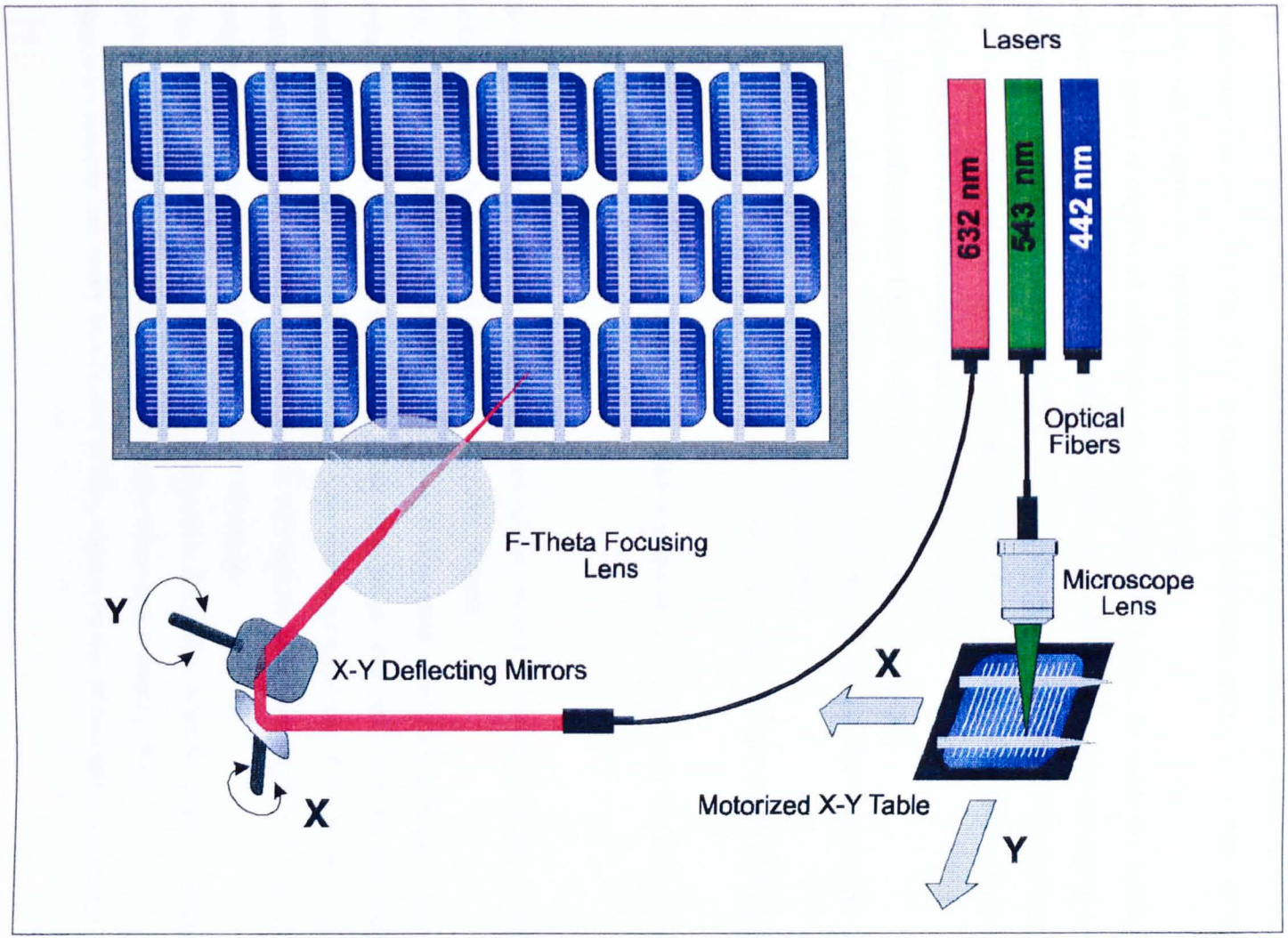

Fig. 2.16 - Simplified Scheme of the ESTI Scan Facility

2.2.4.2 Data Acquisition

The short-circuit current of the device under test is amplified by a transconductance amplifier and acquired by an analogue input data acquisition board. The maximum data acquisition rate of this board is 80 kilosamples/second.

The in-house developed *ESTIScan* program controls both scanning systems in a Windows environment as shown in Fig. 2.17. It moves the laser beam across the surface of the PV-device and acquires the current induced by this beam.

The program is capable of subtracting background light, hence, the scans don't have to be performed in a dark room, which simplifies the use. In order to increase the signal-to-noise ratio a high number of measurements for each point can be performed. By averaging the signal over a hundred measurements for each different point, a signal-to-noise ratio less than 1% is obtained, but the scan time is consequently increased.

The "Pseudo-colour Scan Image" is the heart of the program. One can:

- point out interesting points on this image with the mouse and the laser beam will be positioned on the corresponding spot on the cell itself;
- drag with the mouse on the scan image to select a certain area to zoom-in with higher resolution;
- drag a horizontal or vertical line to make a graph of a certain cross section of the scan image.

Besides saving the numerical data, this image can be saved as a bitmap. It is also possible to retrieve previously measured data and make plots of them.

The range of the colour scale is user definable. Before each scan a spot-measurement of the induced current (voltage) is performed, to set an average reference value for the scaling of pseudo-colours. This procedure allows the visualisation of small signal variations across the entire device surface. Local variations due to cell defects can be distinguished from random noise enlarging the colour scale of the acquired image.

The amount of measurements per point is also user definable. A better signal to noise ratio (S/N) is obtained by measuring each point more times and averaging them.

Hardware settings can easily be adjusted in the program by use of configuration forms.

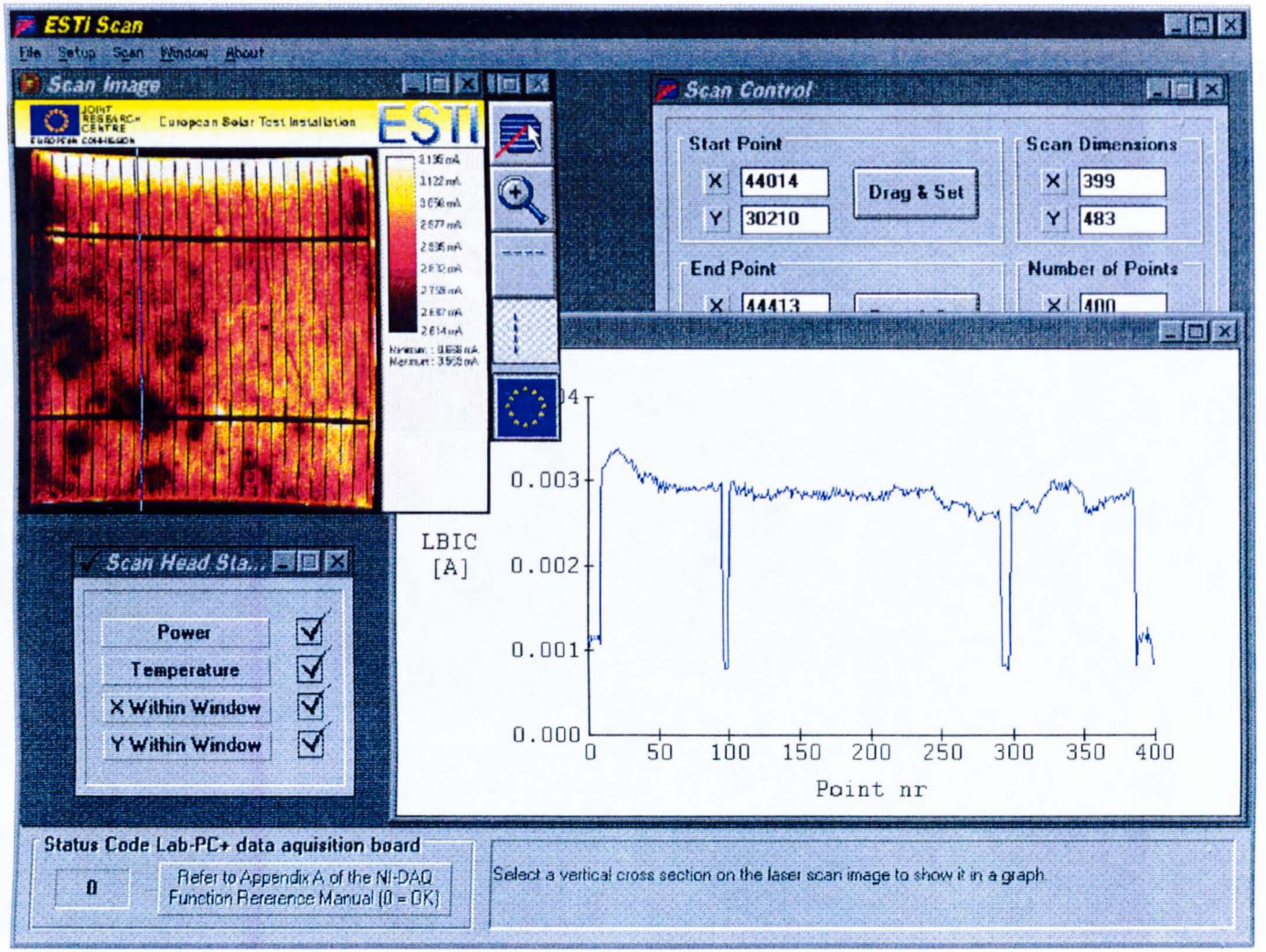

Fig. 2.17 - ESTIScan user interface

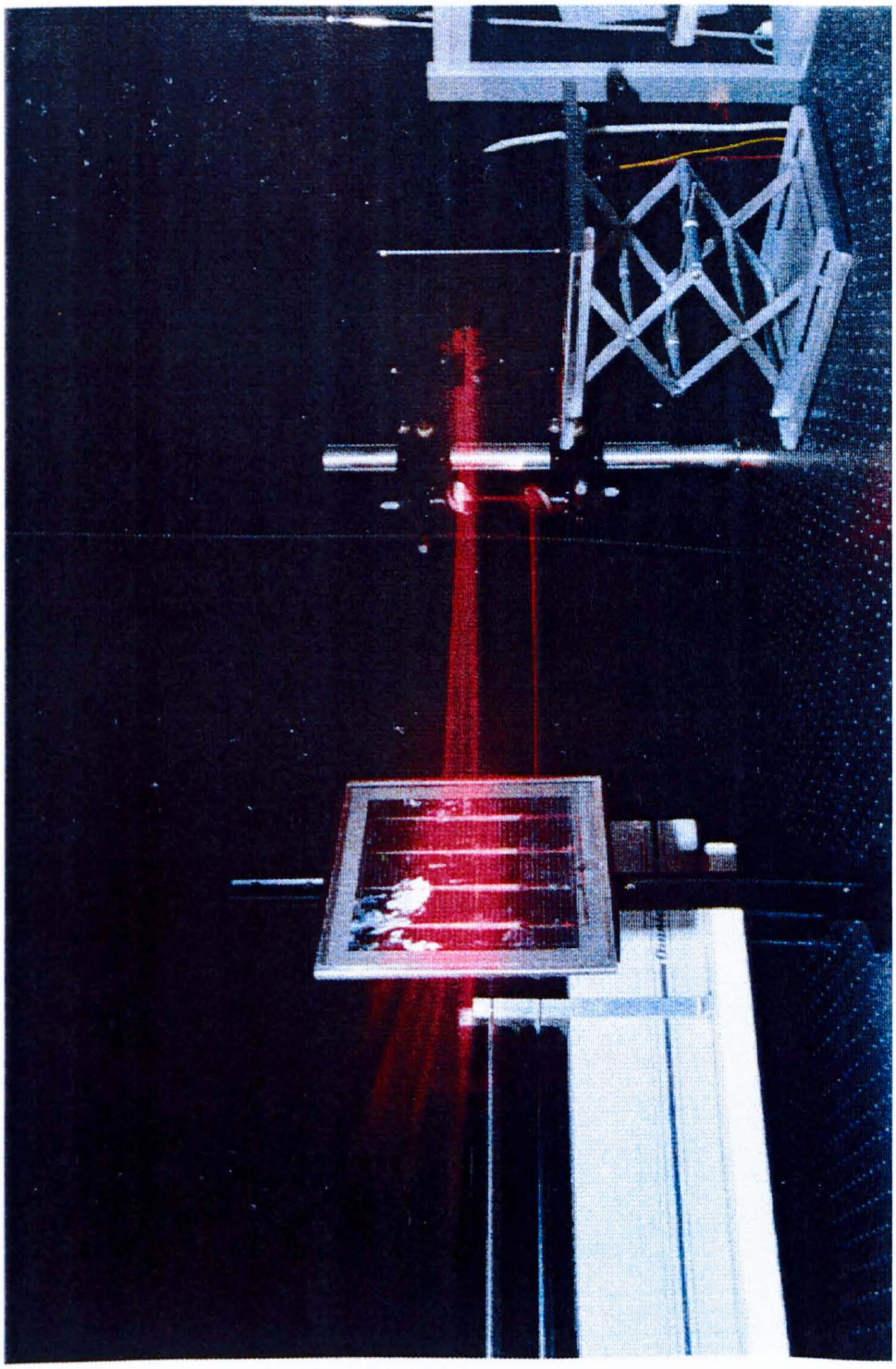

Fig. 2.18 - Picture of the ESTIScan facility

2.2.5 *Efficiency Calculation under Laser Light*

The J_{sc} of a PV-device under monochromatic light illumination is given by:

$$Jsc[A/cm^2] = qNQE \qquad \textit{Eq. 2. 16}$$

where:

$$N[photons/cm^2/\text{sèc}] = P_{inc.}/h\upsilon \qquad \textit{Eq. 2. 17}$$

$$h\upsilon[eV] = q(1.24/\lambda) \qquad \textit{Eq. 2. 18}$$

$$QE = Ext.QuantumEfficiency \qquad \textit{Eq. 2. 19}$$

and λ is expressed in μm. Thus Eq. 2.16 becomes:

$$Jsc = QEP_{inc}(\lambda / 1.24) \qquad \textit{Eq. 2. 20}$$

The power of a PV-device under normal illumination is:

$$P[W] = VocFFJsc \qquad \textit{Eq. 2. 21}$$

For laser illumination, Eq. 2.21 becomes:

$$P_{laser}[W] = VocFFJsc = VocFFQEP_{inc}(\lambda / 1.24) \qquad \textit{Eq. 2. 22}$$

This leads to an efficiency for laser illumination which is:

$$\eta_{laser} = \frac{P}{P_{inc}} = VocFFQE(\lambda / 1.24) \qquad \textit{Eq. 2. 23}$$

while the solar efficiency is:

$$\eta_{laser} = \frac{P}{P_{sunr}} = VocFFJsc / P_{sun} \qquad \textit{Eq. 2. 24}$$

where P_{sun} is given for AM0 and for AM1.5:

AM0 $P_{sun} = 0.137$ W/cm^2 *Eq. 2. 25*

AM1.5 $P_{sun} = 0.100$ W/cm^2 *Eq. 2. 26*

2.2.6 *Light Beam Induced Current (LBIC) Measurements*

Some examples of LBIC images acquired at the *ESTI Scan* facility are shown below.

Even though the resolution of the LBIC technique is usually limited by the employed optics, it has been experimentally verified that the resolution of this system is less affected by the spot size than by two other major factors: the positioning precision and step-size of the system, and the number of averages performed over a single point. In particular, this last factor drastically reduces the signal to noise ratio, allowing the detection of very small signal variations even at low irradiation intensities.

Scans of the same polycrystalline silicon cell have been carried out by using different focusing lenses and the recorded LBIC signals over grain boundaries (size < 10 μm) have been compared.

The first image shown in Fig. 2.19, refers to a very high resolution scan of a polycrystalline silicon cell, performed with the X-Y table system equipped with the 10 μm microscope lens, employing the HeNe red laser and averaging the signal over 100 measurements.

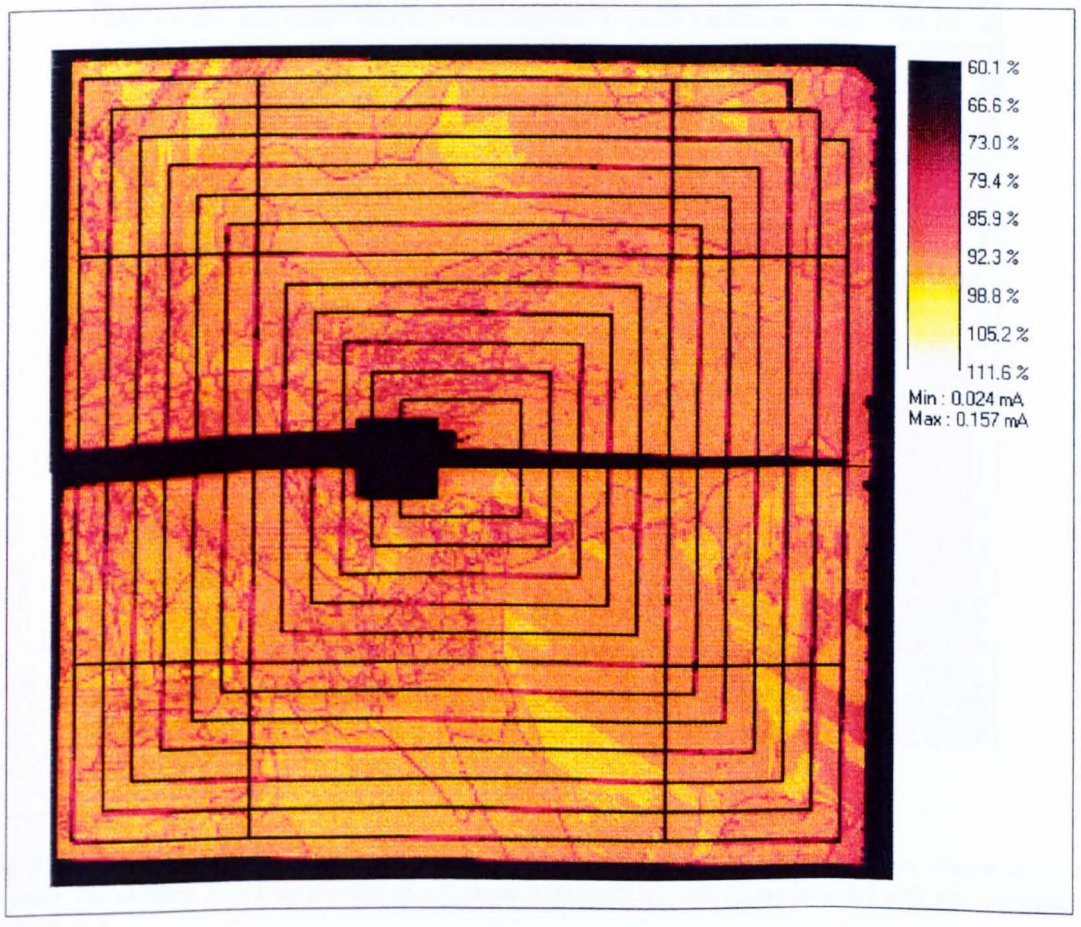

Fig. 2.19 - High resolution LBIC image of a polycrystalline silicon cell, obtained with the HeNe red laser with an optical resolution of 10 μm. 100 averages have been performed at each point in order to improve the signal to noise ratio.

Fig. 2.20 shows a region of the same cell scanned with the same laser. The outlined area of the image, which clearly shows the grain boundaries of the polycrystalline material, has been scanned with an optical resolution of 20 μm, averaging the signal point by point over 100 measurements. The rest of the scan has been performed with the same optical resolution but the number of averages was reduced to 10 and the step size of the table was reduced by one third. The difference between the qualities of the two regions of Fig. 2.20, both performed with an optical resolution of 20 μm, is definitely more evident than the one between Fig. 2.19 and Fig. 2.20 scanned with two different optical resolutions and the same step-size and averages.

It must be noticed that another advantage of this scanning system is that small regions of the sample can be precisely zoomed-in and different images can be perfectly overlapped, thanks to the very accurate positioning of the X-Y stage.

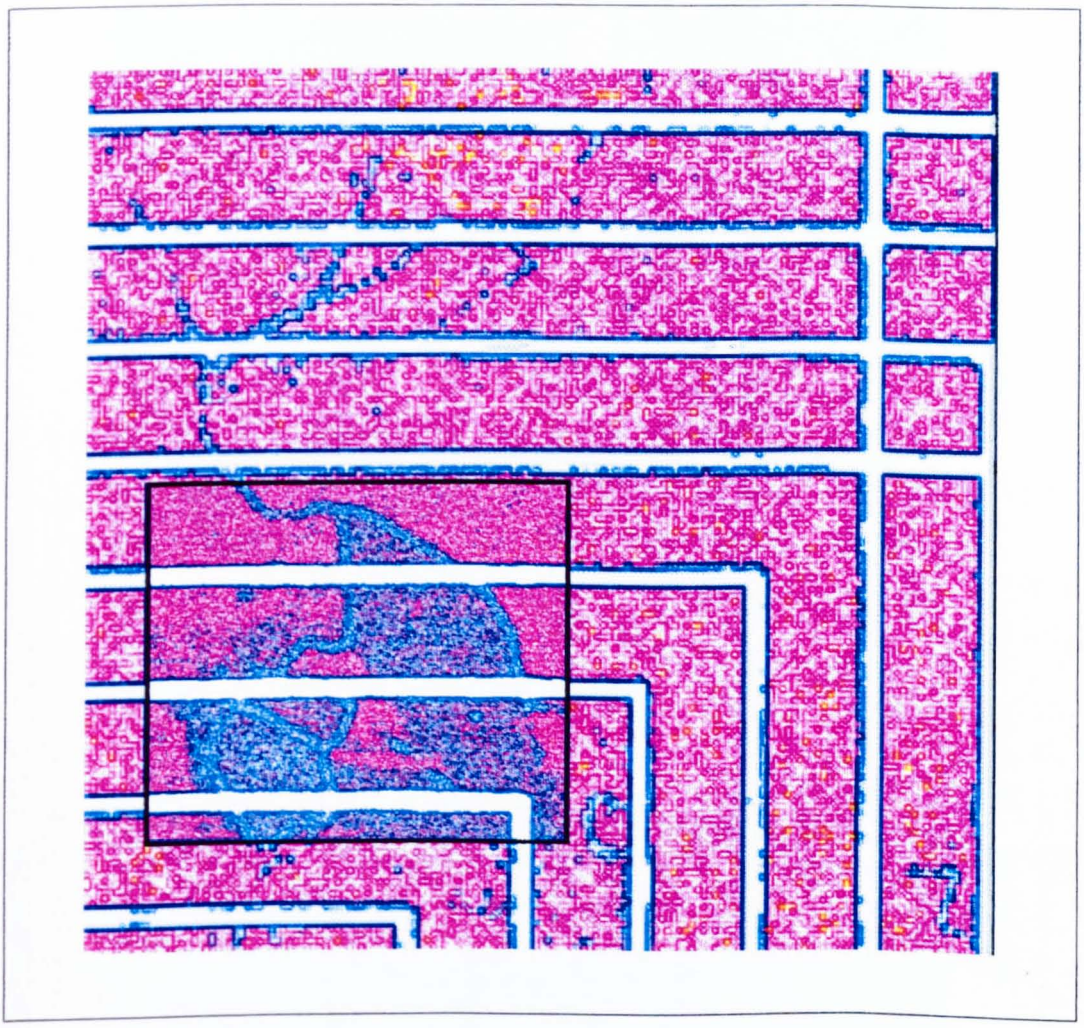

Fig. 2.20 - LBIC of the same cell obtained with the same equipment, but with only 10 averages at each measured point. The outlined area is an overlap of a different scan made with the 20 μm lens and with 100 averages.

In Fig. 2.21 the LBIC image of a monocrystalline silicon module (1.3 x 0.7 m) is shown to demonstrate the possibility of scanning devices of any size. The scan has been performed with

the X-Y mirrors but without the focusing lens, at a distance of about two metres. Even though the beam was not very focused (the spot diameter is 0.7 mm), the resolution of the image is sufficient to indicate clearly which are the most active cells of the module and the amount of the contribution of each cell to the overall output current. This information is normally not available with the standard electrical measurements and can be fundamental to identify the cause of low module performance.

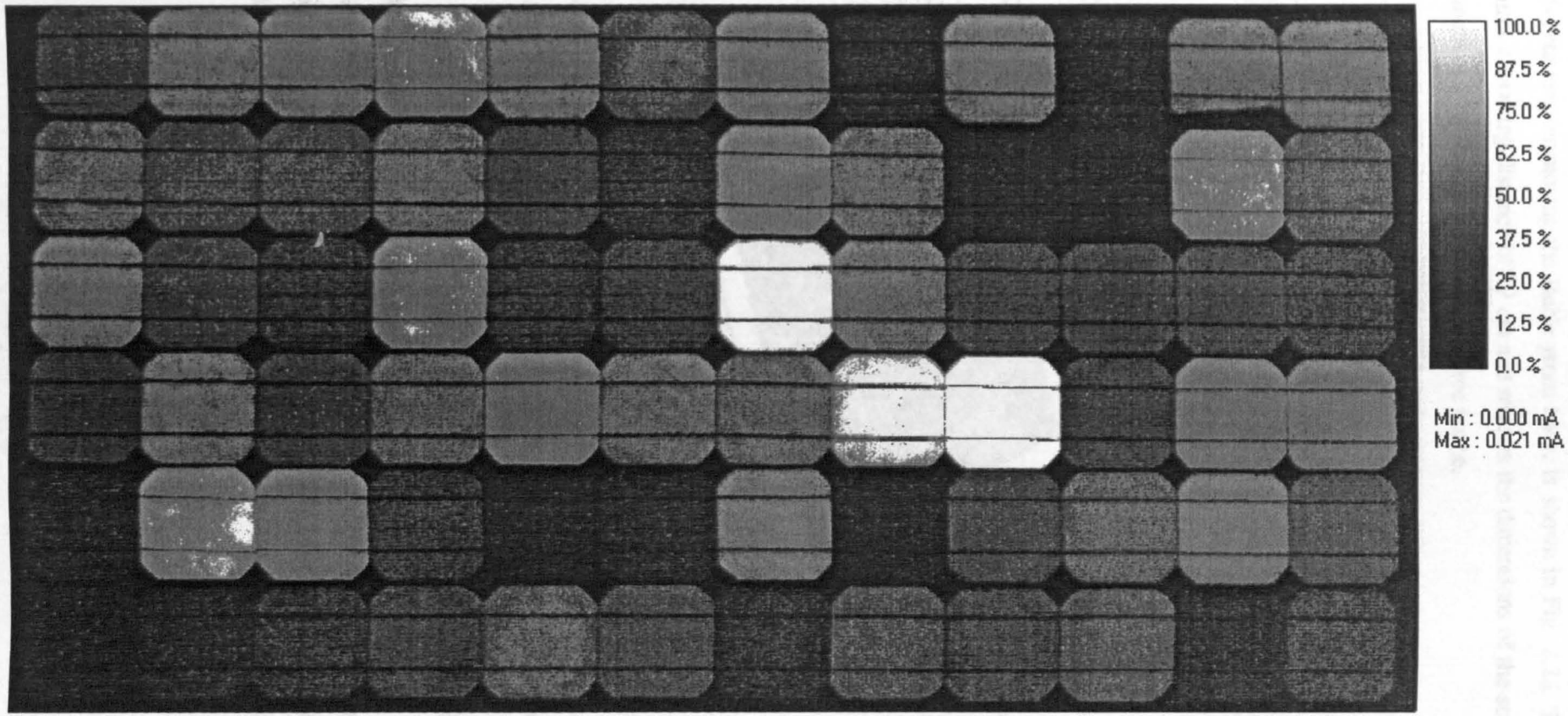

Fig. 2.21 - Low resolution LBIC image of a standard monocrystalline silicon module (size: 1.3 x 0.7 m), obtained with the HeNe red laser.

Another scan of a small module (size 10 x 4 cm), performed with the X-Y mirrors equipped with the f-theta lens, employing the HeNe green laser, is shown in Fig. 2.22. The use of the lens, requires a working distance of 19 cm and reduces the dimensions of the scanned surface to a maximum of 30 x 30 cm, for a distortion-free image.

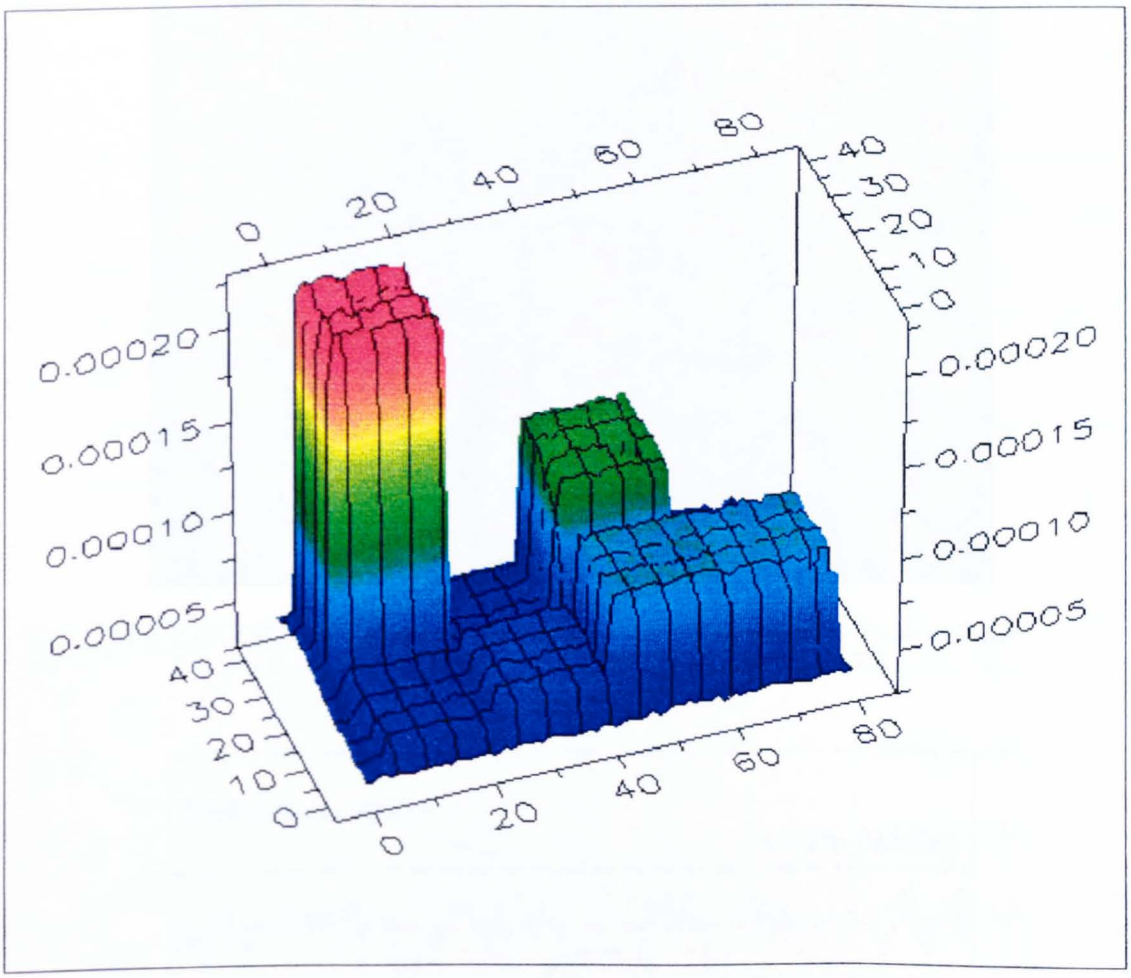

Fig. 2.22 - LBIC image of a small module obtained with the HeNe green laser and with the f-theta focusing lens.

A typical example of qualitative image of a monocrystalline cell is shown in Fig. 2.23. The LBIC signal measured across the defect is plotted in Fig. 2.24.

Even though the signal fluctuation due to the low number of averages on a single point measurement, is estimated to be around 5 % of the signal, the defect can be still clearly distinguished. A 10 % scaling around the reference value was assumed in this measurement.

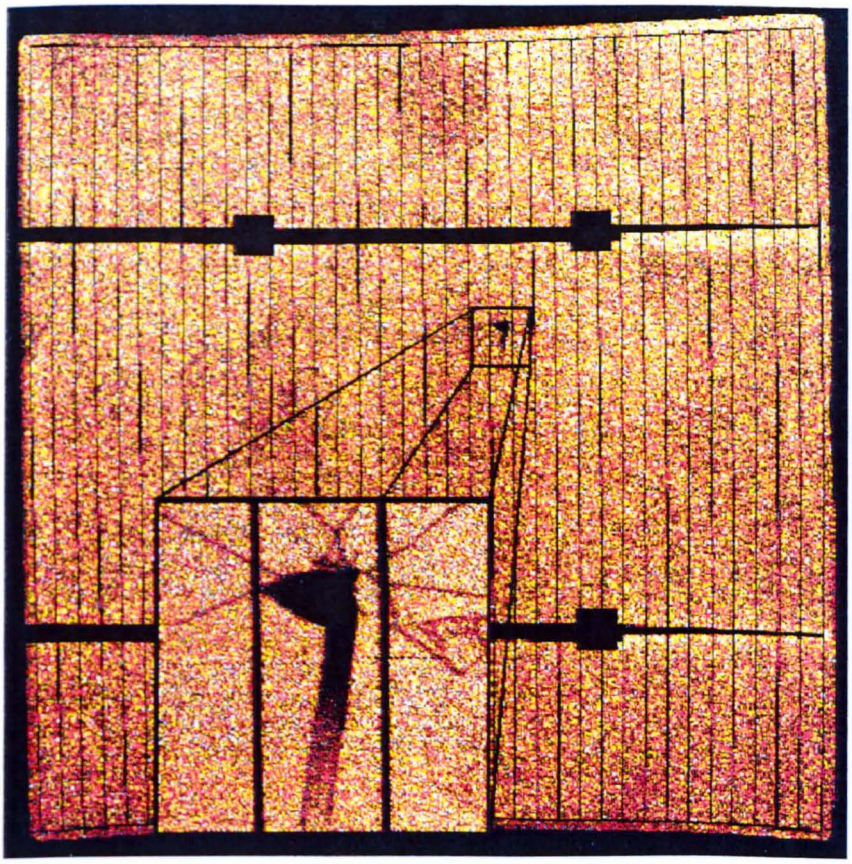

Fig. 2.23 - LBIC image of a polycrystalline silicon cell obtained with the He-Ne red laser (l = 32.8 nm, P = 10 mW) which shows a small structural defect.

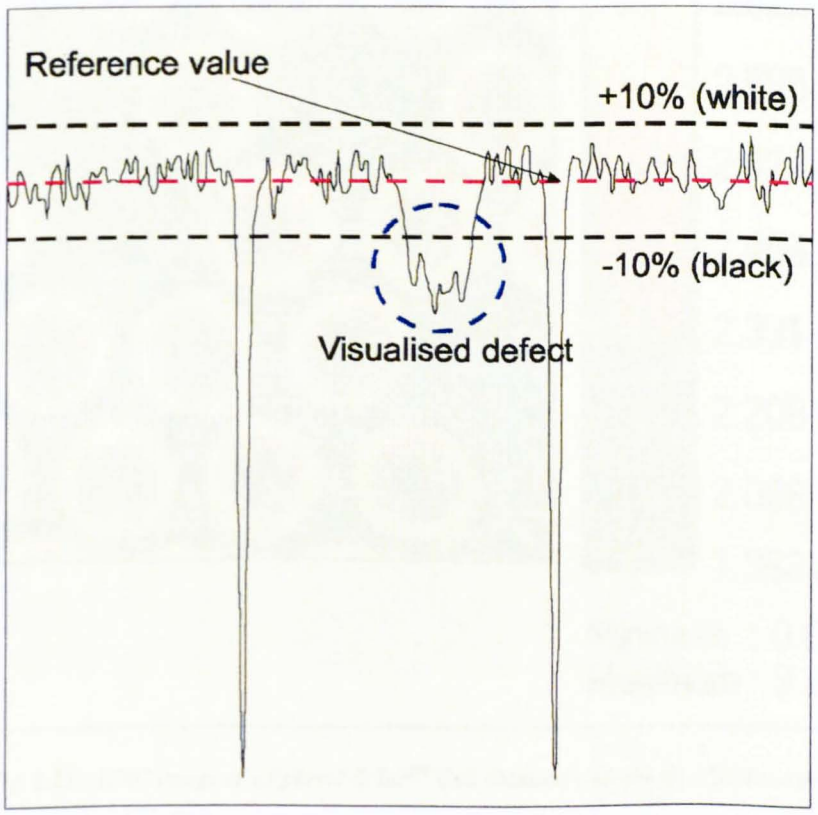

Fig. 2.24 LBIC signal of a cross-section of the cell defect.
The pseudo colours are scaled around a reference value which is obtained by a spot-measurement.

2.2.7 LBIC Measurements of Spheral Solar™ Cells

The main aim for the development of the *ESTIScan* facility has been since the beginning the interest in verifying by laser scanning the simulated generation profile of Spheral Solar™ Cells. Therefore, the resolution of the facility had to be sufficiently high to allow the visualisation of the contribution of each individual sphere to the overall cell current generation. Being the sphere diameter dimension 700 µm, a beam spot size of at most of 100 µm was needed.

As demonstrated in the previous paragraph the spatial resolution of the *ESTIScan* facility (both systems) is of the order of 10 µm. With such a resolution very accurate pseudo-colour images of Spheral Solar™ Cells could be measured.

The same area of the device under test was scanned with the three different lasers in order to investigate the current generation at different penetration depths into the cell.

Three LBIC images with 250 x 250 points of 15 mm^2 of the cell TE004, measured with the X-Y deflecting mirrors are shown below in Fig. 2.25, Fig. 2.26 and Fig. 2.27.

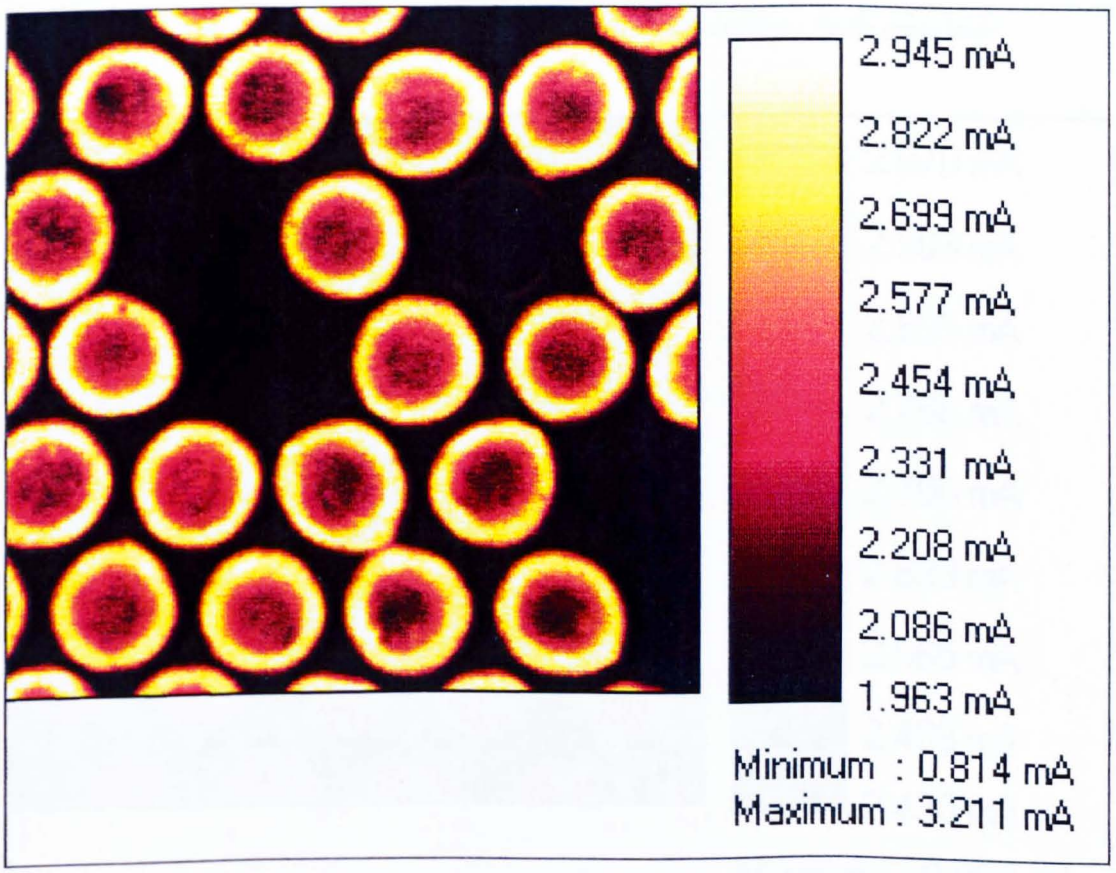

Fig. 2.25 - LBIC image of a Spheral Solar™ Cell obtained with the He-Cd blue laser

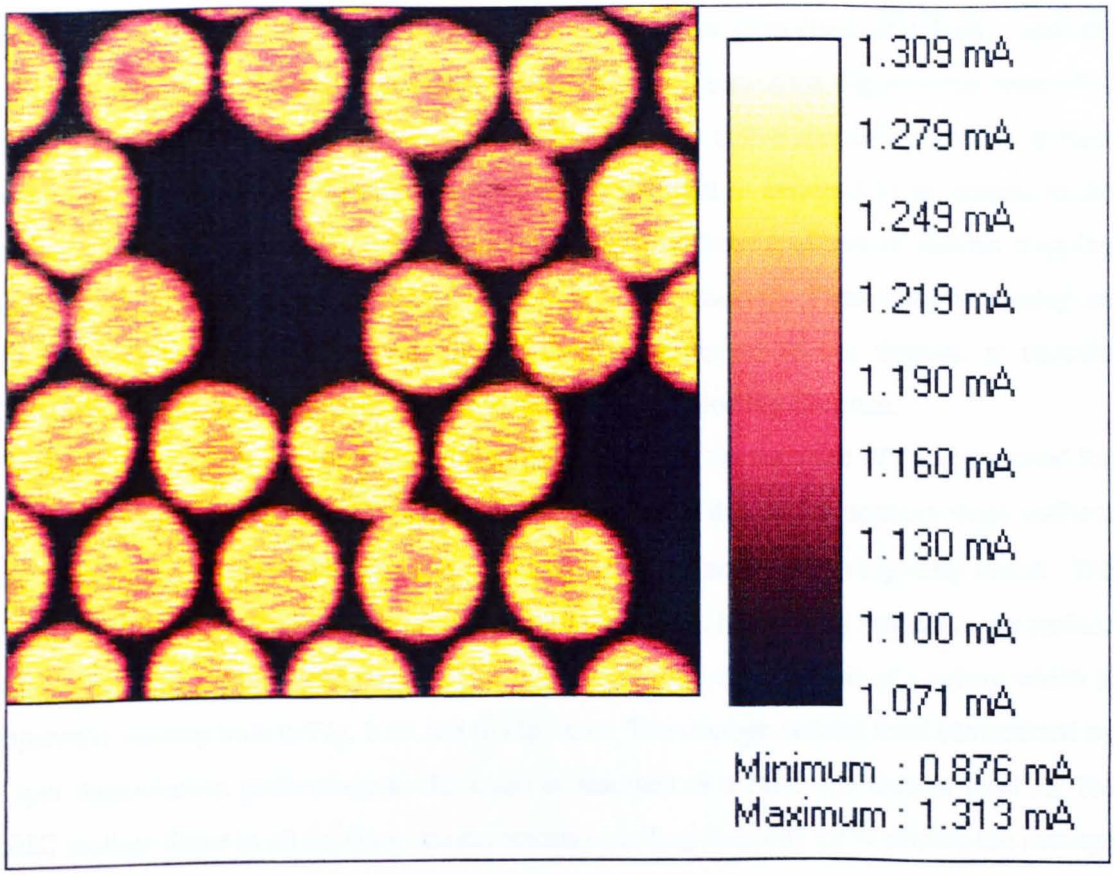

Fig. 2.26 - LBIC image of a Spheral Solar™ Cell obtained with the He-Ne green laser

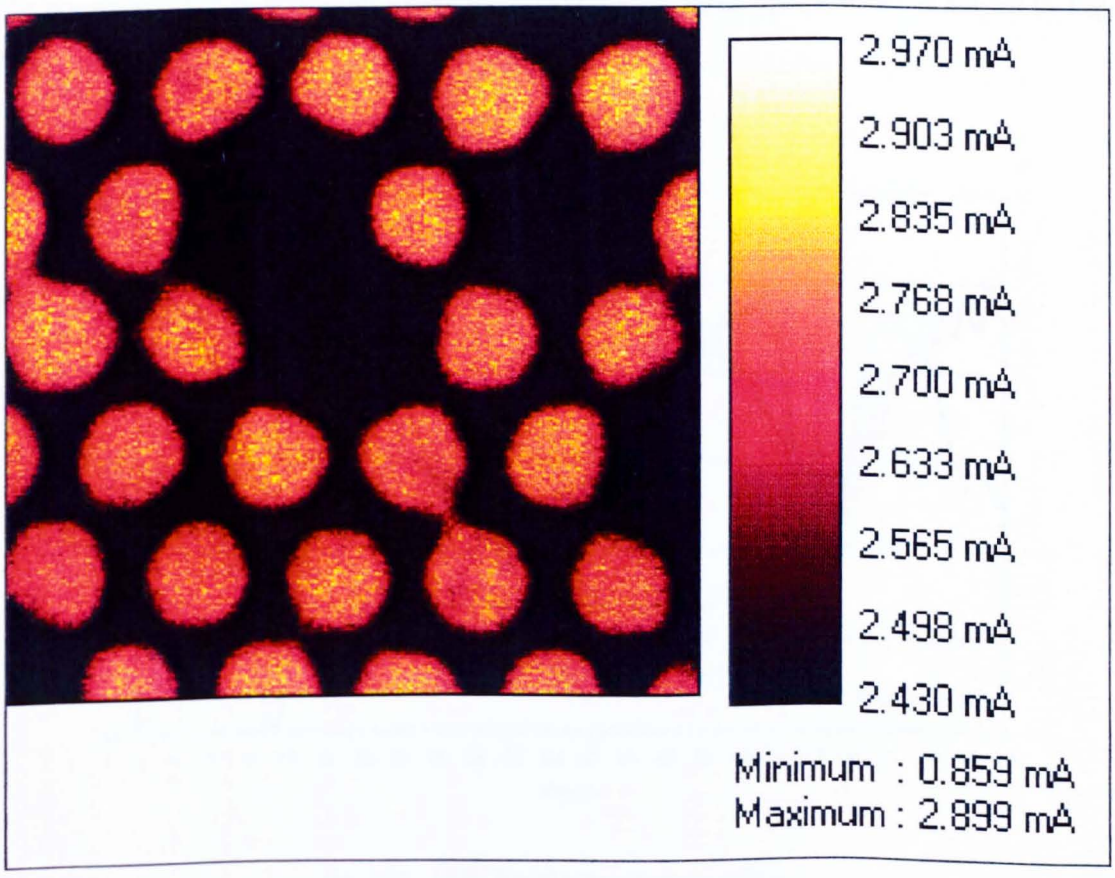

Fig. 2.27 - LBIC image of a Spheral Solar™ Cell obtained with the He-Ne red laser

Interesting to notice is the different absorption of the two monochromatic lights, and the effective optical size of the spheres which changes with the penetration depth of the beam. The first image induced by the blue laser, indicates that the most active area of the spheres is their surface. In particular, the top of the sphere, where the light is assumed to be normal to the surface, is not the most active region. This is the first time that the effects of indirect trapping mechanisms, characterising the spherical geometry, are observed. These effects causing an absorption enhancement in Spheral Solar™ Cells with respect to flat devices, at specific illumination conditions, will be illustrated in details in the following Sections.

The image of Fig. 2.26, acquired with the green laser, shows the response of the cell around the junction (~ 1-1.5 μm from the surface). The absorption in this region appears more uniform and phenomena related to the spherical symmetry of the geometry are completely absent. The average contribution of this region to the current collection is higher with respect to the surface (blue image) and the bulk (red image). This is proved by the visualisation of a sphere which is apparently missing both in Fig. 2.26 and in Fig. 2.27. The average current level (determined by a spot measurement preliminary to the scan) is assumed as a reference current level for the LBIC scaling. Since in all the three measurements a scaling factor of 10 % around the average was assumed, the missing sphere contribution appears to be above the average only for light being absorbed directly at the cell junction.

The normalised signal across an individual sphere by the three light sources is shown in Fig. 2.28.

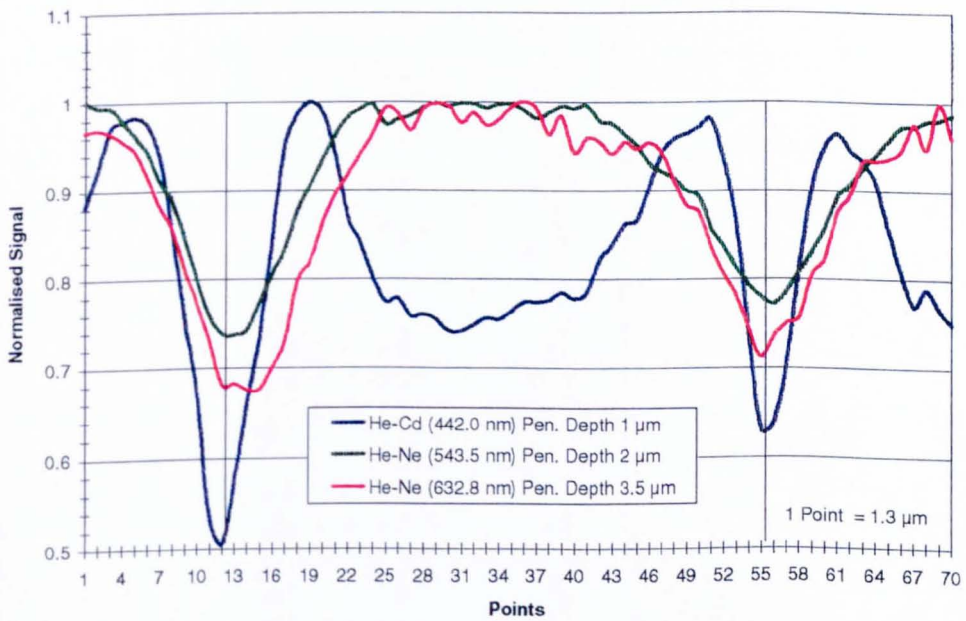

Fig. 2.28 - LBIC Signal across a single sphere

The plot clearly indicates the uniformity of the current generation in the bulk of the sphere and the presence of combined optical effects in the surface layer depending on the geometry. Therefore, the blue light, which is absorbed at the sphere surface, will be employed for verifying these geometry dependent optical effects.

SECTION 3

OPTICAL MODELLING

OF

SPHERAL SOLAR™ CELLS

3.1. Development of a Dedicated Simulation Tool for Spheral Solar™ Cells

Even though several computer codes are available for the optical simulation of PV-devices [22, 23] they do not contemplate the specific geometry which allows the modelling of the unique structure of Spheral Solar™ Cells. Therefore, a Monte Carlo ray-tracing program *WinTrace* [24, 25] has been developed, which realistically reproduces the optics of these devices.

The Monte Carlo method, combined with standard ray-tracing techniques, is the *core* of *WinTrace*, since it allows both the simulation of the random interaction of light with the device and the history of each traced event to be followed, for a statistically significant number of generated events.

3.1.1 The Basics of Monte Carlo Simulations

The expression *"Monte Carlo Method"* is actually very general. Monte Carlo (MC) methods are stochastic techniques meaning they are based on the use of random numbers and probability statistics to investigate problems [26].

The use of Monte Carlo methods to model physical problems allows the examination of very complex systems. Solving equations which describe the interactions between two atoms is fairly simple; solving the same equations for hundreds or thousands of atoms is impossible.

With Monte Carlo methods, a large system can be sampled in a number of random configurations, and that data can be used to describe the system as a whole.

The Monte Carlo method is often referred to as the *"method of last resort"* as it is apt to consume large computing resources. Monte Carlo programs have historically had to be executed upon the fastest computers available at the time, and employ the most advanced algorithms, implemented with substantial programming acumen. With the advent of high-speed supercomputers, the field has received increased attention, particularly with parallel algorithms which have much higher execution rates.

An accurate description of the Monte Carlo routines implemented in the code *WinTrace* is given in Section 4. Then random numbers generation and the choice of the appropriate statistics is also discussed.

3.2. Optical Model Description

The absorption of sunlight by solar cells depends on many parameters, such as the cell material, the surface structure, multi-layer AR-coatings, back surface reflector, encapsulation, illumination geometry and illumination spectrum.

Any component of the devices simulated by the developed code, such as the silicon spheres, the aluminium substrate, the spherical AR-coating and encapsulant layers, as well as the incident light rays, is treated as a class of objects, with physical and optical properties, which can interact through optical processes. This represents a very innovative approach to ray-tracing calculations based on object-oriented programming.

3.2.1 Light Rays

The incident light rays are modelled as electromagnetic waves (vectors as shown in Fig. 3.1) described by the following geometrical and optical properties:

- DIRECTION & SIGN: Array of three Direction Cosines;
- ORIGIN: Array of three Cartesian Co-ordinates;
- DESTINATION: Array of three Cartesian Co-ordinates;
- INTENSITY: Scalar value between 1 and 0;
- WAVELENGTH: Scalar value expressed in nm;
- REFRACTION INDEX: Scalar value depending on the crossed medium.

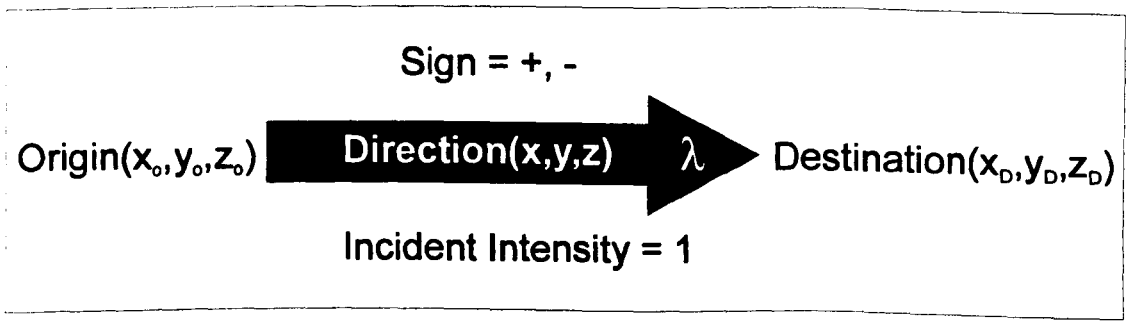

Fig. 3.1 - Object Ray

Each ray can exist either as incident or as one of its reflected, refracted, absorbed and transmitted components. These components are produced by different optical processes. The history of each component, into which an incident ray is split, is followed separately.

Any incident ray propagates from air into the cell with an intensity equal to one and it survives until the intensity of each component becomes less than the 1‰. In this case, the

remaining intensity is stored as lost intensity and a new ray is traced. The only limit for the number of simulated incident rays is the program run time.

3.2.2 Silicon Sphere

This object has been created in order to simulate the more than 17,000 silicon spheres embedded in the device under study. Each sphere has been optically modelled with an external structure composed by a variable number of layers of given thickness (i.e. AR-coatings) and a silicon core of fixed diameter. Any sphere directly illuminated is assumed to be the central element of a hexagonal *lattice* of identical spheres lying in the same plane.

The multi-layered sphere, illustrated in Fig. 3. 2, is described by the following properties:

- CENTRE: Array of three Cartesian Co-ordinates;
- RADIUS: Scalar value;
- POSITION IN THE XY-PLANE: Two indices: m to make steps in the X direction
  n to make steps in the Y direction;
- NUMBER OF LAYERS: Scalar value;
- LAYER THICKNESS: Scalar value;
- REFRACTION INDEX: Scalar value (for each layer);
- ABSORBED INTENSITY: Percentage (for each layer);

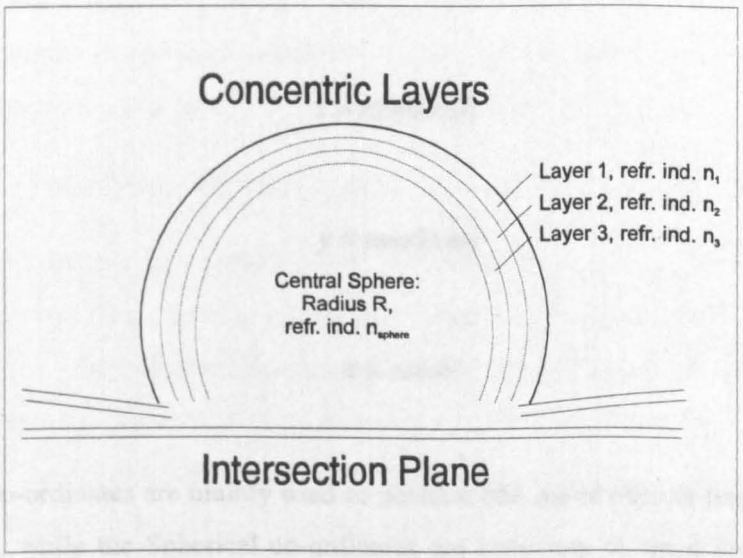

Fig. 3.2 - Object Sphere (multiple layers)

The reflectivity of each spherical layer is seen to be dependent on the wavelength. Hence, optical data such as the real and imaginary parts of the refraction indexes of the different materials are given as standard data files (see Appendix B).

3.2.3 System of Co-ordinates

The system of co-ordinates is an object that transforms its components from Cartesian into Spherical and vice versa, depending on the calculation to perform. In both cases, the centre of this system is assumed to correspond to the centre of the sphere which is directly illuminated.

The transformation from Cartesian $P(x,y,z)$ into Spherical $P(r,\theta,\varphi)$ co-ordinates is expressed by the following set of equations:

$$r = \sqrt{x^2 + y^2 + z^2} \qquad \textit{Eq. 3. 1}$$

$$\theta = arccos\frac{z}{r} = arctan\frac{\sqrt{x^2 + y^2}}{z} \qquad \textit{Eq. 3. 2}$$

$$\varphi = arctan\frac{y}{x} = arcsin\frac{y}{\sqrt{x^2 + y^2}} = arccos\frac{x}{\sqrt{x^2 + y^2}} \qquad \textit{Eq. 3. 3}$$

while the inverse transformation is:

$$x = rsin\theta cos\varphi \qquad \textit{Eq. 3. 4}$$

$$y = rsin\theta sin\varphi \qquad \textit{Eq. 3. 5}$$

$$z = rcos\theta \qquad \textit{Eq. 3. 6}$$

The Cartesian co-ordinates are mainly used to position and move objects (rays and spheres) in the 3d-space, while the Spherical co-ordinates are necessary to trace the path of a ray inside a multi-layered sphere. For example, to define the intersection point between a ray and a sphere the Spherical co-ordinates are employed.

3.2.4 Substrate

This object represents the aluminium plane in which the spheres are embedded. This plane does not necessarily correspond to the plane through the sphere's centres but, as in the real cells, it is shifted below the centre by a small negative quantity Δz (Fig. 3.3).

The intersection plane has the following properties:

- Δz_SHIFT: Scalar value, distance from the XY-plane;
- MIRROR_ON: Boolean, to consider this plane as a reflecting surface.

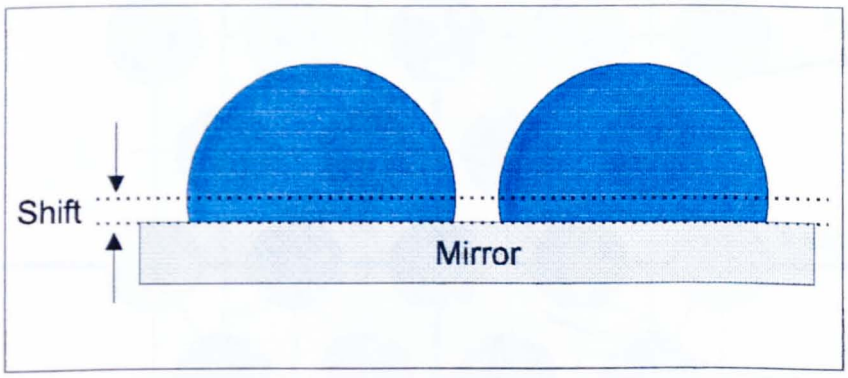

Fig. 3.3- Shift of the intersection plane

The contribution of the substrate is fundamental for the calculation of the global reflectance of the cell. In fact, the aluminium acts as a mirror redirecting the incident light toward the spheres. The substrate is optically described by its spectral reflectance which has been experimentally measured and is passed to the code as a standard data file.

3.2.5 Choice of the Simulation Surface

In the first set of simulations the complete spherical surface was considered. Incident rays were assumed to be generated over the entire sphere section and the history of each ray was followed among a user-defined lattice of spheres. In principle, all the 17.000 silicon spheres of a real cell could be included into the calculations and considered as absorbing objects.

In order to identify the different spheres encountered on the path of a secondary ray a system of indexes similar to the one used in crystallography (Miller's indexes) was employed.

Each sphere could be localised by a pair of integer indexes (n, m) related to the X and Y directions on the XY-plane, and by the centre distance (*Centre_Dist*). The sphere directly illuminated (the one where the direct cell was chosen) was identified by $n = 0$ and $m = 0$.

The co-ordinates of the centres (X, Y) of the other spheres, were calculated through the following equations:

$$Sphere(n, m).Centre(X) = n \cdot Centre\_Dist / 2 \qquad Eq.\ 3.7$$

$$Sphere(n, m).Centre(Y) = m \cdot Sqr(Centre\_Dist^2 - (Centre\_Dist / 2)^2) \quad Eq.\ 3.\ 8$$

A scheme of the hexagonal lattice of spheres with relative position indexes is given in Fig. 3.4.

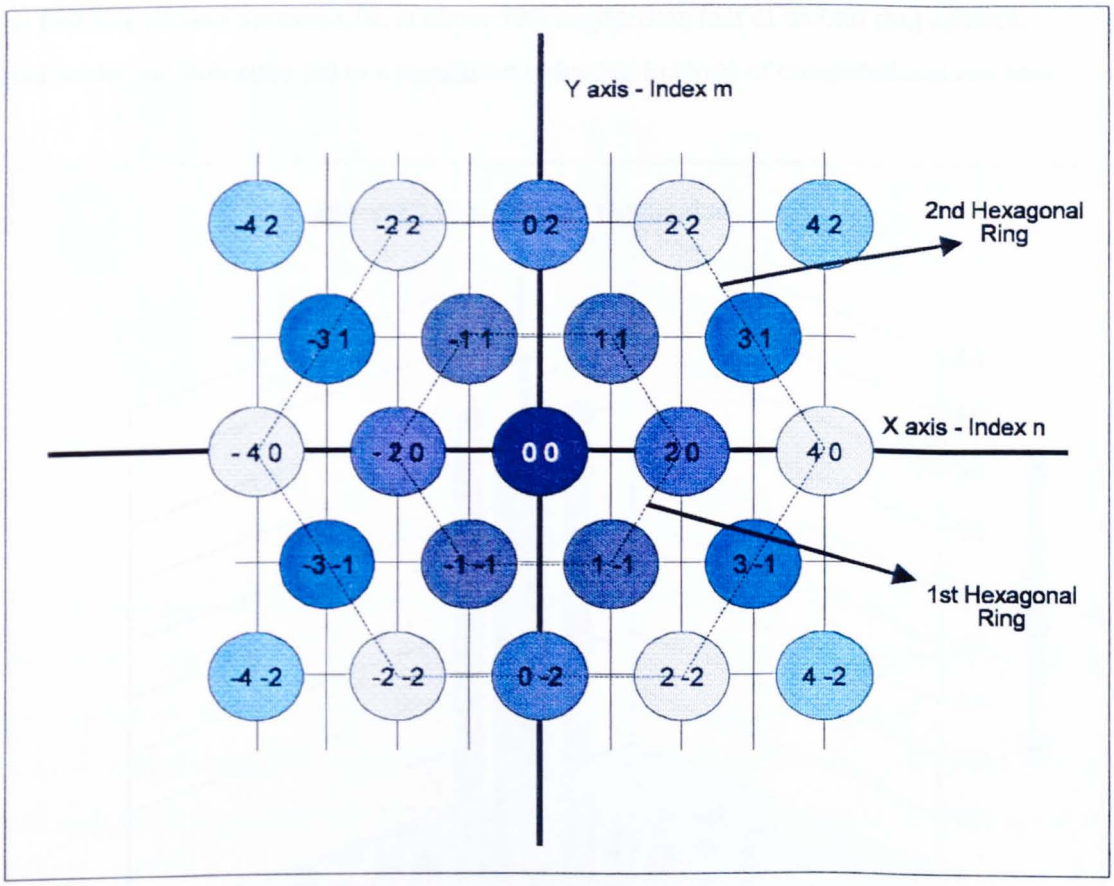

Fig. 3.4 - Hexagonal lattice of spheres; n and m indexes.

It was necessary to introduce the concept of *Indirect Trapping Contribution* as the absorption contribution of each individual sphere (indirectly illuminated) to be evaluated by ray-tracing calculations.

The *Indirect Trapping Contribution* of the first ten concentric *"rings"* of spheres (n_{max} = 10 and m_{max} = 10) surrounding Sphere(0, 0) is illustrated in Fig. 3.5. Secondary rays were assumed to be completely absorbed when their intensity reached a value lower then 1 ‰ of the incident ray intensity. The distribution of the spheres which are touched at least by one secondary ray reflects the hexagonal symmetry. In the *X*-direction the most distant sphere to be touched was lying in the 7th hexagonal ring while in the *Y*-direction some rays reached the 10th ring.

Theoretically it could be possible to trace an ideal path among the spheres, in which a light-ray could be trapped until its incident intensity has been completely transferred to the spheres.

Theoretically it could be possible to trace an ideal path among the spheres, in which a light-ray could be trapped until its incident intensity has been completely transferred to the spheres.

The results of this preliminary calculation were very useful, in fact, they suggested the possibility of limiting the calculations to the *Indirect Trapping Contribution* of those spheres which are directly facing the central one. In fact, the contribution of the spheres belonging to the first ring around Sphere(0, 0), is about 90% higher than that of second ring spheres.

This model simplification led to a significant reduction in terms of computational run-time.

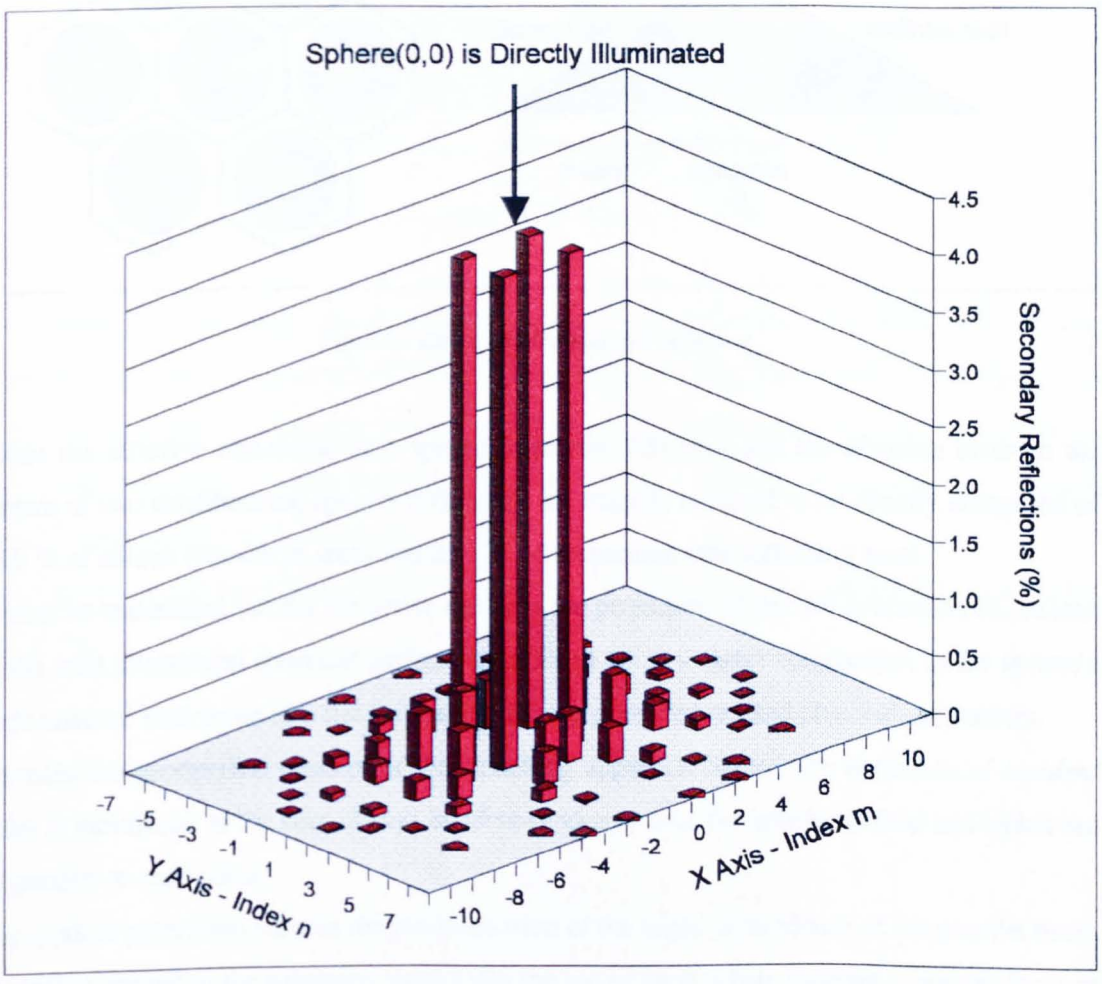

Fig. 3.5 - Indirect Trapping Contribution of (n, m) spheres

3.2.6 Simplified Cell Geometry

For an accurate reproduction of Spheral Solar™ Cells in reasonable run-times (< 1 hour), a reduction of the complicated cell geometry into a much simpler scheme was necessary. Therefore, it was very important to accurately define the so-called *direct cell* for simulation. The choice of this *cell* was dictated both by the spherical and the hexagonal symmetries of the cell geometry. As illustrated in Fig. 3.6, the minimum area, sharing the symmetries of the

hexagonal lattice, is represented by the outlined triangle formed by one twelfth of the sphere and by the corresponding aluminium sector which constitutes the substrate.

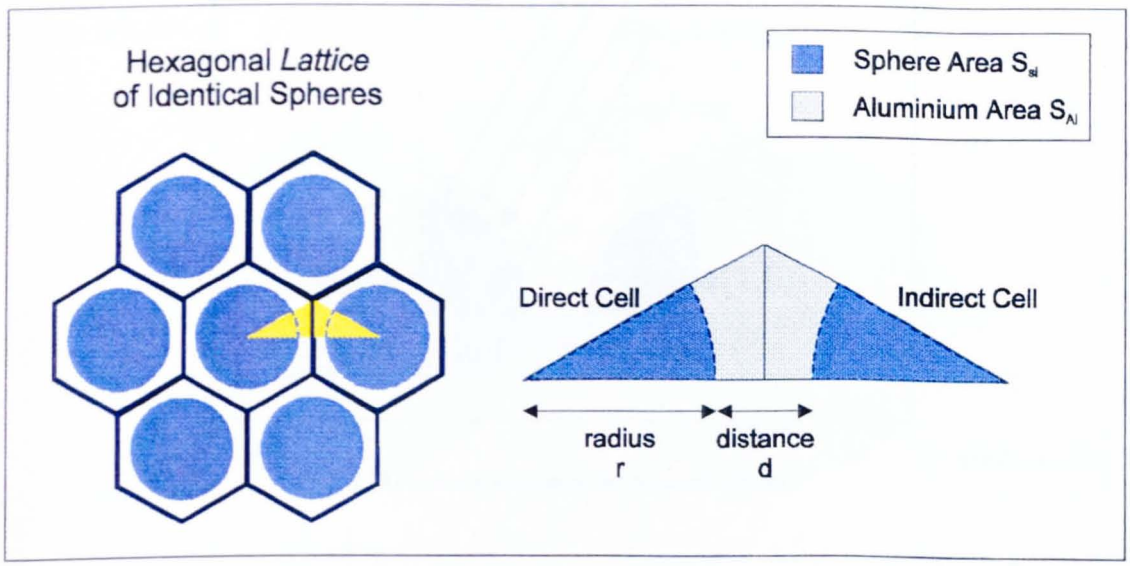

Fig. 3.6 - Direct and Indirect cell definition

Given the effective dimension of a sphere (diameter 700 μm) and the distance between the centres of two neighbouring spheres (760 μm), the triangle is found to be exactly composed of 76.9 % of silicon (the active area) and 23.1 % of aluminium (the reflecting area).

It must be underlined that for the active cell area the projection of the cell is considered, instead of the total illuminated spherical surface, in order to allow a direct comparison of the sphere's performances with those of a flat cell having the same active area and physical parameters.

To make the geometrical concept of the modelling approach clearer, the definition of *incident beam* is introduced as the sum of rays incident randomly over the sphere surface and which are all parallel to each other.

The random generation ensures the randomisation of the angle of incidence of the parallel beam impinging normal to the substrate plane (only the top of each sphere receives a normal incident ray).

It is now of fundamental importance to include in the modelling also the influence of different beam inclination angles on the overall cell absorptance, for a complete and successful simulation of Spheral Solar™ Cells.

Secondary rays are considered as those which are reflected from the direct sphere surface undergoing *secondary reflections*.

It is thus necessary to introduce the concept of *indirect cell* which is active only for trapping rays reflected from the first (*direct*) sphere or from the aluminium substrate. The cross section of the two-*cell* system *(direct and indirect cell)* is shown in Fig. 3.7.

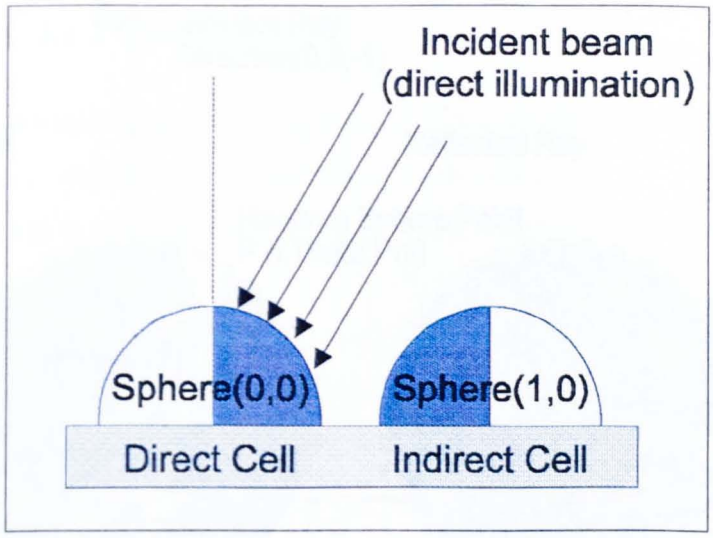

Fig. 3.7 - Cross section of the two-cell system.

The *indirect cell* is treated as a non-ideal mirror, in fact it does not absorb locally the secondary rays but it attenuates and redirects them towards other cell regions. The contribution to the overall cell current brought about by the *indirect cell* in the two-cell system is defined as *Non-Local Trapping*. A more detailed illustration of light trapping mechanisms of Spheral Solar™ Cells, will be given in the next Chapter.

A global view of the simplified geometrical model implemented in the code *WinTrace* is shown in Fig. 3.8.

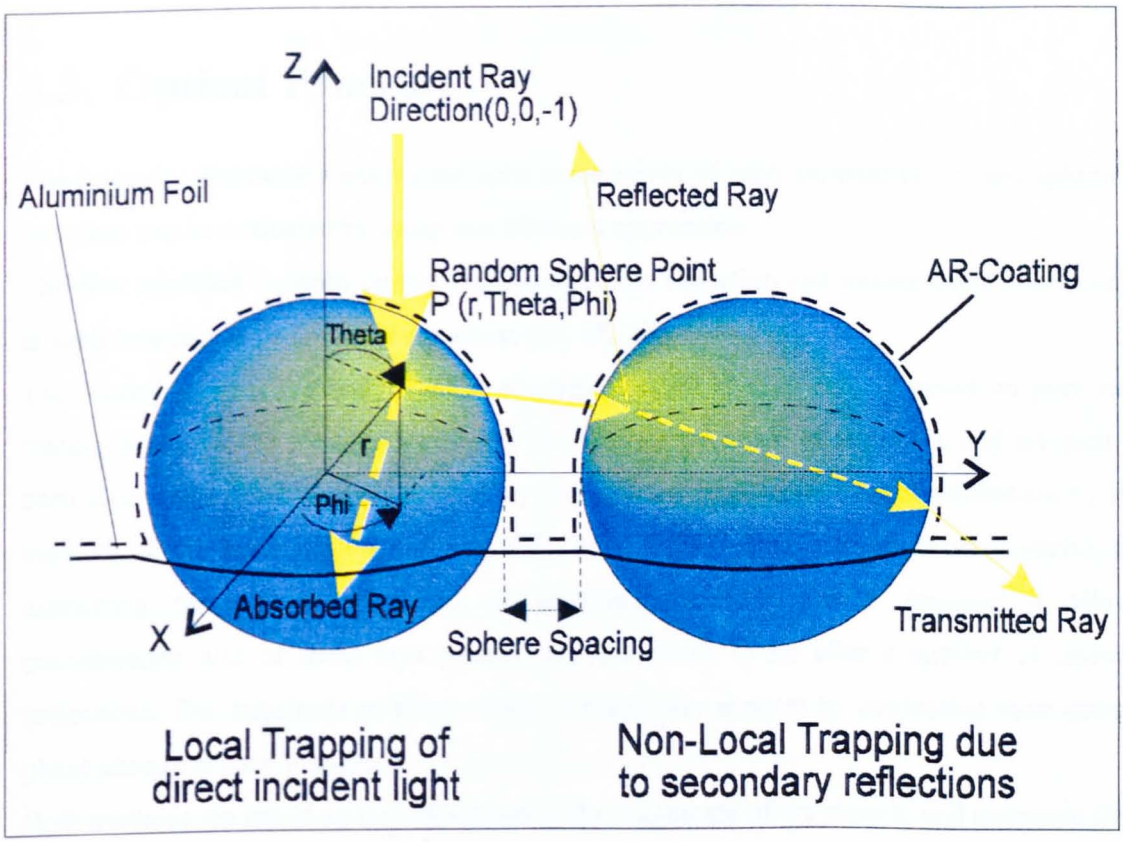

Fig. 3.8 - 3d model of Spheral Solar™ Cells geometry

3.3. Optical Processes

The intensity distribution among the split components of each incident ray at any spherical interface can be evaluated by using two different approaches.

The first approach is based on the calculation of the reflection and transmission coefficients at each interface with Fresnel's equations [27, 28, 29].

The second approach, mainly used to simulate a multi-layered cell, is based on pure ray-tracing through different spherical layers to calculate the angle of incidence and the path in each layer and evaluating only at the very end of a ray history, its overall reflectance by the method of the transmission matrices [30, 31, 32, 33]. This method is very useful for estimating the global reflectance of stratified dielectric media, because it allows consideration also of those rays (waves) reflected back to air after a number of internal reflections. The amplitude of these waves is taken into account by evaluating their optical phase change at each interface.

Both methods are based on the calculation of the magnitude of the electric and magnetic field vectors along the cell structure in terms of the incident field magnitudes, when the light is represented by a transverse electromagnetic plane wave [34, 35].

3.3.1 Transmission Matrix Method

The transmission matrices relate the electric-magnetic field couple (arranged as a column vector) at the beginning and at the end of a medium. Since (in the absence of charge sheets) the Maxwell equations require the continuity of the transverse components of these fields, the matrix of several media is simply obtained by multiplication of the matrices of the media involved.

For oblique incidence, as in the present case (for a parallel beam impinging perpendicularly to the X-Y plane, only the top of each sphere gives normal incidence), the reflection and transmission coefficients of the incident wave are different for normal and parallel polarisation and some modifications must be introduced in order to fulfil the boundary conditions for normal components.

Therefore, the assumption of media without losses and circularly polarised light has been made. For any other polarisation we can use this formula by weighting the terms inside the parentheses, since the first one corresponds to parallel polarisation and the second one to transverse polarisation.

The matrix corresponding to a single layer of dielectric is [27]:

$$M = \begin{vmatrix} \cos\delta & -(i/p_M)\sin\delta \\ -ip_M \sin\delta & \cos\delta \end{vmatrix} \qquad \textit{Eq. 3. 9}$$

where δ is given by:

$$\delta = \frac{2\pi}{\lambda_0} nd\cos\theta_{inc} \qquad \textit{Eq. 3. 10}$$

where λ_0 is the wavelength of the monochromatic light component *in vacuum*, d the layer thickness and θ_{inc} the angle of incidence of the light on the layer.

When the light has oblique incidence the parameter p_M can take different values depending on whether the plane of polarisation of the electric or magnetic vector is normal to the layer. In the first case (transverse polarisation):

$$p_M = (\varepsilon/\mu)^{1/2}\cos\theta \cong n\cos\theta \qquad \textit{Eq. 3. 11}$$

and in the second one (parallel polarisation):

$$p_M = (\varepsilon/\mu)^{1/2}\cos\theta \cong \frac{1}{n}\cos\theta \qquad \textit{Eq. 3. 12}$$

These formulae use relative values of ε and μ with respect to the vacuum.
The complex reflection factor is:

$$r_L = \frac{m_{11}p_{Me} - m_{22}p_{Mo} + m_{12}p_{Me}p_{Mo} - m_{21}}{m_{11}p_{Me} + m_{22}p_{Mo} + m_{12}p_{Me}p_{Mo} + m_{21}} \qquad \textit{Eq. 3. 13}$$

The elements m_{ij} are the elements of the matrix formed by multiplication of matrices like the one in Eq. 3.9; in non-absorbing media m_{12} and m_{21} are imaginary. p_{Me} and p_{Mo} are the p_M parameters of the entrance and output media. The coefficient of reflection for power is:

$$R_L = |r_L|^2 \qquad \textit{Eq. 3. 14}$$

For media with losses, n can be considered as a complex variable such that:

$$\tilde{n} = n - ik \qquad \textit{Eq. 3. 15}$$

where k is related to the absorption coefficient of light in a dielectric material through the following formula:

$$\alpha_\lambda = 4\pi k / \lambda_0 \qquad \textit{Eq. 3. 16}$$

For media without losses the transmission coefficient is:

$$T_L = 1 - R_L \qquad \textit{Eq. 3. 17}$$

If losses occur the conservation of energy can be applied to calculate R_L.

3.3.2 Fresnel's Formalism

The simplest configuration is the reflection in the boundary between two thick layers. In this case $\delta \rightarrow 0$ and the matrix in Eq.3.9 becomes unity. Substituting its elements in Eq.3.14 we obtain:

$$R_L = \left(\frac{p_{Me} - p_{Mo}}{p_{Me} + p_{Mo}}\right)\left(\frac{p_{Me} - p_{Mo}}{p_{Me} + p_{Mo}}\right)^* \qquad \textit{Eq. 3. 18}$$

where we can use the complex indexes of refraction if media with losses are considered.
If one medium is a semiconductor with high α_λ, the loss term k can be considered. The differences if it is neglected are however quite small, less than 1% in most cases of interest.
For normal incidence Eq. 3.18 is used substituting p_{Me} and p_{Mo} by n_e and n_o.
For oblique incidence different coefficients are found for normal and parallel polarisation. However it is common to consider that most of the light arrives with circular polarisation, so that:

$$R_L = \frac{1}{2}\left(R_{Lp} + R_{Lt}\right) \qquad \textit{Eq. 3. 19}$$

$$R_L = \frac{1}{2}\left[\left(\frac{\tan(\theta_e - \theta_o)}{\tan(\theta_e + \theta_o)}\right)^2 + \left(\frac{\sin(\theta_e - \theta_o)}{\sin(\theta_e + \theta_o)}\right)^2\right] \qquad \textit{Eq. 3. 20}$$

which is valid for media without losses and circularly polarised light. For any other polarisation we can use this formula by weighting the terms inside the parentheses, since the first one corresponds to parallel polarisation and the second one to transverse polarisation. For normal incidence of any polarisation equation Eq. 3.20 becomes:

$$R_L = \frac{(n_e - n_o)^2 + k_0^2}{(n_e + n_o)^2 + k_0^2} \qquad \textit{Eq. 3. 21}$$

where only the semiconductor is considered to have losses, so that $\tilde{n}_o = n_o - ik_o$.

The added complication of using the term k_o is, as mentioned, of little use in most cases for semiconductors and dielectrics. For instance in silicon at 400 nm, $\alpha_\lambda \cong 10^5$ cm^{-1}, $k_o = 0.32$ and $n_0 = 4.9$. By using these values in the air-silicon interface ($n_e = 1$) we obtain $R_L = 0.4370$ without losses and $R_L = 0.4386$ with losses.

The reflectivity of a layer is seen to be dependent on the wavelength. To evaluate the role of an AR-coating on the cell we write:

$$J_{sc} = q\cos\theta \sum_\lambda N_{ph\lambda}(1 - R_{L\lambda})\chi_\lambda \qquad \textit{Eq. 3. 22}$$

where χ_λ is the internal quantum efficiency at a given wavelength, defined as the fraction of photon flux inside the semiconductor multiplied by q and divided by the current out. $(1 - R_{L\lambda})\chi_\lambda$ is the external quantum efficiency for the same wavelength. An average transmission can be defined as:

$$\langle T_L \rangle = \frac{\sum_\lambda N_{ph\lambda}(1 - R_{L\lambda})\chi_\lambda}{\sum_\lambda N_{ph\lambda}\chi_\lambda} = 1 - \langle R_L \rangle \qquad \textit{Eq. 3. 23}$$

which depends somewhat on the cell internal quantum efficiency acting as a weighting factor. For the air-silicon interface (n_e = 1) the value of n which gives the same reflection coefficient, is called the averaged index of refraction. This depends on the cell quality and type. For Spheral Solar™ Cells n = 3.7 and so for the normal transmittance $<T_l>$ = 0.67.

3.4. Light Trapping in Spheral Solar™ Cells

Semiconductors used in solar cells usually have refractive indices of about 3.5. Since this is a quite large refractive index, there is a wide margin for increasing the light concentration. However, suitable transparent optical media with such a high refractive index do not exist. Nevertheless, it is possible to take advantage indirectly of the high refractive index of semiconductors by confinement of light, typically referred to as *"trapped"* in their interior. This effect is termed internal confinement or *light trapping*. By means of internal confinement, the rays of light follow a much longer path inside the cell (up to 50 times longer) than in a conventional cell without confinement (in which the path is approximately equal to the thickness of the cell). This means that the radiation is still absorbed even if very thin cells are used. This improvement in absorption is important in silicon for photons of energy close to the bandgap.

This mechanism is very important in the design of the Spheral Solar™ Cells. In fact, in this surface design, as in the structured surfaces, light has multiple chances of being coupled into the cell.

Theoretically, it should be possible to trace a path among the spheres in which a light-ray could be trapped until its incident intensity has been completely transferred to the spheres.

As already mentioned in the previous Chapter, the total absorption of an entire cell is assumed to be the effect of the sum of two trapping contributions [24]: the *Local* and the *Non-Local Trapping*. The *Local* contribution is due to the incident light which is directly coupled into the cell after the primary reflection (for a flat interface air-Si, with $n_{air} = 1$ and $n_{Si} = 3.7$, it is about 70 %) and absorbed by the *direct cell*.

The *Non-Local* contribution is assumed to be the rate of intensity absorbed by the *direct cell* during secondary reflections on the two-cell system. It corresponds to the *Indirect Trapping Contribution* defined in the system of (n, m) spheres.

3.4.1 Optical Factors Contributing to Non-Local Trapping

When a ray is generated on a specific region of the *direct cell*, and only for some specific beam inclination angles, its reflected component is tracked to intersect the *indirect cell*. There, the reflected ray undergoes a secondary reflection, as illustrated in Fig. 3.9, and the intensity absorbed or reflected during this secondary process is assumed to be absorbed or reflected at the symmetrical point of the *direct cell*.

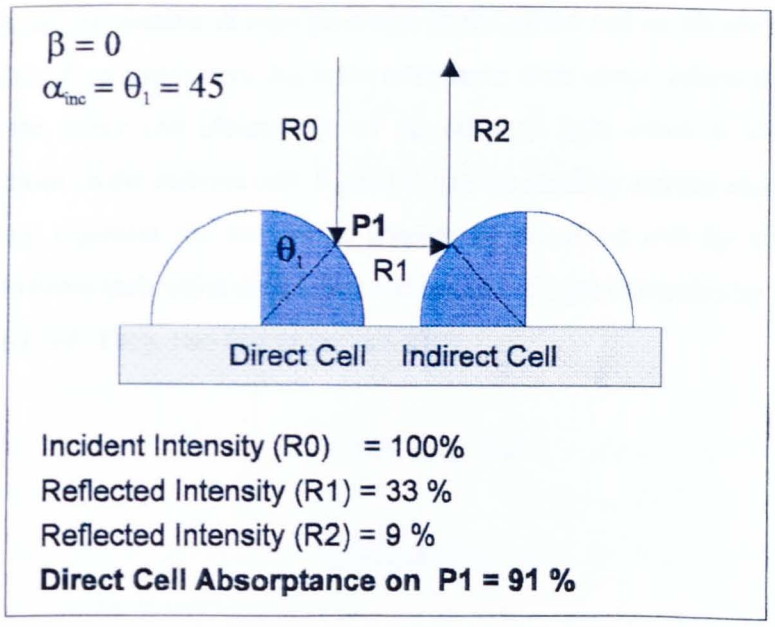

Fig. 3.9 - Secondary reflections on the indirect cell

The same procedure is applied to those rays directly impinging on or being reflected to the aluminium substrate and redirected towards the *direct* or the *indirect* cell (Fig. 3.10).

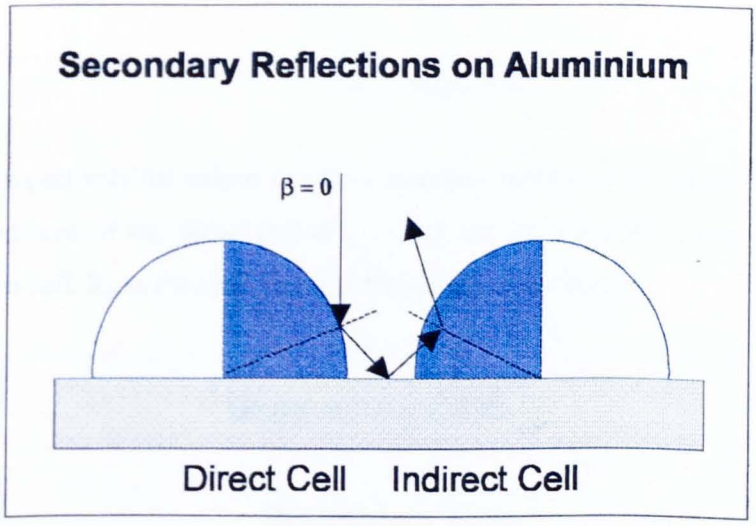

Fig. 3.10 - Other secondary reflections caused by rays redirected by the aluminium substrate.

The total intensity reflected by the *direct cell*, which is a function of the angle of incidence (α_{inc}), the beam inclination angle (β) and of the wavelength of light (λ), is given by:

$$R_{tot}(\alpha_{inc}, \beta, \lambda) = \{n_{sph} \cdot [R_{dr}(\alpha_{inc}, \lambda) - (A_{sr}(\alpha_{inc}, \beta, \lambda) + F_{sh}(\alpha_{inc}, \beta))] + n_{al} \cdot F_{al}(\alpha_{inc}, \beta)\}/n_{to}$$

Eq. 3. 24

where n_{sph} and n_{al} are the number of rays generated on the sphere and on the aluminium and n_{tot} is the total number of generated rays. R_{dr} is the reflectance from direct reflections on the *direct cell* and A_{sr} is the *direct cell* absorptance of the reflected light which is absorbed during secondary reflections on the *indirect cell*. F_{sh} and F_{al} are the *shading* and the *aluminium* factors respectively. They represent the amount of shading of the *direct cell* by the surrounding spheres at certain beam inclination angles, and the amount of light redirected by the aluminium towards the *direct cell*. These two factors are given by:

$$F_{sh} = (S_{sph} - S_{sh}) \qquad \textit{Eq. 3. 25}$$

$$F_{al} = [R_{al}(\lambda)\cdot(S_{al} - S_{it})] \qquad \textit{Eq. 3. 26}$$

where:

$$S_{sph} = \pi\cdot r^2 \qquad \textit{Eq. 3. 27}$$

$$S_{sh} = \pi\{r^2-[r\cdot(2-(\cos(\beta)^{-1}))]^2\} \qquad \textit{Eq. 3. 28}$$

$$S_{al} = \{[\tan(30)\cdot(r+d/2)]- \pi r^2\} \qquad \textit{Eq. 3. 29}$$

$$S_{it} = \pi[r/\cos(\beta)]^2 \qquad \textit{Eq. 3. 30}$$

S_{sph} and S_{al} are respectively the silicon and the aluminium surface of the *direct cell*, S_{sh} and S_{it} are the shadowed area of the *direct cell* (Fig. 3.11) and the aluminium area which reflects towards the *direct cell*. R_{al} is the reflectance of the aluminium substrate.

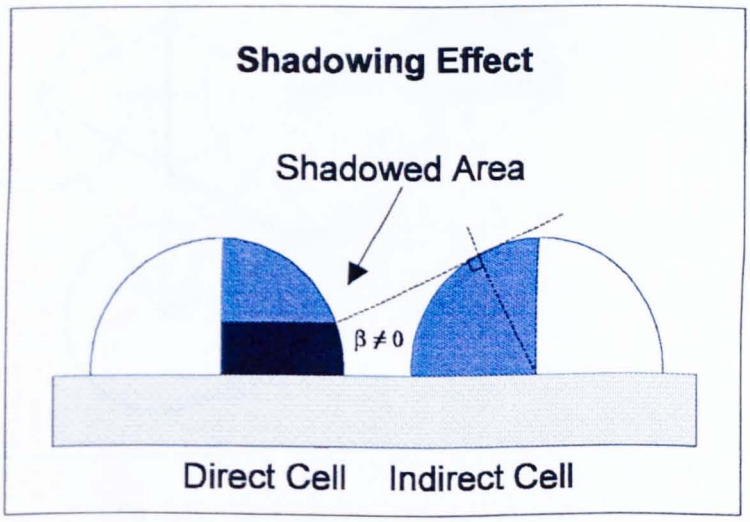

Fig. 3.11 - Shadowed area

3.4.2 Determination of Characteristic Angles

The optical factors introduced into the expression of the cell reflectance become effective at specific angles (θ, β and φ) which have been analytically determined.

Variation of the angles α_{inc} and φ

Following the variation of the angle of incidence (α_{inc}) on the sphere surface (where $\alpha_{inc} = \theta - \beta$), for a normal incident beam (β=0), the first characteristic angle is found to be $\alpha_{inc} = \theta =$ 40.37 deg.. At this specific angle, determined by employing a routine calculation implemented in the code *WinTrace*, the secondary reflections on the indirect cell start. In the same way it was found that for a normal incident beam they stop at 54.68 deg.. Moreover, these secondary reflections take place only at angles < φ_1, where φ_1 is defined as:

$$\varphi_1 = \arcsin\left(\frac{r}{2r+d}\right) \qquad \textit{Eq. 3. 31}$$

Fig. 3.12 illustrates the variation of φ with respect to the possible secondary reflections.

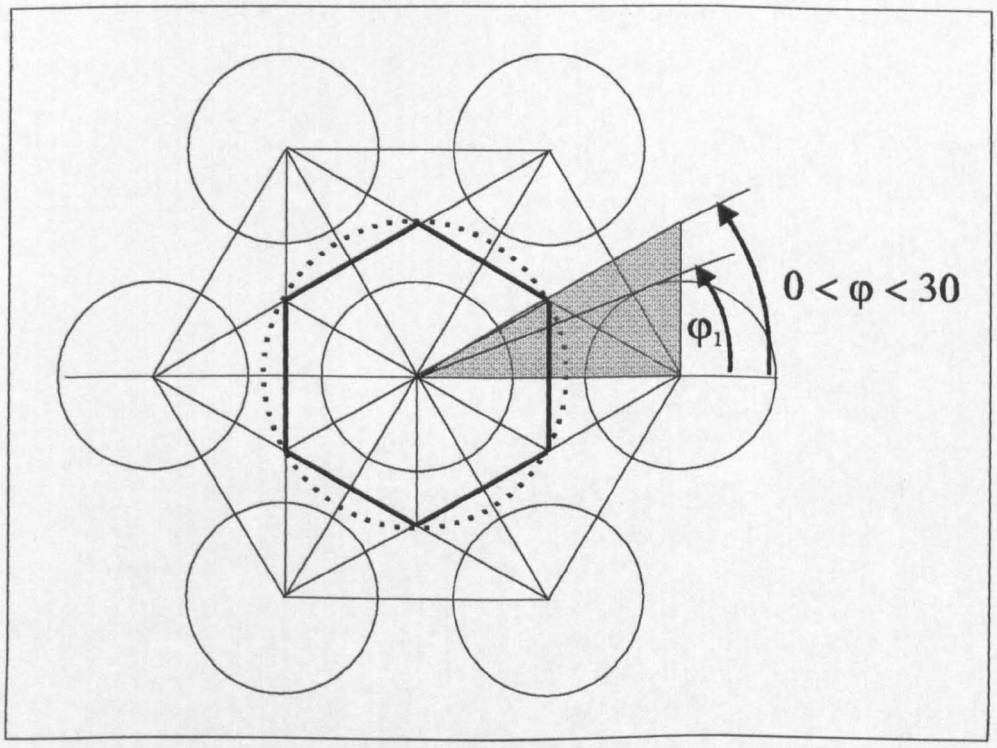

Fig. 3.12 - Variation of φ and secondary reflections

A front view of the region of the direct cell reflecting towards the indirect cell is illustrated in Fig. 3.13.

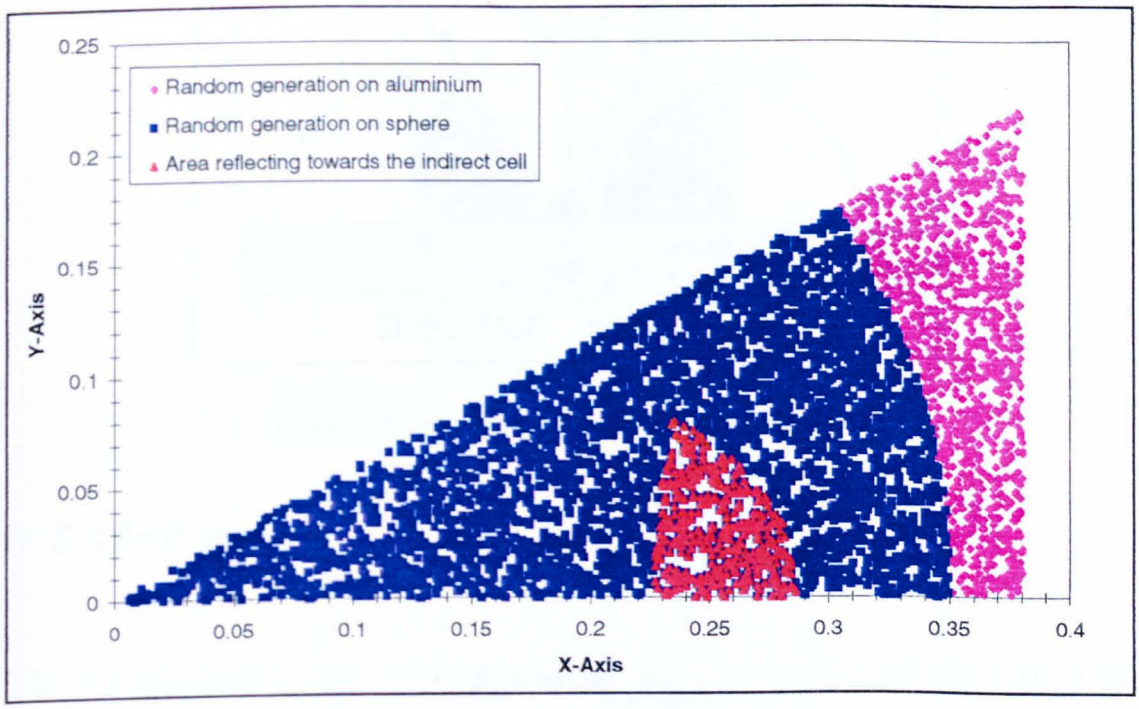

Fig. 3.13 - Randomisation of the incident point on the direct cell. Area reflecting towards the indirect cell.

Variation of the angle β

Following now the variation of the beam inclination angle β from 0 to 90 deg., with respect to the XY-plane, for $0 < \beta < \beta_1$ where β_1 is given by:

$$\beta_1 = \arccos\left(\frac{r}{r + d/2}\right) \qquad \textit{Eq. 3. 32}$$

some of the incident rays impinging on the aluminium substrate are redirected towards the direct cell, as illustrated in Fig. 3.14.

At $\beta = \beta_1$ all the rays reflecting on the aluminium substrate undergo a second reflection on the direct cell. Therefore, at this illumination condition the aluminium substrate can be considered as an active part of the cell.

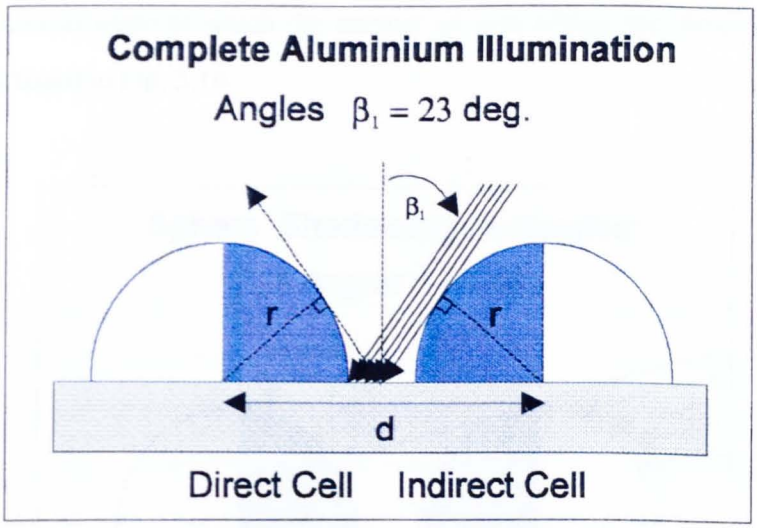

Fig. 3.14 - β_1, characteristic angle for aluminium reflections

For $\beta_1 < \beta < \beta_2$, where β_2 is:

$$\beta_2 = \arccos\left(\frac{r}{r+d}\right) \qquad \textit{Eq. 3. 33}$$

The aluminium sector belonging to the direct cell starts to be shaded by the indirect cell and consequently n_{al} is progressively reduced as well as the active cell area, as shown in Fig. 3.15. When $\beta = \beta_2$ the aluminium sector is completely shadowed by the indirect cell. Nevertheless, the aluminium factor n_{al} is still effective, since the reflected component of the rays impinging on the direct cell, can be redirected to the indirect cell.

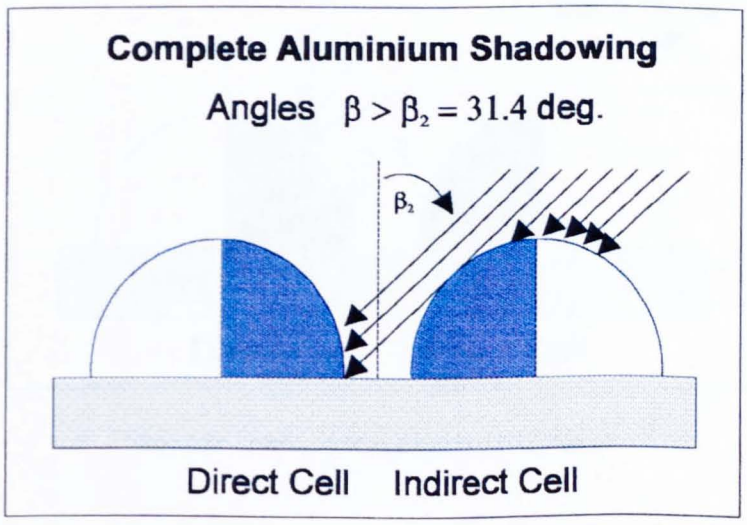

Fig. 3.15 - Shadowing of the aluminium substrate

β_2 is also the critical angle at which the number of rays hitting the direct cell starts to be reduced, as illustrated in Fig. 3.16.

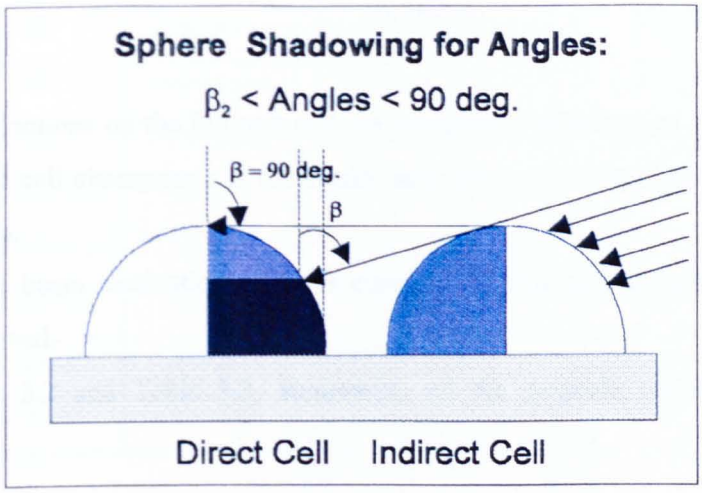

Fig. 3.16 - Shadowing of the sphere surface

The next characteristic angle which is found (β_3) fulfils the condition for which the Z co-ordinate, of the oriented direction relative to the reflected component of the rays hitting the direct cell, becomes positive. This change of sign in the reflected direction produces a drastic increase of the cell reflectance, because all the incident rays are reflected by the direct cell back to air.

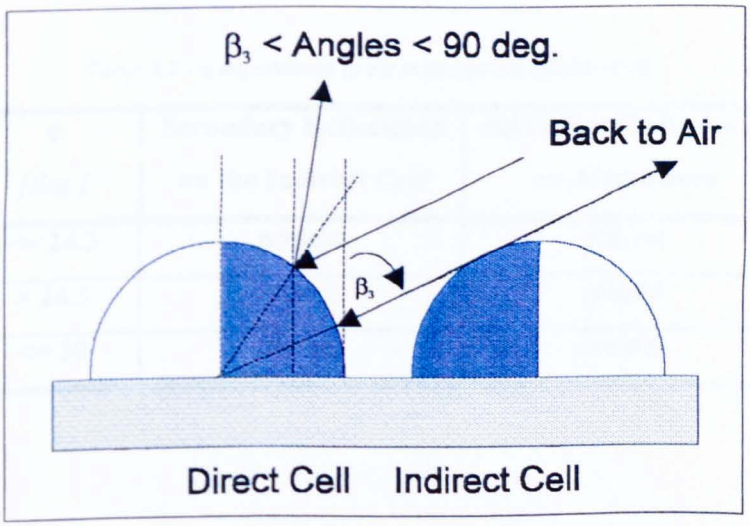

Fig. 3.17 - Reflected component goes back to air

For angles $\beta > \beta_3$ where β_3 is given by:

$$\beta_3 = \arccos\left(\frac{r}{2r+d}\right) \qquad \textit{Eq. 3. 34}$$

the secondary reflections on the indirect cell are completely eliminated ($A_{sr} = 0$) for any θ and φ. Hence, the cell absorptance is drastically reduced as a consequence of an enhanced overall reflectance.

Finally, when the beam inclination angle is equal to 90 deg. n_{sph} is zero and the cell is completely shadowed.

Table 3.1, Table 3.2 and Table 3.3, summarise all the possible angular combinations discussed above.

Table 3.1 - θ dependence of the secondary reflections assuming β=0.

θ *[deg.]*	**Secondary Reflections on the Indirect Cell**
< 40.37	absent
=> 40.37	present
=> 54.68	absent

Table 3.2 - φ dependence of the main optical effects, (β=0)

φ *[deg.]*	**Secondary Reflections on the Indirect Cell**	**Secondary Reflections on Aluminium**
<= 24.3	present	present
> 24.3	absent	present
<= 30	absent	present

Table 3.3 - β dependence of the main optical effects, given the exact geometrical parameters of the cell

β *[deg.]*	**Direct Illumination**	**Al Refl.**	**Secondary Refl.**	**Al Shadowing**	**Sphere Shadowing**
$<\beta_1=22.9$	full	increasing	depending on θ & φ	absent	absent
$=\beta_1=22.9$	full	maximum	depending on θ & φ	starting	absent
$<\beta_2=31.4$	full	decreasing	depending on θ & φ	increasing	absent
$=\beta_2=31.4$	decreasing	absent	depending on θ & φ	full	starting
$<\beta_3=62.6$	decreasing	absent	depending on θ & φ	full	increasing
$=\beta_3=62.6$	decreasing	absent	absent	full	increasing
$<\beta_4=90.0$	decreasing	absent	absent	full	increasing
$=\beta_4=90.0$	absent	absent	absent	full	full

SECTION 4

THE MONTE CARLO RAY-TRACING CODE

"WINTRACE"

4.1. *WinTrace* Structure

All the physical concepts and the trapping schemes illustrated in the previous Section have been implemented in the computer code *WinTrace*. The program is implemented in object oriented Visual Basic Pro. for Windows, and therefore it presents a user-friendly interface as shown in Fig. 4.1.

The runtime depends on the complexity of the cell structure. Typical runtimes (33 MHz 486) for the present calculations vary between less than 10 seconds for a simple bare cell simulation to several hours for the case of a complex system in which all the secondary effects are considered.

The minimum system requirements to run the code *WinTrace* are the following:

1. IBM-compatible personal computer;
2. at least 386-CPU;
3. numeric co-processor;
4. MS-DOS 5.0 or later versions;
5. approximately 550 kByte of free RAM;
6. EGA or VGA compatible graphics adapter.

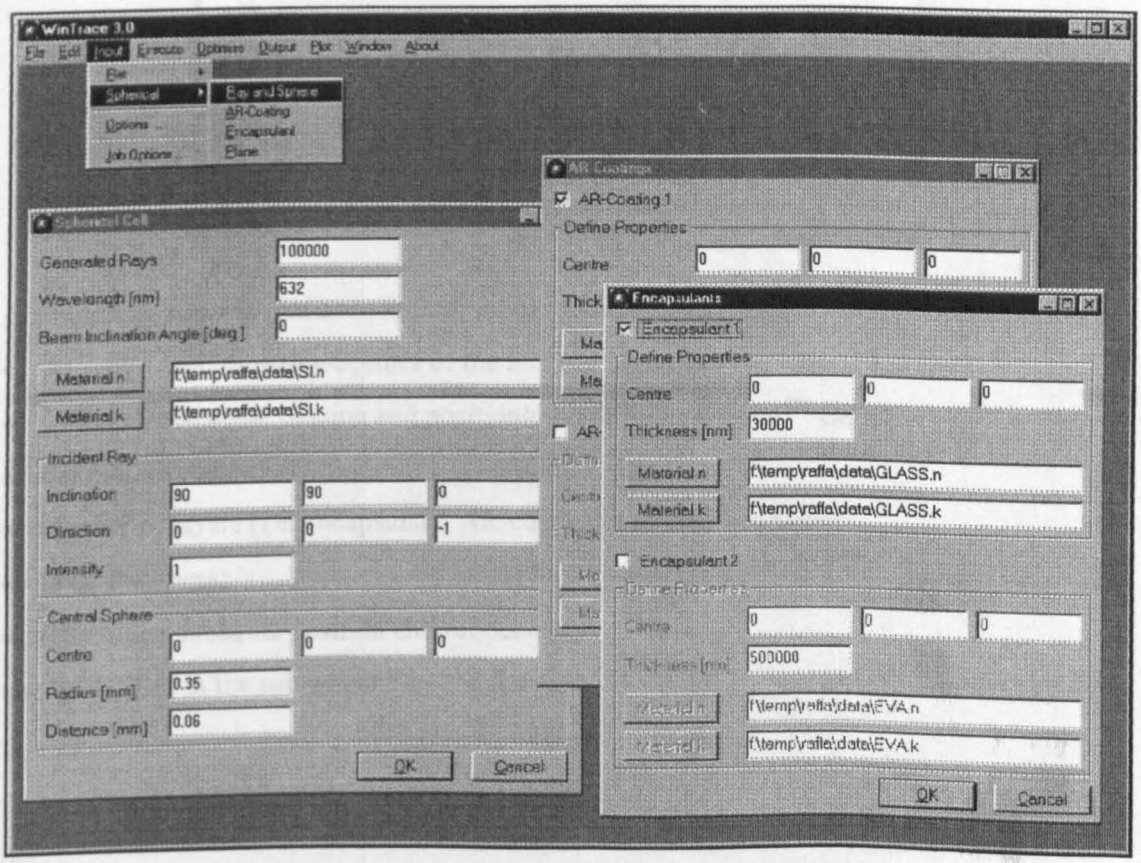

Fig. 4.1 - WinTrace User Interface

To run the programme it is first necessary to install it into an appropriate directory structure. The executable file WINTRACE.EXE must be located in the main directory "wintrace". The various optical files necessary to run the programme are located in the subdirectory "wintrace/data", which contains optical data such as real and imaginary index of refraction (*.n, *.k), materials reflectance (*.ref), illumination spectra (*.sp) etc. The description of the optical file format is given in Appendix B.

The *File* menu controls the handling of the output files, which are stored in the default directory "wintrace\output". It allows the opening, closing and saving of an output file by standard MS Windows common dialogue controls. The output files can be also edited through the standard *Copy*, *Cut* and *Paste* commands available in the *Edit* menu.

4.1.1 Input Parameters

So far, two different cell types have been implemented in the program: flat and spherical cells. Before running each calculation one of these types must be chosen and defined through the *Input* menu. The *Input* menu is structured as follows:

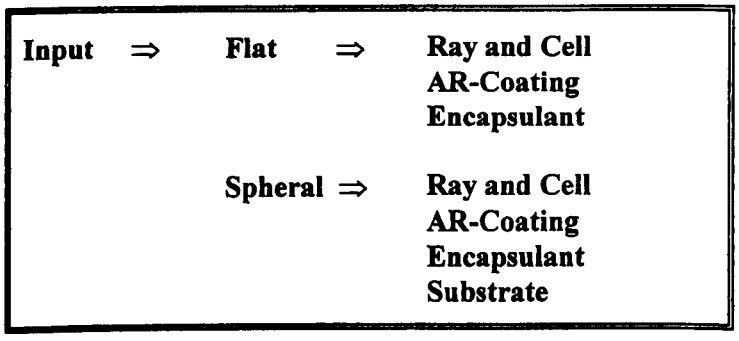

Fig. 4.2 - Input menu structure

Illumination, *geometrical* and *physical* input parameters such as:

- intensities and direction cosines of the incident sun rays;
- sphere dimensions, spacing and positioning on a Spheral Solar™ Cell;
- flat cell geometry;
- number of layers (i.e. encapsulant, AR-coating) and their geometry;
- layer thickness;
- aluminium substrate position and reflectance;

can be defined in the submenus *Flat* and *Spheral*.

A set of input parameters physically reproducing a flat and a Spheral Solar™ Cell are available as default parameters, as shown in Table 4.1. The optical files describing the simulated materials are listed in Appendix B.

Table 4.1 - Default Input Parameters

Spheral Solar™ Cell	Sphere Diameter	700 μm
	Centres Distance	60 μm
	Sphere Material	MG-Si
	AR-Coating Thickness	100 μm
	AR-Coating Material	TiO_2
	Aluminium Substrate Shift	-170 μm
	Incident Ray Direction (X,Y,Z)	(0,0,-1)
Flat Cell	Flat Cell Thickness	500 μm
	Flat Cell Material	Si
	AR-Coating Thickness	100 μm
	AR-Coating Material	SiO_2

A single ray-tracing problem is considered to be a *Simulation* (i.e. during a *Simulation* a single wavelength is chosen), while a complete problem is considered to be a *Job*.

A *Job* is defined through the choice of several options stored in a batch file which allows sequential *Simulations* to be run and sequential output files to be stored. *Simulation* and *Job* can be separately defined by choosing some specific input *Options* as illustrated in Fig. 4.3.

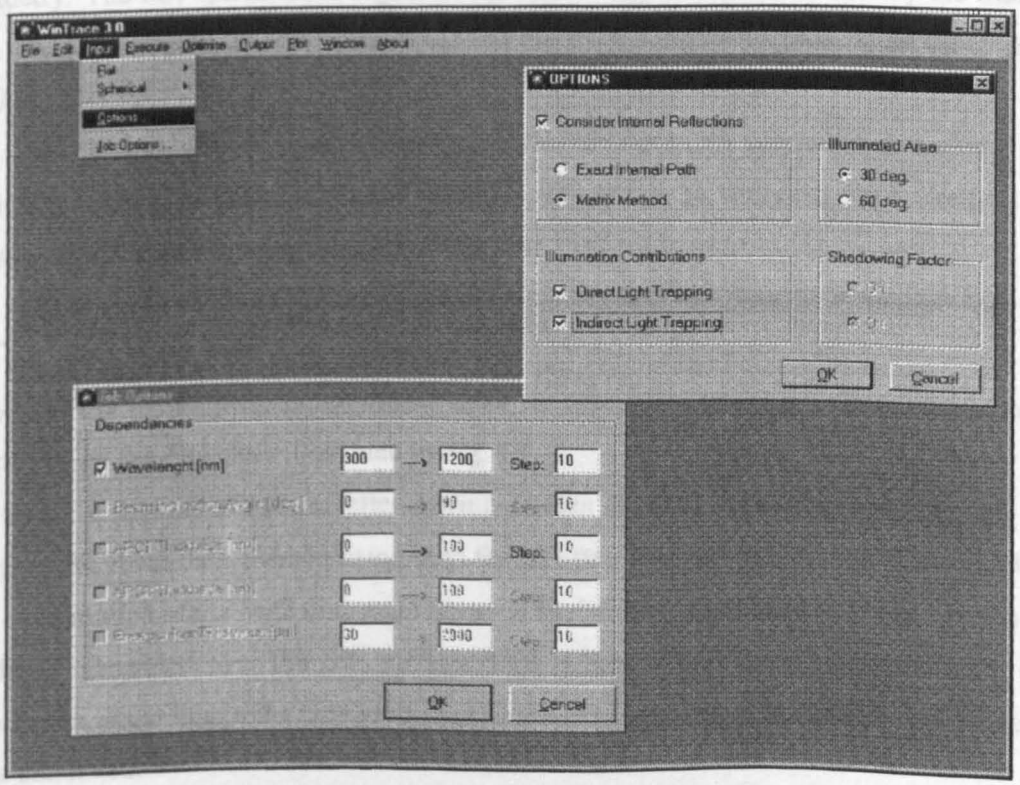

Fig. 4.3 - Simulation and Job Options

The *Option* window allows internal reflections among consecutive layers to be included in the calculations. This option appears automatically disabled for bare cell simulations (or jobs) and it is enabled only when either one AR-coating or one encapsulant layer is considered. In this case it is possible to choose the calculation method for internal reflections. One possibility is to follow each ray-path until the intensity of the internally reflected ray is totally absorbed (*Exact Method*). The global cell reflectance is then calculated by adding to the front surface reflectance the contribution of each single ray emerging from the multi-layered system. In this kind of simulation, algorithms to check for total internal reflections are implemented.

Another possibility is to calculate only the optical phase change of an internally reflected ray among consecutive layers through the *Transmission Matrix Method* illustrated in Section 3. In this method each ray is considered as a wave and the global cell reflectance is calculated as the sum of two contributions: one coming from the reflected wave and the other coming from the wave reflected back from the multi-layered structure.

Another option allows the estimation of the *Direct* (or *Local*) and *Indirect* (or *Non-Local*) trapping contributions to the overall cell absorptance. By choosing only the *Direct* trapping contribution, the distance between spheres is assumed to be infinite and therefore the *Indirect Cell* trapping is excluded.

The random generation of the incident rays can be performed both for 0 deg.$< \varphi <$30 deg. and for 0 deg.$< \varphi <$60 deg. The first option is enough to keep the symmetries of the spherical geometry. The last option takes regard of the shadowing of the *Direct Cell* by the *Indirect* one. This option is also important to evaluate the shadowing of the aluminium substrate by the *Indirect Cell*.

The *Job Options* allow several consecutive *Simulations* to be run without wasting time setting the input parameters. Those variables which can be automatically redefined are illustrated in the *Job Options* window of Fig. 4.3.

4.1.2 Principal Ray-Tracing Routines

A typical run of the programme started from the *Execute* menu (i.e. a *Simulation*) can be simplified by the flowchart illustrated in Fig. 4.4.

Following a typical sequence, after having chosen the cell type (flat or spherical) and assigned the input data characterising both the cell structure and the illumination conditions, the *core* routine starts with the main loop: a statistically significant number of rays are randomly generated over the cell surface. Two different ray-tracing calculations are then undertaken, according to the number of layers (AR-coatings and/or encapsulants) which have to be simulated.

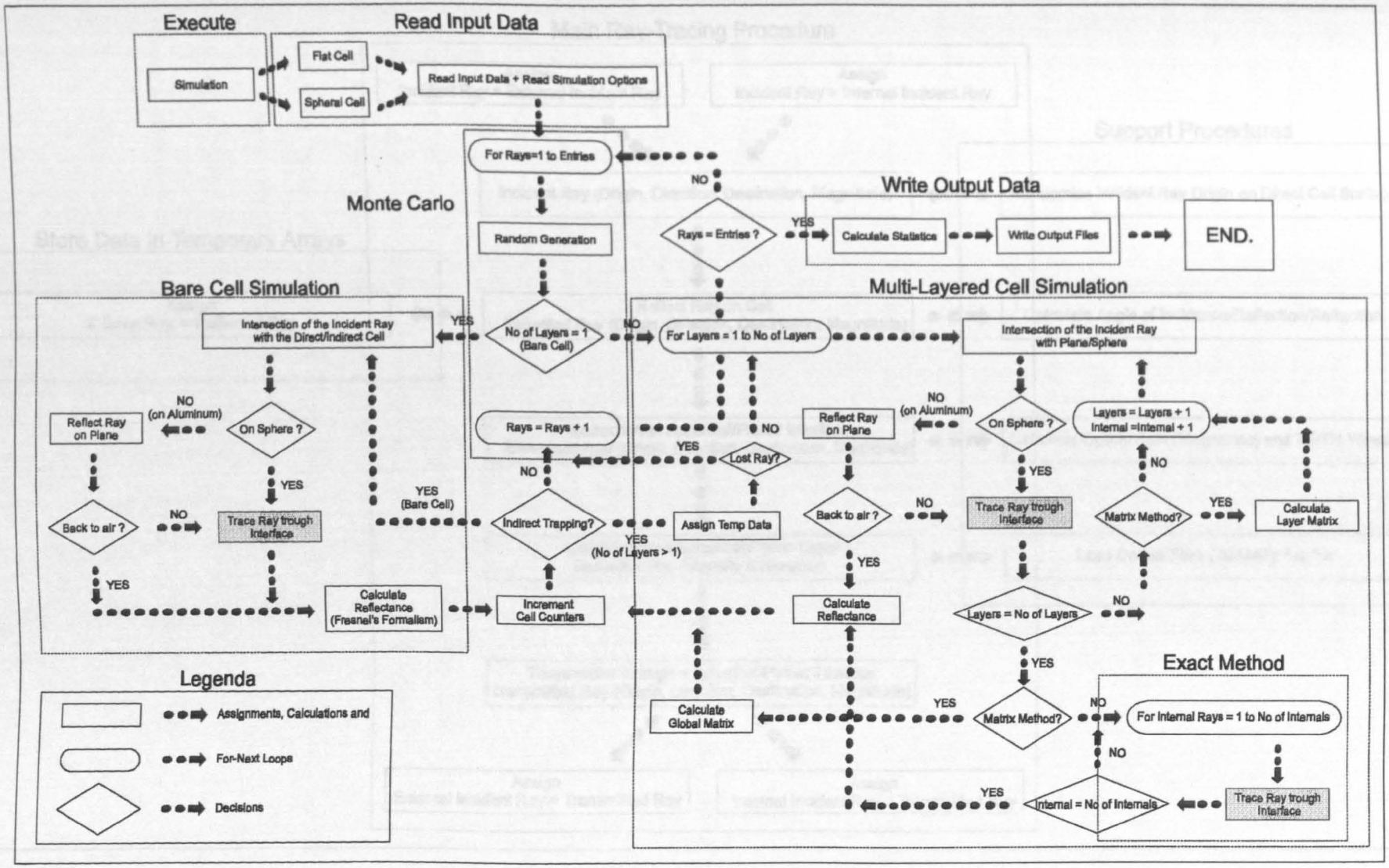

Fig. 4.4 - "Simulation" routine. The greyed blocks are detailed in Fig. 4.5

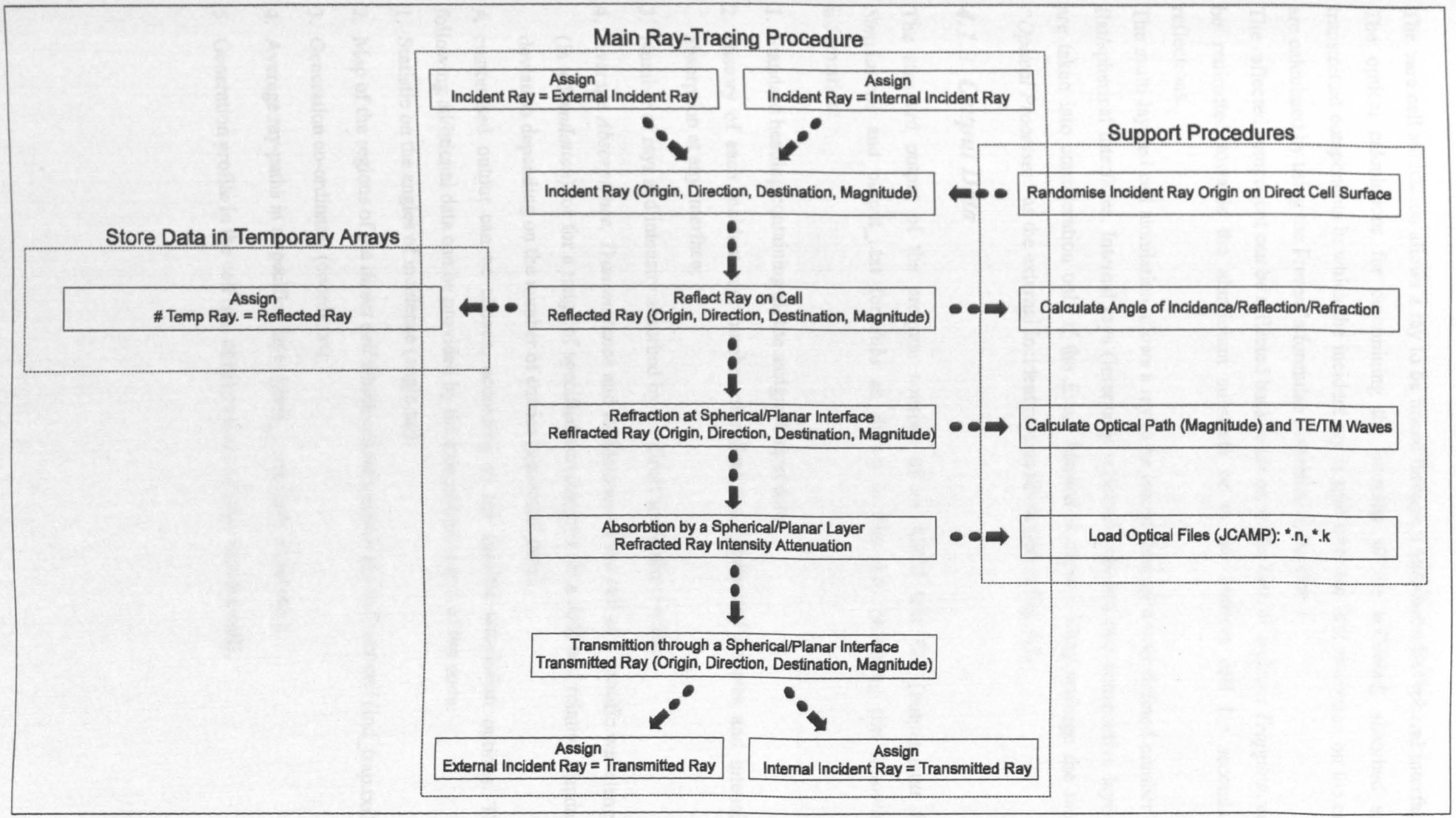

Fig. 4.5 - "Ray-Tracing" routine

The bare cell simulation allows a ray to be traced through a air/silicon-flat/spheral interface. The optical calculations for determining the intensity of the reflected, absorbed and transmitted components in which the incident ray is split after the first reflection on the cell are calculated by using the Fresnel's formulae illustrated in Section 3.

The reflected component can be reflected back to air or, in the case of *Indirect Trapping*, can be redirected towards the aluminium substrate or to the indirect cell for secondary reflections.

The multi-layered cell simulation allows a ray to be traced through a user defined number of flat/spherical interfaces. Internal rays (internally reflected between two consecutive layers) are taken into consideration only if the *Exact Method* is chosen. They undergo the same *"Optical Processes"* as the external incident rays as illustrated in Fig. 4.5.

4.1.3 Output Data

The standard output of the program consists of an ASCII text file (output_s.txt for *Simulations* and output_j.txt for *Jobs* as shown in Fig. 4.6) providing the following information:

1. Standard heading containing all the assigned input data;
2. History of each incident ray: number of reflections, intersected spheres and intensity absorption at any interface;
3. Number of rays and intensity absorbed by the direct and indirect cells;
4. Average *Absorptance, Transmittance* and *Reflectance* of the cell at a specific wavelength (in a *Simulation*), or for a range of specified wavelengths (in a *Job*) and relative standard deviation depending on the number of entries (generated rays).

A customised output can be chosen, according to the specific simulation options. The following additional data can be provided by the customised output of the code:

1. Statistic on the angles of incidence (angle.txt);
2. Map of the regions of the *direct cell* which reflect towards the *indirect cell* (ind_trap.txt)
3. Generation co-ordinates (coords.txt);
4. Average ray-paths in a specified layer (path_l1.txt, path_l2.txt etc.);
5. Generation profile in the cell (no. of rays vs. no. of steps into the cell).

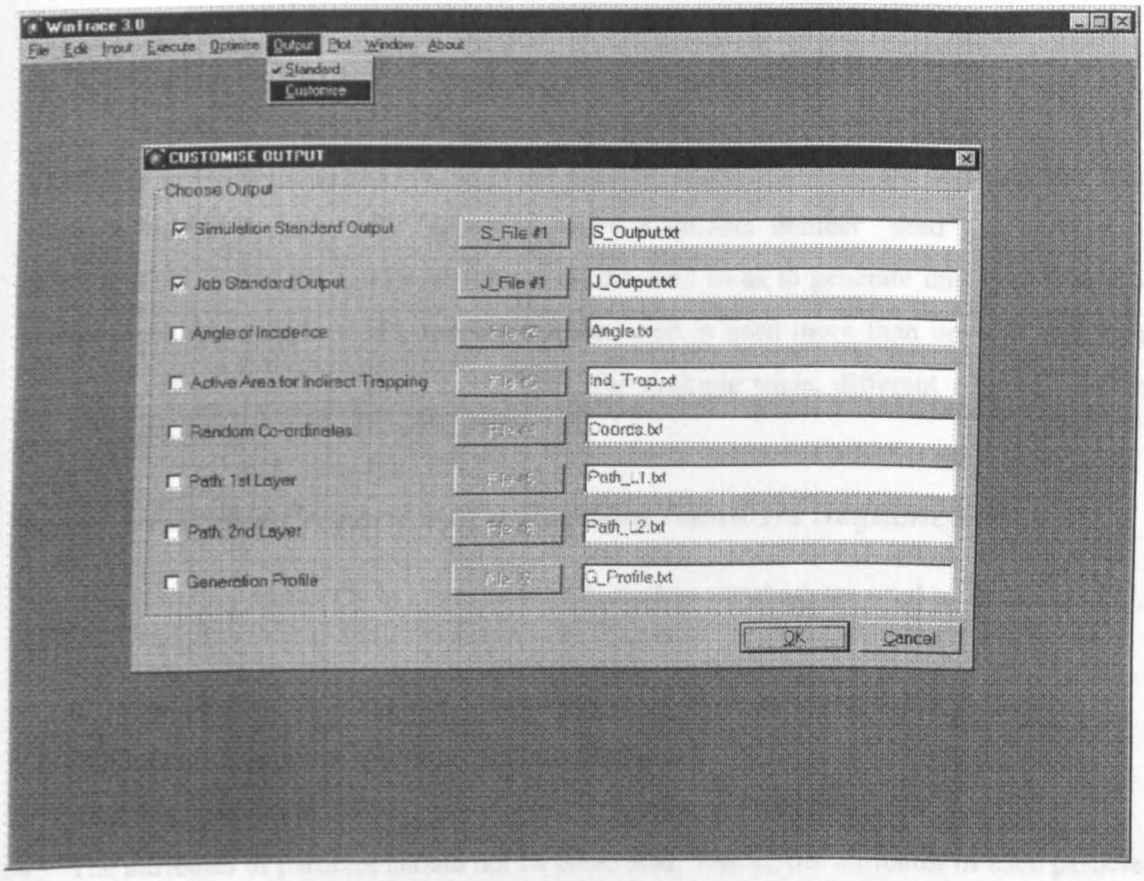

Fig. 4.6 - Standard and Customised output files

Some of the calculated data, such as Reflectance, Absorptance and Transmittance spectra, angles distribution, paths distribution and generation profile, can be plotted and printed directly in *WinTrace* through the *Plot* menu.

4.2. Generation of Random Numbers

Computer-generated numbers are not really random, since computers are deterministic. But, given a number to start with (generally called a random number "seed"), a number of mathematical operations can be performed on the seed so as to generate unrelated (pseudo-random) numbers. In fact, if a random number seed is used more than once, it will give identical random numbers every time. Thus, for multiple trials, different random number seeds must be used.

4.2.1 Desirable Properties of a Random Numbers Sequence

When performing Monte Carlo simulation [36], random numbers are used to determine [37, 38]:

(1) attributes (such as outgoing direction, energy, etc.) for launched particles(photons);

(2) interactions of particles (photons) with the medium.

Viewing this process physically, the following properties are desirable:

- The attributes of particles should not be correlated. That is, the attributes of each particle should be independent of those attributes of any other particle.
- The attributes of particles should be able to fill the entire attribute space in a manner which is consistent with the physics. For example, if we are launching particles into a hemispherical space above a surface, then we should be able to approach complete filling of the hemisphere with outgoing directions, as we approach an infinite number of particles launched. At the very least, "holes" or sparseness in the outgoing directions should not affect the answers significantly. Also, if we are sampling from an energy distribution, with an increasing number of particles, we should be able to duplicate the energy distribution better and better, until our simulated distribution is "good enough".

Mathematically speaking, the sequence of random numbers used to effect a Monte Carlo model should possess the following properties:

1. Uncorrelated Sequences - The sequences of random numbers should be serially uncorrelated. This means that any sub-sequence of random numbers should not be correlated with any other sub-sequence of random numbers. Most especially, n-couples of random numbers should be independent of one another. For example, if we are using the random number generator to generate outgoing directions so as to fill the hemispherical space above a point (or area), we should generate no unacceptable geometrical patterns in the distribution of outgoing directions.

2. Long Period - The generator should be of long period (ideally, the generator should not repeat; practically, the repetition should occur only after the generation of a very large set of random numbers). More explanation is provided below.
3. Uniformity - The sequence of random numbers should be uniform, and unbiased. That is, equal fractions of random numbers should fall into equal "areas" in space. For example, if random numbers on [0, 1] are to be generated, it would be poor practice for more than half to fall into [0, 0.1], presuming the sample size is sufficiently large. Often, when there is a lack of uniformity, there are n-couples of random numbers which are correlated. In this case, the space might be filled in a definite, easily observable pattern. Thus, the properties of uniformity and uncorrelated sequences are loosely related.
4. Efficiency - The generator should be efficient. In particular, the generator used on vector machines should be vectorizable, with low overhead. On massively parallel architectures, the processors should not have to communicate among themselves, except perhaps during initialisation. This is not generally a significant issue. With minimal effort, random number generators can be implemented in a high level language, and be observed to consume much less than 1% of overall CPU time over a large suite of applications.

4.2.2 The Uniform Distribution

The property of *"uniformity"* of a sequence of random numbers (x) already mentioned in the previous paragraph, is mathematically described by the following probability density $f(x)$:

$$f(x) = k \qquad for \qquad a \le x \le b \qquad \text{Eq. 4. 1}$$
$$f(x) = 0 \qquad \text{elsewhere}$$

where a and b are the limits of the randomisation range.
This density is normalised for $k = 1/(b-a)$, as:

$$\int_{-\infty}^{+\infty} f(x)dx = \int_{b}^{a} kdk = k(b-a) \qquad \text{Eq. 4. 2}$$

is equal to 1 for $k = 1/(b-a)$. In order to calculate the average (μ) the following translation is necessary:

$$y = x - \frac{b+a}{2} \qquad \text{Eq. 4. 3}$$

therefore assuming c = (b-a)/2 :

$$f(y) = k \quad \text{for} \quad -c \le y \le c \qquad \textit{Eq. 4. 4}$$
$$f(y) = 0 \quad \text{elsewhere}$$

Defining the first order momentum ($m_1(y)$) of the uniform distribution:

$$m_1(y) = \int_{-\infty}^{+\infty} yf(y)dy = k\int_{-c}^{+c} ydy = 0 \qquad \textit{Eq. 4. 5}$$

the average (μ) of a continuum variable (x), according to this distribution, is given by:

$$\mu = m_1(x) = m_1(y) + \frac{b+a}{2} \qquad \textit{Eq. 4. 6}$$

and the standard deviation (σ) can be calculated from:

$$\sigma^2 = \int_{-\infty}^{+\infty} f(y)y^2 dy = k\int_{-c}^{+c} y^2 dy = \frac{2}{3}kc^3 = \frac{(b-a)^2}{12} \qquad \textit{Eq. 4. 7}$$

which gives:

$$\sigma = \frac{(b-a)}{\sqrt{12}} \qquad \textit{Eq. 4. 8}$$

The cumulative function of a given distribution is also of particular interest, because it estimates the probability of generating values lower then a given value X. This function is given by:

$$P(X) = \int_{-\infty}^{X} p(x)dx \qquad \textit{Eq. 4. 9}$$

It is a limited function uniformly distributed, ranging between 0 and 1.

4.2.3 Analysis of a Sequence of Random Numbers Generated by the "RND" Function of Visual Basic

The output of the random number generator used in the code *WinTrace,* has been tested to ensure that generated numbers are random in relation to one another, in order to fulfil all the desirable properties illustrated in the previous paragraphs.

The four sequences of random numbers of Table 4.2, have been generated by the built-in function of Visual Basic (RND), and the respective average and standard deviation have been calculated.

It was found that the same random-number sequence is generated every time the program is run because each successive call to the RND function uses the previous random number as a seed for the next number in the random-number sequence. In order to generate a different random-number sequence each time the calculation program is run, the "RANDOMISE" statement has to be employed without an argument to initialise the random-number generator before RND is called.

The values of the average and the standard deviation calculated for a uniform distribution, in the range [0, 1] according to Eq. 4.6 and Eq. 4.8, are listed at the bottom of the table.

Table 4.2 - Random sequences generated in the range [0,1]

Entries	Average (μ)	Standard Deviation (σ)
10	0.58927	0.26304
100	0.52581	0.28625
1.000	0.50784	0.28407
10.000	0.50087	0.28848
Uniform Distribution	***0.50000***	***0.28867***

As an example, the statistical distribution of the sequence of 10.000 rays is shown in Fig. 4.7. The lower part of the graph shows the histogram plot of the number of events per channel, where a channel is considered to be an interval of 0.01. The upper graph represents the cumulative function, obtained by integrating over the number of events.

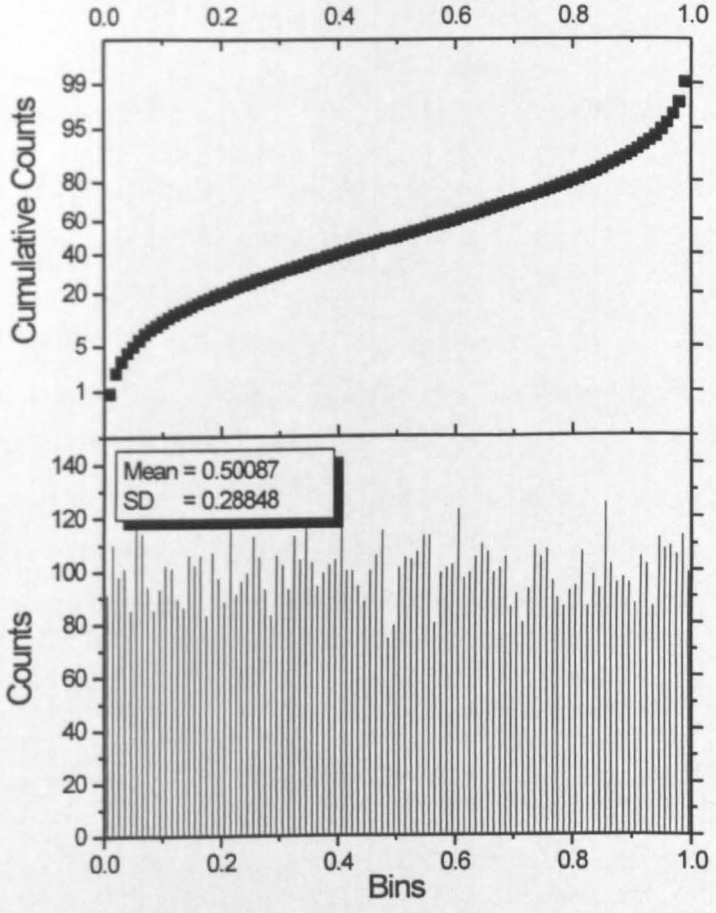

Fig. 4.7 - Distribution of 10^4 random numbers uniformly generated between 0 and 1.

4.3. Randomisation Procedures

4.3.1 Randomisation over the Angle of Incidence $\alpha_i(x)$

Since for a given illumination angle the intensity reflected by a planar surface is constant, the ray-tracing of one single ray for each wavelength is enough to calculate exactly the reflectance spectrum of a flat cell.

The necessity of applying the Monte Carlo approach to a flat device came out from the interest in comparing the reflectance of a silicon flat cell illuminated by isotropic light to the reflectance of a Spheral Solar™ Cell illuminated by a normally incident beam which, due to the cell geometry, causes the same effects as the isotropic illumination of a flat surface.

Therefore, in order to allow the simulation of a flat cell, which could in some way approximate the behaviour of a Spheral Solar™ Cell, the randomisation of the illumination angle (between two user defined values) was implemented.

Assuming randomisation of the angle of incidence $\alpha_i(x)$ uniformly between 0 deg. and 90 deg., the expected value for the average of the uniform distribution is 45 and for the standard deviation is 25.98.

The distribution obtained by generating 10^4 rays is shown in Fig. 4.8. The calculated average of the population is 44.87 while the standard deviation is 25.96, therefore the uncertainty introduced into the calculations by the statistics over 10^4 entries is $\pm$ 0.29 %. The statistics displayed in the lower part of the graph of Fig. 4.8, are relative to the linear fit of the data represented by the red line. Even though in a perfectly uniform distribution (events all equally probable) the parameter B of the linear fit should be equal to zero, it is possible to consider the distribution as uniform, because B is very small.

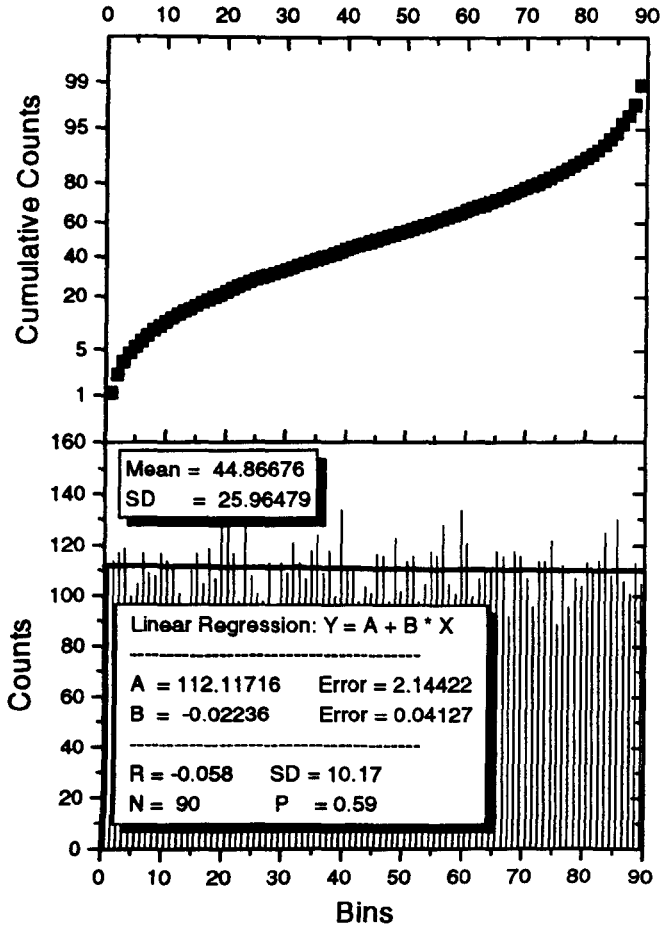

Fig. 4.8 - Distribution of 10^4 angles of incidence uniformly generated between 0 and 90 deg..

4.3.2 Randomisation over the Point of Incidence P(X, Y, Z)

In all the procedures simulating interaction of light with a Spheral Solar™ Cell, the randomisation was performed over the incidence point P(X, Y, Z) on the *generation area* shown in Fig. 4.9, which is a function of the three Cartesian co-ordinates. As already illustrated (Section 2) the *generation area* is the minimum surface which can be chosen in order to keep the symmetries of the spherical geometry.

The uniform generation of P(X, Y, Z) could be simplified into a two variable, only X and Y, uniform distribution with constant density ρ (number of points /cm^2). In order to reproduce this generation the so-called *randomisation area* had to be defined, which differs from the *generation area* as shown in Fig. 4.9 and is a circular extension of the *generation area.*

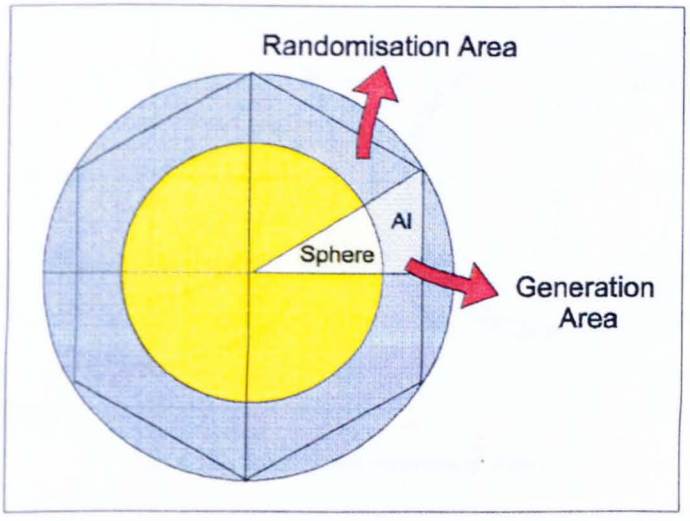

Fig. 4.9 - Generation and Randomisation Areas

In polar co-ordinates the point of incidence P(X,Y) is defined by the radius r and by the angle ϕ, where:

$$0 \le r \le R \qquad and \qquad 0 \le \phi \le \pi/6 \qquad \textit{Eq. 4. 10}$$

The probability densities of these two polar co-ordinates are $p(\phi)d\phi$ and $p(r)dr$.

$p(\phi)d\phi$ is given by the ratio between the number of points contained in the infinitesimal sector of Fig. 4.10(a), and the total number of points:

$$p(\phi)d\phi = \frac{\rho(R^2 d\phi / 2)}{\rho\pi R^2} = \frac{d\phi}{2\pi} \qquad \textit{Eq. 4. 11}$$

In the same way, an infinitesimal variation of the radius r is considered, as shown in Fig. 4.10(b):

$$p(r)dr = \frac{\rho 2\pi r dr}{\rho\pi R^2} = \frac{2r}{R^2}dr \qquad \textit{Eq. 4. 12}$$

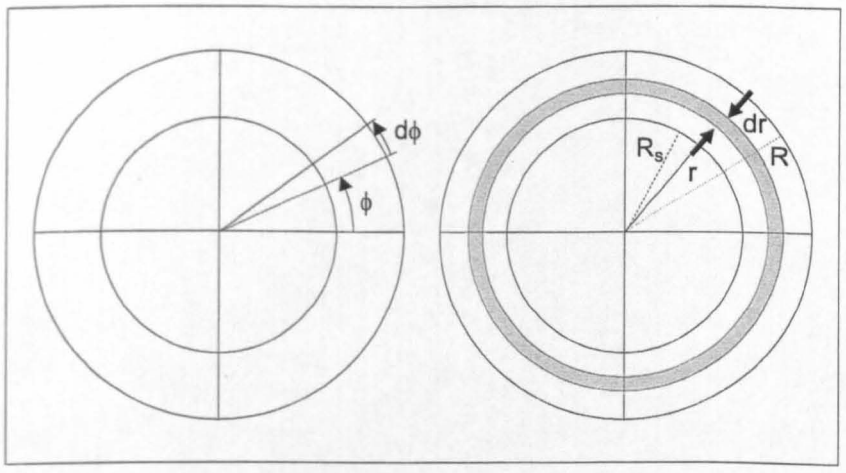

Fig. 4.10 - Infinitesimal variation of ϕ and r.

The cumulative functions associated with the two probability densities are:

$$P(\phi) = \int_0^{\phi} p(\phi) d\phi = \frac{\phi}{2\pi} \qquad \textit{Eq. 4. 13}$$

$$Q(r) = \int_0^{r} p(r) dr = \frac{r^2}{R^2} \qquad \textit{Eq. 4. 14}$$

As already mentioned in Par. 4.2.2, the cumulative functions $P(\phi) = Ran1$ and $Q(r) = Ran2$ are uniformly distributed variables. Hence, by integrating Eq. 4.13 and Eq. 4.14, over the desired interval, we obtain:

$$\phi = \frac{\pi}{6} Ran1 \qquad \text{and} \qquad r = R\sqrt{Ran2} \qquad \textit{Eq. 4. 15}$$

where *Ran*1 and *Ran*2 are the two computer generated random numbers.

After having generated (ϕ, r) pairs of values, the *(X, Y)* Cartesian co-ordinates can be calculated through a co-ordinates system transformation. Among the *(X, Y)* pairs extracted on the *randomisation area*, only those belonging to the *generation area* are chosen, such as $X \leq (R_s + d/2)$, where R_s (the radius of the sphere) is 350 μm and *d/2* (the half of the inter-sphere spacing) is 30 μm. Some of these points are generated on the sphere sector (about 77%) and the remaining on the aluminium sector. The geometrical condition which has to be fulfilled by those points which belong to the sphere sector is: $0 \leq r \leq R_s$.

Given the *2d* point of incidence *P(X, Y)*, the *Z* co-ordinate on the sphere surface can be determined by substituting *X*, *Y* and R_s into the analytical equation of the sphere in S^3:

$$X^2 + Y^2 + Z^2 = R_s^2 \qquad \textit{Eq. 4. 16}$$

For those points laying on the aluminum substrate the *Z* co-ordinate corresponds to the shift of the aluminum plane with respect to the plane intersecting the sphere centres.

The Visual Basic routine *"Randomise_Coords"* which contains the algorithms described in this Section is illustrated in Appendix C.

4.3.3 Statistical Error

The goodness of the statistics, the number of generated events (light rays) required to achieve a specified level of accuracy, was investigated prior to the calculation execution. For this purpose, a ray-tracing simulation of a silicon planar wafer randomly illuminated was performed.

After each reflection on the planar wafer, the front surface reflectance was calculated, and then a new ray was traced. The new reflectance was then assumed to be the average of those of the previous rays. This process was repeated until tracking more rays no longer altered the calculated average reflectance. This was in practice achieved after tracking a thousand rays, when the statistical error became completely negligible, as shown in Fig. 4.11.

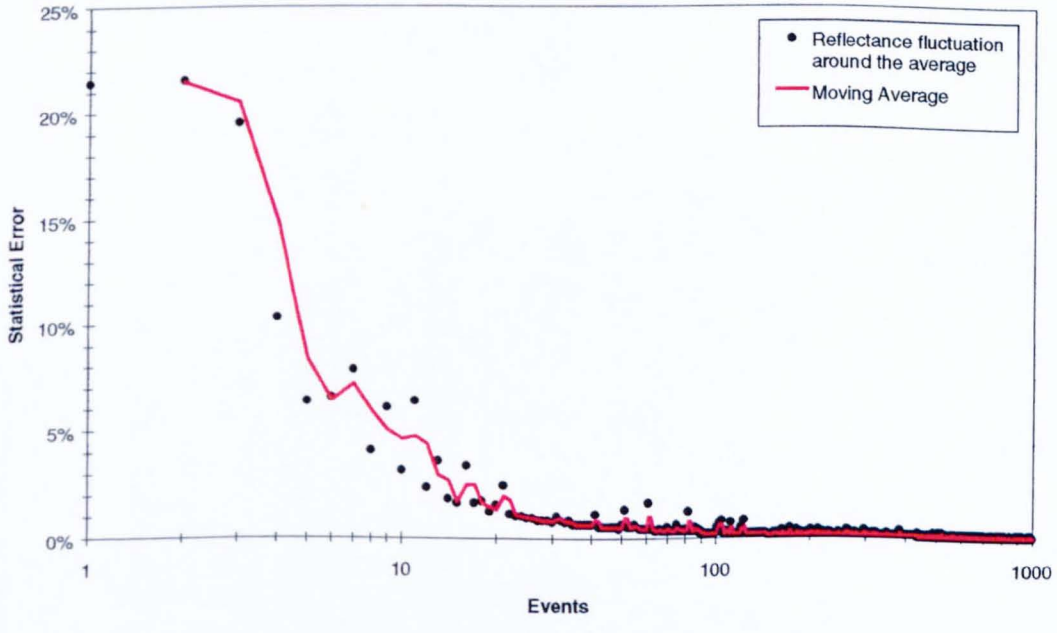

Fig. 4.11 - Accuracy of the statistics on the calculated reflectance as a function of the number of generated rays

Therefore, according to the statistical considerations of the previous paragraphs, 10^4 rays will be assumed as the default number of events in all the following simulations and the statistical error on the calculated data will be neglected.

SECTION 5

SIMULATION RESULTS AND MODEL VALIDATION

5.1. Optical Model Validation

A set of standard simulations of simple PV-devices which could be experimentally reproduced have been carried out in order to validate the algorithms implemented in the code *WinTrace* for the calculation of the global reflectance of a multi-layered system.

In particular, the simulation of a planar device coated with a single layer AR-coating of known thickness was performed to check the reliability of the simulation routines. Furthermore, the simulation of a *"real"* Spheral Solar™ Cell was carried out to validate the calculation procedures involving spherical co-ordinates.

The experimental verification of the code *WinTrace* is of fundamental importance for the future utilisation of the simulation tool for the design of the optimised structured cover. In fact, such a cover for Spheral Solar™ Cells will be exclusively designed on the base of ray-tracing simulations performed leading to a light trapping maximisation.

5.1.1 Transmission Matrix Validation

The reflectance of a silicon wafer coated with 105 nm of SiO_2, simulated with the code *WinTrace* has been compared both to that simulated by a similar programme RAYN [39], using the same transmission matrix method, and to the one measured at the ESTI laboratories by using the Spectrophotometer described in Section 2. The same set of optical values has been employed for the two simulations.

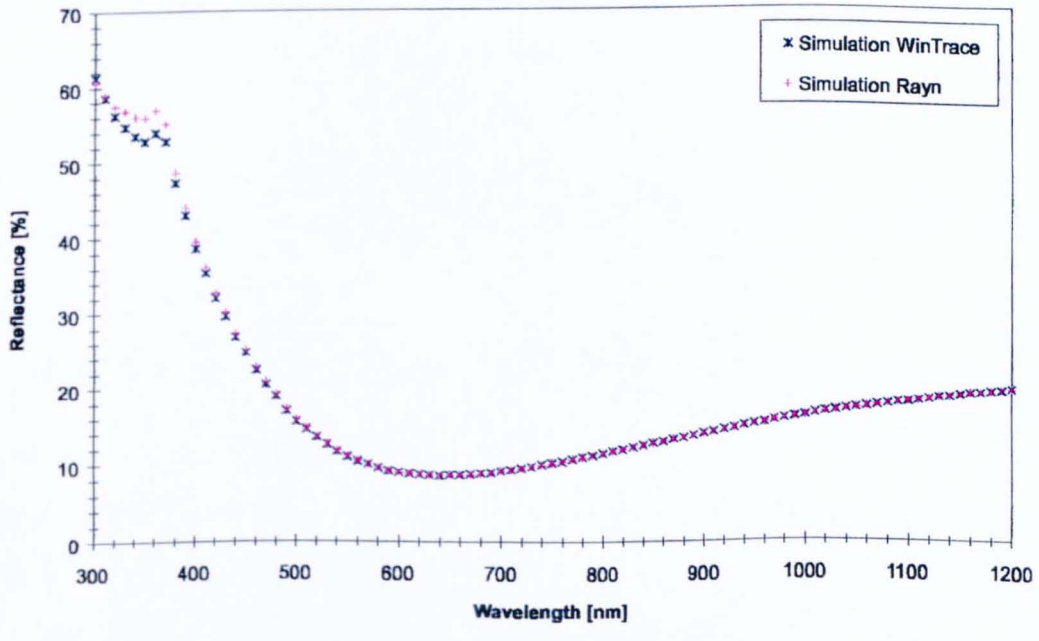

Fig. 5.1- Comparison between simulated and measured reflectance of a flat silicon wafer coated with 105 nm SiO_2

The entire reflectance spectrum of the same wafer, against the angle of incidence is plotted in Fig. 5.2.

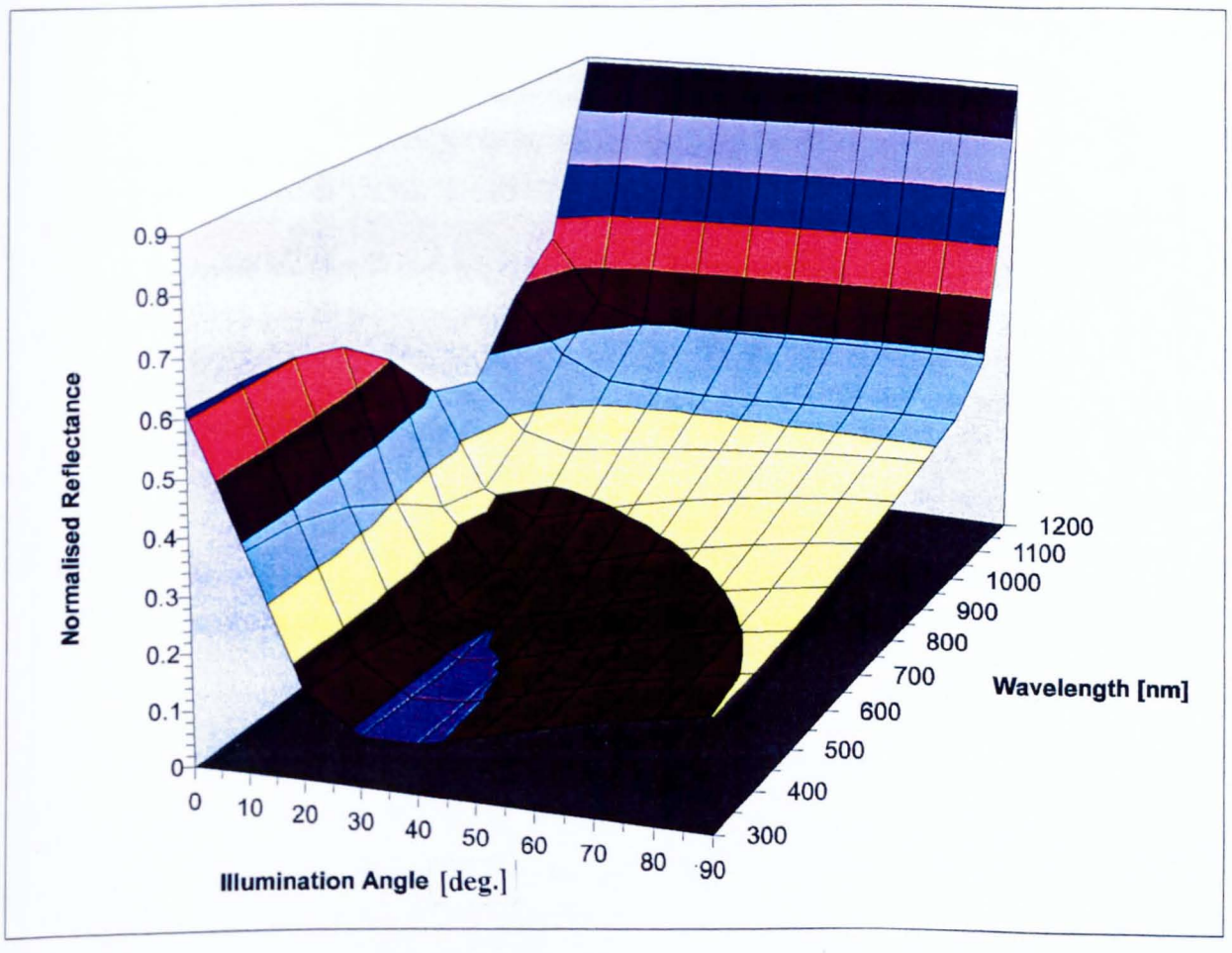

Fig. 5.2 - Reflectance of a silicon wafer coated with 105 nm SiO_2 , vs. illumination angle

The minimum of this plot corresponds to the optimised wavelength according to the principle of the quarter wavelength AR-coating, which gives: $\lambda_{min} = 4 \cdot (n_{SiO2} \cdot t_{SiO2}) = 609$ nm, where $n_{SiO2} = 1.45$ and $t_{SiO2}=105$ nm.

5.1.2 Simulation of an Isolated Sphere

The simulation of an isolated sphere was performed (assuming 10^4 incident rays), without including in the calculations the indirect trapping option, for estimating the difference between the reflectance of a silicon flat layer and the one of a spherical layer, both illuminated with a normal beam. The simulation results are plotted in Fig. 5.3.

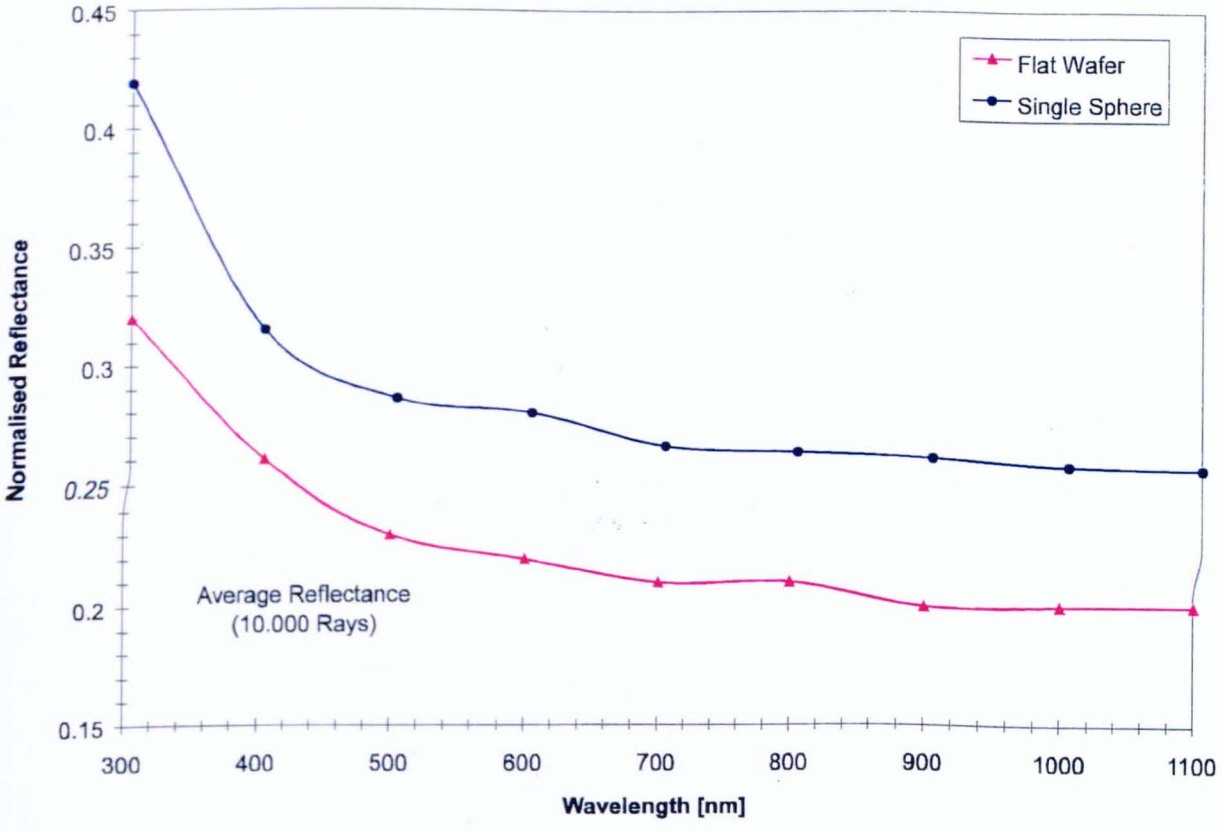

Fig. 5.3- Reflectance spectra of a single spherical layer and of a flat silicon one

In Fig. 5.4 the reflectance is plotted against the angle of incidence, assuming normal illumination with incident light of 632 nm. The increase of the reflectance of the spherical layer is proportional to the cosine of the angle of incidence.

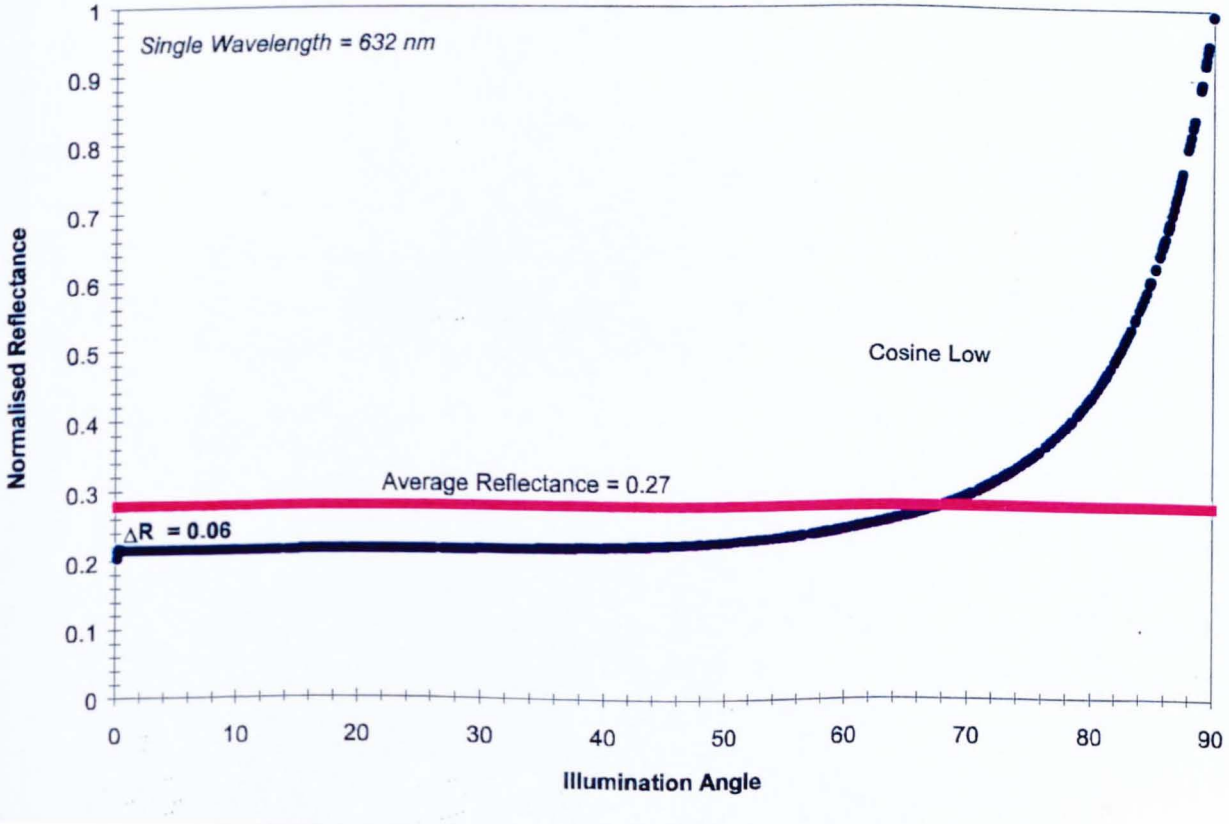

5.1.3 Optical Performances of Spheral Solar™ Cells

5.1.3.1 Bare Cell Simulation

To simulate a bare cell (where bare means without any AR-coating layer), the indirect trapping option was included in order to consider secondary reflections on indirectly illuminated spheres. The calculated cell reflectance, which results from the combined optical effects is illustrated in Fig. 5.5. The picture shows the comparison between the reflectance spectrum of a Spheral Solar™ Cell and that of a flat cell with illumination angle randomisation. The spectrum of the isolated sphere is also shown to illustrate the reflectance reduction caused by indirect trapping.

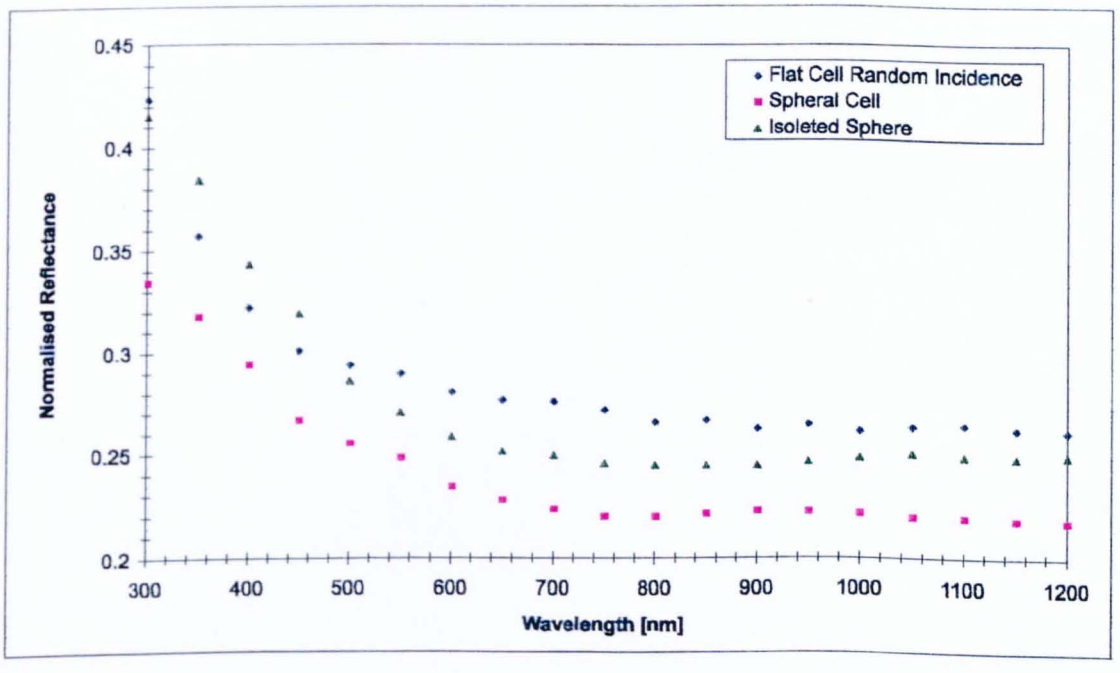

Fig. 5.5- Comparison between the reflectance of a bare spherical cell and that of a flat cell

The enhancement factor of the bare cell reflectance with respect to the one of the isolated sphere is plotted in Fig. 5.6. This enhancement, due to the combined light trapping mechanisms among the spheres, appears to be higher in the low wavelengths range according to what was found by laser scanning. In fact, the centre of the sphere follows the typical behaviour of an isolated sphere not being affected by the indirect light trapping, while the external ring presents a current generation enhancement because of the presence of the hexagonal lattice of spheres.

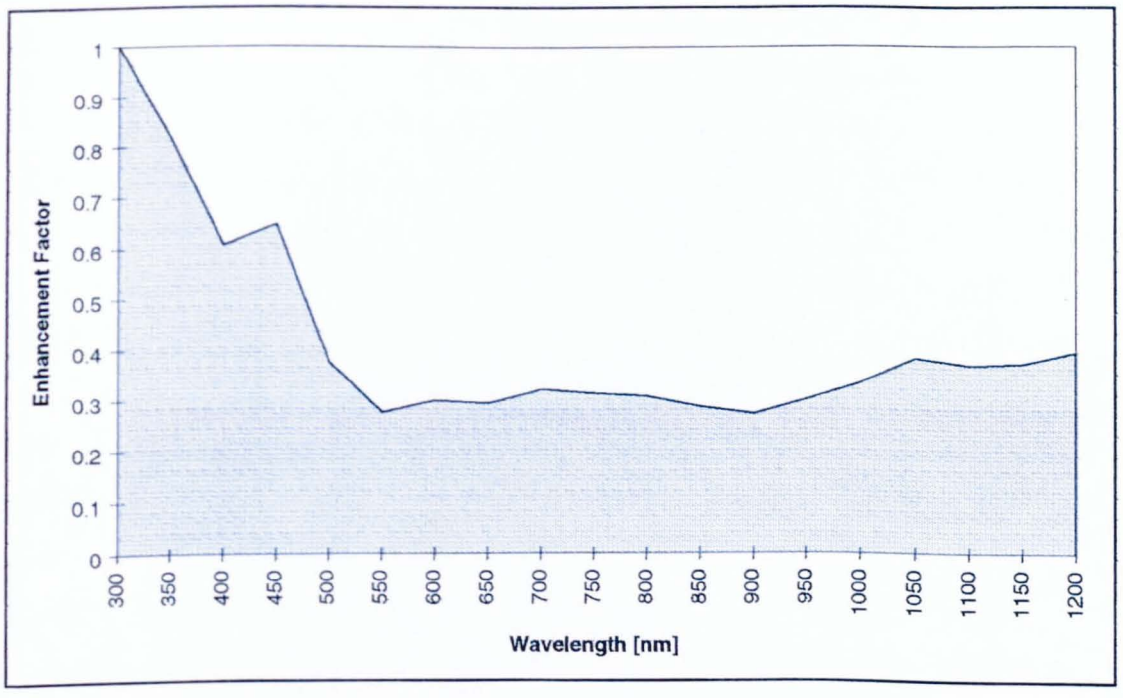

Fig. 5.6- Enhancement factor of bare Spheral Cells compared to a single sphere, as a function of wavelength

5.1.3.2 TiO_2 Transmissivity

The effect of a variable thickness TiO_2 AR-coating has been evaluated because the exact thickness of the AR-layer deposited on Spheral Solar™ Cells was not supplied by the manufacturer. The curves calculated for the three different TiO_2 layers are plotted in Fig. 5.7.

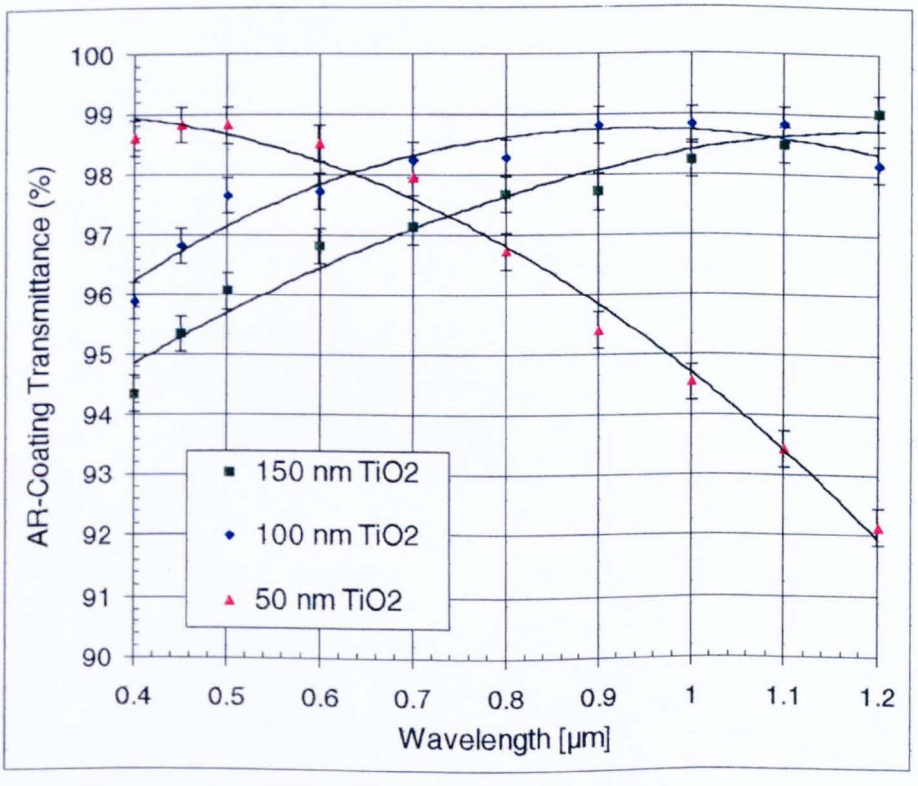

Fig. 5.7- Transmissivity of different layers of TiO_2 of constant thickness

Since in the visible region of the spectrum even small thickness variations produce a remarkable transmittance shift, the estimation of the correct coating thickness is fundamental for the following simulations. Therefore, assuming an optimised photon wavelength around 600 nm, the optimised coating thickness resulting from the quarter wavelength law, is about 70 nm. The choice of this thickness is also justified by the appearance of the devices which look blue to the eye, indicating that the coating layer is not optimised for the low visible wavelengths.

Moreover, fundamental for the simulation of the cell reflectance by using the transmission matrix method is the determination of the optical thickness of the AR-coating. In fact, the optical thickness of a spherical AR-coating layer deposited on the silicon spheres is not constant for a given beam inclination angle, as for flat wafers, since it depends on the elevation of the point of incidence on the spherical surface.

The upper and lower limits of the optical thickness, necessary to estimate the amount of light absorbed by the AR-coating, have been simulated for different beam inclination angles.

Fig. 5.8(a) shows a comparison between the optical thickness of a 70 nm TiO_2 layer deposited on a flat wafer and on a silicon sphere.

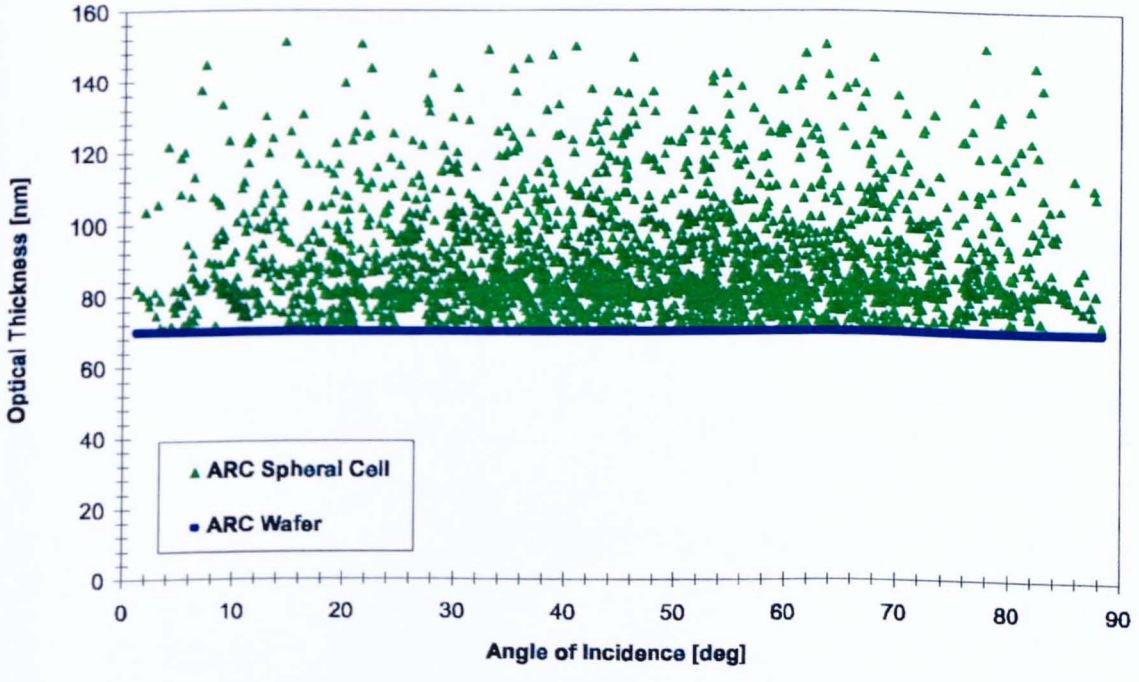

Fig. 5.8(a) - Optical thickness of a planar and a spherical AR-coating layer with the beam incident on a random position on the sphere

Since the optical thickness of the planar coating is constant it is represented by the straight line. On the contrary, the optical thickness of the spherical coating layer changes with the illumination angle between 70 nm (effective thickness) and 150 nm. This thickness corresponds

to the one of the flat layer only when the illumination is normal to the surface of the sphere, when the path of light is exactly 70 nm.

Fig. 5.8 (b) shows the comparison between the normalised reflectance of a spherical and of a planar layer under different illumination angles.

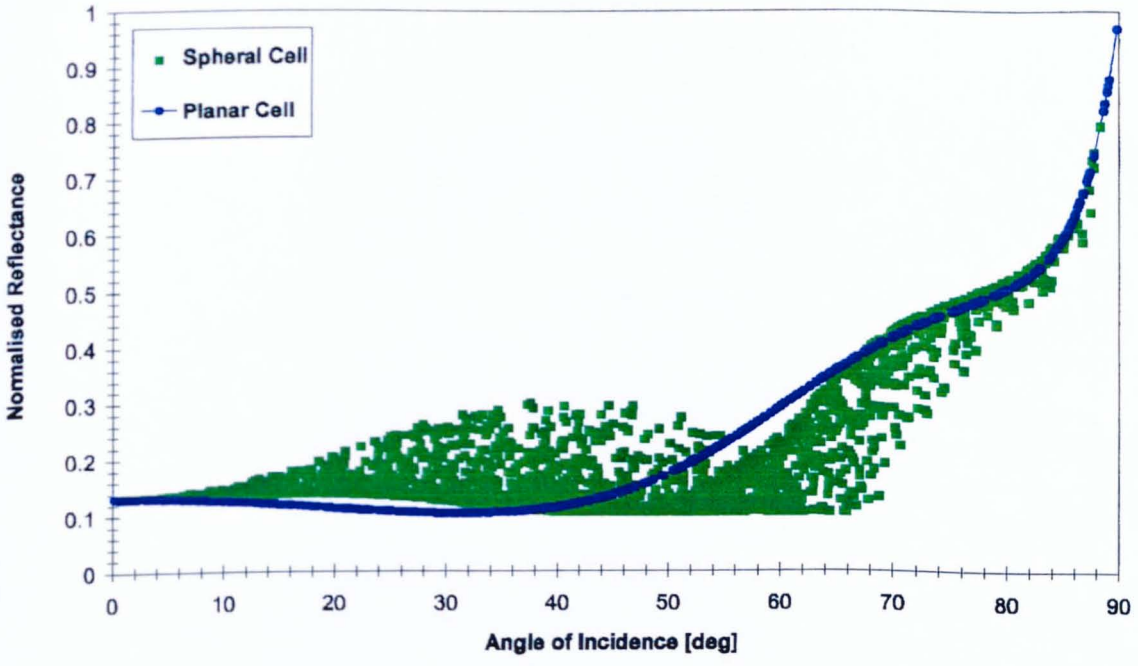

Fig. 5.8 (b) - Normalised Reflectance of a planar and a spherical AR-coating layer

In this case, the continuous line represents the planar layer reflectance while the points represent the variable spherical layer reflectance which depends both on the illumination angle and on the elevation on the sphere surface of the point of incidence. Since the optical thickness of the coating layer changes according to these two angles also the overall front surface reflectance, calculated with the transmission matrix method and therefore based on the optical thickness of the involved layers, will change accordingly.

5.1.3.3 Simulation of the Spheral Solar™ Cell Absorption Profile

The absorptance of the entire Spheral Solar™ Cell has been simulated assuming a single layer anti-reflective coating (70 nm, TiO_2).

Fig. 5.9 shows the simulated optical absorptance compared to the one measured at the ESTI *laboratories.*

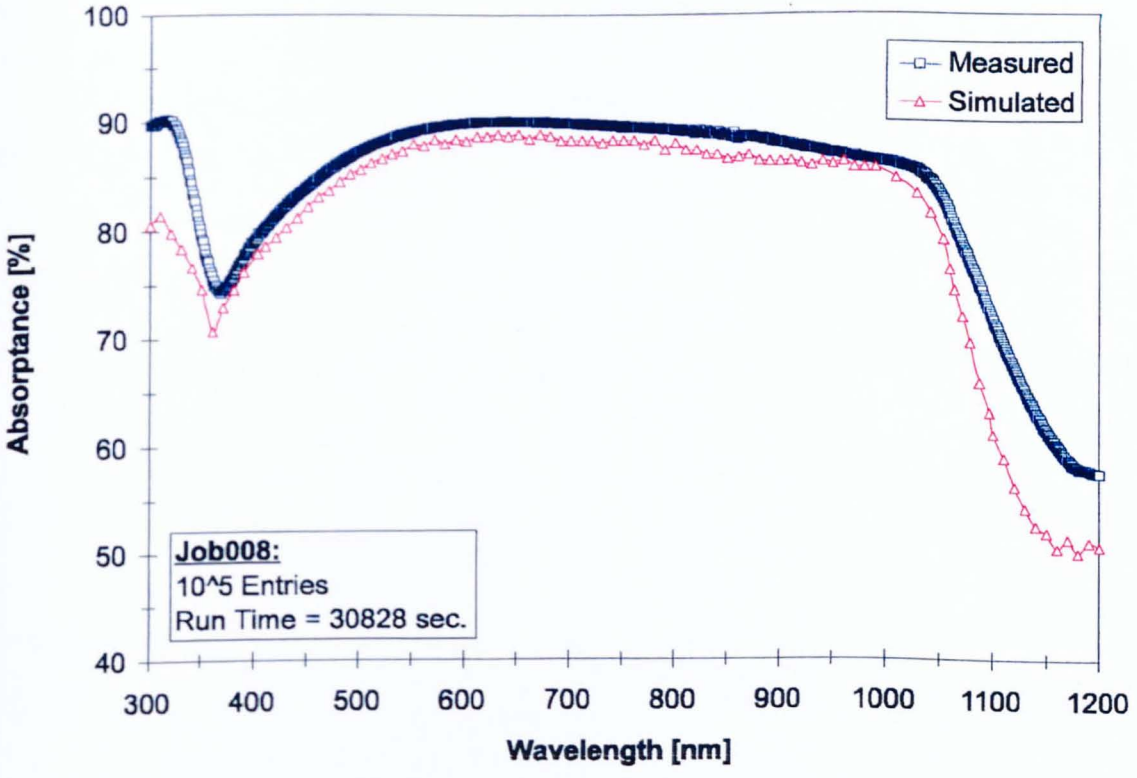

Fig. 5.9- Comparison between measured and simulated absorption spectra.

Since the sample was placed inside the integrating sphere, the real measured quantity was the sum of the hemispherical cell reflectance and transmittance. Hence, the optical absorptance was analytically determined assuming that the sum of absorptance, transmittance and reflectance must be equal to the unity.

The measurement error resulted from the average of three independent measurements, is estimated to be lower than 2 % along the entire spectrum.

The difference between the two curves at long wavelengths, can be explained because the measured curve includes also the light absorbed by the AR-coating and by the aluminium back reflector (which is not useful for photocurrent generation), while the theoretical curve only estimates the light coupled into the silicon spheres.

Simulation results indicate that Spheral Solar™ Cells present an enhanced optical light coupling with respect to standard flat devices, especially in the long wavelengths range, because the average path of light in the silicon spheres is longer with respect to standard flat cells as shown in Fig. 5.10. This is due both to the presence of the aluminium substrate, which can be considered as a back reflector, because of the sphere dimensions and because of the reflections inside the spheres.

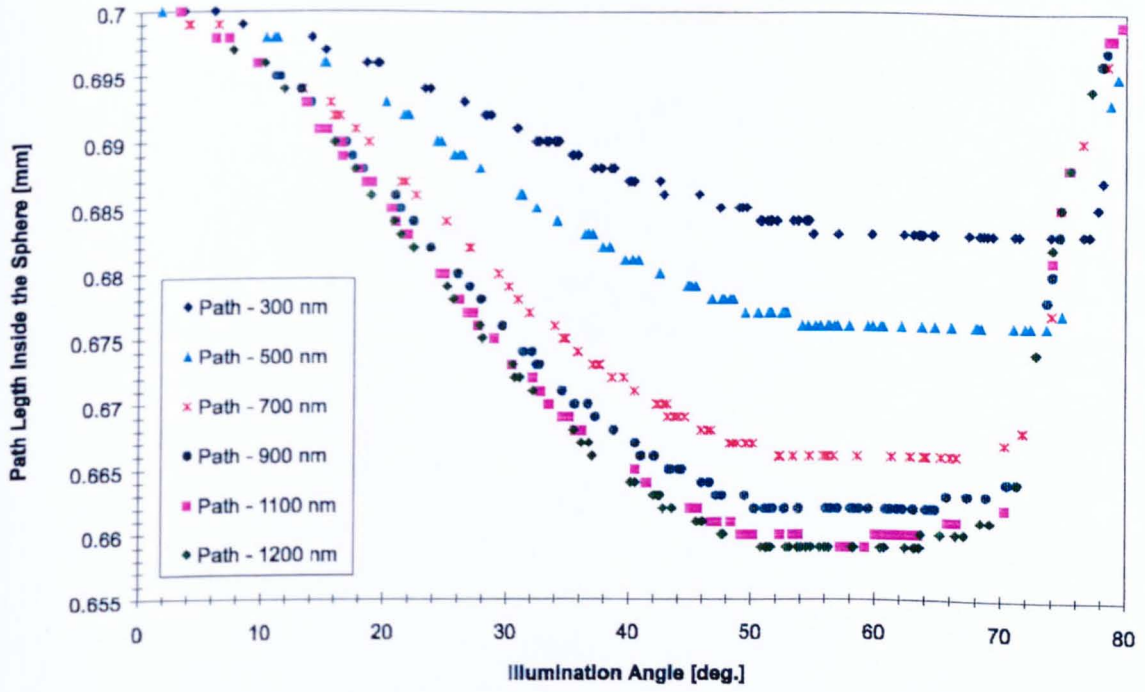

Fig. 5. 10 - Optical path of a ray impinging on the top of a silicon sphere with an inclination angle varying from 0 deg. to 90 deg. The maximum path is only possible for normal incident light on the top of the sphere.

On the other hand, the cell efficiency in this region is still poor (as shown by the spectral responsivity), mainly because of the grade of purity of the employed material.

The good accordance between simulated and measured curves, especially in the visible range, proves the correct estimation of the three parameters characterising the spherical geometry: F_{sh} (effective only for off-normal illumination), F_{al} and A_{sr}.

5.1.3.4 Cell Active Areas

WinTrace also provided important information on active cell areas which could be experimentally verified by laser scanning.

The absorption profile of a sector of a quarter of sphere, simulated assuming a normal incident beam of 442 nm is plotted in Fig. 5.11 and the corresponding absorption map is given in Fig. 5.13.

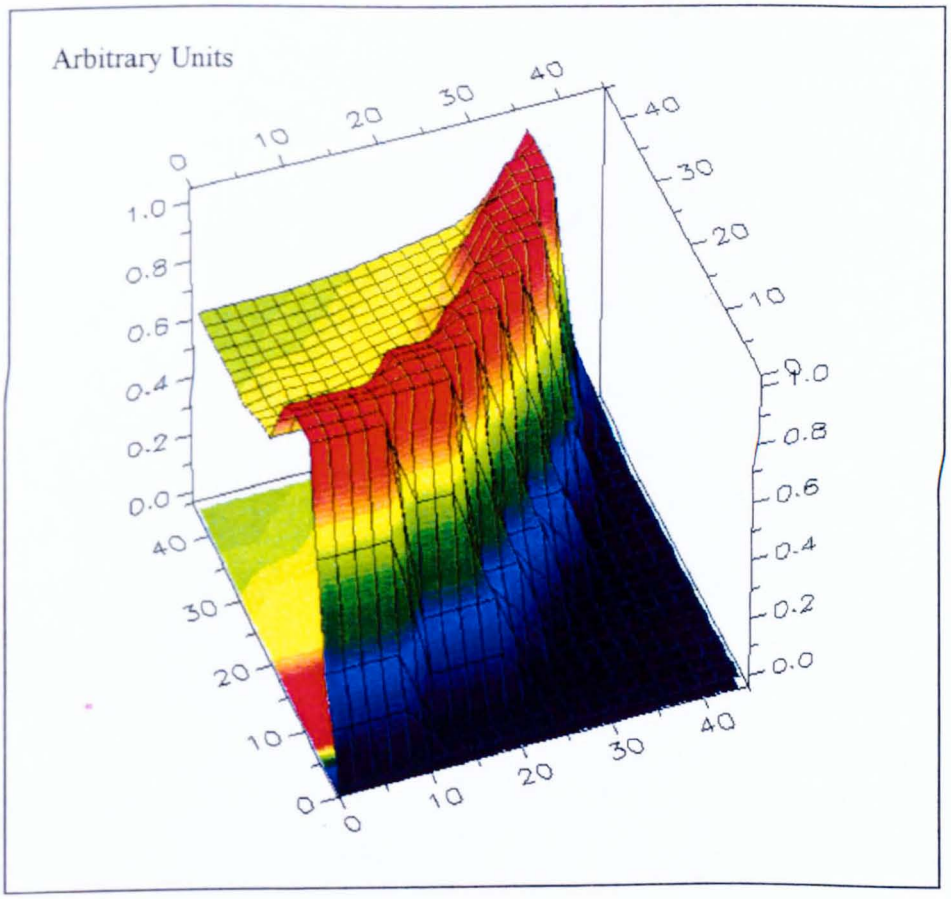

Fig. 5.11 - 3d view of the simulated absorption profile of a quarter sector of a sphere

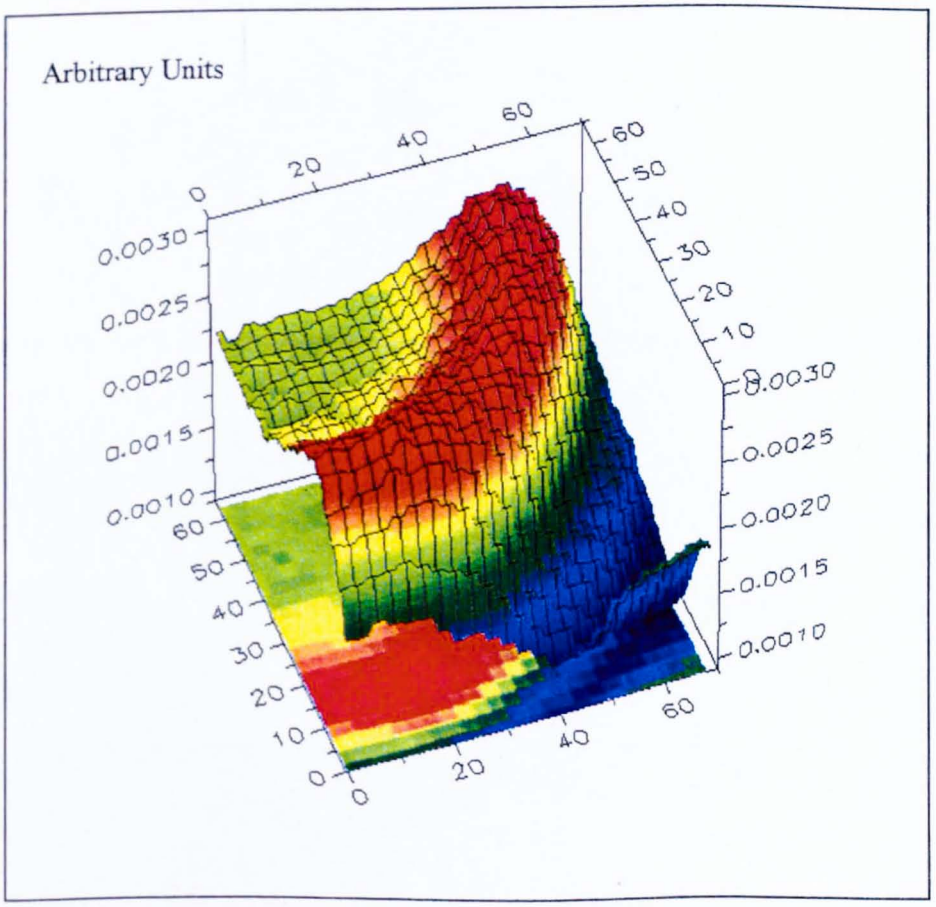

Fig. 5.12 - 3d view of the measured absorption profile of a quarter sector of a sphere

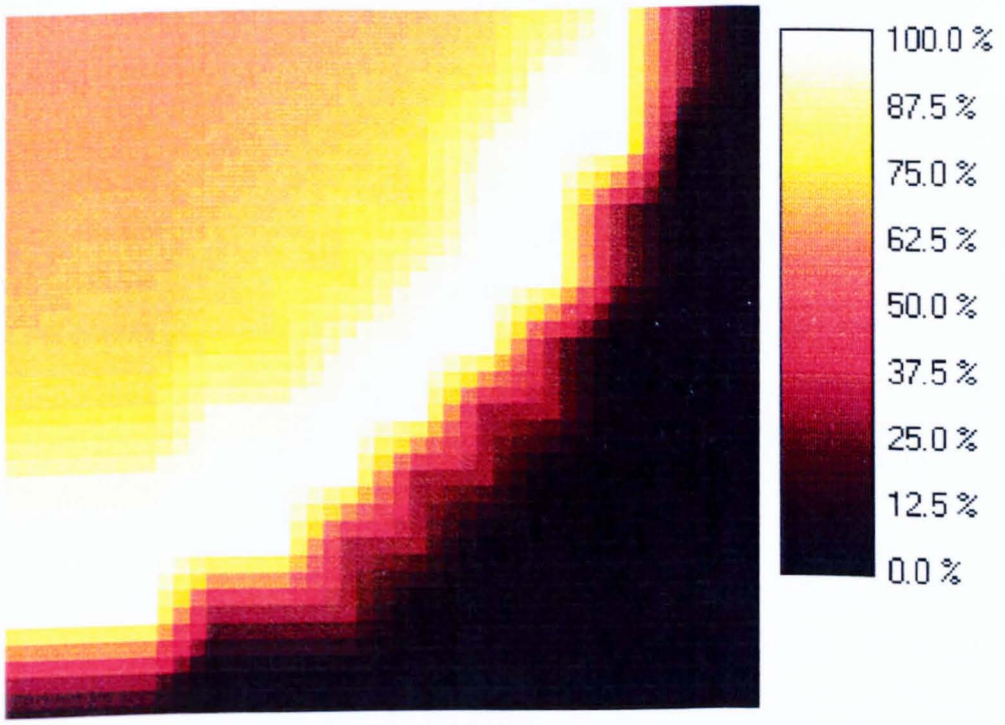

Fig. 5.13- Simulated absorption map of a quarter sector of a sphere

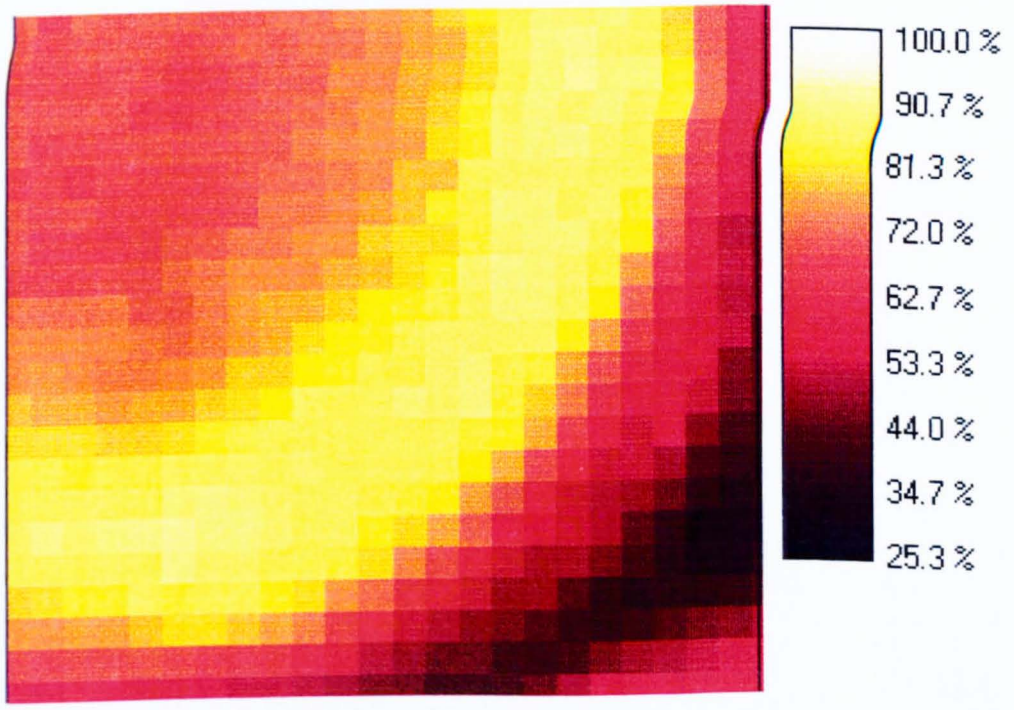

Fig. 5.14 - Measured absorption map of a quarter sector of a sphere

The blue light was chosen for these optical simulations because the most interesting region of the sphere for observing indirect light trapping is the most superficial spherical layer (< 1 μm), where the blue light is absorbed.

The most active region of the sphere surface, as given by *WinTrace* calculations, is not the top but the ring, corresponding to an elevation (θ) between 42 deg. and 65 deg. on the sphere surface, where the indirect trapping of the rays reflected from the surrounding spheres and from the aluminium takes place. In this region, mainly at short wavelengths (where the penetration depths are reduced and light is absorbed more at the surface) the absorption at normal incidence is increased by more than 20 %, because of a drastic reduction of the overall reflectance due principally to the reduction of F_{al} and increase of A_{sr}. This effect, numerically discussed in Section 3, is verified by the two experimental LBIC images shown in Fig. 5.12 and Fig. 5.14. These images have been measured over an individual sphere at the *ESTIScan* facility, by using a 30 mW HeCd laser of 442 nm wavelength.

The results illustrated confirm that secondary reflections play a fundamental role in the light trapping schemes of the spherical geometry, increasing the non-local trapping contribution to the overall cell absorptance and validate the optical model implemented in the code.

5.2. Performance Enhancement at off-Norm al Illumination Angles

The electrical performance of Spheral Solar™ Cells at specific illumination angles has been investigated to demonstrate that it is strictly related to the optical enhancement caused by indirect trapping.

A considerable enhancement of the cell performance with respect to standard flat cells at specific wavelengths and illumination angles has been experimentally verified, by undertaking a comparative study between angular dependencies of optical and electrical parameters.

5.2.1 Angular Dependency of Optical Factors

A complete job reproducing a Spheral Solar™ Cell illuminated from different angles (with β varying from 0 to 90 deg. with respect to the XY plane) was run, in order to visualise the angular dependency of the indirect trapping factors (mainly secondary reflections and aluminium factor). Active areas for indirect trapping were visualised by mapping the co-ordinates of the points of incidence of the secondary rays.

The graph of Fig. 5.15 summarises the tendency of these active areas to shift towards lower elevation angles on the sphere as the beam inclination angle increases.

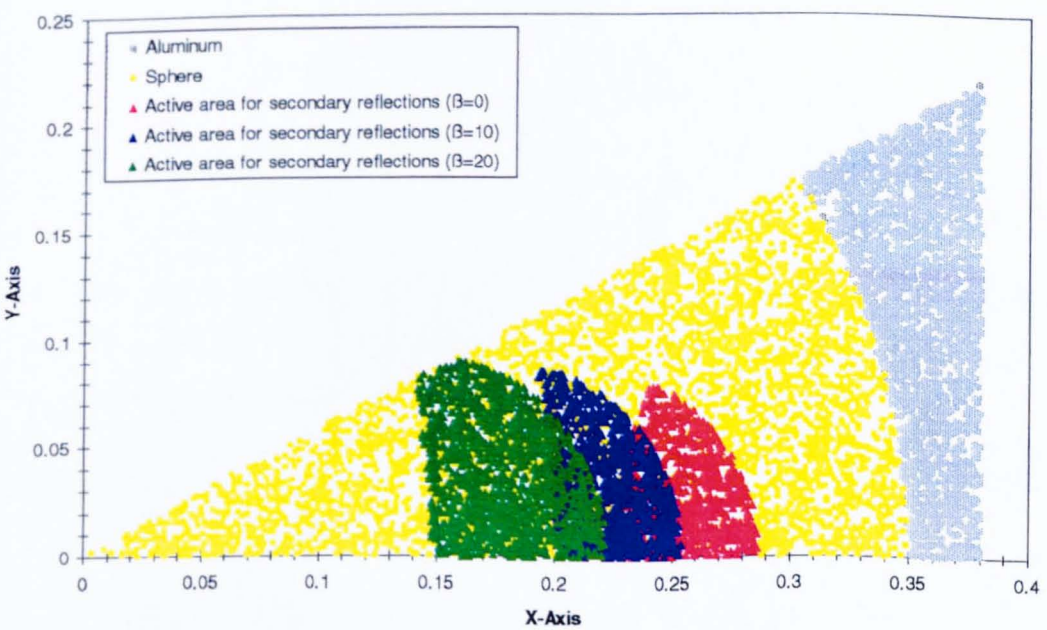

Fig. 5.15 - Progressive shift of the area of the direct cell which reflects towards the indirect cell: active area for secondary reflections

According to what was analytically predicted in Section 3, for *beam inclination* angles (β) greater then 20 deg., the aluminium substrate becomes entirely effective in reflecting primary rays towards the direct cell, inducing a significant increase of the indirect trapping and a consequent decrease of the overall reflectance.

The indirect trapping enhancement can be experimentally verified by normalising the values of reflectance against illumination angle plotted in Fig. 2.13. The graph of the normalised reflectance is shown in Fig. 5.16.

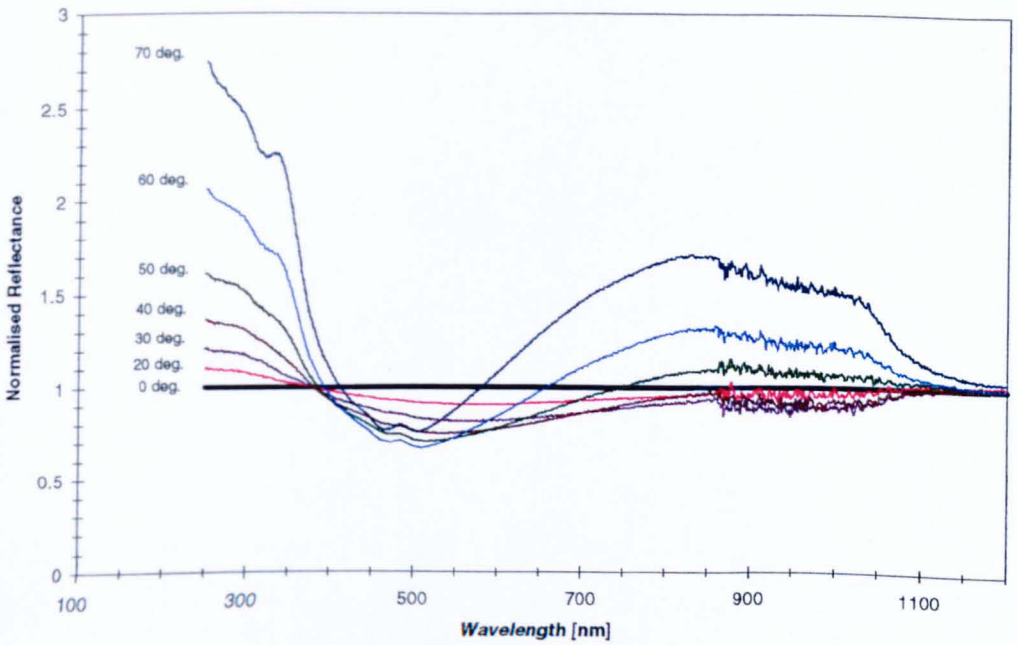

Fig. 5.16 - Normalised Reflectance Spectra

The minimum of the reflectance is found for wavelengths around 500 nm, according to what was found by simulating an AR-coating with a thickness of about 70 nm.

In particular, the optical enhancement is present at wavelengths greater then 400 nm, under illumination angles lower than 50 deg..

The influence of the optical enhancement, has been observed also in the electrical performance of the cells, even though slightly reduced by the quality of the material, as will be discussed in the next paragraph.

5.2.2 *Angular Dependency of Electrical Parameters*

5.2.2.1 I-V Characteristics

The measured I-V characteristics plotted in Fig. 2.3, have been extrapolated to STC, according to IEC 904-1, by performing a correction to the same irradiance level.

The curves have also been corrected for the series resistance calculated at the maximum power point, which resulted to be 7.7 mW.

In Fig. 5.17 some of the extrapolated I-V curves, corresponding to normal and off-normal illumination, are shown.

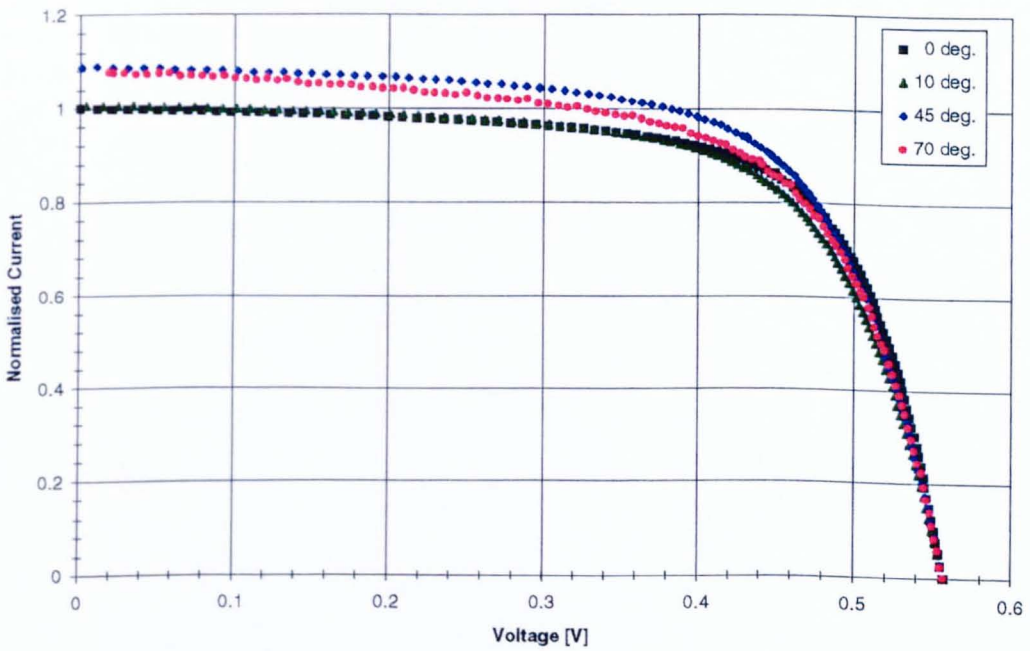

Fig. 5.17 - I-V characteristics extrapolated to STC conditions.

5.2.2.2 Short Circuit Current

The short circuit current against the illumination angle of both a flat and a Spheral Solar™ *Cell, are plotted in Fig.* 5.18. Their normalised enhancement factors are also shown.

The difference between flat and spherical device *performance at normal* incidence, is more and more significant as the illumination angle increases. It presents a maximum at angles between 40 and 60 deg. which proves the effectiveness of the indirect trapping factors in this range.

As theoretically predicted, for angles greater then 60 deg. the indirect trapping contribution starts to decrease, since the Z co-ordinate of the oriented direction of reflected rays becomes positive, and they are sent back to air.

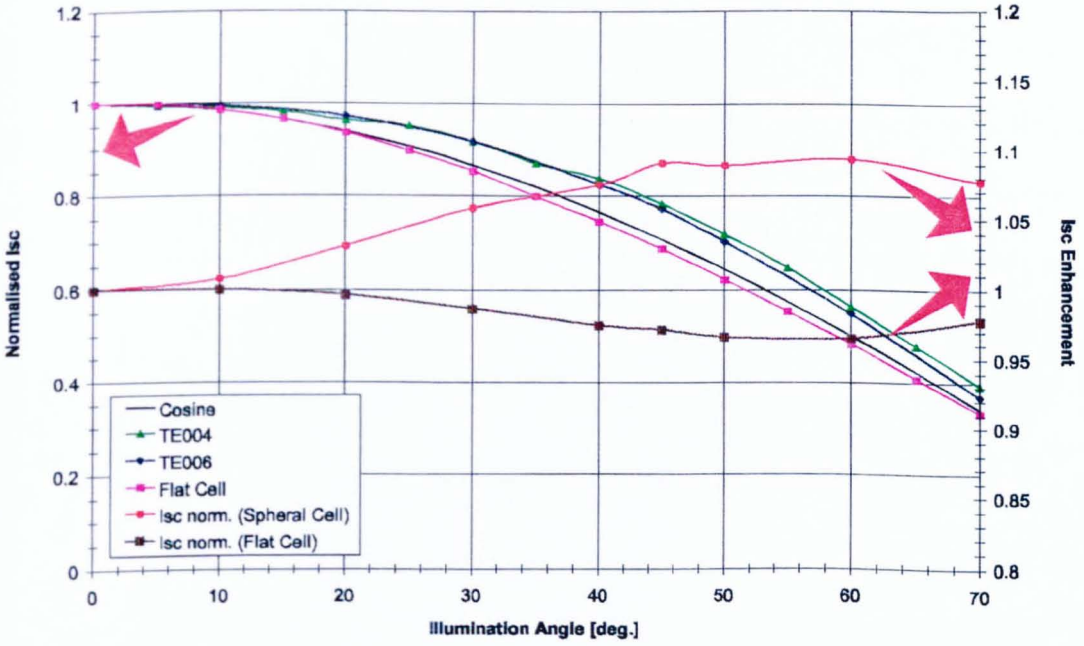

Fig. 5.18 - Comparison between normalised Isc vs. illumination angles of different devices. The normalised Isc enhancement of Spheral Solar™ Cells (ESTI code: TE004 and TE006) is also plotted.

5.2.2.3 Spectral Responsivity

The measured data of the spectral response against the illumination angle shown in Fig. 5.19, have been normalised to normal incidence in order to obtain the spectral response enhancement factor.

A 3d plot of this factor against the wavelength and the illumination angle is shown in Fig. 5.19. Also in this case it is confirmed that a 30 percent enhancement is present at low wavelengths (400-500 nm) and at illumination angles lower then 60 deg..

The data relative to the very high beam illumination angles (i.e. 70 - 80 deg.) are not plotted for clearness, because they are affected by a higher measurement error.

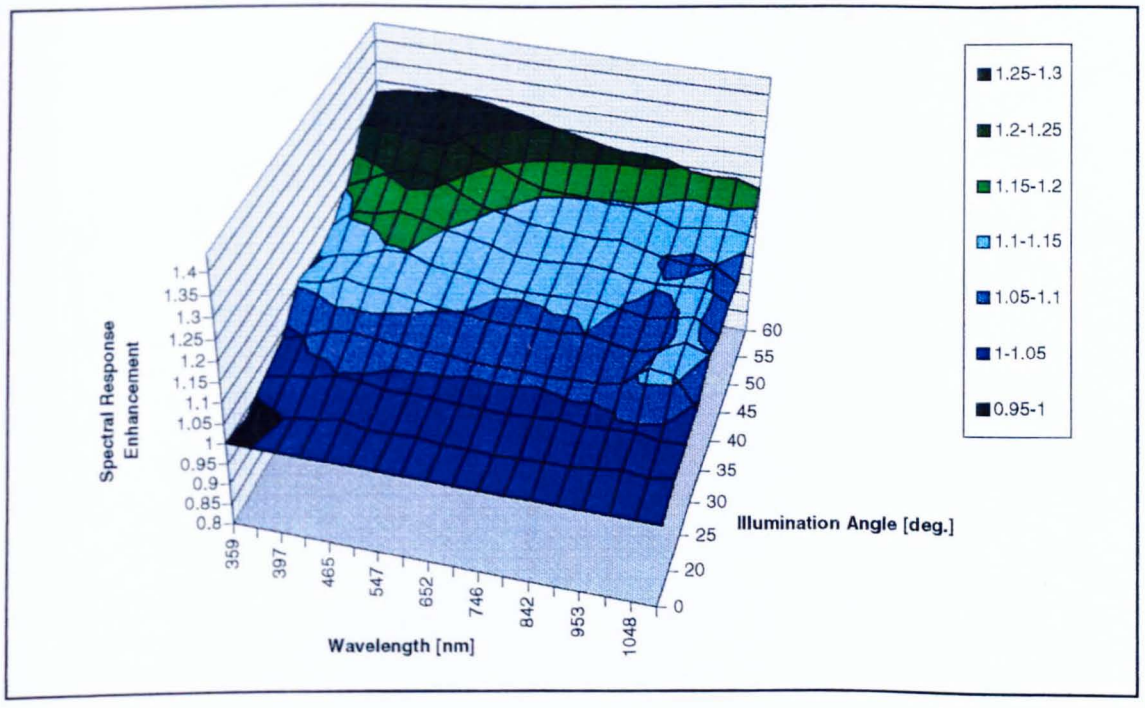

Fig. 5.19 - Spectral responsivity enhancement of a Spheral Solar™ Cell vs. illumination angle

SECTION 6

DESIGN OF AN OPTIMISED COVER FOR SPHERAL SOLAR™ CELLS

6.1. Conventional Module Encapsulation

The construction of modules has improved over the years to give modules that can be guaranteed to last for more than 20 years. All solar devices require transparent covers. In particular, terrestrial PV-devices require covers encapsulating against corrosion, environmental degradation and giving them structural rigidity. Furthermore, it is advantageous if the cover itself could also serve the purpose of reflectance reduction.

In this chapter, conventional cover structures as well as new types of light trapping covers, providing such a means of reducing surface reflection without requiring any surface modification of the cell, are discussed.

6.1.1 Typical Structures

A typical module design is shown in Fig. 6.1. The diagram shows the cross-sectional structure, which reveals the following elements or layers:

1. The *front cover*: usually a low iron (or iron-free) content glass (n ~ 1.5), to minimise the absorption of light.
2. The *encapsulant*: necessary to perform lamination; this is typically a polymer that is transparent, electrically insulating and thermoplastic. Normally EVA (ethylene-vinyl-acetate) is used.
3. The *solar cell.*
4. The *back cover*: normally one or more layers of EVA, PVF or Tedlar™ or other glass are employed. Sometimes a porous fibreglass sheet is added.

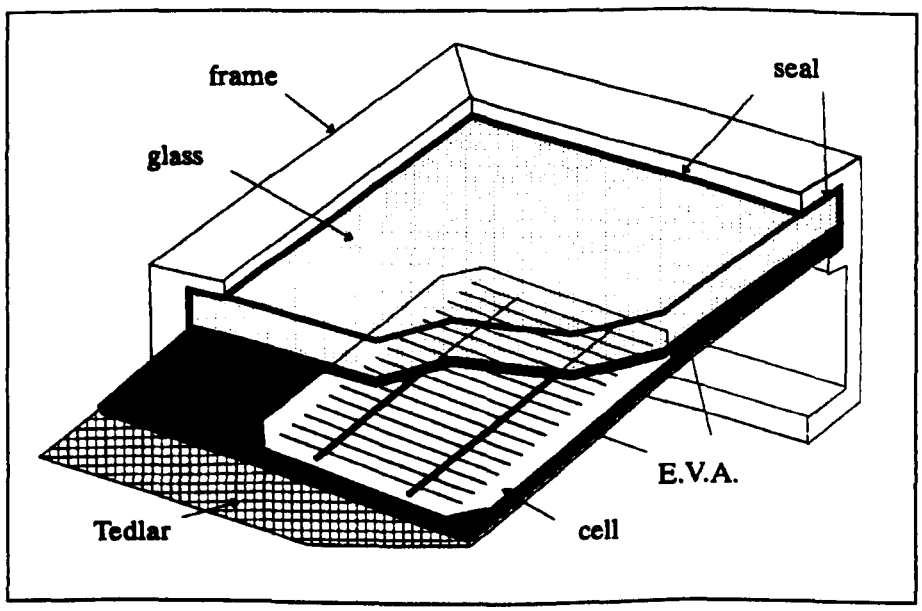

Fig. 6.1 - Module cross-section. Reproduced from [40]

All these layers are laminated together by the application of heat, vacuum and mechanical pressure. Apart from the mentioned layers, compounds are included to improve the adhesion among them. The layers are protected against fraying by means of a neoprene seal.
The module is then usually mounted in an aluminium frame and finally, metal terminals are placed at the output and protected against the weather by a watertight box.
Recently, it has been observed [41, 42] that there is some tendency for EVA to become coloured (yellowing effect) and lose its transparency, due to the degradation of additives used to absorb ultraviolet radiation. The phenomenon becomes serious only when the modules are used in conditions of high temperature and illumination, for example in combination with optical concentrators.

6.1.2 Optical Losses

Optical losses are usually subdivided into two main categories, according to their origin.

Fresnel Losses

These losses are due to the change in refractive index and therefore arise in all refractive elements. Their value depends on the values of the refractive index on each side of the interface between two media and on the angle of incidence of the radiation. At the external surface of a cover-glass for example, the refractive index changes between 1 (in air) and 1.5 (in glass). Fresnel losses for normal incidence are then of the order of 4 % (according to Fresnel's formulas for reflection). For angles of incidence less then 50 deg. to the normal they are around 5 %. Since, usually, there is at least an additional interface to take into consideration before the solar cell (for example the interface cover-encapsulant and/or encapsulant/AR-coating/cell) these losses amount to at least 8 - 10 % as results from the calculation with the transmission matrix method.

Absorption Losses

These are due to absorption of light in optical materials. To avoid them, the material has to be chosen carefully and the distance travelled by the rays within the material has to be kept to a minimum. Absorption losses less than 1 % can be achieved by an accurate choice of the materials.

6.1.3 A Light Trapping Cover

High efficiency solar cells require a minimisation of the optical losses. This is usually achieved by using AR-coatings. For crystalline solar cells, further reflectance reduction can be achieved by texturing the front surface with pyramids, grooves, or inverted pyramids, typically by an anisotropic etch process [43, 44]. In a textured surface cell, light which is reflected on initial incidence is redirected to a second surface. Thus the light has two

opportunities to be absorbed, and the total reflectance from both encounters is equal to the square of the single bounce reflectivity. However, texturing has certain disadvantages:

* it adds a step to the processing sequence;
* it increases the junction area potentially reducing the open-circuit voltage;
* it may be difficult or even impossible to accomplish on more advanced materials such as thin-film solar cells, polycrystalline materials, etc..

Recently, studies have been performed [45, 46] which resulted in the design of an optimised light-trapping cover-glass for flat devices. It has been demonstrated that encapsulants and covers can be geometrically configured to trap incident light, and hence decrease the effective reflection at the cover/cell (encapsulant/cell) interface, without texturing the cell itself.

Theoretical considerations of light trapping [47, 48] show that a material of refractive index n can be configured so that the average incident ray intersects the rear surface of the cover (i.e. the front surface of the cell) n^2 times. For a typical solar cell cover-glass with refractive index ~ 1.5, this factor is over two. This can be achieved by a randomly structured cover and is the theoretical maximum for omnidirectional light.

However, while the average ray may make two passes, for a randomly structured cover-glass nearly 50 % of the reflected light is lost after the first pass. It is then possible to do better than this for normally incident light, by using a geometrically structured cover designed to maximise the total internal reflection of the reflected light.

6.2. Spheral Power ™ Modules

Photovoltaic modules made with Spheral Solar™ Cells, known as Spheral Power™ Modules (shown in Fig. 6.2), have several unique features due to the structure of the cells themselves. Aluminium, for instance, is chosen for low cost and ease of manufacturing, but it presents a challenge in two aspects of module design.

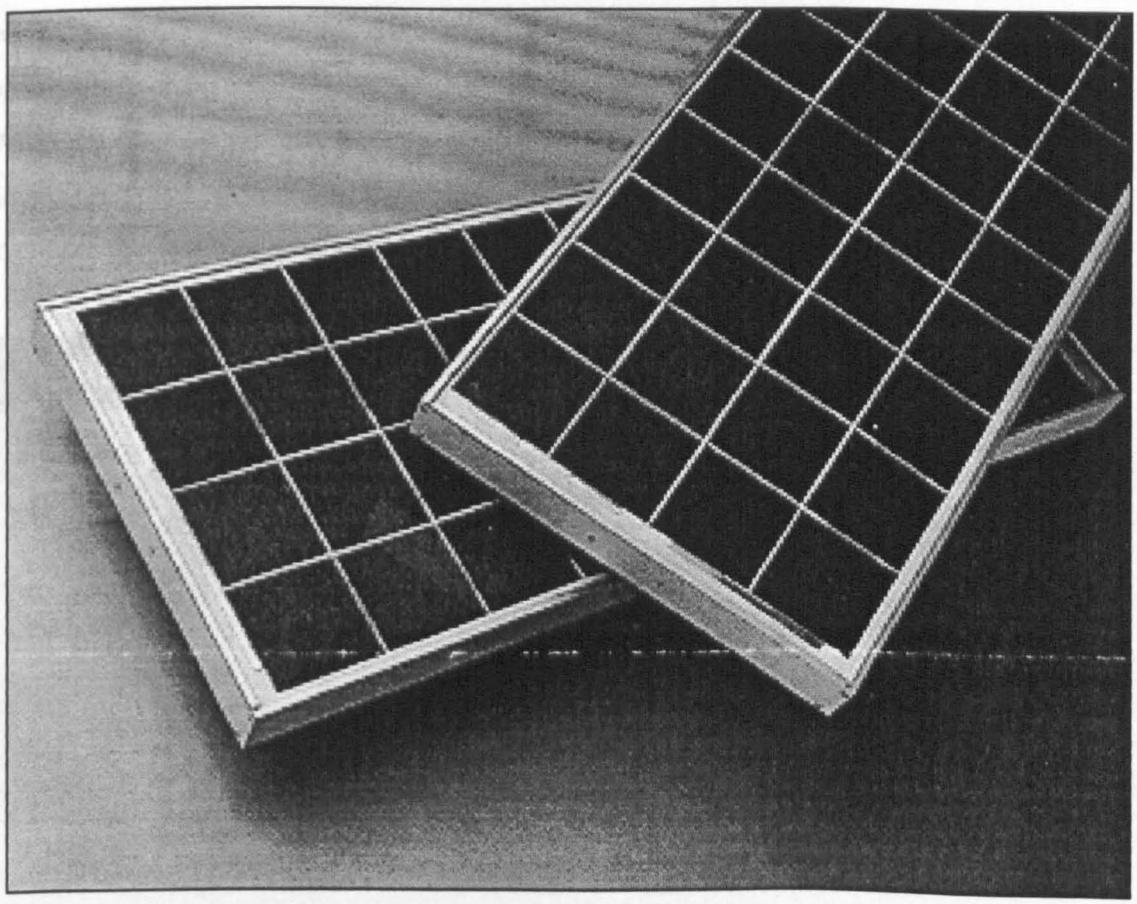

Fig. 6.2 - Spheral Power™ Module

The first is the interconnection between the series-connected cells, which requires the front foil of one cell to be connected to the back foil of the adjacent cell.

The second is making the transition from the aluminium conductors within the module to the copper terminals in the custom designed junction box. Copper terminals are necessary to allow copper wiring to be used when wiring modules in a system, but making the joint between the copper and aluminium had to be engineered to eliminate galvanic corrosion.

6.2.1 Cell Interconnection

Because the Spheral Solar™ Cell's positive and negative conductors are both aluminium, this offers the opportunity for simplifying the method for interconnecting the cells. Ultrasonic welding of two components of the same material is a proven technique for long-life connections. Ultrasonic welding is a process that has no consumables and it is readily automated for low-cost production.

The system developed for the Spheral Power™ Modules is a simple lap joint. The front foil is cut with a small tab extending out one side, and the back foil has a corresponding tab at the opposite side of the cell.

When the cells are assembled into a circuit for the module, the front foil tab of one cell is placed over the back foil tab of the adjacent cell and the two tabs are ultrasonically welded together. This is shown schematically in Fig. 6.3.

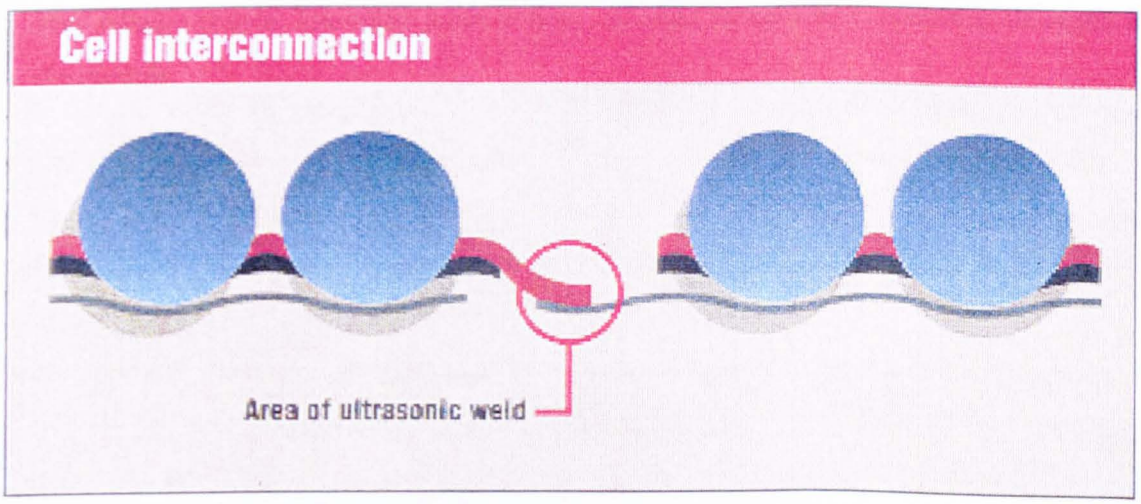

Fig. 6.3 - Cell Interconnections

This system has potential for higher reliability than conventional interconnections that use solder to join dissimilar metals, such as tin-plated copper straps to silver metalisation.

The welded aluminium has at least four advantages:

1. no coefficient of thermal expansion mismatch;
2. no dissimilar metals to cause galvanic corrosion;
3. no additional pieces used in module assembly, making it much easier to automate;
4. no solder used, no cleaning required.

Additionally, without the silver and solder in the laminate, the potential degradation modes that can arise through interactions of these metals with the encapsulant are eliminated.

6.2.2 Aluminium-to-Copper Transition and Junction Box

While the use of aluminium conductors has advantages inside the laminate, it has one potential disadvantage at the junction box. A photovoltaic system generally is wired using standard copper wires, so at some point a transition from aluminium to copper must be made. However, the incompatibility of aluminium and copper in typical connections is well documented.

The best method for overcoming this incompatibility is to use copper clad aluminium. In cladding technology the two metals are intimately joined with temperature and pressure, with the resultant bond eliminating the problems inherent in conventional joints.

The Spheral Power™ Module incorporates a short section of copper clad aluminium between the aluminium strap exiting the laminate and the tin-plated copper terminals in the junction box.

The clad section is welded to both the aluminium ribbon and the copper terminal, forming a very reliable system. The entire junction box, including the terminals, is custom-designed for the module.

6.3. Optimisation of the Cell Superstrate

As illustrated above, present Spheral Power™ Modules are encapsulated with proven industry standard materials: tempered glass super-strate, EVA encapsulant, Tedlar® laminate backskin and extruded aluminium frame.

The features that are unique in this initial design are the cell interconnection scheme and the junction box but, until now, only very few efforts have been undertaken to find an alternative front cover exploiting the two main features of Spheral Solar™ Cells: *their uneven surface* and *their flexibility*.

To achieve the design optimisation, the performance of several reflectance-reducing covers of different materials and structures have been investigated, by using the code *WinTrace*. The performance of the covers analysed has been calculated both for normal incident light and off-normal incidence.

6.3.1 Choice of an Optimised Cover Material

In order to allow an optimised light coupling as well as easy manufacturing of the cover, a preliminary analysis of suitable materials available on the PV-market has been undertaken.

Typical cell covers are made either of iron-free glass or quartz, in the case of rigid modules, or of Tedlar® (polyvinyl fluoride) or Tefzel® (tetrafluoroethylene), in the case of flexible ones.

Among these materials, the rigid ones have not been taken into consideration both because they do not exploit the flexibility of the cells and because quite delicate and expensive embossing processes are necessary for producing on their surface micro-structures focusing light onto the spheres.

In the case of Tedlar®, the experience in module testing and qualification acquired at the European Solar Test Installation in the last twenty years, suggested that even though it is durable and chemically inert, it does not show enough permeability to humidity and its optical properties are not adequate for being employed for cell front covers. Furthermore, a Tedlar® cover would necessarily need to be applied on the top of an additional encapsulant material. In fact, since Tedlar® has a very high melting temperature ($T > 200°C$) it does not melt during lamination ($T \sim 180°C$), and therefore it does not attach perfectly to the cell front surface.

Thus, Tefzel® was found to be the best choice for this application, both for its resistance to atmospheric agents and because it can be easily laminated to the cell and even structured.

Tefzel® fluoropolymers are melt-processable thermoplastics of the family of fluorine-based products of Du Pont. A variety of natural and reinforced compositions, listed in Table 6.1, is available permitting the selection of resins based on specific applications or processing needs.

Table 6.1 - Tefzel® Fluoropolymers Commercially Available from Du Pont

TEFZEL 200	General purpose, moulding and extrusion resin.
TEFZEL 280	A higher molecular weight (lower melt flow number) resin for applications requiring extra resistance to unusual environmental extremes, to stresses in processing such as lined chemical equipment, for parts with moulded-in inserts, thick sections, or where in contact with solvents that affect stress crack resistance.
TEFZEL 210	A lower molecular weight (higher melt flow number) resin designed for high-speed wire extrusion in very thin sections, where high-speed processing is required and physical property demands are minimal.
TEFZEL HT-2004	A 25 % glass-filled composition for use where maximum compressive properties are required and the use of a glass filler is acceptable.
TEFZEL HT-2000	Compacted fluoropolymer powder with properties similar to TEFZEL 200.
TEFZEL HT-2010	Compacted fluoropolymer powder with properties similar to TEFZEL 280.
Colour Concentrates	Standard colours are available as concentrates for incorporation by the processor.

Tefzel® can be best described as a rugged thermoplastic with an outstanding balance of properties.

Mechanically, it is very tough and has medium stiffness (1.170 MPa, 170.000 psi), impact and abrasion resistance.

Flexibility depends upon the grade used, with Tefzel® 280 being higher than the other grades.

The glass reinforced compound (Tefzel® HT-2004) has higher tensile strength (83 MPa, 12.000 psi), stiffness (6.555 Mpa, 950.000 psi), and creep resistance than unfilled grades. However, it is still tough and impact resistant.

Tefzel® is typically considered to have a no load continuous use temperature of 150 °C.

In certain specific applications, Tefzel® can have an upper service temperature in excess of 230 °C.

Tefzel® is weather resistant, inert to most chemicals, hydrolitically stable as well as very resistant to long-term outdoor exposures, showing only few detrimental effects. It has

substantially better resistance to radiation then Teflon® but is not immune to damage by long-term exposure to gamma radiation, especially at elevated temperatures.

Electrically, Tefzel® is an excellent low-loss dielectric, with a uniformity of electrical properties not normally found with other thermoplastics.

The optical properties of Tefzel® are also excellent. The index of refraction of Tefzel® is 1.407 and Fig. 6.4 shows the data of the Transmittance vs. Wavelenght of a cured Tefzel® film [*Du Pont Italiana*, private comunications], normalised to 0.025 mm..

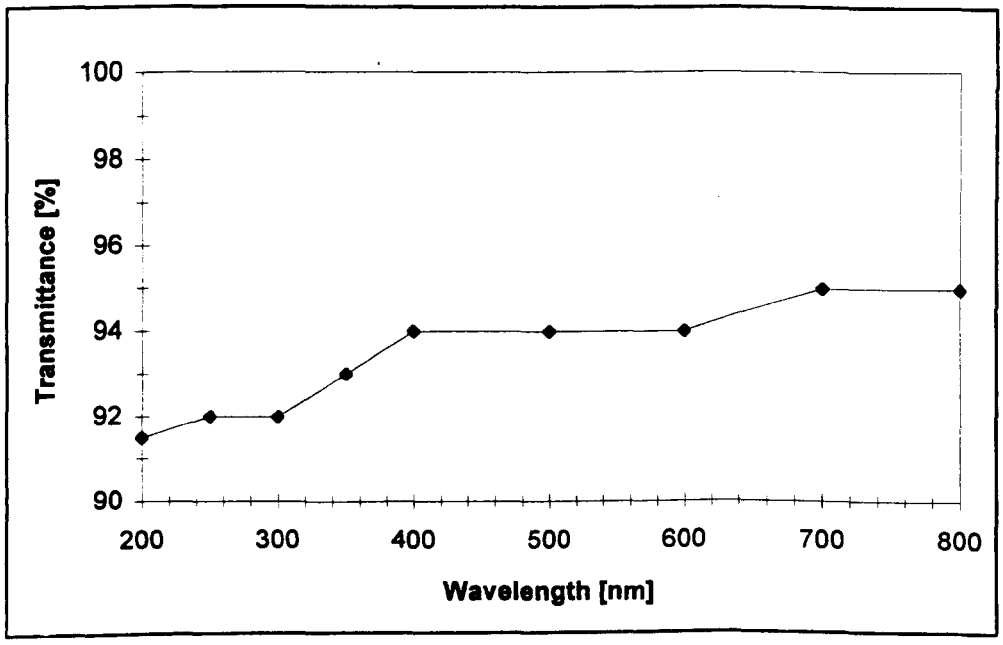

Fig. 6.4 - Transmittance of a cured Tefzel® film normalised to 0.025 mm.

Tefzel® films are also available in a wide range of thickness, for electrical, chemical and other different applications. The three main types of films are:

1. type LZ: general purpose film;
2. type CLZ: treated one side for improved cementability;
3. type CLZ-20: treated both sides for improved cementability.

The optimised type for being used as an encapsulant is the CLZ, which would be suited for being attached directly to the cell, without adding any EVA intermediate encapsulant layer.

6.3.2 Suggested Tefzel® Assembling Techniques

Among the several different techniques which can be used for assembling Tefzel® to the solar cell, the most interesting are spin welding, ultrasonic welding and melt bonding.

Spin Welding

Spin welding is an efficient assembling technique for joining circular surfaces of similar materials. The matching surfaces are rotated at high speed relative to each other (one surface

is fixed) and then brought into contact. *Frictional heat melts the interface and when motion is* stopped, the weld is allowed to solidify under pressure.

Ultrasonic Welding

The ultrasonic welding of Tefzel® has been demonstrated with weld strengths up to 80 % of the strength of the base resin. The success of this technique depends on experimentally determined welding parameters of contact time and pressure. Typical welding conditions are 25 psi contact pressure and one- or two-second cycle time.

Melt Bonding

Tefzel® responds well to melt bonding. It has been successfully bonded to untreated aluminium, steel and copper with peel strengths in excess of 20 lb/in.

6.3.3 Optimised Cover Structure

An optimised coupling of light directly into the spheres would result in an "optical" reduction of the main efficiency limitation of Spheral Solar™ Cells (from an optical point view), that is the low sphere packing density. In previous studies carried out by TI [15], polymer front covers were already considered, which being laminated to the cell had the characteristic of conforming to the cell shape, thus increasing the number of rays which, once refracted by the cover, could be reflected back from the aluminium substrate towards the silicon spheres.

On the other hand, the idea originating the present study, was not only to have a polymer cover which could be laminated to the cell, but also to texture this cover with a precise structure which could minimise the reflectance losses either by focusing light directly onto the silicon spheres or by increasing the effectiveness of the indirect trapping mechanisms [17] present in the spherical design.

For this reason, is it been fundamental to acquire exact knowledge of the optics of the devices, as illustrated in the previous Sections.

6.3.3.1 Flat Cover

Under a flat cover of index of refraction $n_1 = 1.5$, with the back surface conformed to the cell shape, as shown in Fig. 6.5, the condition for total internal reflection (TIR), to be fulfilled by those rays reflected by the cell, would be:

$$\alpha_{int.refl} > \Phi_{TIR} = \sin^{-1}(n_0/n_1) \qquad \text{Eq. 6. 1}$$

where $n_0 = 1$ is the index of refraction of air. Φ_{TIR} results to be about 45 deg..

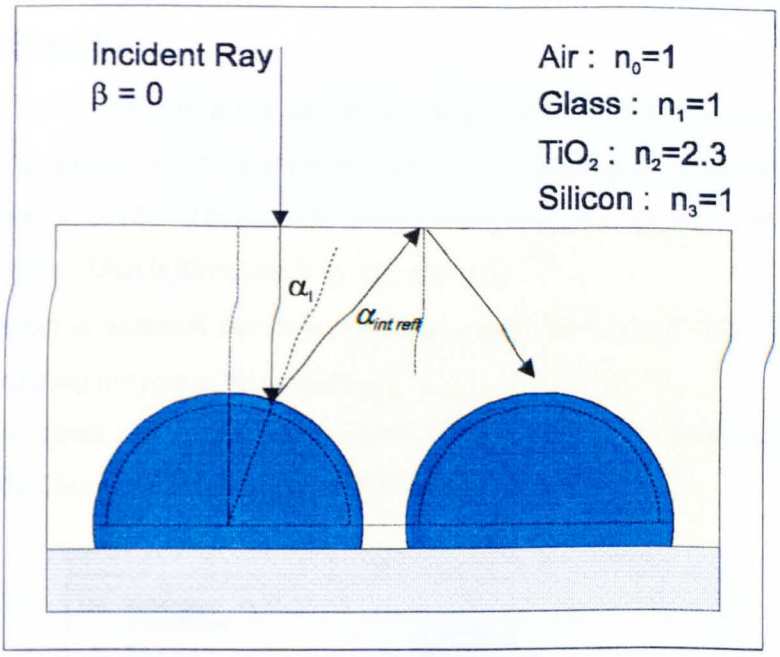

Fig. 6.5 - Scheme of a flat cover

The angle of internal reflection $\alpha_{int.refl}$ can be expressed as $\alpha_{int.refl} = 2 \cdot \alpha_i$, where the angle of incidence on the sphere α_i is a function of the elevation θ of the point of incidence on the sphere, and of the beam inclination angle β:

$$\alpha_i = \theta - \beta \qquad \text{Eq. 6. 2}$$

Thus, for a normal incident beam, being $\beta = 0$, the condition for TIR becomes:

$$\alpha_{int.refl} = 2 \cdot \alpha_i = 2(\theta - \beta) > \Phi_{TIR} = 45 \text{ deg.} \Rightarrow \alpha_i = \theta > \mathbf{22.5\ deg.} \qquad \text{Eq. 6. 3}$$

This means that the reflected component of all those rays impinging on the sphere surface in a point of elevation greater then 22.5 deg. will have at least a second chance of being absorbed by the cell.

For any other incidence ($\beta \neq 0$), the condition for TIR is limited. For example for $\beta = 20$ deg., the condition for TIR becomes: $\theta > 42.5$ deg.

The condition for TIR becomes impossible (is never fulfilled) when $\beta = 67.5$ deg. In fact, in this case $\theta > 90$ deg.

6.3.3.2 Spherical Cover

The approach to the design of a focusing cover, consisted of considering first a spherical lens, concentric to the spheres, which could enlarge the optical dimensions of the spheres to the limit of touching spheres, as shown in Fig. 6.6. Such a cover would produce a 40 % reduction of the aluminium portion which is illuminated by primary rays.

This lensing effect is achieved assuming an encapsulant thickness of only 30 μm, which, in practice, is absolutely too low to be processed.

The map of the direct cell with a planar cover and the one with a spherical focusing lens, simulated by *WinTrace*, are given in Fig. 6.7(a) and (b).

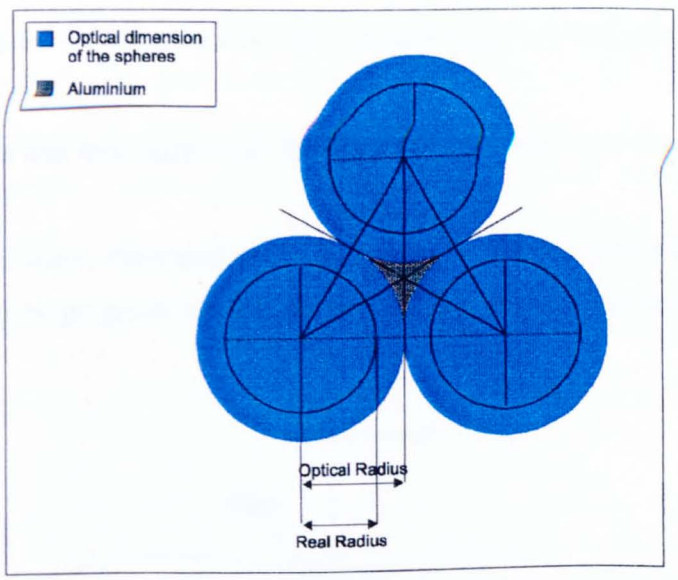

Fig. 6.6 - Extension of the optical dimension of the spheres under a concentric spherical lens of 30 μm thickness.

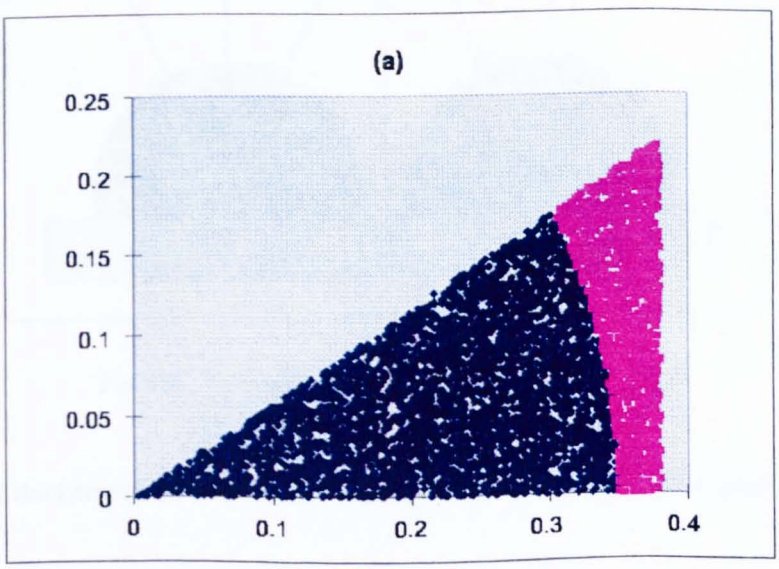

Fig. 6.7 (a) - Map of the direct cell with a planar cover

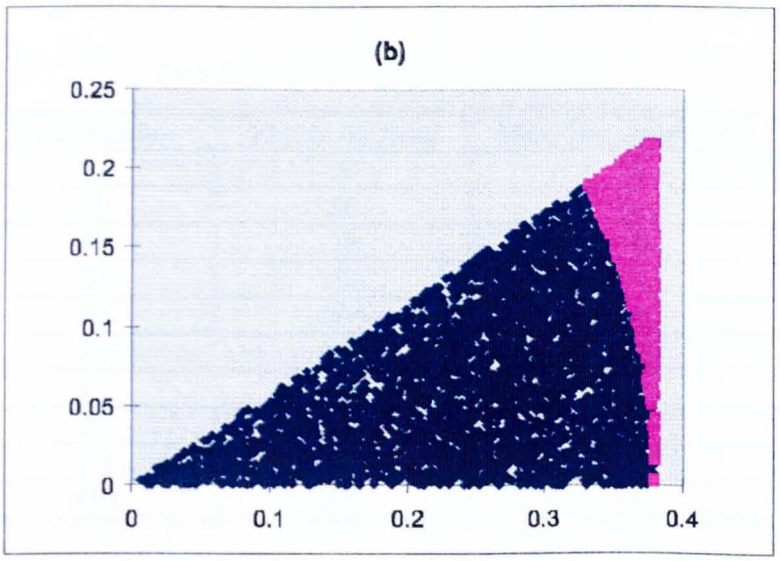

Fig. 6.7 -(b) Map of the same region covered by a spherical lens of 30 μm.

A set of simulations was then carried out, in which the cover thickness was increased from 30 μm up to 2 mm.

The simulated cover shape, illustrated in Fig. 6.8, presents a cusp, which allows the maximum angle of incidence to be progressively reduced from 90 deg. to 9 deg. at a thickness of 2 mm.

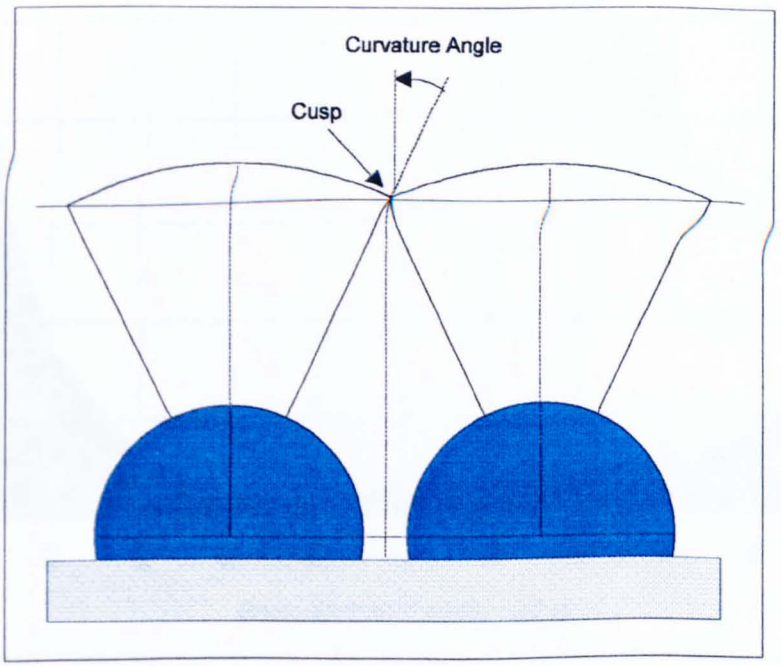

Fig. 6.8 - Cross-section of the structure; sizes not to scale.

The simulated thicknesses and the corresponding maximum angles of incidence are listed in Table 6.1.

Table 6.2 - Simulated geometrical parameters

Combination	*Thickness [μm]*	*Max. Inc. Angle [deg.]*
#1	30	90
#2	50	61
#3	70	56
#4	100	51
#5	200	44
#6	300	36
#7	400	30
#8	500	24
#9	1000	15
#10	2000	9

The reduction of the maximum possible angle of incidence achieved by the cover thickness increase, not only reduces the optical losses, but also improves the light coupling on the most active parts of the spheres, the central ring.

Fig. 6.8 gives the variation of the optical losses of the cell, simulated assuming the different combinations of Table 6.2.

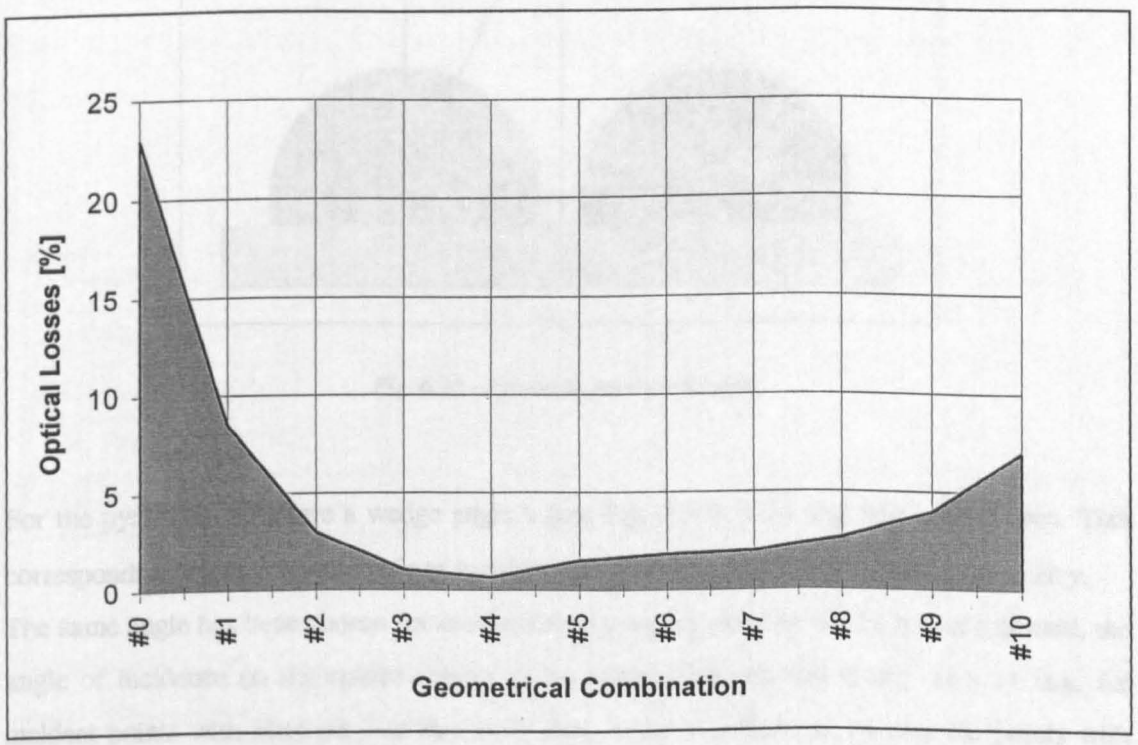

Fig. 6.8 - Optical losses of the cell calculated for different geometrical combinations

The optical losses depend both on the focusing effectiveness of the encapsulant, maximum over 100 μm, and on the indirect trapping of those rays undergoing their primary reflection on the aluminium. These rays can be either directly redirected to the cell or reflected back from the

cover and then trapped by the spheres, and, in this case, total internal reflections are preferred for minimising the optical losses. By increasing the cover thickness, the flatness of the cover also increases, and for angles of incidence greater then 22.5 deg. corresponding to a thickness of about 500 μm, the condition for TIR is never fulfilled. This explains the increase of the optical losses with the increase of the structure flatness.

6.3.3.3 Alternative Structures

Two alternatives to the proposed cover structures, showing equivalent lensing-power, are:

1. Pyramids (Fig. 6.10);
2. Truncated Pyramids (Fig. 6.10 - b).

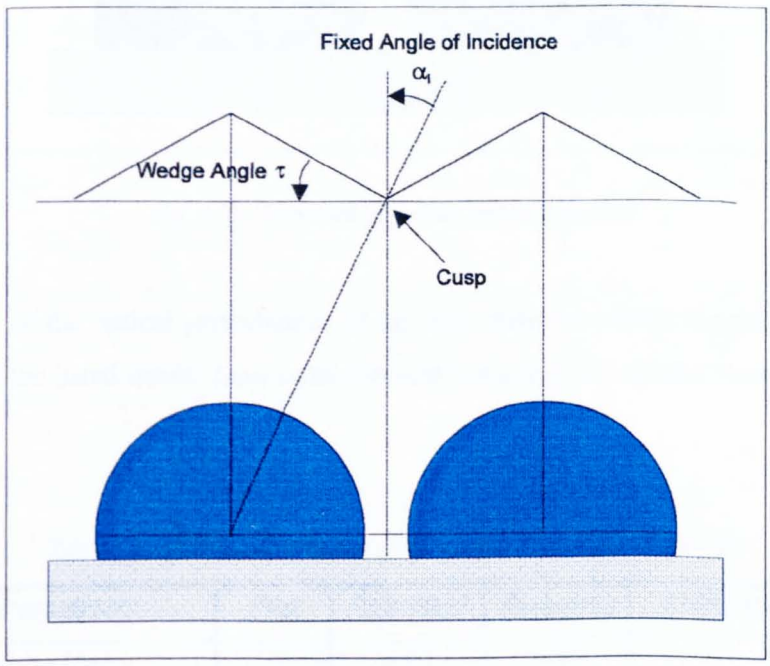

Fig. 6.10 - Pyramids, sizes not to scale

For the pyramidal structure a wedge angle τ (see Fig. 6.10) of 24 deg. has been chosen. This corresponds to the maximum angle of incidence at the cusp point, in the spherical geometry.
The same angle has been chosen for the truncated pyramid (see Fig. 6.11), but in this case, the angle of incidence on the sphere results to be randomised between 0 deg. and 24 deg. for incident points with abscissa less then 0.15 mm, while it is fixed at 24 deg. for points with abscissa in the range 0.15 - 0.38 mm.

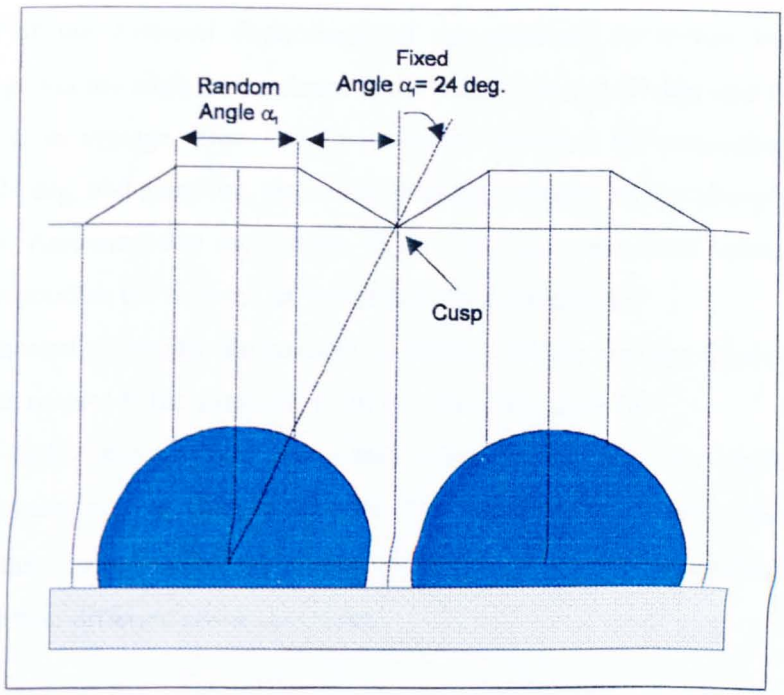

Fig. 6.11- Truncated pyramids, sizes not to scale

A comparison of the optical performance of the four different covers considered, is given in Table 6.3. All the listed results have been obtained assuming an incident beam wavelength of 632 nm (red).

Table 6.3 - Optical performance of the analysed structures at 632 nm

Simulated Parameters	***Flat***	***Spherical***	***Pyramids***	***Truncated Pyramids***
Focusing Ratio [%]	77	~ 97	~ 97	~ 97
Ext. Reflectance [%]	10.5	7.6	12.5	9.8
Tot. Reflectance [%]	~ 15	11	13	11.8
Optical Enhancement [%]	-	**26.6**	**13**	**21.3**

The spherical cover considered in this table is the one with the geometrical specifications named in the previous paragraph: Combination #8.

From the simulation performed, the *Focusing Ratios* of the three structured covers result to be almost the same, at least within the range of the simulation error. This means that the number of primary rays impinging on the aluminium substrate can be minimised (almost at the same level) both by a spherical and by a pyramidal structure.

The value of the *External Reflectance* of the spherical cover has been evaluated by randomising over the angle of incidence in the range 0 deg. to 24 deg. and therefore has to be considered as an average value. For the pyramidal structure, the external angle of incidence is fixed at 24 deg. and therefore, the direction of the refracted rays is always oriented towards the spheres. Assuming this inclination, in fact, the ray component refracted through the cover never touches the aluminium substrate among the spheres.

For the truncated pyramids, the concept is similar, but the average *External Reflectance* is reduced with respect to the pyramids from 12.5 % to about 10 %.

The *Total Reflectance*, which takes into consideration also the reflectance from the aluminium substrate, is calculated with the Transmission Matrix Method. It can be considered the absolute reference parameter which allows the comparison of the lensing-power of the four different cover structures.

Examples of the described alternative structures on glass and plastic are illustrated in Fig. 6. 12, Fig. 6. 13, Fig. 6. 14 and Fig. 6. 15.

These photographs are taken from different applications and they do not represent prototypes expressly made for this work. Even so, they are very interesting for demonstrating the manufacturability of the proposed structures.

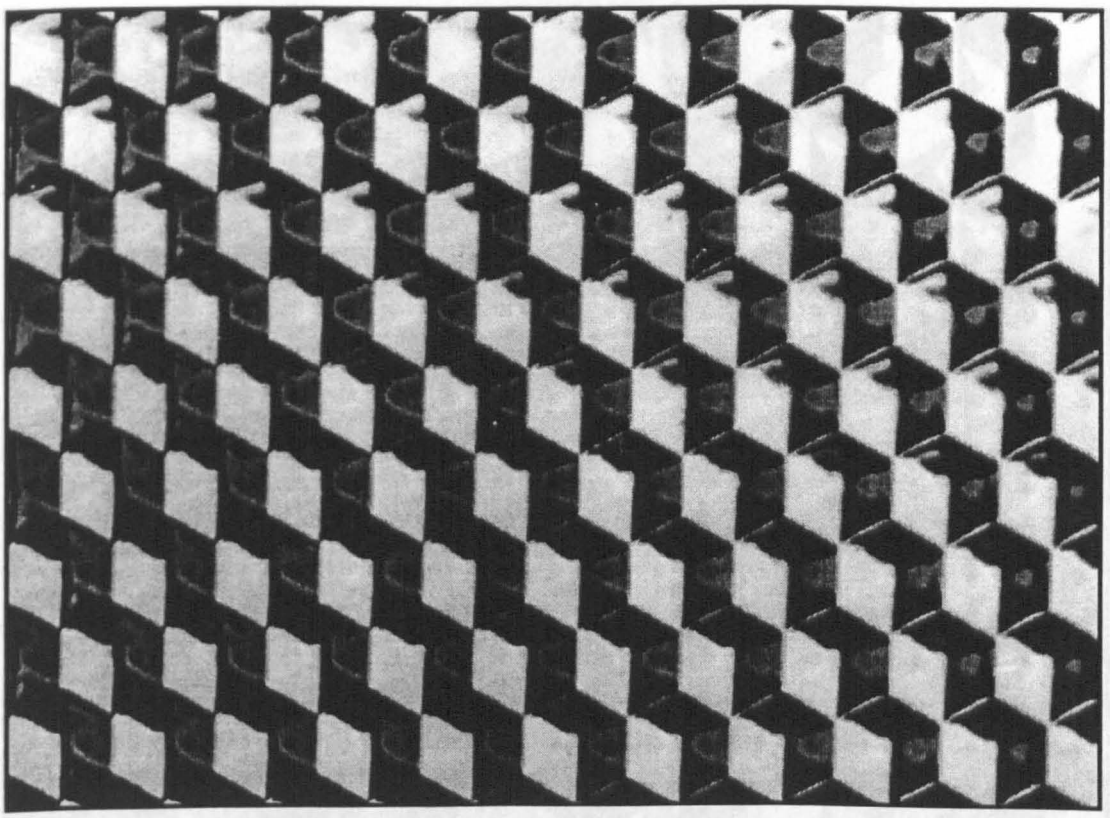

Fig. 6. 12 - Structure with pyramids on glass

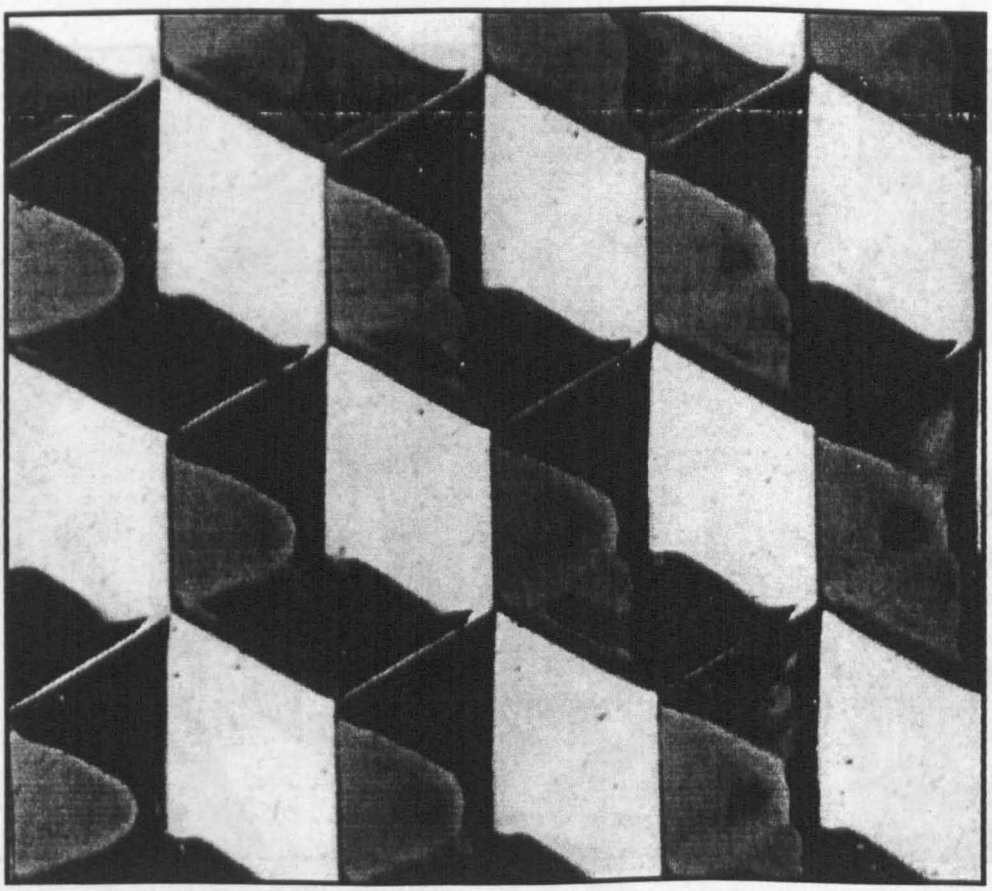

Fig. 6. 13 - Close-up of the pyramid structure

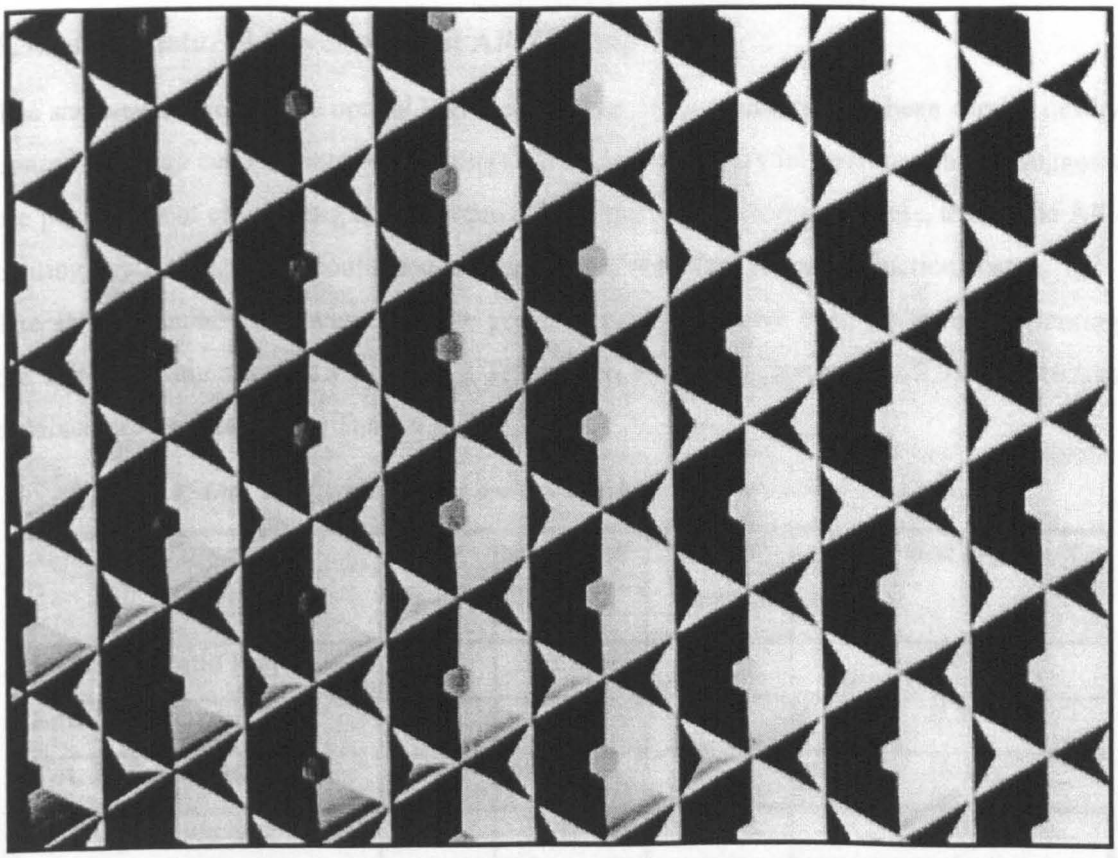

Fig. 6. 14 - Structure with truncated pyramids on plastic

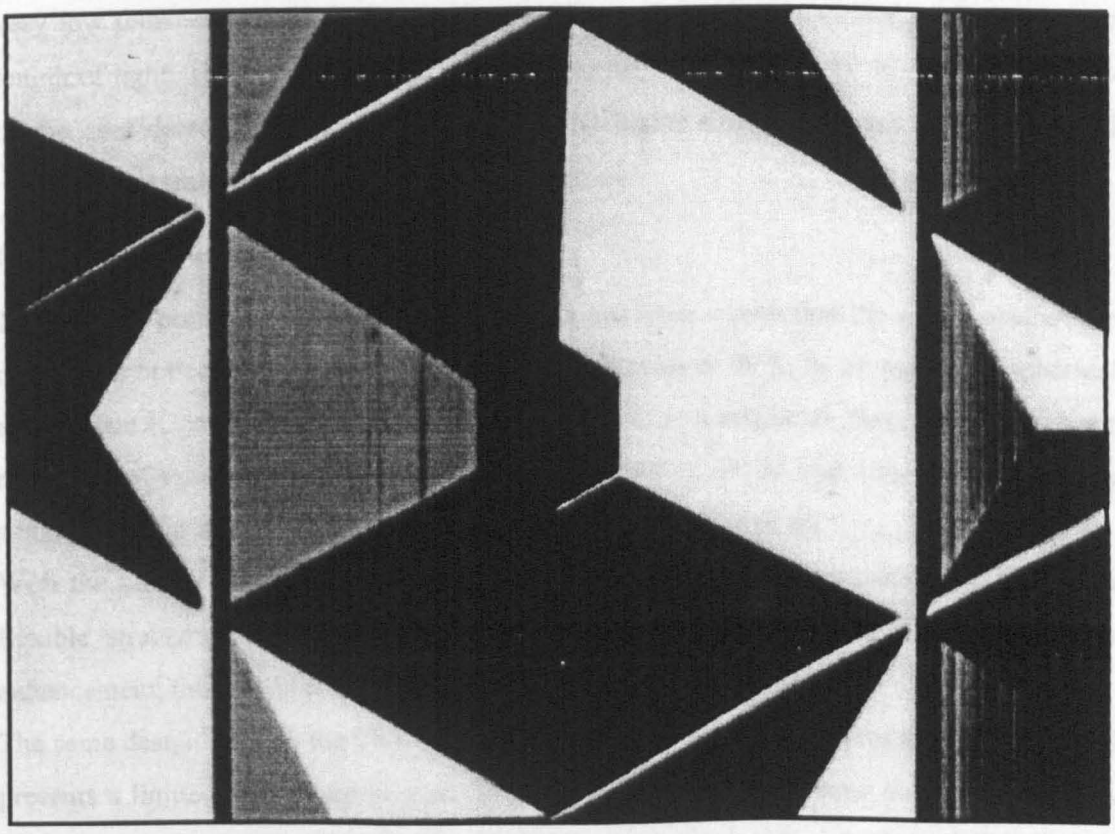

Fig. 6. 15 - Close-up of one truncated pyramid

6.3.3.4 Structured Cover without AR-Coating

The same evaluation of the optical losses of the four cover structures has been carried out by assuming a bare cell (without AR-coating). This analysis is very interesting, since it suggests the possibility of eliminating an important step of the manufacturing process, that is the AR-coating deposition, which could lead to a significant reduction of the production costs.

The same calculations discussed in the previous paragraph have been performed assuming the following interfaces: air ($n_0 = 1$) / Tefzel® ($n_1 = 1.6$) / Silicon ($n_2 = 3.7$). The results obtained are summarised in Table 6.4.

Table 6.4 - Optical performance of the analysed structures at 632 nm, assuming no AR-coating

Simulated Parameters	*Flat*	*Spherical*	*Pyramids*	*Truncated Pyramids*
Focusing Ratio [%]	77	~ 97	~ 97	~ 97
Ext. Reflectance [%]	10.5	7.6	12.5	9.8
Tot. Reflectance [%]	~ 20	17	19.3	18.1
Optical Enhancement [%]	-	**15**	**3.5**	**9.5**

The *Focusing Ratio* has been considered independent from the AR-coating since, due to its very low thickness, the optical path of light in the coating is comparable to the coherence length of light. The high percentage of Total Internal Reflections (> 80 %), obtained thanks to the considered cover structures, balances the higher Fresnel's losses, allowing a still reasonable overall reflectance for the spherical cover.

6.3.3.5 Concluding Remarks

Through the previous ray-tracing simulations it has been shown that the active area of the cell can be optically increased from 77 % to a maximum of 99 % by an optimised spherical encapsulant (Combination #4). This would correspond to a maximum theoretical reflectance reduction of more than 30 %. Since combination #4 is not reproducible in practice, the suggested cover structure was taken to be the one of Combination #8.

With the chosen geometrical parameters the feasible optical enhancement produced by a flexible structured Tefzel® cover is around 27 %. Translated into a module efficiency enhancement, this would theoretically raise it from 8 % up to about 11 %.

The same design without the TiO_2 AR-coating layer, produces higher Fresnel losses, but still presents a limited reflectance because of the very high number of total internal reflections. With this configuration, a 15 % enhancement is still achievable, which could result in a module efficiency around 9.5 %.

Discussion and Conclusions

Spheral Solar™ Cells are a patented PV-technology originated by Texas Instruments and developed there to the pilot line stage. The technology is now owned by Ontario Hydro Technologies (Ontario-Canada) and since early 1996 many efforts have been undertaken in order to move the technology towards commercial production.
Spheral Solar™ Cells represent now an extremely promising approach for a significant production cost reduction. They comprise more than 17,000 purified silicon "beads" bonded into aluminium. Spheral Solar™ Cells are therefore quite flexible and durable, unlike other crystalline silicon devices.

A great deal of work was done at TI on the production technology for optimum electrical characteristics. However, little effort has been devoted to studying the optical characteristics and optimising the light gathering of the cells, so the concept needed an optical optimisation of cell/module efficiency.
Today, conversion efficiencies of about 9% have been achieved, but on cells with flexible encapsulants the efficiency should improve to >11%. This is due to the unique light-gathering properties of the technology resulting from the uneven surface formed by the closely spaced spheres.

Measurements at ESTI have shown that light-gathering could be greatly enhanced by conformable optical AR-coatings/encapsulants. This represented the very beginning of the present work, finalised to acquire a deep understanding of the optics of these spheral devices in order to be able to design a reflectance-reducing cover.

After a preliminary wide search in literature seeking a suitable ray-tracing programme which with minor modifications could model the spherical geometry of the devices, the decision was taken to develop a new optical code *WinTrace* by employing both ray-tracing and Monte Carlo techniques. The code *WinTrace*, written in Visual Basic 4 Pro. (object oriented language), allows the simulation of the interaction of light rays with a user-defined number of spherical (and flat when necessary) layers of specified materials.
The most complicated tasks of the programming were the implementation of the spherical geometry in S^3, consisting of continuous transformations between Polar and Cartesian co-ordinate systems, as well as the study and the optimisation of the randomisation procedures. Furthermore, a very delicate part of the theoretical work was the choice and definition of the cell areas to be simulated in order to reduce the calculations (run time) while maintaining the

geometrical symmetries of the devices. *Analytical considerations, preliminary to the* programming, were of fundamental importance to define the angular dependencies of these devices and to find the specific illumination angles to be simulated.

The choice of the statistical significant number of rays to be simulated, dictated by the Monte Carlo approach, was also discussed and supported by statistical considerations of different sets of simulation results.

In parallel with the development of the simulation tool necessary to model the unique geometry of Spheral Solar™ Cells, experimental activities were carried out.

A complete set of electrical performance measurements was carried out by using the facilities already available at the ESTI laboratories. Non-standard angular measurements (Isc, Voc, Spectral Responsivity vs. illumination angle) were also performed by introducing minor changes to the existing experimental set-up.

Two experimental facilities were expressly designed and constructed for this study.
The first is the Spectrophotometer Lambda 19, already existing in version Lambda 9 but only used for transmission measurements. This instrument was upgraded and equipped on purpose with an integrating sphere, in order to perform reflectance measurements on PV-devices.
The second is the multi-laser scan facility *ESTIScan*. This facility did not exist at the time this study was undertaken and has been entirely designed and realised in the frame of this research work. It consists of a double scanning system (a high precision/resolution one and a large area one) in which any kind of cell up to module size can be measured.
Besides representing a very important tool for verifying light trapping in PV-devices, it can be employed also in other fields of interest, such as for the measurement of spatially resolved spectral response, for the exact determination of cell dimensions etc.

The consolidation of the experimental methods was also undertaken by investigating the reliability of instruments and experimental results.
The photometrical measurements were verified by comparing identical results obtained in four different laboratories on the same samples. For the *ESTIScan* facility, the major point was the determination of the upper limit of the system resolution. This was deduced by identifying grain boundaries on polycrystalline cells, and the conclusion was that the spatial resolution is around 20 μm. Such a low resolution combined with the 1 μm step size (minimum) of the high precision system allowed the acquisition of a considerable number of points over a single sphere, which resulted in very good quality LBIC images.

Additionally, the reliability of the algorithms implemented in *WinTrace* was verified in two independent ways on the basis of different simulations and of experimental measurements. First, the comparison was made between *WinTrace* results relative to standard multi-layer flat cells (also implemented in the code), and *RAYN* [31] results. These two simulation results were additionally confirmed by experimental data. Moreover, the direct comparison between Spheral Solar™ Cells simulated and measured reflectance spectra was performed.

On the basis of the LBIC images induced by different lasers and of the measured hemispherical reflectance as well as of the simulated light trapping, the active areas of the single spheres were outlined. The imaging techniques combined with the ray-tracing simulations, allowed the identification of the spherical regions where the incident light should impinge in order that it could be trapped to the maximum extent.

The optical modelling provided the basis for the design of the geometry and material to be chosen for a reflectance-reducing cover. In particular, different alternatives, such as structured rigid encapsulants and flexible front covers, have been investigated. The available materials were critically examined to check both their flexibility, their optical performance and the possibility of being structured.

The results of this work have led to the following key results and conclusions:

1. A potential increase in efficiency of Spheral Solar™ Cells can be achieved by enhancing the light gathering into the cells.
2. The optical dimensions of the silicon spheres (active part of the cell) have been determined experimentally by LBIC measurements.
3. The active area of each silicon sphere, at least under low wavelength illumination, is not the centre of the sphere but the external ring. This has been both theoretically predicted by ray-tracing calculations and experimentally measured by laser scanning.
4. An important innovation which could boost Spheral Power™ Module efficiency to more than 10 % (cell efficiency to more than 11%), is an alternative reflectance-reducing front cover. Such a cover could exploit the flexibility of the cell as well as enhance the off-normal light coupling by precisely focusing light onto the silicon spheres, minimising the light impinging on the aluminium substrate of the cells.
5. Among the available materials, Tefzel® is the one suggested for the module front cover, since it is sufficiently resistant to environmental conditions and at the same time it is flexible and easy to be structured.
6. The specific geometries have been designed both to minimise the number of rays which undergo a primary reflection on the cell substrate and to maximise the total internal

reflection at the cover/air interface. On the basis of the experiments made on bare cells, the performance of different cover structures has been evaluated.

7. Among the analysed structures the spherical one (concentric to the spheres) is the one which showed the highest performance, but valid alternatives are pyramids and truncated pyramids.

The spin-off of the research project is the realisation of the optimised encapsulant according to the suggested specifications, which will entirely depend on future agreements with the manufacturers.

The results of the research project support the tasks of the European Solar Test Installation of the European Commission's Joint Research Centre (Ispra), namely providing pre-normative research on methodologies and support to industry. These results have provided the acquisition of enough expertise also to move into a favourable position in future competitive actions.

References

[1] W. Wettling, R. P. Mertens, W. C. Sinke and H. W. Schock, Proc. Eurosun '96, 10th Internatiolnales Sonnenforum, Freiburg, September 1996.

[2] M. A. Green, *Solar Cells*, University of New South Wales, Kensington, 1992.

[3] M. A. Green, *Silicon Solar Cells*, Centre for PV Devices and Systems, University of New South Wales, Sydney, 1995.

[4] Larry D. Partain, *"Solar Cells and their Applications"*, John Wiley & Sons Inc., 1995.

[5] R. S. Ohl, *"Light Sensitive Electric Device"*, US Patent 240252, filed 27 March 1941; *"Light Sensitive Electric Device Including Silicon"*, US Patent 2443542, filed 27 May 1941.

[6] C.M. Chong, PhD Thesis, University of New South Wales, 1989.

[7] J. Zhao, W. Wang and M. A. Green, Prog. Photovoltaics 2, 227-230, 1994.

[8] A. K. Ghosh, C. Fishman and T. Feng, J. Appl. Phys., 51(1980)446.

[9] W.H.Bloss, Proc. 12th European Photovoltaic Solar Energy Conference, Amsterdam, 1994.

[10] T. Chu et al., 11th European Photovoltaic Solar Energy Conference, Montreux, 1992.

[11] C. Ferekides and J. Britt, 11th European Photovoltaic Solar Energy Conference, Montreux, 1992.

[12] V. Nadenau et. al, Progress in Photovoltaics, Vol. 3 (1995) 363.

[13] J.D.Levine, G.B.Hotchkiss and M.D.Hammerbacher, Proc. 22nd IEEE- PVSC, Las Vegas, 1991.

[14] R.R.Schmit, J. S.Reynolds, J. K.Arch and G. D. Stevens, Proc. 1st. World Conference on PV Energy Conversion, Hawaii, 1994.

[15] R.R.Schmit, B.Felder and G.B.Hotchkiss, Proc. 23rd IEEE- PVSC, 1993.

[16] J.K.Arch, J. S.Reynolds, M.D.Hammerbacher, R.K. Ahrenkiel, S.Asher, K.Jones and M. Al-Jassim, Proc. 1st. World Conference on PV Energy Conversion, Hawaii, 1994.

[17] R.K. Ahrenkiel, D.H. Levi and J.K. Arch, Proc. 1st. World Conference on PV Energy Conversion, Hawaii, 1994.

[18] R. Bisconti, E. Haverkamp and W. J. Zaaiman, *"Performance at STC Measurements - Spheral Solar™ Cells - Texas Instruments"*, Technical Note No. I.96.10, Institute for Systems Engineering and Informatics, EC - JRC.

[19] R. Bisconti and H. A. Ossenbrink, Solar Energy Materials and Solar Cells, Proc. PVSEC-9, November 1996.

[20] R. J. Matson, K. A. Emery, I. L. Eisgruber and L. L. Kazmerski, 12th EU PVSEC, Amsterdam, (1994).

[21] J. W. Bishop, PhD Thesis, University of London, 1988.

[22] R. Brendel, Proc. 12th European Photovoltaic Solar Energy Conference, Amsterdam, 1994.

[23] *"IQE1D"*, R. Brendel and R. Plieninger, distributed by Garshing Innovation GmbH.

[24] R. Bisconti and H. A. Ossenbrink, Proc. 13th European Photovoltaic Solar Energy Conference, Nice, 1995.

[25] R. Bisconti and H. A. Ossenbrink, Solar Energy Materials and Solar Cells, Proc. PVSEC-9, November 1996.

[26] *"Applications of the Monte Carlo Method in Statistical Physics"*, K. Binder, Springer-Verlag, Berlin, 1984.

[27] *"Optics"*, M. V. Klein and T. E. Furtak, John Wiley & Sons Inc., 1993.

[28] Sol Nudelman and S. S. Mitra, *"Optical Properties of Solids"*, Plenum Press, New York, 1969.

[29] *"Optical Properties of Solids - New Developments"*, Ed. by B. O. Seraphin, North-Holland, 1976.

[30] J. Zhao and M. Green, IEEE Transactions of Electron Devices, Vol. 38, No. 8, August 1991.

[31] W. R. Runyan, *"Silicon Semiconductor Technology"*, Texas Instruments Electronic Series, McGraw-Hill, 1965.

[32] H. F. Wolf, *"Silicon Semiconductor Data"*, Pergamon Press, 1969.

[33] *"Principles of Optics"*, M. Born and E. Wolf, 5th ed., New York Pergamon, 1975.

[34] M. Herzberger, *"Modern Geometrical Optics"*, Interscience Publishers Inc., New York, 1958.

[35] E. B. Brown, *"Modern Optics"*, Reinhold Publishing Corp., New York, 1965.

[36] J. M. Hammersly and D. C. Handscomb, *"Monte Carlo Methods"*, Methuen, London, 1964.

[37] *"A Current View of Random Number Generators"*, Computer Science and Statistics, Elsevier Science Publ. B.V. (North Holland), 1995.

[38] N. S. Altman, J. Sci. Comput., 9 (5) (1988) 941.

[39] J. Schumacher, S. Sterk, B. Wagner and W. Warta, Proc. 13th European Photovoltaic Solar Energy Conference, Nice, 1995.

[40] *"Solar Electricity - Engineering of Photovoltaic Systems"*, E. Lorenzo et al., Progensa, 1994.

[41] J.H. Wohlgemuth and R. Petersen, Photovoltaic Module Reliability Workshop, NREL, Golden, CO, 1992, pp. 313-327.

[42] F. J. Pern and A. W. Czanderna, Solar Energy Mater. Solar Cells, 25(1992)3-23.

[43] S. Bailey, G. Landis and N. Fatemi, 13th European Photovoltaic Solar energy Conf., Nice, France, October 1995.

[44] P. Jenkis, G. Landis, N. Fatemi and S. Bailey, Solar Energy Mater. Solar Cells, Vol. 33-2(1994)125-133.

[45] G. A. Landis, 21st IEEE Specialists Conference, Orlando, FL, May 1990.

[46] G. A. Landis, 25th IEEE Specialists Conference, Washington DC, May 1996.

[47] E. Yablonovitch and G. Cody, IEEE Trans. Electron. Dev. ED-29, 300-305, (1982).

[48] D. Redfield, Appl. Phys. Lett. Vol. 25 - 11 (1974) 647-648.

Appendix A Mismatch Calculation

Reference Detector: Sol533
Test Cell: TE004

Device area [mm^2]		400			10000	
Integral		28025.0	28239.4		21713.77	21148.14
Current [A]		0.112	0.113		**2.2561**	**2.1973**
		A1	A2		A3	A4
MisMatch factor	(A3*A2)/(A4*A1)			**1.0267**	**IEC904-7**	

WaveL [nm]	AM15G [W·m^{-2}]	PASAN [W·m^{-2}]	Sol533 [A/W]	Rsr*Ssp [A·m^{-2}/nm]	Rsr*Tsp [A·m^{-2}/nm]	TE04 [A/W]	Tsr*Ssp [A·m^{-2}/nm]	Tsr*Tsp [A·m^{-2}/nm]
300	0.0	0.0	0.0000	0.0	0.0	0.0000	0.0	0.0
310	42.3	0.0	0.0001	0.0	0.0	0.0001	0.0	0.0
320	181.0	110.5	0.0029	0.5	0.3	0.0023	0.4	0.3
330	395.3	275.8	0.0070	2.8	1.9	0.0058	2.3	1.6
340	435.3	441.1	0.0110	4.8	4.8	0.0093	4.0	4.1
350	483.7	852.7	0.0115	5.6	9.8	0.0099	4.8	8.5
360	520.3	1291.6	0.0131	6.8	17.0	0.0116	6.0	14.9
370	666.2	1236.5	0.0239	15.9	29.6	0.0215	14.3	26.6
380	712.5	1181.4	0.0347	24.7	41.0	0.0319	22.7	37.7
390	720.7	1194.2	0.0526	37.9	62.8	0.0480	34.6	57.3
400	1013.1	1252.2	0.0754	76.4	94.4	0.0679	68.8	85.1
410	1158.2	1327.5	0.0961	111.3	127.6	0.0861	99.8	114.3
420	1184.0	1407.1	0.1169	138.5	164.5	0.1042	123.4	146.6
430	1071.9	1478.6	0.1368	146.7	202.3	0.1232	132.1	182.2
440	1302.0	1517.4	0.1532	199.4	232.4	0.1399	182.2	212.3
450	1526.0	1554.2	0.1695	258.6	263.4	0.1565	238.8	243.2
460	1599.6	1582.5	0.1863	298.0	294.8	0.1723	275.7	272.7
470	1581.0	1610.9	0.2031	321.1	327.2	0.1883	297.7	303.3
480	1628.3	1595.0	0.2200	358.3	351.0	0.2044	332.8	326.0
490	1539.2	1512.8	0.2373	365.2	358.9	0.2208	339.9	334.1
500	1548.7	1430.5	0.2545	394.1	364.1	0.2373	367.5	339.5
510	1586.5	1415.9	0.2655	421.2	375.9	0.2475	392.7	350.5
520	1484.9	1418.1	0.2763	410.4	391.9	0.2576	382.5	365.3
530	1572.4	1420.3	0.2873	451.8	408.1	0.2677	421.0	380.3
540	1550.7	1384.5	0.2960	459.1	409.9	0.2758	427.6	381.8
550	1561.5	1348.8	0.3048	475.9	411.1	0.2836	442.8	382.5
560	1531.5	1332.6	0.3159	483.9	421.0	0.2931	448.9	390.6
570	1501.5	1316.3	0.3270	491.0	430.5	0.3025	454.2	398.2
580	1448.5	1297.9	0.3377	489.1	438.3	0.3114	451.1	404.2
590	1395.5	1274.0	0.3467	483.8	441.7	0.3188	444.9	406.2
600	1440.4	1250.2	0.3556	512.3	444.6	0.3262	469.8	407.8
610	1485.3	1223.5	0.3635	540.0	444.8	0.3327	494.2	407.1
620	1459.7	1196.5	0.3716	542.5	444.7	0.3394	495.4	406.1
630	1434.1	1169.9	0.3808	546.1	445.5	0.3470	497.6	405.9
640	1427.0	1143.2	0.3899	556.4	445.7	0.3546	505.9	405.3
650	1419.9	1116.6	0.3990	566.6	445.6	0.3621	514.1	404.3
660	1406.1	1101.6	0.4040	568.0	445.0	0.3650	513.2	402.1
670	1392.3	1089.4	0.4095	570.1	446.1	0.3683	512.7	401.2
680	1261.2	1062.1	0.4193	528.9	445.4	0.3753	473.4	398.7
690	1130.0	1034.8	0.4293	485.1	444.2	0.3824	432.1	395.7
700	1223.4	1007.5	0.4391	537.2	442.4	0.3893	476.3	392.2
710	1316.7	994.3	0.4456	586.7	443.1	0.3929	517.4	390.7
720	1020.6	982.6	0.4521	461.4	444.2	0.3965	404.7	389.6
730	1103.5	970.9	0.4585	506.0	445.2	0.4000	441.4	388.4
740	1211.2	959.3	0.4650	563.2	446.1	0.4034	488.6	387.0
750	1197.4	947.6	0.4715	564.5	446.8	0.4060	486.1	384.7
760	909.3	923.8	0.4764	433.2	440.1	0.4059	369.1	375.0
770	1050.8	897.0	0.4814	505.9	431.8	0.4059	426.5	364.0
780	1131.1	870.1	0.4863	550.1	423.2	0.4056	458.8	352.9

WaveL [nm]	AM15G [W•m^{-2}]	PASAN [W•m^{-2}]	Sol533 [A/W]	Rsr*Ssp [A•m^{-2}/nm]	Rsr*Tsp [A•m^{-2}/nm]	TE04 [A/W]	Tsr*Ssp [A•m^{-2}/nm]	Tsr*Tsp [A•m^{-2}/nm]
790	1106.4	843.3	0.4914	543.6	414.4	0.4054	448.5	341.9
800	1081.6	816.5	0.4963	536.8	405.2	0.4048	437.9	330.5
810	936.4	1042.8	0.4993	467.5	520.6	0.4021	376.5	419.3
820	815.8	1297.3	0.5022	409.7	651.5	0.3993	325.8	518.1
830	891.1	1260.5	0.5052	450.2	636.8	0.3965	353.3	499.8
840	959.9	932.3	0.5082	487.8	473.8	0.3936	377.8	367.0
850	969.4	604.1	0.5112	495.5	308.8	0.3879	376.0	234.3
860	978.9	729.5	0.5119	501.1	373.4	0.3796	371.6	276.9
870	956.1	905.2	0.5127	490.2	464.1	0.3714	355.1	336.2
880	933.2	1043.7	0.5134	479.1	535.8	0.3632	338.9	379.0
890	859.3	1095.2	0.5142	441.9	563.2	0.3549	305.0	388.7
900	785.4	1146.8	0.5149	404.5	590.5	0.3448	270.8	395.4
910	708.0	1115.6	0.5134	363.5	572.8	0.3292	233.1	367.2
920	678.9	1075.3	0.5118	347.4	550.3	0.3135	212.9	337.2
930	403.6	1035.0	0.5102	205.9	528.1	0.2981	120.3	308.5
940	273.4	1006.8	0.5086	139.0	512.0	0.2826	77.3	284.5
950	338.7	1006.9	0.5071	171.7	510.5	0.2673	90.5	269.1
960	464.1	981.1	0.4974	230.8	488.0	0.2454	113.9	240.8
970	566.7	944.2	0.4878	276.4	460.5	0.2231	126.4	210.7
980	646.4	895.4	0.4780	309.0	428.0	0.2014	130.2	180.4
990	720.8	798.8	0.4684	337.6	374.1	0.1805	130.1	144.2
1000	738.9	702.2	0.4587	339.0	322.1	0.1634	120.7	114.7
1010	726.8	617.7	0.4270	310.4	263.8	0.1425	103.6	88.0
1020	714.7	536.2	0.3953	282.6	212.0	0.1231	88.0	66.0
1030	702.6	492.5	0.3636	255.5	179.1	0.1050	73.8	51.7
1040	690.5	486.8	0.3319	229.2	161.6	0.0884	61.1	43.1
1050	672.8	481.1	0.3003	202.0	144.5	0.0760	51.2	36.6
1060	655.2	462.2	0.2697	176.7	124.6	0.0747	48.9	34.5
1070	637.5	439.9	0.2391	152.4	105.2	0.0719	45.8	31.6
1080	562.5	417.7	0.2085	117.3	87.1	0.0677	38.1	28.3
1090	487.6	395.5	0.1780	86.8	70.4	0.0620	30.2	24.5
1100	412.6	373.2	0.1474	60.8	55.0	0.0548	22.6	20.5
1110	260.8	411.6	0.1294	33.7	53.2	0.0512	13.3	21.1
1120	108.9	465.2	0.1113	12.1	51.8	0.0467	5.1	21.7
1130	189.1	518.7	0.0931	17.6	48.3	0.0413	7.8	21.4
1140	158.1	572.3	0.0751	11.9	43.0	0.0351	5.5	20.1
1150	244.2	625.8	0.0570	13.9	35.7	0.0280	6.8	17.5
1160	330.4	651.9	0.0469	15.5	30.6	0.0241	8.0	15.7
1170	396.3	671.1	0.0367	14.6	24.6	0.0198	7.8	13.3
1180	460.0	690.3	0.0265	12.2	18.3	0.0149	6.8	10.3
1190	441.8	709.5	0.0163	7.2	11.6	0.0095	4.2	6.8
1200	423.6	728.7	0.0062	2.6	4.5	0.0037	1.6	2.7

Appendix B Optical Data Files

SILICON: n (Real)

##TITEL= Si.N
##JCAMP
##DATA TYPE = n of Silicon
##SAMPLE DESCRIPTION= Data from M.A.Green, ""High Efficiency Cells"","
##(Trans Tech Publications, Aedermannsdorf, 1987), p 228"
##DATE= 6.8.95
##XFACTOR= 1
##YFACTOR= 1
##FITSTX= 250
##LASTX= 1250
##NPOINTS= 101
##XYDATA=

WL [nm]	*n (Si)*	*WL [nm]*	*n (Si)*	*WL [nm]*	*n (Si)*
250	1.6	600	3.933	950	3.59
260	1.98	610	3.916	960	3.586
270	2.214	620	3.892	970	3.583
280	3.244	630	3.872	980	3.579
290	4.473	640	3.854	990	3.575
300	4.894	650	3.84	1000	3.572
310	4.953	660	3.816	1010	3.568
320	4.983	670	3.8	1020	3.565
330	5.092	680	3.787	1030	3.562
340	5.234	690	3.774	1040	3.559
350	5.451	700	3.762	1050	3.556
360	6.147	710	3.751	1060	3.553
370	6.89	720	3.741	1070	3.55
380	6.51	730	3.731	1080	3.548
390	6.053	740	3.721	1090	3.546
400	5.619	750	3.711	1100	3.543
410	5.374	760	3.702	1110	3.541
420	5.13	770	3.693	1120	3.539
430	4.989	780	3.685	1130	3.536
440	4.824	790	3.678	1140	3.534
450	4.737	800	3.671	1150	3.532
460	4.608	810	3.664	1160	3.53
470	4.525	820	3.657	1170	3.528
480	4.454	830	3.651	1180	3.526
490	4.347	840	3.645	1190	3.524
500	4.281	850	3.639	1200	3.522
510	4.256	860	3.633	1210	3.52
520	4.207	870	3.627	1220	3.518
530	4.159	880	3.622	1230	3.517
540	4.112	890	3.617	1240	3.515
550	4.084	900	3.612	1250	3.513
560	4.049	910	3.607	##END	
570	4.025	920	3.603		
580	3.987	930	3.598		
590	3.958	940	3.594		

SILICON: k (Imaginary)

##TITEL= Si.k
##JCAMP
##DATA TYPE = k of Silicon
##SAMPLE DESCRIPTION= Data from M.A.Green, ""High Efficiency Cells"","
##(Trans Tech Publications, Aedermannsdorf, 1987), p 228"
##except the value for 1250 nm
##DATE= 6.8.95
##XFACTOR= 1
##YFACTOR= 1
##FIRSTX= 250
##LASTX= 1250
##NPOINTS= 101
##XYDATA=

WL [nm]	*k (Si)*	*WL [nm]*	*k (Si)*	*WL [nm]*	*k (Si)*
250	3.580989	610	0.019854	970	0.00088
260	4.344934	620	0.018847	980	0.000741
270	4.748392	630	0.017798	990	0.000622
280	5.236202	640	0.016705	1000	0.000509
290	4.915505	650	0.015621	1010	0.000411
300	3.939088	660	0.014548	1020	0.000324
310	3.552341	670	0.013489	1030	0.000248
320	3.259496	680	0.012662	1040	0.000187
330	3.12501	690	0.011915	1050	0.000136
340	3.030313	700	0.011141	1060	9.36E-05
350	3.008031	710	0.010509	1070	6.81E-05
360	2.979383	720	0.009798	1080	5.33E-05
370	2.155278	730	0.009178	1090	4.08E-05
380	0.882992	740	0.008598	1100	3.06E-05
390	0.527599	750	0.008009	1110	2.38E-05
400	0.340592	760	0.007463	1120	1.78E-05
410	0.254489	770	0.006942	1130	1.35E-05
420	0.191511	780	0.006449	1140	9.16E-06
430	0.158431	790	0.005979	1150	6.22E-06
440	0.129552	800	0.005532	1160	3.88E-06
450	0.109578	810	0.005105	1170	2.05E-06
460	0.092978	820	0.004705	1180	6.10E-07
470	0.081535	830	0.004326	1190	3.41E-07
480	0.069519	840	0.003971	1200	2.20E-07
490	0.061999	850	0.003626	1210	1.25E-07
500	0.054909	860	0.003305	1220	7.48E-08
510	0.04789	870	0.003005	1230	3.72E-08
520	0.042208	880	0.002724	1240	1.48E-08
530	0.039097	890	0.002458	1250	5.00E-09
540	0.034807	900	0.002206	##END	
550	0.031294	910	0.00197		
560	0.028743	920	0.00175		
570	0.026943	930	0.001547		
580	0.025062	940	0.001361		
590	0.022396	950	0.001187		
600	0.021008	960	0.001024		

TiO_2: n (Real)

##TITEL= TiO2.N
##JCAMP
##DATA TYPE = n of TiO2
##SAMPLE DESCRIPTION = Data from Handbook of Optical Constants of Solids"""
##DATE= 6.8.95
##XFACTOR= 1
##YFACTOR= 1
##FIRSTX= 210
##LASTX= 1440
##NPOINTS= 67
##XYDATA=

WL [nm]	*n (TiO_2)*	*WL [nm]*	*n (TiO_2)*
210	1.46	880	2.635
217	2.04	900	2.635
228	2.06	920	2.63
251	2.19	940	2.625
266	2.205	960	2.625
270	2.51	980	2.62
272	2.545	1000	2.62
273	2.755	1020	2.615
288	3.195	1040	2.61
294	3.625	1060	2.61
306	3.42	1080	2.61
318	4.69	1100	2.61
335	4.045	1120	2.605
360	3.625	1140	2.6
412	3.12	1160	2.6
420	3.1	1180	2.6
440	3.02	1200	2.6
460	2.96	1220	2.6
480	2.915	1240	2.595
500	2.87	1260	2.59
520	2.84	1280	2.59
540	2.815	1300	2.59
560	2.79	1320	2.59
580	2.77	1340	2.59
600	2.75	1360	2.59
620	2.735	1380	2.59
640	2.725	1400	2.59
660	2.71	1420	2.59
680	2.7	1440	2.59
700	2.69	##END	
720	2.68		
740	2.675		
760	2.67		
780	2.66		
800	2.655		
820	2.655		
840	2.645		
860	2.645		

TiO_2: k (Imaginary)

##TITEL= TiO2.k
##JCAMP
##DATA TYPE = k of TiO2
##SAMPLE DESCRIPTION = Data from Handbook of Optical Constants of Solids"""
##DATE= 6.8.95
##XFACTOR= 1
##YFACTOR= 1
##FIRSTX= 210
##LASTX= 1440
##NPOINTS= 67
##XYDATA=

WL [nm]	*k (TiO_2)*	*WL [nm]*	*k (TiO_2)*
210	1.117	840	0
217	1.1605	860	0
228	1.24	880	0
242	1.369	900	0
251	1.5	920	0
260	1.678	940	0
265	1.889	960	0
272	2.372	980	0
279	2.491	1000	0
284	2.583	1020	0
294	2.725	1040	0
306	2.295	1060	0
318	1.985	1080	0
335	0.799	1100	0
360	0.184	1120	0
412	0.015	1140	0
420	0	1160	0
440	0	1180	0
460	0	1200	0
480	0	1220	0
500	0	1240	0
520	0	1260	0
540	0	1280	0
560	0	1300	0
580	0	1320	0
600	0	1340	0
620	0	1360	0
640	0	1380	0
660	0	1400	0
680	0	1440	0
700	0	##END	
720	0		
740	0		
760	0		
780	0		
800	0		
820	0		

Appendix C Examples of *WinTrace* Routines

This appendix contains some examples of *WinTrace* routines.

The chosen routines correspond to the greyed blocks in the flowchart of Fig. 4.4 page 111, and they belong to the **Calc.bas** module as indicated in the flowchart shown below. In this flowchart all the Modules and Forms belonging to the programme are listed from the lowest level ones (i.e. the programme interface) to the **Simul.bas** which is the most structured one.

Moreover, in order to let the reader understand the meaning of the *defined variables* used in the programme routines, a print out of the module **Global.bas**, containing all the global declarations, is also given.

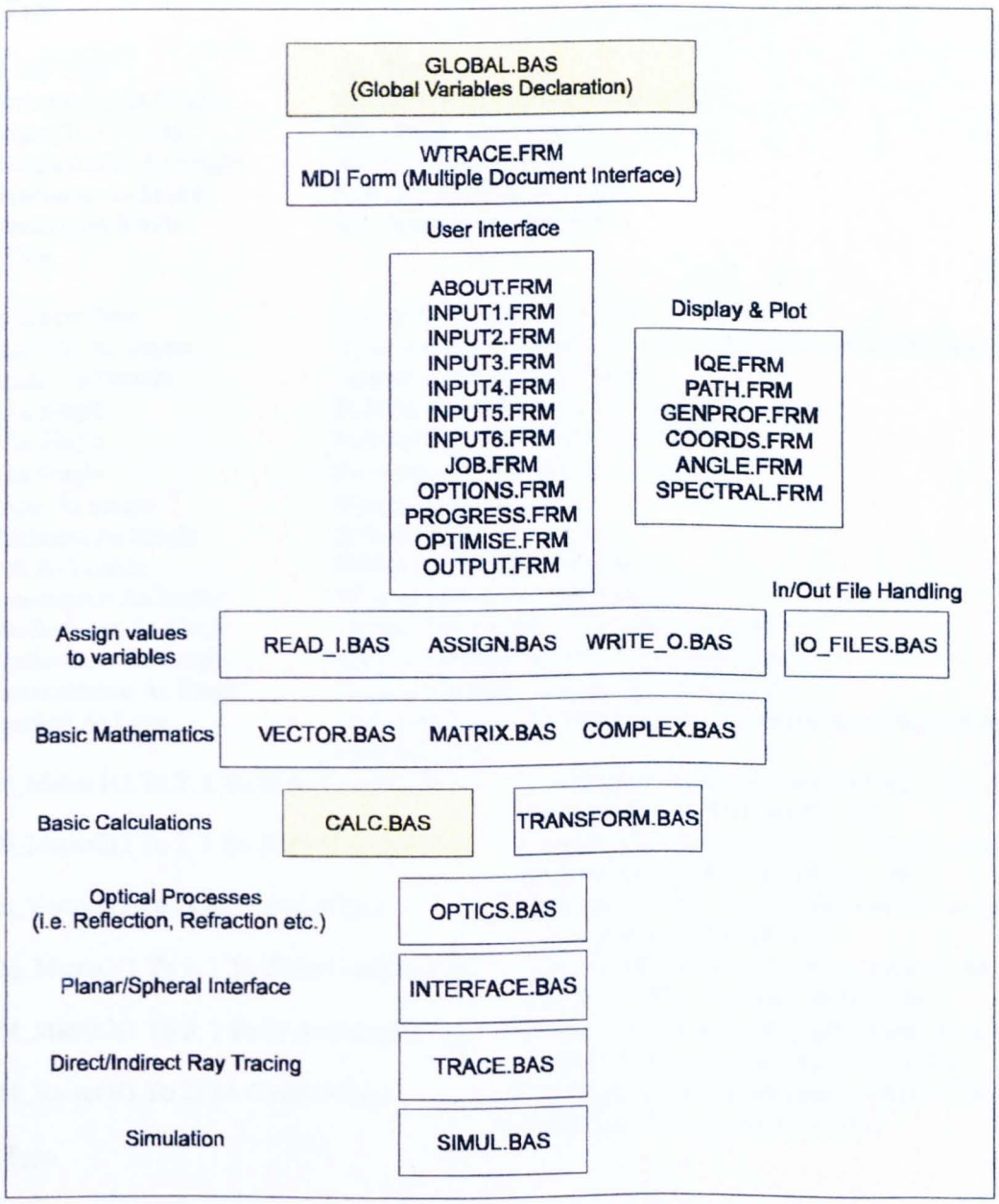

Flowchart of the Visual Basic Modules and Forms of the programme *WinTrace*

MODULE GLOBAL.BAS

```
'Global Constants
Global Const ZERO = 1E-30                          'Very small number approximating zero
Global Const EPSILON = 1E-08                       'Very small number
Global Const Pi = 3.14159265359                    'The number π
Global Const DEGRAD = 1.74532925199433E-02         'Number transforming angles expressed in
                                                   degrees into radians
Global Const RADDEG = 57.2957795131                'Number transforming angles expressed in
                                                   radians into degrees
Global Const NAIR = 1#                             'Index of Refraction n (real) of Air
Global Const KAIR = 0#                             'Index of Refraction k (imaginary) of Air

'User Defined Types
Type ComplexType                   'Complex-Number Type
  RealPart As Single               'Real component
  ImmPart As Single                'Imaginary component
End Type

Type RayType                       'Ray Type
  Direction(2) As Single           'Ray Direction Cosines: vector in S^3
  Origin(2) As Single              'Ray Origin: vector in S^3
  Destination(2) As Single         'Ray Destination: vector in S^3
  Magnitude As Single              'Ray Magnitude scalar value
  Intensity As Single              'Ray Intensity: scalar value
End Type

Type SphereType                    'Sphere Type (defining a spherical layer)
  Centre(2) As Single              ' Sphere Centre: vector in S^3, individuating the simulated sphere
  Radius As Double                 ' Sphere Radius: scalar value
  n As Single                      'Index of Refraction n of the material
  k As Single                      'Index of Refraction k of the material
  a As Single                      'Absorption coefficient α = 4πλk/c
  Angle As Single                  'Elevation on the sphere
  Thickness As Single              'Spherical Layer Thickness
  Path As Double                   'Optical Path inside the sphere
  Absorptance As Single            'Absorptance of the Spherical Layer
  DReflectance As Single           'Diffuse Reflectance of the Spherical Layer
  SReflectance As Single           'Specular Reflectance of the Spherical Layer
  Transmittance As Single          'Transmittance through the Spherical Layer
  Touched As Long                  'Intersected Layer Number (layers are counted from the external
                                   to the internal)
  TE_Matrix1(1 To 2, 1 To 2) As ComplexType   'Transmission Matrix (Electric wave) to be used
                                              when the layer is the external one
  TE_Matrix2(1 To 2, 1 To 2) As ComplexType   'Transmission Matrix (Electric wave) to be used
                                              when the layer is not the external one
  TE_Vector3(1 To 2) As ComplexType           'Transmission Vector (Electric wave) to be used
                                              when the layer is the last one
  TM_Matrix1(1 To 2, 1 To 2) As ComplexType   'Transmission Matrix (Magnetic wave) to be
                                              used when the layer is the external one
  TM_Matrix2(1 To 2, 1 To 2) As ComplexType   'Transmission Matrix (Magnetic wave) to be
                                              used when the layer is not the external one
  TM_Vector3(1 To 2) As ComplexType           'Transmission Vector (Magnetic wave) to be
                                              used when the layer is the last one
End Type
```

```
Type PlaneType                          'Plane(Flat Layer) Type
  Direction(2) As Single                'Plane Direction Cosines: vector in S^3
  n As Single                           'Index of Refraction n of the material
  k As Single                           'Index of Refraction k of the material
  a As Single                           'Absorption coefficient α = 4πλk/c
  Shift As Single                       'Shift of the Al plane with respect to the sphere centres
  Thickness As Single                   'Plane Thickness
  Absorptance As Single                 'Absorptance of the Flat Layer
  DReflectance As Single                'Diffuse Reflectance of the Flat Layer
  SReflectance As Single                'Specular Reflectance of the Flat Layer
  Transmittance As Single               'Transmittance of the Flat Layer
  Touched As Long                       'Intersected Layer Number
  TE_Matrix1(1 To 2, 1 To 2) As ComplexType   'Transmission Matrix (Electric wave) to be used
                                              when the layer is the external one
  TE_Matrix2(1 To 2, 1 To 2) As ComplexType   'Transmission Matrix (Electric wave) to be used
                                              when the layer is not the external one
  TE_Vector3(1 To 2) As ComplexType           'Transmission Vector (Electric wave) to be used
                                              when the layer is the last one
  TM_Matrix1(1 To 2, 1 To 2) As ComplexType   'Transmission Matrix (Magnetic wave) to be
                                              used when the layer is the external one
  TM_Matrix2(1 To 2, 1 To 2) As ComplexType   'Transmission Matrix (Magnetic wave) to be
                                              used when the layer is not the external one
  TM_Vector3(1 To 2) As ComplexType           'Transmission Vector (Magnetic wave) to be
                                              used when the layer is the last one
End Type

Type CellType                           'Cell Type
  Active_DT As Single                   'Direct Trapping Contribution to the Cell
  Active_IT As Single                   'Indirect Trapping Contribution to the Cell
  NotActive_DT As Single                '% of the Cell area not active for Direct Trapping
  Absorptance As Single                 'Cell Absorptance
  DReflectance As Single                'Cell Diffuse Reflectance
  SReflectance As Single                'Cell Specular Reflectance
  Transmittance As Single               'Cell Transmittance
End Type

'Global Arrays
Global n0 As ComplexType                'Refraction Index before any interface
Global n1 As ComplexType                'Refraction Index after any interface

'Global Counters
Global RUNS As Integer                  'Number of Simulations in a Job
Global Run_Time As Long                 'Calculation Run Time
Global Entries As Long                  'No. of Incident Rays (Monte Carlo Events) for a simul.
Global Total_Entries As Long            'Tot. No. of Incident Rays (Monte Carlo Events) for a job
Global Generations As Long              'Counter for Entry
Global No_of_Reflections As Integer     'No. of Reflections of a single ray (or ray-components)
Global Direct_Intensity As Long         'Counter for Direct Intensity Absorption
Global Indirect_Intensity As Long       'Counter for Indirect Intensity Absorption
Global Externally_Lost_Intensity As Single 'Counter for Intensity back to air
Global TIRefl As Long                   'No. of Rays undergoing Total Internal Reflection (TIR)
Global Lost_Intensity As Single         'Counter for Lost Intensity: Externally Lost + Internally
                                        Lost (emerging from layers when there is no TIR)
Global LostRays As Single               'Rays which are not touching any active part of the cell
Global No_of_Layers As Integer          'No. of Input layers
Global Layer_Number As Integer          'Layer Identification Number
```

```
'Global Flags
Global Break As Boolean                          'Job interruption
Global Intersection As Boolean                   'Analytical Intersection ray-sphere = true
Global Gen1 As Boolean                           'Generation over 30 deg.
Global Gen2 As Boolean                           'Generation over 60 deg.
Global Lost As Boolean                           'Lost Ray
Global ONSphere As Boolean                       'Primary Ray impinging on a sphere
Global ONAluminium As Boolean                    'Primary Ray impinging on the aluminium
Global ONPlane As Boolean                        'Primary Ray impinging on a flat wafer
Global Direct_Trapping As Boolean                'Calculation option: only direct trapping
Global Indirect_Trapping As Boolean              'Calculation option: direct & indirect trapping
Global Secondary_Reflections As Boolean          'Calculation option: considering surrounding spheres
Global Normal_Incidence As Boolean               'Calculation option: only normal incident beam
Global Flat As Boolean                           'Calculation option: flat cell simulation
Global Internal As Boolean                       'Calculation option: following internal rays
Global Shadowing As Boolean                      'Calculation option: considering shadowing effect
Global Exact_Method As Boolean                   'Calculation option: Applying Fresnel's Formulas
Global Matrix_Method As Boolean                  'Calculation option: Applying Transmission Matrix Method
Global ARC1 As Boolean                           'Calculation option: only one AR-coating layer
Global ARC2 As Boolean                           'Calculation option: double AR-coating layer
Global Encaps1 As Boolean                        'Calculation option: only one encapsulant layer
Global Encaps2 As Boolean                        'Calculation option: double encapsulant layer
Global Last_Layer As Boolean                     'Calculation option: last interface
Global Aluminium As Boolean                      'Calculation option: considering aluminium reflections

'Global Variables
'Vectors in S3
Global V1XV2(2) As Single                        'Vector Product
Global V1PlusV2(2) As Single                     'Vector Sum
Global V1MinusV2(2) As Single                    'Vector Difference
Global VDir(2) As Single                         'Vector Direction
'Matrix in S2 & S3
Global M1xM2(1 To 2, 1 To 2) As Single           'Matrix Product
Global M1xV2(1 To 2) As Single                   'Matrix by Vector Product
Global Trans_Matrix(2, 2) As Single              'Transformation Matrix
Global CM1xCM2(1 To 2, 1 To 2) As ComplexType    'Complex Matrix Product
Global CM1xCV2(1 To 2) As ComplexType            'Complex Matrix by Vector Product
Global TE_Matrix(1 To 2, 1 To 2) As ComplexType  'Transformation Matrix TE mode
Global TM_Matrix(1 To 2, 1 To 2) As ComplexType  'Transformation Matrix TM mode
Global Temp_TE_Matrix(1 To 2, 1 To 2) As ComplexType 'Temporary Transformation Matrix
Global Temp_TM_Matrix(1 To 2, 1 To 2) As ComplexType 'Temporary Transformation Matrix
Global Temp1_TE_Matrix(1 To 2, 1 To 2) As ComplexType 'Temporary Transformation Matrix
Global Temp1_TM_Matrix(1 To 2, 1 To 2) As ComplexType 'Temporary Transformation Matrix
Global Coeff_TE(1 To 2) As ComplexType           'Transformation Coefficient TE mode
Global Coeff_TM(1 To 2) As ComplexType           'Transformation Coefficient TM mode
'Angles (expressed in radians) and Angle Cosines
Global Beam_Inclination_Angle As Single          'Incident Illumination Angle
Global Elevation As Single                       'Elevation Angle on the Sphere Surface
Global Angle_Inc As Single                       'Angle of Incidence
Global Angle_Refl As Single                      'Angle of Reflection
Global Angle_Refr As Single                      'Angle of Refraction
Global Cos_Inc As Single                         'Cosine of the Angle of Incidence
Global Cos_Refl As Single                        'Cosine of the Angle of Reflection
Global Cos_Refr As Single                        'Cosine of the Angle of Refraction
'Lengths
Global Centre_Dist As Single                     'Distance between two sphere centres
Global Sphere_Distance As Single                 'External Sphere Spacing
```

```
'Optical Properties
Global Wavelength As Single                 'Incident Wavelength
Global NrOfData As Single                   'No. of data in an optical data file
Global Material() As Single                 'To identify the optical data file to read
'Rays
Global Incident As RayType                  'Incident Ray Component
Global ExternalIncident As RayType          'External Incident Ray Component
Global TempIncident As RayType              'Temporary Incident Ray Component
Global Reflected As RayType                 'Reflected Ray Component
Global Refracted As RayType                 'Refracted Ray Component
Global Transmitted As RayType               'Transmitted Ray Component
Global Absorbed As RayType                  'Absorbed Ray Component
Global TempTransmitted As RayType           'Temporary Transmitted Ray Component
Global Normal As RayType                    'Normal Direction
'Sphere Indexes
Global Index_n As Integer                   'Index for localising the Sphere Centre (X dir.)
Global Index_m As Integer                   'Index for localising the Sphere Centre (Y dir.)
'Spheres
Global Sphere(0 To 3, 0 To 3) As SphereType          'Multi-spherical layers
Global ARC(2, 0 To 3, 0 To 3) As SphereType          'AR-coating layers
Global Encapsulant(2, 0 To 3, 0 To 3) As SphereType  'Encapsulant layers
'Plane
Global Substrate As PlaneType               'Aluminium layer
Global Layer(1 To 3) As PlaneType           'Planar Cell layers
'Cell
Global Cell As CellType                     'Cell
'Input Files
Global Filename As String                   'This variable keeps track of the filename information for opening
                                            and closing files
Global nboffiles As Integer                 'Number of Files
Global nameoffile() As String               'Name of File
Global Directory As String                  'Working Directory
Global SphereFileN As String                'Optical File name (for n)
Global SphereFileK As String                'Optical File name (for k)
Global ARC1FileN As String                  'Optical File name (for n)
Global ARC1FileK As String                  'Optical File name (for k)
Global ARC2FileN As String                  'Optical File name (for n)
Global ARC2FileK As String                  'Optical File name (for k)
Global Encaps1FileN As String               'Optical File name (for n)
Global Encaps1FileK As String               'Optical File name (for k)
Global Encaps2FileN As String               'Optical File name (for n)
Global Encaps2FileK As String               'Optical File name (for k)
'Output Files
Global SOutputFile1  As String              'Standard Output File for Simulation (#1)
Global JOutputFile1  As String              'Standard Output File for Job (#1)
Global OutputFile2  As String               'Customised Output File (#2)
Global OutputFile3  As String               'Customised Output File (#3)
Global OutputFile4  As String               'Customised Output File (#4)
Global OutputFile5  As String               'Customised Output File (#5)
Global OutputFile6  As String               'Customised Output File (#6)
Global OutputFile7  As String               'Customised Output File (#7)
```

FROM MODULE CALC.BAS

```
Sub Random_Point(LayerData As SphereType)
'Random choice of the intersection point of a primary incident ray on a spherical layer

'Variables declaration at the procedure level
Dim Ran1, Ran2, Yhigh, Xv, Yv, fi, r, XP1, YP1

Do      'Loop to randomise the co-ordinates of the point of incidence in the simulated region
   Randomize    'Initialises the random number generators
   Ran1 = Rnd   'First random number generator
   Ran2 = Rnd   'Second random number generator
   If Gen1 Then      'Generation over 30 deg.
      Xv = Centre_Dist / 2
      Yv = Tan(DEGRAD * 30)
      Incident.Destination(0) = Ran1 * Xv
      Incident.Destination(1) = Ran2 * Yv
      r = Sqr(Incident.Destination(0) ^ 2 + Incident.Destination(1) ^ 2)
      fi = Atn(Incident.Destination(1) / Incident.Destination(0))
   ElseIf Gen2 Then   'Generation over 60 deg.
      Xv = Centre_Dist / 2
      Yv = Tan(DEGRAD * 30)
      Incident.Destination(0) = Ran1 * Xv
      Incident.Destination(1) = Ran2 * Yv
      r = Sqr(Incident.Destination(0) ^ 2 + Incident.Destination(1) ^ 2)
      fi = Atn(Incident.Destination(1) / Incident.Destination(0))
      If Generations Mod 2 = 0 Then
         XP1 = r * Cos(DEGRAD * 60 - fi)
         YP1 = r * Sin(DEGRAD * 60 - fi)
         r = Sqr(XP1 ^ 2 + YP1 ^ 2)
         fi = Atn(XP1 / YP1)
      End If
   End If
Loop Until fi <= (DEGRAD * 30)  'End of Do Loop

'Check if the chosen Random Point is on the sphere
If Sqr(Incident.Destination(0) ^ 2 + Incident.Destination(1) ^ 2) <= LayerData.Radius Then
   Incident.Destination(2) = Sqr( LayerData.Radius ^ 2- Incident.Destination(0) ^ 2 +
                              - Incident.Destination(1) ^ 2)
   ONSphere = True
'Determination of the possible sphere for secondary reflections on the basis of the elevation of the
random point on the sphere surface
   If fi >= 0 And fi <= Atn(fi / Sqr(-fi * fi + 1)) Then
      Temp_Index_n = 2
      Temp_Index_m = 0
      XTempo = Incident.Destination(0)
      YTempo = Incident.Destination(1)
      ZTempo = Incident.Destination(2)
   ElseIf fi >= Atn(fi / Sqr(-fi * fi + 1)) And fi <= 30 Then
      Temp_Index_n = 3
      Temp_Index_m = 1
   End If
Else     'The chosen Random Point is on the aluminium substrate
   ONAluminum = True
   Substrate.Touched = Substrate.Touched + 1
End If
If frmCustomise.Check4.Value = 1 Then Print_Random_Coords_#4   'Print Data on File #4
End Sub
```

```
Sub Calc_Intersection_Ray_Sphere(RayData As RayType, LayerData As SphereType)
'This procedure calculates analytically the intersection point between an oriented direction and a
sphere in S3

'Variables declaration at the procedure level
Dim a1, b0, b1, b2, b, C, Delta, Root1, Root2, Dist1, Dist2
Static IntP1(2) As Single
Static IntP2(2) As Single

Intersection = False

'Calculation of the different parameters comparing in a second order equation
a1 = (RayData.Direction(0)) ^ 2 + (RayData.Direction(1)) ^ 2 + (RayData.Direction(2)) ^ 2
b0 = RayData.Origin(0) - LayerData.Centre(0)
b1 = RayData.Origin(1) - LayerData.Centre(1)
b2 = RayData.Origin(2) - LayerData.Centre(2)
b = RayData.Direction(0) * b0 + RayData.Direction(1) * b1 + RayData.Direction(2) * b2
C = (b0) ^ 2 + (b1) ^ 2 + (b2) ^ 2 - (LayerData.Radius) ^ 2
Delta = b ^ 2 - a1 * C

If Delta >= 0# Then        'Real solutions to the second order equation
  If a1 <> 0# Then
    'Two real solutions (roots) of the second order equation
    Root1 = (-b + Sqr(Delta)) / a1
    Root2 = (-b - Sqr(Delta)) / a1
    'Intersection point 1
    IntP1(0) = RayData.Origin(0) + RayData.Direction(0) * Root1
    IntP1(1) = RayData.Origin(1) + RayData.Direction(1) * Root1
    IntP1(2) = RayData.Origin(2) + RayData.Direction(2) * Root1
    'Intersection point 2
    IntP2(0) = RayData.Origin(0) + RayData.Direction(0) * Root2
    IntP2(1) = RayData.Origin(1) + RayData.Direction(1) * Root2
    IntP2(2) = RayData.Origin(2) + RayData.Direction(2) * Root2
    'Case of two coincident solutions: ray tangent to the sphere
    If IntP1(0) - IntP2(0) = 0 And IntP1(1) - IntP2(1) = 0 And IntP1(2) - IntP2(2) = 0 Then
      RayData.Destination(0) = IntP1(0)
      RayData.Destination(1) = IntP1(1)
      RayData.Destination(2) = IntP1(2)
      Dist1 = VECT_Dist(IntP1(), RayData.Origin())
      RayData.Magnitude = Dist1
    'Case of two different solutions
    ElseIf Abs(RayData.Origin(0) - IntP1(0)) < EPSILON Then      'Intersection point previous
                                                                 layer coincident with IntP1
      Dist1 = 0
      Dist2 = VECT_Dist(IntP2(), RayData.Origin())
    ElseIf Abs(RayData.Origin(0) - IntP2(0)) < EPSILON Then      'Intersection point previous
                                                                 layer coincident with IntP1
      Dist1 = VECT_Dist(IntP1(), RayData.Origin())
      Dist2 = 0
    Else  'Case of two different solutions: calculation of the two distances between the ray
          origin (intersection point on the previous layer) and the current two intersection points
      Dist1 = VECT_Dist(IntP1(), RayData.Origin())
      Dist2 = VECT_Dist(IntP2(), RayData.Origin())
    End If
```

```
'Choice of one of the two solutions on the basis of the shortest distance between the ray origin and
the ray destination

    If Dist1 < Dist2 Then          'Choice of IntP1()
      RayData.Destination(0) = IntP1(0)
      RayData.Destination(1) = IntP1(1)
      RayData.Destination(2) = IntP1(2)
      RayData.Magnitude = Dist1
      'Ray Path Calculation [cm]
      If ARC1 = False And Encaps1 = False Then
        RayData.Destination(0) = IntP2(0)
        RayData.Destination(1) = IntP2(1)
        RayData.Destination(2) = IntP2(2)
        LayerData.Path = VECT_Dist(IntP2(), IntP1())
      Else
        If No_of_Reflections = No_of_Layers Or Last_Layer = True Then
          LayerData.Path = VECT_Dist(IntP2(), IntP1())
        Else
          LayerData.Path = VECT_Dist(RayData.Origin(), RayData.Destination())
        End If
      End If
    Else                           'Choice of IntP2()
      RayData.Destination(0) = IntP2(0)
      RayData.Destination(1) = IntP2(1)
      RayData.Destination(2) = IntP2(2)
      RayData.Magnitude = Dist2
      'Path Calculation [cm]
      If ARC1 = False And Encaps1 = False Then
        RayData.Destination(0) = IntP1(0)
        RayData.Destination(1) = IntP1(1)
        RayData.Destination(2) = IntP1(2)
        LayerData.Path = VECT_Dist(IntP2(), IntP1())
      Else
        'If there is only one spherical layer or if the condition "last layer" is true then the path is the
        optical path in the sphere calculated by the distance between the two solutions IntP1 and IntP2
        If No_of_Reflections = No_of_Layers Or Last_Layer = True Then
          LayerData.Path = VECT_Dist(IntP2(), IntP1())
        Else
          LayerData.Path = VECT_Dist(RayData.Origin(), RayData.Destination())
        End If
      End If    'Path Calculation
    End If      'Choice of Intersection Point
Else    'If Delta < 0 then imaginary solutions to the second order equation
  Intersection = False
End If

End Sub
```

```
Sub Calc_Spherical_Layer_Matrix(SphericalInterface As SphereType)
'Calculation of the matrices for TE and TM waves impinging on a spherical layer

'Variables declaration at the procedure level
Dim I
Dim OpticalPhaseChange, TEp, TMp
Dim No_One As ComplexType

  If No_of_Reflections = 1 Then  'Matrix for the incident medium (AIR)
    'Electric Component Matrix1
    TEp = n0.RealPart * Cos_Inc
    TMp = (1 / n0.RealPart) * Cos_Inc
    SphericalInterface.TE_Matrix1(1, 1).RealPart = TEp
    SphericalInterface.TE_Matrix1(1, 2).RealPart = -1
    SphericalInterface.TE_Matrix1(2, 1).RealPart = TEp
    SphericalInterface.TE_Matrix1(2, 2).RealPart = 1
    SphericalInterface.TE_Matrix1(1, 1).ImmPart = 0
    SphericalInterface.TE_Matrix1(1, 2).ImmPart = 0
    SphericalInterface.TE_Matrix1(2, 1).ImmPart = 0
    SphericalInterface.TE_Matrix1(2, 2).ImmPart = 0
    'Magnetic Component Matrix1
    SphericalInterface.TM_Matrix1(1, 1).RealPart = TMp
    SphericalInterface.TM_Matrix1(1, 2).RealPart = -1
    SphericalInterface.TM_Matrix1(2, 1).RealPart = TMp
    SphericalInterface.TM_Matrix1(2, 2).RealPart = 1
    SphericalInterface.TM_Matrix1(1, 1).ImmPart = 0
    SphericalInterface.TM_Matrix1(1, 2).ImmPart = 0
    SphericalInterface.TM_Matrix1(2, 1).ImmPart = 0
    SphericalInterface.TM_Matrix1(2, 2).ImmPart = 0
  End If

  If No_of_Reflections < No_of_Layers Then  'Matrices for the dielectric layers
    TEp = n1.RealPart * Cos_Inc
    TMp = (1 / n1.RealPart) * Cos_Inc
    OpticalPhaseChange = (2 * Pi / Wavelength) * n1.RealPart * Cos_Inc * SphericalInterface.Path
                         * 10 ^ 6
    If OpticalPhaseChange > Pi Then
      OpticalPhaseChange = OpticalPhaseChange - Pi
    End If
    'Electric Component Matrix2
    'Real Part
    SphericalInterface.TE_Matrix2(1, 1).RealPart = Cos(OpticalPhaseChange)
    SphericalInterface.TE_Matrix2(1, 2).RealPart = 0
    SphericalInterface.TE_Matrix2(2, 1).RealPart = 0
    SphericalInterface.TE_Matrix2(2, 2).RealPart = Cos(OpticalPhaseChange)
    'Immaginary Part
    SphericalInterface.TE_Matrix2(1, 1).ImmPart = 0
    SphericalInterface.TE_Matrix2(1, 2).ImmPart = -(TEp ^ -1) * Sin(OpticalPhaseChange)
    SphericalInterface.TE_Matrix2(2, 1).ImmPart = -TEp * Sin(OpticalPhaseChange)
    SphericalInterface.TE_Matrix2(2, 2).ImmPart = 0
    'Magnetic Component Matrix2
    'Real Part
    SphericalInterface.TM_Matrix2(1, 1).RealPart = Cos(OpticalPhaseChange)
    SphericalInterface.TM_Matrix2(1, 2).RealPart = 0
    SphericalInterface.TM_Matrix2(2, 1).RealPart = 0
    SphericalInterface.TM_Matrix2(2, 2).RealPart = Cos(OpticalPhaseChange)
    'Immaginary Part
    SphericalInterface.TM_Matrix2(1, 1).ImmPart = 0
    SphericalInterface.TM_Matrix2(1, 2).ImmPart = -(TMp ^ -1) * Sin(OpticalPhaseChange)
```

```
    SphericalInterface.TM_Matrix2(2, 1).ImmPart = -TMp * Sin(OpticalPhaseChange)
    SphericalInterface.TM_Matrix2(2, 2).ImmPart = 0
  Else   'Vector for the silicon sphere (last layer)
    No_One.RealPart = 1
    No_One.ImmPart = 0
    'Electric Component Vector3
    SphericalInterface.TE_Vector3(1).RealPart = 1
    SphericalInterface.TE_Vector3(1).ImmPart = 0
    SphericalInterface.TE_Vector3(2) = Complex_ScalarProduct(n1, Cos_Inc)
    'Magnetic Component Vector3
    SphericalInterface.TM_Vector3(1).RealPart = 1
    SphericalInterface.TM_Vector3(1).ImmPart = 0
    SphericalInterface.TM_Vector3(2) = Complex_ScalarProduct(Complex_Ratio(No_One, n1),
    Cos_Inc)
  End If

End Sub
```